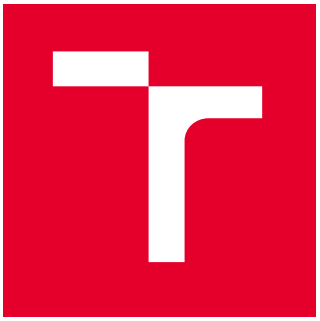

BRNO UNIVERSITY OF TECHNOLOGY

VYSOKÉ UČENÍ TECHNICKÉ V BRNĚ

FACULTY OF CHEMISTRY

FAKULTA CHEMICKÁ

INSTITUTE OF PHYSICAL AND APPLIED CHEMISTRY

ÚSTAV FYZIKÁLNÍ A SPOTŘEBNÍ CHEMIE

STUDY OF CHEMICAL PROCESSES IN EXTRATERRESTRIAL ATMOSPHERES

ŠTÚDIUM CHEMICKÝCH PROCESOV V MIMOZEMSKÝCH ATMOSFÉRACH

DOCTORAL THESIS

DIZERTAČNÍ PRÁCE

AUTHOR — **Ing. Stanislav Chudják**

AUTOR PRÁCE

SUPERVISOR — **prof. RNDr. František Krčma, Ph.D.**

ŠKOLITEL

BRNO 2022

BRNO UNIVERSITY OF TECHNOLOGY
FACULTY OF CHEMISTRY

Assignment Doctoral Thesis

Department:	Institute of Physical and Applied Chemistry	Academic year: 2021/22
Student:	**Ing. Stanislav Chudják**	
Study programme:	Physical Chemistry	
Study field:	Physical Chemistry	
Head of thesis:	**prof. RNDr. František Krčma, Ph.D.**	

Title of Doctoral Thesis:

Study of Chemical Processes in Extraterrestrial Atmospheres

Doctoral Thesis:

The aim of the work is study of chemical processes in extra–terrestrial atmospheres and the synthesis of organic compounds formed in electrical discharges in related gaseous mixtures. The study will be focused on the atmosphere of Titan, i.e. the gaseous mixture of methane in nitrogen. Measurements with trace amounts of oxygen and carbon dioxide will be performed, too. The experiments also will vary the discharge power. The measurements will be carried out at laboratory temperature as well as at the liquid nitrogen temperature. The proton transfer reaction mass spectrometry, ion mobility spectrometry and Fourier transform infrared spectroscopy will be used for the discharge exhaust gas measurement, plasma conditions will be studied by optical emission spectrometry.

Deadline for Doctoral Thesis delivery: 31.5.2022:

Ing. Stanislav Chudják student	prof. RNDr. František Krčma, Ph.D. Head of thesis	prof. Ing. Miloslav Pekař, CSc. Head of department

In Brno dated 1.9.2021

prof. Ing. Martin Weiter, Ph.D.
Dean

ABSTRACT

The aim of the present work is study of chemical processes in extraterrestrial atmospheres and the synthesis of organic compounds formed in electrical discharges in gaseous mixtures. In particular, this study focuses on the simulation of the atmosphere of Titan, the second largest moon of the solar system. Thus, the most common composition of the gaseous mixture was methane (1-4 sccm) in 200 sccm of nitrogen. Measurements with trace amounts of oxygen and carbon dioxide were also performed. In addition to the composition of the gas mixture, the experiments also varied the value of the electrical power delivered from 2 W - 12 W. The measurements were carried out at laboratory temperature but also at liquid nitrogen temperature, which made the experiment much closer to the real conditions on Titan where the surface temperature is only 94 K.

One of the main objectives of the dissertation was identification of the synthesized gaseous products in the reactor, which was carried out in the majority by proton ionization mass spectrometry. Measurements were then carried out abroad in Bratislava using ion mobility spectrometry and Fourier transform infrared spectrometry. The discharge itself was characterised by optical emission spectrometry, confirming the presence of active nitrogen species and radicals arising from methane. In addition, the first negative and nitrogen second positive systems as well as the violet CN radical system were identified in the measured spectra. The intensities of the selected spectral systems were studied under selected conditions, i.e. different gas mixture composition and power. From the nitrogen second positive system, the rotational temperature was determined to be approximately 2300-2400 K. The vibrational temperature was also determined from this system depending on the concentration of the gas mixture composition from 3100-3400 K. Next, the vibrational temperature was calculated from the nitrogen first negative system, but it decreased slightly with methane concentration and increased with power in the interval from 3950-4350 K. The vibrational temperature obtained for the violet spectral CN system had a very similar dependence, with values ranging from 5900-7700 K.

A number of aliphatic hydrocarbons, some aromatic hydrocarbons and also amino or cyano compounds were detected at laboratory temperature using a proton ionization mass spectrometer with time-of-flight analyzer. The highest molecular weights at laboratory temperature were up to 150 $g \cdot mol^{-1}$ with hydrogen cyanide, acetylene or acetonitrile being the most abundant compounds. In experiments closer to real conditions, temperature proved to be extremely important. In measurements at liquid nitrogen temperature, nearly 200 substances up to a molecular weight of 500 $g \cdot mol^{-1}$ were identified. Even in low temperature measurements, acetonitrile or diacetylene were the dominant substances, but hydrogen cyanide was not so abundant as at ambient temperature. Furthermore, a small amount of oxygen was also used in the measurements and under these conditions, e.g. formamide or acetone were among the significant detected substances. Formamide was probably also formed in liquid and crystalline state in the experiments, which was also measured by FTIR. In both laboratory and low-temperature measurements, it was confirmed that with increasing methane concentration, higher molecular weight substances were formed and lower number of simple substances were formed, which were probably consumed for more complex

substances. The same dependence was observed with increasing power delivered to the system.

The thesis also includes measurements by ion mobility spectrometry. The most important gas detected was ammonia, followed by propane-2-ol, ethanol and most likely diethylamine.

The last set of measurements was FTIR measurements, which are in agreement with the PTR-TOF-MS results. The basic discharge spectrum is the methane structure and the spectrum shows intense bands belonging to both aliphatic hydrocarbons (3050-2800 cm^{-1}) and aromatic compounds (benzene at 1506 cm^{-1}), bands belonging to nitrogen substituted hydrocarbons (1350-1600 cm^{-1} and 3200-3400 cm^{-1}, respectively) were identified too. The spectrum further contains peaks of HCN (713 cm^{-1}) and C_2H_2 (729 cm^{-1}) from which graphs of methane concentration dependence have been obtained. Comparing the overall spectra at different methane concentrations, it can be seen that much of the methane passes through the reactor into the detector unreacted. However, this proportion of unreacted methane decreases significantly with increasing power supplied to the system.

The substances detected in this work are in good agreement with the available literature and also with substances detected in Titan's atmosphere by the Cassini interplanetary probe with the Huygens module. An important detected substance is also formamide, which is considered to be an ideal precursor of prebiotic synthesis.

KEYWORDS

Titan moon, theories about origin of the life, electrical discharges in gases, optical emission spectrometry, proton transfer time of flight mass spectrometry, experiments at low temperature, Fourier transform infrared spectroscopy

ABSTRAKT

Cieľom predkladanej práce je štúdium chemických procesov v mimozemských atmosférach a syntéza organických zlúčenín vznikajúcich v elektrických výbojoch v plynnej zmesi. Táto štúdia je zameraná najmä na simuláciu atmosféry Titanu, druhého najväčšieho mesiaca slnečnej sústavy. Najčastejšie zloženie plynnej zmesi bolo teda metán (1-4 sccm) v 200 sccm dusíku. Prebiehali tiež merania so stopovým množstvom kyslíku a oxidu uhličitého. Okrem zloženia plynnej zmesi sa v experimentoch menila aj velkosť dodávaného elektrického výkonu od 2 W – 12 W. Merania prebiehali za laboratórnej teploty ale aj pri teplote kvapalného dusíka, čím sa experiment výrazne priblížil reálnym podmienkam na Titane, kde je povrchová teplota len 94 K.

Jedným z hlavných cieľov dizertačnej práce bola identifikácia syntetizovaných plynných produktov v reaktore, ktorá prebiehala v absolútnej väčšine pomocou hmotnostnej spektrometrie s protónovou ionizáciou. Na zahraničnej stáži v Bratislave potom prebehli aj merania pomocou iónovej mobilnej spektrometrie a infračervenej spektrometrie s Fourierovou transformáciou. Samotný výboj bol charakterizovaný pomocou optickej emisnej spektrometrie, ktorá potvrdzuje prítomnosť aktívnych foriem dusíka a radikálov vznikajúcich z metánu. Okrem toho boli v nameraných spektrách identifikované aj prvý negatívny a druhý pozitívny systém dusíku a tiež fialový systém radikálu CN. Intenzity vybraných spektrálnych systémov boli študované za vybraných podmienok, t.z. rôzne zloženie plynnej zmesi a výkonu. Z druhého pozitívneho systému dusíka bola stanovená rotačná teplota na približnú hodnotu 2300-2400 K. Vibračná teplota bola stanovená tiež z tohto systému v závislosti na zložení plynnej zmesi od 3100-3400 K. Ďalej bola vibračná teplota vypočítaná z prvého negatívneho systému dusíka, ktorá ale s koncentráciou metánu mierne klesala a rástla s výkonom v intervale od 3950-4350 K. Veľmi podobnú závislosť mala aj vibračná teplota získaná pre fialový spektrálny systém CN, ktorej hodnota sa nachádzala v intervale od 5900 do 7700 K.

Pomocou hmotnostného spektrometra s protónovou ionizáciou a s analyzátorom doby letu bolo detegovaných za laboratórnej teploty množstvo alifatických uhľovodíkov, niektoré aromatické uhľovodíky a tiež amino či kyano zlúčeniny. Najvyššie molekulové hmotnosti za laboratórnej teploty boli do 150 $g \cdot mol^{-1}$ pri čom najviac zastúpenými látkami boli kyanovodík, acetylén či acetonitril. Pri experimentoch bližších reálnym podmienkam sa ukázala byť nesmierne dôležitá teplota. Pri meraniach za teploty kvapalného dusíka bolo identifikovaných až okolo 200 látok do molekulovej hmotnosti až 500 $g \cdot mol^{-1}$. Aj pri meraniach za nízkej teploty boli dominantnými látkami acetonitril či diacetylene, no kyanovodík už tak dominantným nebol. Ďalej bolo v meraniach použité aj malé množstvo kyslíka, a za týchto podmienok boli významnými detegovanými látkami napr. formamide či acetón. Formamide pri experimentoch vznikal pravdepodobne aj v kvapalnom a kryštalickom skupenstve, čo bolo premerané aj pomocou FTIR. Pri meraniach za laboratórnej aj nízkej teploty platilo, že so vzrastajúcou koncentráciou metánu vznikalo viac látok s vyššou molekulovou hmotnosťou a menej jednoduchých látok, ktoré sa pravdepodobne spotrebúvali na syntézu zložitejších látok. Rovnaká závislosť bola sledovaná aj pri narastajúcom výkone dodávanom do systému.

Práca obsahuje aj merania pomocou iónovej mobilnej spektrometrie. Najvýznamnejším detegovaným plynom bol amoniak, ďalej bol detegovaný propan-2-ol, etanol a s najväčšou pravdepodobnosťou aj dietylamín.

Poslednou sadou meraní boli merania pomocou FTIR, ktoré sú v zhode s výsledkami z PTR-TOF-MS. Základným spektrom plynu prechádzajúceho reaktorom je štruktúra metánu. V spektre sú tiež vidieť intenzívne pásy prislúchajúce jak alifatickým uhľovodíkom (3050-2800 cm^{-1}), tak aromatickým zlúčeninám (benzén na 1506 cm^{-1}) a takisto aj pásy prislúchajúce dusíkom substituovaným uhľovodíkom (1350-1600 cm^{-1} a 3200-3400 cm^{-1}). V spektre sú ďalej viditeľné píky HCN (713 cm^{-1}) a C_2H_2 (729 cm^{-1}), z ktorých boli zostrojené grafy závislostí na koncentrácii metánu. Pri porovnaní celkových spektier pri rôznych koncentráciach metánu je vidieť, že veľká časť metánu prechádza reaktorom do detektora nezreagovaná. S rastúcim výkonom dodávaným do systému sa však tento pomer nezreagovaného metánu významne znižuje.

Detegované látky v práci sú v dobrej zhode s dostupnou literatúrou a tiež látkami detegovanými v atmosfére Titanu pomocou medziplanetárnej sondy Cassini s modulom Huygens. Významnou detegovanou látkou je tiež formamide, ktorý je dôležitým prekurzorom života.

KĽÚČOVÉ SLOVÁ

Mesiac Titan, teórie o vzniku života, elektrické výboje v plynoch, optická emisná spektrometria, hmotnostná spektrometria protónovou ionizáciou, experimenty pri nízkych teplotách, infračervená spektroskopia s Fourierovou transformáciou

CHUDJÁK, S. *Study of chemical processes in extraterrestrial atmospheres.* Brno: University of technology, faculty of chemistry, 2022. 131 s. Supervisor of dissertation thesis prof. RNDr. František Krčma, Ph.D.

PREHLÁSENIE

Vyhlasujem, že som dizertačnú prácu vypracoval samostatne a že všetky použité literárne zdroje som uviedol správne a úplne. Dizertačná práca je majetkom Fakulty chemickej VUT v Brne a môže byť použitá na komerčné účely len so súhlasom vedúceho práce a dekana Fakulty chemickej VUT v Brne.

…….

podpis

POĎAKOVANIE

V prvom rade by som veľmi rád poďakoval svojmu vedúcemu prof. RNDr. Františkovi Krčmovi, Ph.D. za jeho konzultácie, vedenie a nesmierne užitočné rady. Ďalej by som rád poďakoval RNDr. Ladislavovi Moravskému, Ph.D. za jeho čas a pomoc pri meraní a vyhodnocování dát na FMFI UK v rámci stáže financovanej z programu Erasmus. V neposlednom rade by som veľmi rád poďakoval výukovo-výskumnej sieti CEEPUS AT0063 vďaka, ktorej bolo jednoduchšie dané experimenty realizovať po finančnej stránke.

CONTENT

1. INTRODUCTION

The chemical processes initiated by electrical discharges in prebiotic atmospheres became a hot topic during the last decade because of extensive discovering of exo-planets. Exoplanets or extrasolar planets are planets that run around a star different from the Sun and so they belong to another planetary system. Due to the large distance of the exoplanets from the Earth, we have very limited information about them that can be compared with laboratory results. Therefore, the work will continue to deal just with the second largest month of the Solar System Titan and marginally also about the atmosphere of Mars as these have currently the biggest atmospheric data collection available [1]. Titan atmosphere is composed mainly from nitrogen and methane at low temperature of about 94 K and pressure about 1.5 atmospheres at its surface [2] and the composition od Mars atmosphere is carbon dioxide and nitrogen at temperature about 210 K and pressure 600-1000 Pa [3].

The question of the prebiotic atmosphere composition at the time of the life origin on Earth still troubles a large group of scientific teams. So far, despite advanced techniques and new discoveries, it has not been possible to accurately determine and prove its composition, and so several hypotheses have emerged over the last century dealing with its potential composition. Theories of reducing atmosphere or neutral atmosphere still play a role among the most important hypotheses about the composition of the prebiotic atmosphere [4]. At present, the opinion of the scientific community regarding these two main theories is gradually changing in favor of the neutral composition of the prebiotic atmosphere, but the question of the ancient atmosphere real composition at the time of the life origin on Earth remains unconfirmed [5].

Laboratory mimic studies of processes running in the exo-planetary atmospheres became a hot topic during the last years because many exo-planets were discovered very recently, and their number increases very rapidly. Moreover, the successful space missions like Cassini-Huygens bring a huge data collection from the *in situ* observations that are impossible using the current Earth techniques [6], [7]. The main interest is focused on the search of life traces or life molecular precursors and consequent discovering the possible pathways leading to the life origins formation. The majority of studies were carried out in the Titan's atmosphere up to know because there are many *in situ* available data and its atmosphere seems to be very similar as Earth's before life creation [8], [9]. Besides the exo-planetary atmospheric processes initiated by UV and VUV radiation and particles fluxes coming from the space, the electrical discharge phenomena can play an important role in the planetary atmosphere chemistry [9]. Lightning on Earth is a highly complex phenomenon involving physical processes on various spatial and temporal scales [8], [10], [11] starting from electron avalanches and resulting in the formation of hot, conducting lightning leaders. The early stages of lightning discharges are formed by streamers, thin and short duration ionized plasma channels. Lightning was confirmed in more planetary atmospheres [8], [12]. While the occurrence of lightning on Venus is still a controversial question [13], [14], there are clear evidences of lightning in the atmospheres of the gas giants like Jupiter, Saturn and Uranus [14], [15], [16]. Lightning is also believed to take place at Neptune [14], [17]. Thus,

we can suppose that electrical discharge phenomena can contribute to the overall chemical processes also in the Titan's atmosphere [11], [18]. However, their direct evidence was not confirmed, yet.

The planetary scale processes can be simulated by laboratory experiments using various discharges: corona and DBD conditions are similar as the St. Elmo's fire, spark and arc relates to lightning, and corona and glow discharge conditions are similar to conditions in aurora borealis [9], [11]. There could be also transient luminous event (TLE) which belongs to a group of short-lived electrical-breakdown phenomena that occur above the altitudes of normal lightning and storm clouds. TLE event was also observed in Jupiter's upper atmosphere [19]. Upper-atmospheric lightning is believed to be electrically induced forms of luminous plasma [19], [20]. Nearly all laboratory studies of Titan atmosphere discharge initiated processes up now were carried out at ambient temperatures and pressure that are not fully reflecting real Titan surface conditions [11], [18]. The aim of the presented Phd study is to give the first results obtained by glow discharge generated in the Titan like atmosphere (nitrogen-methane mixture) in the flowing regime at the liquid nitrogen temperature, too.

The presented work deals with laboratory simulation of chemical processes reflecting atmospheric composition of exoplanets under conditions that are close to the real conditions. The ongoing chemical processes, the resulting products and their transformation into more complex substances will be studied by optical emission spectroscopy (OES) and mass spectrometry with proton ionization (PTR-MS) *in situ*. There were also done measurements of discharge exhaust gas at Comenius University Faculty of Mathematics, Physics and Informatics in Bratislava using ion mass spectrometry as well as measurements with Fourier-transform infrared spectroscopy.

The solar system itself is different in size, chemical composition, temperature, relative density or distance from the Sun, and in the exoplanets these differences are even greater. That is why we are looking for planets that are similar to the Earth as much as possible [21].

2. THEORETICAL PART

2.1. Titan

Although the composition of the atmosphere during the time life originated on Earth is debated, other bodies in the Solar System have atmospheres which may be more conducive to atmospheric organic synthesis. One example is the largest Saturn's moon Titan, which has an upper atmosphere consisting of 98 % N_2 and 2 % CH_4. It is expected that the photochemistry of these molecules leads to the formation of complex hydrocarbons and nitriles [2], [22].

However, due to Titan's low temperature (ca 94 K), most of its water is present as ice in the crust and mantle, acting similar to bedrock on the Earth. In contrast, the early Earth was likely above the freezing point of water for long periods of time, with possible early fluctuations above and below the conditions at which water can exist as a liquid. Titan's atmosphere is of particular interest because of a small planetary mass, with a surface pressure 1.5 times that of Earth, but with an inferred loss rate because of low gravity [23], [24].

The atmosphere of Titan is painted in orange-brown color, as seen in Fig. 1. This coloration is due to the non-transparent aerosol or some kind of haze that is presented in large quantities in the atmosphere and spreads over the entire surface of the moon. Therefore, the surface of the moon itself can not be seen in the visible spectrum [25], [26].

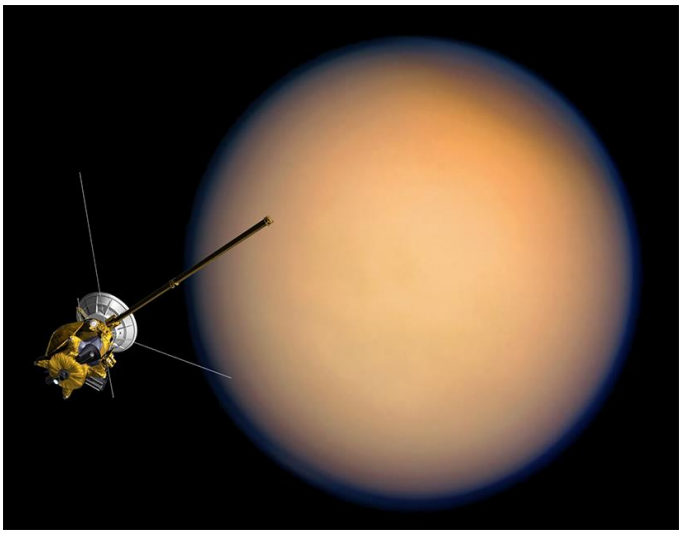

Fig. 1: The surface of Titan, Saturn's largest moon, cannot be seen by human eyes because of its thick and dense atmosphere [25].

The energetic processes of Titan's present atmosphere are likely somewhat different than that which acted upon the primitive Earth's. Titan's atmosphere is exposed to various types of energetic processes, producing higher molecular weight organic species known as tholins (Fig. 2) [25], [26].

Tab. 1: Comparing the selected mean characteristics of Earth, Mars and Titan [3], [27].

Attribute	Earth	Mars	Titan
Diameter	12 756 km	6 805 km	5 150 km
Mass	$5\ 974\times10^{24}$ kg	0.6418×10^{24} kg	0.1345×10^{24} kg
Surface temperature	288 K	210 K	94 K
Density	5 515 kg/m³	3.934 g/cm^3	1.88 g/cm^3
Atmospheric pressure	$1\cdot10^5$ Pa	600-1000 Pa	$1.5\cdot10^5$ Pa
Distance from the Sun.	1 a.u.	1.52 a.u.	9.5 a.u.
Gravitational acceleration	9.7801 m/s²	3.69 m/s2	1.35 m/s^2
Surface atmosphere composition	N_2 78.1 % O_2 20.9 % Ar 0.9 %	CO_2 95.3 % N_2 2.7 % Ar 1.6 %	N_2 98 % CH_4 1.8 %

More complex hydrocarbons arise from the small molecules in the upper atmosphere, then descend into the lower layers where methane condenses. Here they can become part of the haze and coagulate further down to the formation of rainfall formed by hydrocarbons. This rain, which is predominantly methane and possibly ethane, creates lakes on Titan. It is assumed that the methane cycle on Titan is similar to the water cycle on Earth [24], [27].

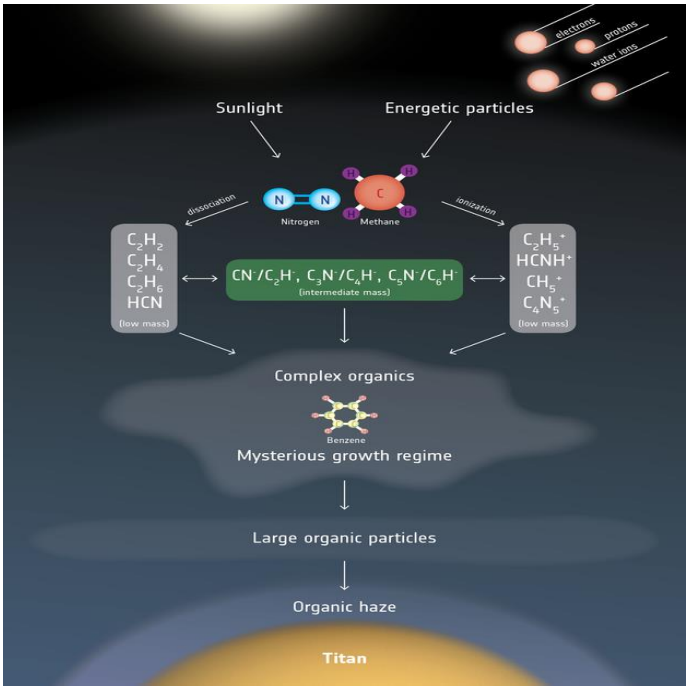

Fig. 2: Creation of tholins on Titan's atmosphere [6].

In the lower layers of the Titan atmosphere, the temperature is only about 94 K. At such a low temperature and thick non-transprent atmosphere there are no reactions possible at low altitude and so reactions only occur at higher layers where they are induced by Saturn magnetosphere or VUV photons from the Sun. Even though lightning has not been observed by cameras or by radio instruments during Cassini's observations or during the descent of the

Huygens landing modul, the atmospheric chemistry suggests the presence of electrical discharges in the atmosphere of Titan. But this could be also caused by the fact that currently it is possible to detect only strong lightning as it is known from Earth (by electromagnetic impulse) and not weaker discharges with lower energies. These would require small charged areas inside the clouds and a shorter discharge length, and they could be of intracloud type. The return stroke energy mainly depends on the length of the lightning channel and the amount of lowered charge [14], [28]. Nevertheless, inception of streamers in Titan's atmosphere strongly depends on the ambient electric field which is still uncertain since it is only provided by models, but not by direct measurements. In general, the important role of ionic chemistry is known. In addition to the ions generated by the discharge, of course, the ions formed by the radiation from the Universe, mainly at upper atmosphere, are important or even dominant. It means that even if no discharge is presented as it is known, the ions would be existing anyway [10], [12].

Therefore, in the atmosphere of Titan, storms are expected, where lightning generates high temperatures, and active particles which allow reactions that are otherwise not possible. Lightning creates intense sound waves [2], [8]. Then the plasma generated from the surrounding gas expands quickly and generates shock waves. The pressure can reach up to 30 atm at this point, but then it decreases to a normal value within microseconds. This means that the time interval of the pressure drop is much smaller than the temperature decrease interval. For this reason, a constant pressure corresponding to a certain altitude in which clouds are formed is used in the simulations, and these are unavoidable for the formation of a storm [22], [23], [24].

For the N_2-rich atmosphere of Titan (as well as those of the Earth, Triton, and Pluto) the emission spectrum of excited nitrogen demonstrates multiple bands from the plethora of excited electronic states available and covers a large part of the electromagnetic spectrum. Airglow is just one of the processes that take place at the high-altitude regions of planetary atmospheres, though, the other being the collisional de-excitation of the different N_2 states that eventually defines the atmospheric local heating rate [8], [26], [27].

Moreover, the Cassini space mission[a] observations demonstrate the dominance of the solar energy input in the dayglow measurements, but also reveal for the first-time emissions from Titan's nightside that are driven by energetic particles originating from Saturn's magnetosphere [9], [11].

Only eight hydrocarbons have been detected in the stratosphere by different techniques as for example ACP-GCSM (Aerosol Collector a Pyrolyser - gas chromatograph with mass spectrometer): CH_4, C_2H_2, C_2H_4, C_2H_6, C_3H_4, C_3H_8, C_4H_2 and C_6H_6. Five nitrogen containing compounds have been detected: HCN, CH_3CN, HC_3N, C_2N_2, C_4N_2. Are there some compounds of these families that might be present with concentrations equal or greater than compounds that have been already measured? Are there C_5 compounds in the atmosphere of

[aa] Cassini–Huygens mission was a collaboration between NASA, the European Space Agency (ESA), and the Italian Space Agency (ASI) to send a probe to study the planet Saturn and its system, including its rings and natural satellites. There were a NASA´s probe and ESA's Huygens lander which landed on Saturn's largest moon, Titan [9], [22].

Titan [2], [11]? Can we predict the abundance of C_7 compounds? How efficient is the incorporation of nitrogen and oxygen atoms into organic molecules? These are some important problems about the chemistry of Titan that are still open. There is a consensus that the present H_2 loss rate is roughly consistent with the rate of photolysis of CH_4 and the subsequent precipitation of larger carbon-containing molecules [8], [23]. However, the present escape rate for carbon and nitrogen containing molecules is small and still being studied. The atmospheric temperature is important for the nitrogen chemistry, the range of accretion temperatures of interest is a secondary effect in determining the escape rate, which is primarily driven by the solar energy absorbed in the upper atmosphere [9], [22], [24], [27].

2.2. Mars

The first observations of Mars began before Christ, as this red planet can also be seen with the naked eye. Mars is also the first planet it has been sent to space mission. The robotic exploration of Mars has yielded a dramatic increase in knowledge about the Martian system. Since 1976, the surface probing of Mars has been carried out with a series of landers: Viking 1 and 2, Mars Pathfinder, the two Mars Exploration Rovers, Phoenix and Mars Science Laboratory. The majority of these missions belong to NASA's Mars Exploration Program whose goals are to determine whether life ever developed on Mars, to characterize the climate, to understand the geology, and eventually to prepare for the human exploration of the planet [29], [30], [31]. Establishing if life ever existed on Mars is one of the outstanding actual scientific questions of our time. To address this important goal, the European Space Agency (ESA) has established the ExoMars program to investigate the Martian environment and to demonstrate new technologies paving the way for a future Mars sample return mission in the next years. ExoMars comprises two missions: First one was ExoMars which has delivered in 2016 the Trace Gas Orbiter, whereas the second mission features a rover and had a launch date in 2020 [32], [33].

Fig. 3 Photo of planet Mars made by Hubble's telescope when the planet was 80 million kilometers far away from the Earth [32].

The reason for such a great attention compared to the other space bodies can be a relatively small distance from the Earth, a solid surface and a sparse atmosphere. Another

important aspect of this red planet is certainly the most acceptable climate conditions for life among all the other planets of the Solar System [34], [35].The main part of Mars' atmosphere is carbon dioxide, but due to very low pressure (600-1000 Pa), it does not produce sufficient greenhouse effect, resulting in large temperature differences between day and night. The atmospheric temperatures on the equator range from 180 K to 260 K, while the surface of Mars can be heated up to 300 K [32], [36].

Apart from temperature differences, Mars also has a change in pressure during the alternation of the seasons. In winter, CO_2 condenses on the surface in the form of snow and in the summer again sublimates back into the atmosphere. Other important components of the Martian atmosphere are the inert gases - nitrogen and argon, the amount of which is constant. However, their percentages may slightly vary depending on the condensation, respectively. Atmosphere on Mars contains 1000x less water vapor compared to Earth, but it is capable to condense and make clouds [29], [35], [36]. In the atmosphere of Mars, methane was also discovered. Methane can´t stay long in the atmosphere because of its degradation by UV radiation that hit the unprotected Mars sturface. The results show that methane is still created somehow on the planet. The most likely theory is that it occurs when the olivine minerals are converted to serpentine in the presence of liquid water which may be hidden somewhere below the surface. Looking at Mars, we can see a red planet with two white polar caps. The red colour is caused by iron oxide, which is basically covering almost the entire surface of Mars [31], [34], [37].

2.3. Theories about origin of the life

Where did life come from, and how can we answer this question? One of the most commonly accepted definitions of life comes from a discussion on astrobiology organized by NASA: “Life is a self-sustaining chemical system capable of undergoing Darwinian evolution”. These scientists were interested in finding a definition that would apply not just to Earth life, but to life on another planet, if we ever find it. It is very significant that evolution was included as a defining feature of life [38].

During the last decade, astronomers have detected hundreds of planets in other star systems, and the increasing sensitivity of these observations means that it is getting progressively easier to detect smaller planets that might be similar to the Earth. It now seems likely that quite a high fraction of stars has Earth-like planets [38], [39].

The sections below deal with some of the most well-known theories of the life origin, which have influenced the development of current researchers.

2.3.1. Theory of panspermia

The theory of panspermia is one of the most daring theories, which emerged in the 19th century after Pasteur's refutation of the hypothesis of self-fertilization. More attention was given to it at the beginning of the 20th century due to the propagation of the Swedish physicist S. A. Arrhenius, according to which microbial genetic information was transmitted to Earth through comets or interstellar dust by pressure of the electromagnetic radiation. Arrhenius believed in his theory that a microbial germ of 0.1-3 μm in the form of thermophilic bacteria

did not have to be absorbed by the gravitational field of the Sun and could thus be carried away in universe by the pressure of the Venus space waves, whose surface temperature was calculated to 320 K [39]. But Arrhenius was aware of the significant problem of the theory of panspermia as he admitted the possibility of burned of microbial germs in size of > 1 μm on entry into the atmosphere. Due to these deficiencies and new findings of modern theories of abiogenesis, the panspermia hypothesis was abandoned during the 1950´s [40], [41].

The panspermia theory revived again the English cosmologists Sir Fred Hoyle and N.C. Wickramasinghe, whose pilot calculations confirmed that particles up to 60 μm would be able to pass through the atmosphere without harm. They also presented a calculation that proved possibility of the transition of 10^{18} viable cells to the Earth in one year [40].

The theory is still fed by the fact that organic matter is found in the Universe to a large extent. The inside of some interplanetary small bodies like commets, meteorities or probably even asteroids, contain large number of polycyclic aromatic hydrocarbons. It is noteworthy, for example, that the Murchinson meteorite, which fell in Australia in 1969, contained D, L-amino acids, of which part of the amino acids were proteinogenic. So, it is possible that there could be the construction stone transition in the form of organic matter has occurred, but this does not guarantee the very beginning of life. Therefore, the hypothesis of panspermia is not a solution to the question of the very origin and development of life on Earth [40], [41].

2.3.2. The theory of the primordial soup

Based on the hypothesis of a strongly reducing prebiotic atmosphere, the Russian biochemist Alexander I. Oparin presented the theory of prebiotic soup in 1924 [42].

The prebiotic atmosphere with reducing properties contained organic compounds (C, O, N, S) in reduced form, such as CH_4, H_2O, NH_3 and H_2S in trace amounts. This initial atmosphere has been exposed to multiple sources of energy from the electrical discharge in the form of lightning, ultraviolet radiation to volcanic heat, resulting in the formation of small organic molecules. The resulting organic molecules, such as amino acids, sugars, bases, and the others, were then to accumulate in the former hydrosphere as an ocean [42], [43].

Oparin coacervates (a droplet-shaped form spontaneously formed in an aqueous solution of macromolecular substances) are essentially protein-based, thus representing a primitive physical pre-cells model that is created in colloidal solutions of different chemical composition by hydrophobic and hydrophilic interactions. Their existentially important property lies in a semi-permeable membrane, the function of which is the separation of the inner and outer coacervate. A common characteristic of each coacervate system is the co-operation or association of molecules in coacervate drops [38], [43].

A frequently criticized disadvantage of the original Oparin hypothesis of prebiotic soup is that the concentration of building materials in viable organisms is very low in the ocean and therefore, due to dilution, synthesis can not be achieved. The hypothesis has grown considerably over the past century by scientific followers and has moved from the ocean to smaller shallows or lakes where alternating flooding and evaporation of prebiotic soup has taken place, thus carrying out the process of gradual concentrating of organic substances [43].

2.3.3. Miller-Urey Experiment

In 1953, Stanley Miller and Harrold Urey reported the production of biomolecules from simple gaseous starting materials, using an apparatus constructed to simulate the primordial Earth's atmosphere-ocean system [44].

Scientists were based on the Oparin's theory of prebiotic soup (chapter 2.3.2), which they decided to experimentally verify. Their model atmosphere was of a reduction character with methane, ammonia, water vapor and hydrogen. The Miller-Urey experiment consisted of an apparatus composed of two glass boilers, one containing a mixture of gases of a prebiotic reduction atmosphere and the other containing an aqueous solution symbolizing the prebiotic ocean. The bank that simulated the prebiotic ocean was filled with water at half its volume, and both banks were interconnected [44], [45]. The apparatus also contained a chamber with tungsten electrodes, including a spark discharge representing the high-energy component of the atmosphere in the form of lightning. For the correct operation of the experiment was the condenser in the apparatus and also the water trap used to acumulate products [46].

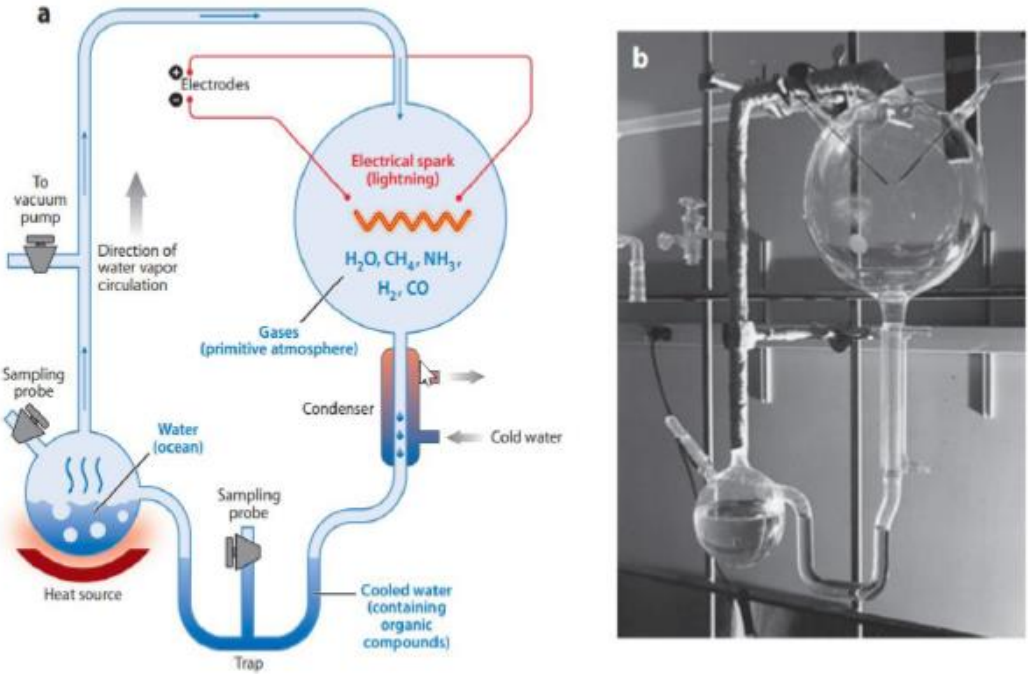

Fig. 4: The spark-discharge apparatus used in the Miller-Urey experiments. (a) Schematic drawing of the apparatus. (b) Photo of the apparatus [44].

During the experiment, there was a spark discharge on the electrode system in one flask, while in the other flask the aqueous solution was boiled. The boiling water solution in the smaller bank represented a natural water cycle in the early Earth's atmosphere and the same time providing circulation with simultaneous mixing of reaction gases with steam. The reaction mixture condensed on the walls of the flask and then rolled down towards the condenser, simulating the whole process as it proceeds to prebiotic Earth. The experiment scheme is illustrated on Fig. 4 [44], [46].

The paper chromatography was performed on the first batch of the sample, which showed the glycine, the simplest amino acid. The experiment then proceeded with a more vigorously boiling, the color of the solution went into pink color. After the week, a second sample of the solution was taken and two-dimensional paper chromatography was performed which revealed a total detection of five basic amino acids including glycine and also α-alanine, β-alanine, α-amino-n-butyric acid and aspartic acid [44], [45], [46].

The result of the Miller-Urey experiment has suggested the possibility that simple chemistry can become more complex under specific conditions. The experiment represents one of the greatest milestones in exploring the possible origins of life on the Prebiotic Earth. Since its implementation, countless alternative experiments have been carried out to date, with different atmospheric compositions and other modifications, but the nature of the technique has remained virtually unchanged. Up to now, about 30 amino acids have been identified by electrical shock experiments based on this progress. It has also been demonstrated that the spark discharge is a suitable source of energy for the formation of hydrogen cyanide and amino acids, these compounds being considered as building blocks of proteins and nucleic acids [45], [46].

2.3.4. Theory of the RNA World

The hypothesis of the RNA world is today one of the most discussed and dominant theories of the possible origin of life in the prebiotic atmosphere of the Earth. The theory is based on the Oparin hypothesis of prebiotic soup, on which it links by its alternative form of living organisms. As early as 1968, Francis Crick proposed the idea that the first genetic molecule could be an RNA molecule that could additionally act as the first enzyme with the current replicator property [39], [47].

RNA molecules have information storage properties, while filling the catalytic role of enzymes. Thus, ribozymes would be able to bind and cleave other RNA molecules even without the existence of proteins while still being able to replicate. This discovery was so revolutionary in the biochemical world that the researchers behind the discovery of ribozymes were awarded the Nobel Prize [38], [47]. Based on the ribozymes discovery, Walter Gilbert came in 1986 with the design of a possible world of RNA molecules that would be the precursor of today's world of DNA, RNA and proteins. The development of today's world of genetic code began with simple ribozymes as the first RNA molecules capable of replication. The process of ribozyme catalysis has achieved a wide range of reactions through a gradual evolution, which has led to the process of synthesizing proteins that have not existed, yet. The last step of the development was in the form of RNA coding for protein synthesis as well as DNA molecules, which proved to be a more suitable and more stable medium for genetic information storing [44], [47]. The DNA molecule subsequently took over the role of storing the longer genetic code, and the whole system moved to the cell. Since the protein system showed higher precision and variability of the catalyzed processes with simultaneous faster processing of genetic information, the original task of ribozymes was taken over by more capable new-formed proteins [39]. As a remainder of the RNA prevalence in the world, individual forms of RNA molecules that have been involved in a large number of cellular

processes remain to this day. The development of the original ribozymes resulted in many of the variations of the ribozymes disappearing, some transforming their function, and a some fraction remained to perform its original role. It was the initial functional differentiation of living organic molecules [47].

Although the RNA theory of the world is very interesting hypothesis about the origin of life as we know it today, it unfortunately does not provide a proven answer to the question how the prebiotic soup has ever occurred to produce the primary RNA molecule. Therefore, the hypothesis is further investigated in order to arrive at a functional and demonstrable developmental pathway for the initial formation of a viable molecule [47].

2.4. Electrical discharges in gases

Plasma generation by electric discharge utilizes the formation of an electric field in the plasma at the passage of current. In the electric field, the electrons acquire kinetic energy by which they are able to ionize gas molecules to compensate the loss of charged particles on surfaces and in the plasma volume [48]. Electric discharges can be described best in terms of the current–voltage (*I*–*V*) characteristics, as illustrated in Fig. 5.

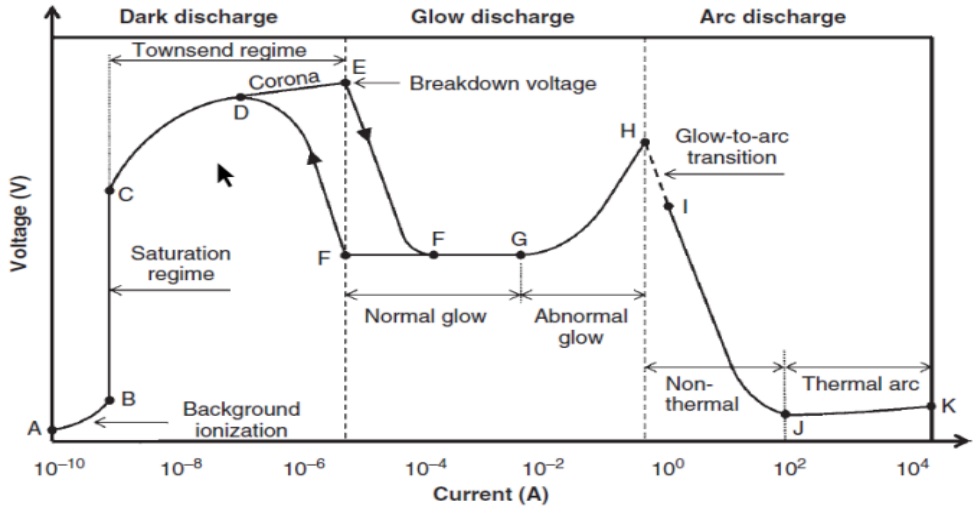

Fig. 5: General current–voltage characteristic of DC low-pressure electrical discharge [48].

Lightning is a natural phenomenon, known as electrostatic discharge, which can heat the air to over 30.000 °C. Lightning is produced in every thunderstorm. Lightning is a natural part of it, just as it is part of our Earth's global electrical circuit. Although we are able to describe its types and the process of its formation relatively well, there is a lot we still do not know about it [49], [50].

The centre of lightning is located roughly in the centre of the cumulonimbus storm cloud, where the positive and negative charges of water droplets, ice crystals and hailstones mix and collide. This energy then generates an electric field around it, which has a potential that can take on different magnitudes. When a storm is brewing, the ground potential is also increased several times so there are two potentials of considerable magnitude [49], [50]. The different potentials that are created in the clouds are discharged between the clouds. However, if the cloud has a positive potential with sufficient energy, a discharge current starts to flow

between the cloud and the ground, which always has a negative potential, through the electrons and ionization of space through the ionized corridor [49], [51]. This discharge current spreads from the cloud to the ground, but also vice versa. If an electron from the cloud and an electron from the ground meet, a corona is formed at this point, which spreads at a speed of $5x10^7$ ms^{-1} towards the clouds and the ground, and we see it in the form of a light glow [49], [50].

Fig. 6: Lightning over the city of Tucson, Arizona [51].

While a thunderstorm can't do without lightning, lightning can do without it. They can be e.g. also part of volcanic activity. The origins and formation of volcanic lightning are still a bit of a mystery, but one theory is that bubbles of magma and volcanic dust are highly electrically charged, and as they move around, they form areas of different charges. Therefore, they probably behave very similarly to storm clouds, but instead of clouds (ice crystals), there is an interaction in the dust or magma. The phenomenon is called triboelectricity [52], [53].

Fig. 7: The Calbuco volcano erupted in two primary phases in April 2015, exploding for the first time since 1972. The lightning-rich blast was captured in vivid detail by photographer Francisco Negroni [54].

The second theory places the source of the lightning in the stratosphere high above the Earth's surface, where ice crystals spawn. This study tracked the location of lightning strikes

during the eruption of the Calbuco volcano in Chile in April 2015. In this case, the lightning strikes occurred about 100 kilometers from the eruption, at near-stratospheric heights (about 20 km) above the Earth's surface. When a volcanic cloud reaches the stratosphere, ice crystals form at the top of the cloud from the water vapor that the eruption also carries. The ice then produces lightning by the same mechanism that storm clouds do [55], [56].

Well above the altitudes of normal lightning and storm clouds there occuer so-called Upper-atmospheric lightning or transient luminous event (TLE). TLE are short-term electrical discharges also considered as electrically induced forms of luminous plasma [57], [58].

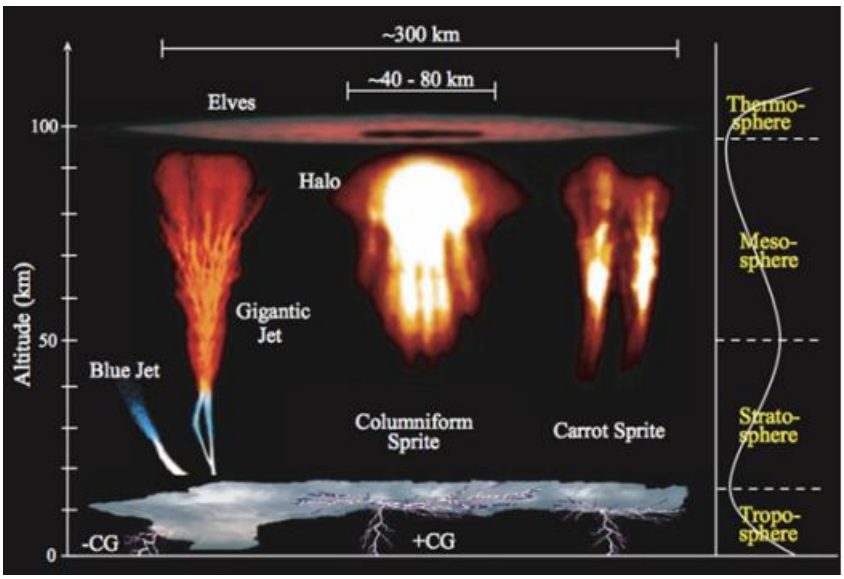

Fig. 8: Different types of ionosperic lightning: Sprites, jets, elves, halos, and gigantic jets in the Earth atmosphere [58].

As it can be seen from Fig. 8 there are several types of ionospheric (superluminal, TLE) lightning. The most common of these is the sprite. Sprites are bright red flashes occurring above a thunderstorm system. So-called C-sprites (columniform sprites) is the name given to vertical columns of red light. C-sprites are also sometimes referred to as carrot sprites. Other types of TLEs (ionospheric lightning) are blue jets, sprite halos, gigantic jets, blue jet, and elves (ELVES - Emission spectrum, Emission of Light) [57], [58].

Ionospheric lightning is a secondary phenomenon that occurs in the upper atmosphere along with primary thunderstorm lightning. TLE flashes generally last for less than a millisecond, up to more than 2 seconds [57].

There were observed in Jupiter [19] and they are considered to be also in Venus and Saturn [59].

Lightning activity has been detected in our solar system on several planets. There are few clear evidences of lightning in the atmospheres of the gas and ice giants. Voyager 1 has approached Jupiter and has imaged lightning flashes from its night side. On Saturn, lightning has been detected optically and by its high-frequency (HF) radio signal. HF radio signals like those observed on Saturn have been detected by the Voyager 2 radio instrument at Uranus.

Lightning is probably also at Neptune due to the detection of lightning whistler like events observed during the encounter of Voyager 2 with this planet, and on Mars, based on the measurements of higher order moments of the electric field by a detector installed on NASA's Deep Space Network and supported by simulations [48], [60], [61]. However, more recent measurements on Mars using the Allen Telescope and the radar receiver of the Mars Express have not found any traces of lightning discharges. So, it is still controversial whether lightning is presented on Mars. Experimentally simulated lightning discharges on Titan, Jupiter and Venus by initiating laser-induced plasmas in various gas mixtures found that the emitted spectral lines of these induced discharges depend significantly on the gas composition. Plasmas in Titan related atmospheres showed spectral lines related to the abundance of the carbon containing molecules CH_4 and CO [48], [62].

2.4.1. Glow Discharge (GD)

GD is one of the most widespread types of gas discharge and it is a self-sustained continuous discharge. Typically, GD is conducted between two conductive electrodes separated by a certain distance within the discharge chamber, which is maintained at low to moderate gas pressure [61], [62]. The chamber is usually filled with noble gas, but there can be also used other gases. GD is mainly characterized by relatively small currents (0.1-100 mA) and high voltages (0.5–20 kV). It is carried out using currents in mA which can be microwave, low frequency or high frequency electric field. In normal GD, the voltage current density is constant, even if the current is changed by several orders of magnitude. With an abnormal GD, the voltage increases linearly with the increase in current [48].
Conditions in GD are very similar to the natural event called Aurora Borealis [63].

Fig. 9: Aurora Borealis [63].

GD can be used to modify surface properties or to apply thin layers. Other applications include material processing and analytical spectrometry.

2.4.2. Gliding Arc Discharge

Gliding Arc Discharge (GlidArc) represents unique non-thermal and non-equilibrium plasma with relatively high plasma density, power and operating pressure compared to other types of discharges. Great interest in gliding arc discharge is due to its unique chemical-physical properties and increased reactivity of activated particles (atoms, radicals, and excited molecules) produced in plasma. GlidArc is one of the most attractive advanced oxidation technique for simplicity of equipment, low operating costs and high efficiency [64],[65], [66].

Plasma is weakly ionized and has a lack of local thermodynamic equilibrium because the electron temperature is significantly higher than the neutral gas temperature (rotational temperature). The electron temperature corresponds to approximately 1 eV ~ 11600 K, while the neutral gas temperature ranges from 2000-3000 K and the translation temperature from 800-2100 K. The electrode system of GlidArc can be made up by a pair or several pairs of arc-shaped electrodes (Fig. 10) [64], [66].

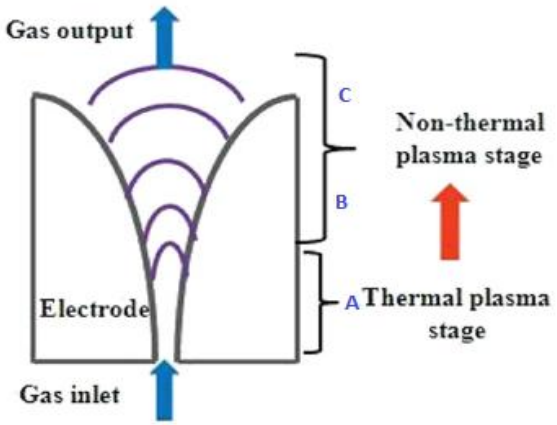

Fig. 10: Origin and phases of gliding arc discharge: A - electric breakdown area; B - equilibrium plasma region; C - non-equilibrium plasma region [64].

The area of the electrical breakdown (Fig. 10A) is where the electrodes are closest to each other (1-2 mm) and the electric discharge occurs. When ignited, the voltage drops sharply while the current increases and the temperature of the gas increases as well [64]. The plasma filament is drifting in the gas stream along the electrodes until it reaches the equilibrium plasma region (Fig. 10B). In this region, the neutral gas temperature (10 000 K) is approximately the same as the electron temperature. When the distance between the electrodes reaches the critical length, the system became the area of non-equilibrium plasma (Fig. 10C). After crossing the critical area, there is also a thermodynamic imbalance because the electron temperature is much higher than the neutral gas temperature. Plasma filament ruptures at a greater distance, breaking the electrical circuit and then the voltage is increasing at the electrodes. The discharge is returned to phase A and the cycle is repeated [65], [66].

2.4.3. Corona Discharge

The corona discharge (or just corona) can only exist in an inhomogeneous electric field and at pressures greater than 1 kPa. It is not stable in a homogeneous field, as it immediately goes into another form of discharge (glow or arc discharge). A non-homogeneous field is formed such that one of the electrodes has a small radius of curvature. With such electrode, an electric field can be generated sufficiently high for a local breakdown in the gap between the electrodes. This electrode is then called a corona electrode. In practice, the corona electrode usually has the shape of a needle or a thin wire [48], [114].

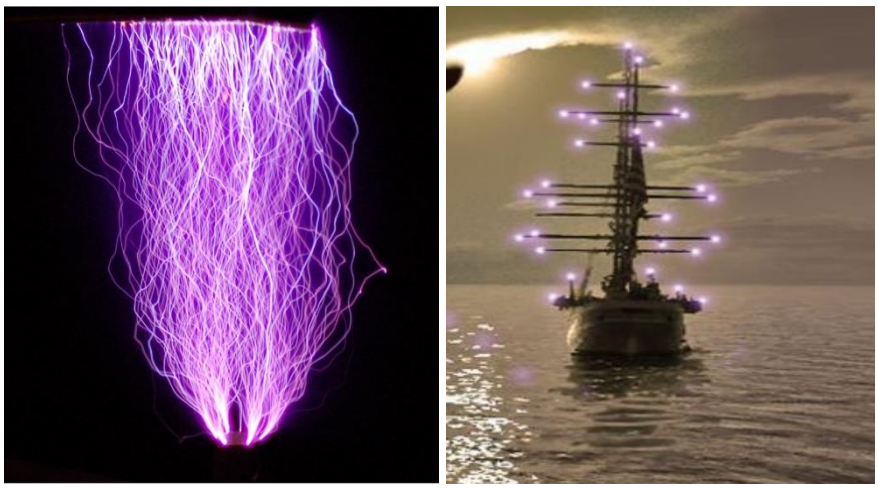

Fig. 11: Corona from Ruhmkorff's inductor on the left side and St. Elmo's fire on the right side created by a corona discharge from a sharp or pointed object in a strong electric field in the atmosphere [67].

There is a strong electric field around the electrode where electron avalanches are formed. However, these avalanches cannot extend to the entire space between the electrodes, because the inhomogeneity makes the field much weaker, so the value of the first Townsend coefficient is close to zero. Thus, the ionization region is bound only to the surroundings of the corona electrode. This region is called the corona layer or ionization layer. It is visually observable as a weakly shining cover of the corona electrode. The other non-ionizing part is called the outer corona discharge area [48], [62].

When increasing the voltage between the electrodes, the dimensions of the corona layer gradually increase until the outer area completely disappears. At that time, the corona layer reaches an electrode with a large radius of curvature and another kind of discharge develops in the space; glow or arc. According to this behavior, it could be assumed that the corona is even a pre-breakdown stage. On the other hand, though, it is already an independent discharge - even though it resembles Townsend's discharge - because it also exists without an external source of primary electrons after ignition [48], [60]. Depending on the polarity of the corona electrode, a positive corona is distinguished (a positive pole of the source is attached to the corona electrode) or a negative corona. There can be also encounter a case where both electrodes, due to their distance, have small - but comparable - radii of curvature. At that time, both electrodes are coronating, and thus one of them is positive and the other is negative corona discharge [61], [62]. This type of discharge is called bipolar corona discharge. The transition of a corona in a spark or arc can be explained by applying the theory of so-called streamers. According to this theory, an electron discharge avalanche produced either by the action of an electron released from the cathode or by an electron generated by some of the elemental processes takes place. Initial electron formation can occur by ionization by cosmic radiation or light radiation [60], [114].

2.4.4. Dielectric Barrier Discharge

DBDs are characterized by the presence of an insulating material which is at least part of the one layer between the planar, cylindrical, or needle electrodes jointed to an AC or pulsed power supply. Typical materials are ceramics, quartz or some polymeric materials.

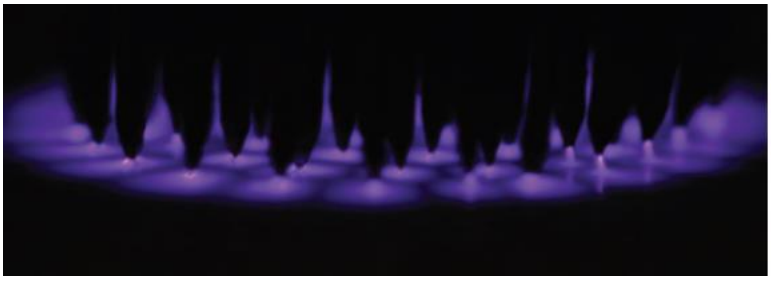

Fig. 12: Dielectric barrier discharge formed using a needle array electrode configuration [48].

The discharge operating frequencies can be from hundred hertz up to the 10 kilohertz. In most gases, DBD undergoes the generation of several light filaments called microdischarges. The accumulation of electric charge on the surface of the dielectric layer creates an electrical potential that limits the flow of charges through the gas and thus prevents the passage of light into the arc. DBD plasma is generally of a filamentary nature, but homogeneous plasma can also be generated under certain conditions. The main advantage of DBDs is the economical and reliable generation of non-equilibrium plasma conditions in gases at atmospheric pressure [48], [62].

2.4.5. Pulsed Electric Discharges

The electrical charge supplied to the electrodes needed to generate the discharge can be either continuous or pulsed with different time duration or duty cycles. The pulses have the advantage of higher performance for dissociation of molecules, and this increases the rate of plasma chemical reactions [48], [62].

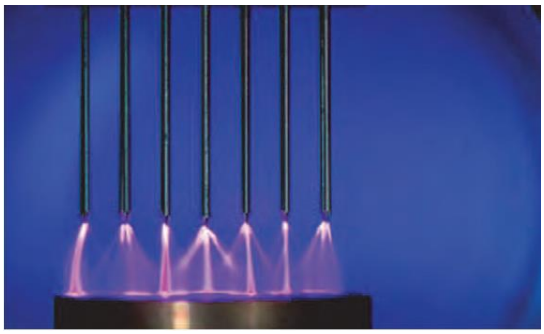

Fig. 13: Multi-tip pulsed corona discharge [48].

Electric discharges that are generated by fast voltage pulses with a rise time in nanoseconds can have significant advantages. The use of high voltage pulses of nanoseconds, for example, allows for substantial overvoltage, which increases the dissociation of primary active substances in the discharge without switching to spark mode. Since a shorter pulse allows the application of a higher electric field to the discharge space, the production of active chemical substances and radicals as well as the rate of chemical reaction increases [48].

2.5. Proton Transfer Reaction Mass Spectrometry

The main analytical method exploited in this work is Proton Transfer Reaction Mass Spectrometry which is used for analysis of products created in electrical discharge in gaseous mixture.

Proton-transfer-reaction mass spectrometry (PTR-MS) is a relatively new analytical method, which was created just in the second half of the 1990s. PTR-MS allows real-time, on-line measurements of atmospheric VOCs with a high sensitivity and fast response time and has overcome some of the disadvantages of traditional techniques with low time resolution. Furthermore, recently available PTR-MS instruments that use time-of-flight (ToF) mass analysers with high mass resolution facilitate the separation of nominally isobaric species, which increases the number of measurable atmospheric VOCs (> 100 species) and reduces possible chemical interferences. PTR-ToF-MS has quickly become a well-established analytical technique for *in-situ* VOC measurements utilized in a wide variety of fields such as atmospheric chemistry, medical and biotechnological applications, and food and flavour sciences [68], [69].

Since the ionization process in PTR-MS is a form of chemical ionisation CI, some general aspects of CI-MS should be considered before moving to the thermodynamics and proton transfer kinetics. An attractive reason for introducing CI was that it provides much more soft ionization than electron ionization (EI), which was the dominant ionization technique available at that time. Typical EI energies used in mass spectrometry are in the range about 70 eV, well above the first ionizing energies of all chemical compounds. Part of the excess energy available can find its way into the cation often leading to abundant fragmentation. That means the M^+ fragments [68], [70]. Useful information may be obtained from the detection of fragment ions, such as the identification of specific functional groups present in the parent molecule. If fragmentation is excessive, it may be very difficult or sometimes even impossible to find a peak in the mass spectrum corresponding to the molecular ion, which in turn makes it challenging to identify the compound responsible for the mass spectrum [69]. This may be a problem if the analyte is a complex mixture of compounds. While the fragmentation process can be reduced by using electrons incident energies close to the ionization threshold, there is also a great loss of sensitivity because the EI cross sections are much lower at these energies than at 70 eV [68], [70].

In CI, there the ionization of the desired molecule is achieved by reaction with an atomic, respectively molecular ion. Various processes are possible, from simple electron transfer to chemical reactions such as proton transfer, hydride ion transfer, or ion-molecule adduct formation. These specific CI processes are listed below [68]:

$X^+ + M \rightarrow M^+ + X$	Charge transfer	(1)
$\mathbf{XH^+ + M \rightarrow MH^+ + X}$	**Proton transfer**	**(2)**
$X^+ + MH \rightarrow M^+ + HX$	Hydride (H^-) transfer	(3)
$X^+ + M^+ Z \rightarrow MX^+ + Z$	Adduct formation	(4)

In the fourth reaction, the substance called Z, is needed to remove some energy to avoid fast dissociation of the MX^+ adduct. Bimolecular ion-molecule reactions, such as these reactions 1-3, are often very rapid and very probable, which makes them useful for efficient ionization of target molecules in mass spectrometry. The energy available for deposition in the product cation is typically low, well below 1 eV when the appropriate CI agent is selected. This low reaction energy means that CI-MS is a soft ionization technique because it tends to leave the parental ions intact [68], [71]. It should also be borne in mind that some ion-molecule reactions may occur through harmonized mechanisms that lead to fragmentation even at much smaller energy surpluses. This means that soft ionization is not necessarily non-fragmenting [68], [69], [70], [71].

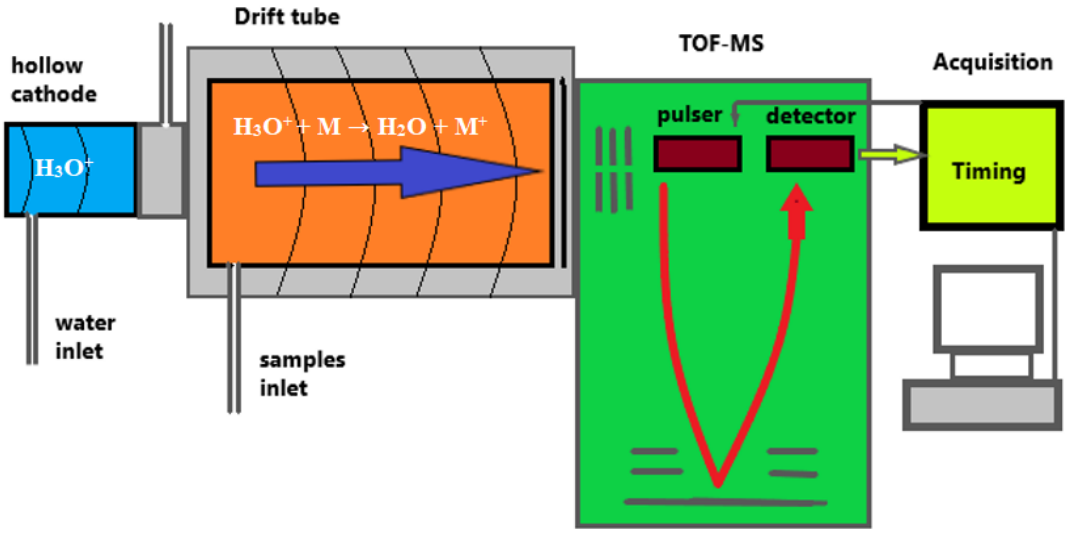

Fig. 14: General scheme of a PTR-ToF-MS instrument [b].

The most commonly used as the reaction gas H_3O^+ ions, which are generated by ionisation of water vapor in a hollow cathode discharge are used in the proton transfer mass spectrometry [68].

Primary reactions in the hollow cathode discharge

$$e^- + H_2O \rightarrow H_2O^+ + 2e^- \quad (5)$$

$$e^- + H_2O \rightarrow H_2^+ + O + 2e^- \quad (6)$$

$$e^- + H_2O \rightarrow H^+ + OH^- + e^- \quad (7)$$

$$e^- + H_2O \rightarrow O^+H_2 + 2e^- \quad (8)$$

Secondary reactions in the hollow cathode

$$H^+ + H_2O \rightarrow H_2O^+ + H \quad (9)$$

$$O^+ + H_2O \rightarrow H_2O^+ + O \quad (10)$$

$$H_2^+ + H_2O \rightarrow H_2O^+ + H_2 \quad (11)$$

$$H_2O^+ + H_2O \rightarrow H_3O^+ + OH \quad (12)$$

[b] the pumping system is omitted for clarity

In the drift tube, the analysed substances are accelerated from the source to the analyser and collide with the primary ions. Proton transfer occurs through ion-molecular reactions due to the higher proton affinity.

The proton affinity of the analyte has to be higher than proton affinity of water molecules - $A_R > PA_{H_2O}$. Thus, it is not sensitive on any of the main gases in our reaction mixture (N_2, CH_4, CO_2...) [68], [72].

$$H_2O{\cdot}H^+ + R \rightarrow RH^+ + H_2O,\ \Delta H = PA_{H_2O} - PA_R\,. \tag{13}$$

However, in addition to reacting with organic gas, unreacted water also creates unwanted cluster ions in the presence of a third specie by the process:

$$H_3O^+(H_2O)_{n-1} + H_2O + X \rightarrow H_3O^+(H_2O)_n + X \tag{14}$$

The key factor in this reaction is that the aqueous clusters have a greater proton affinity than the water molecule itself. Elimination of this undesirable phenomenon is accomplished by dissociation induced by precipitations. Unfortunately, aqueous clusters are still present and may affect the detection of the analyte [68], [73].

Thermodynamics can be used to predict if a reaction can occur under given conditions. The key quantity required is the Gibbs energy change for a reaction, ΔG. Reaction 13 will be thermodynamically spontaneous if the Gibbs energy change for the process is negative. It derives from a difference in the Gibbs energy changes for the following two reactions [68]:

$$R(g) + H^+(g) \rightarrow RH^+(g) \tag{15}$$

$$H_2O(g) + H^+(g) \rightarrow H_3O^+(g) \tag{16}$$

Since Gibbs energy is a function of state, Hess's law applies and so the Gibbs energy change for reaction 13 can be expressed as

$$\Delta G_T^0(13) = \Delta G_T^0(15) - \Delta G_T^0(16) \tag{17}$$

where T is the temperature and the "0" superscript refers to the standard state. The Gibbs energy change is linked to the equilibrium constant, K_{eq}, for Reaction 13 through the following expressions [68]:

$$\Delta G_T^0 = -RTlnK_{eq} \tag{18}$$

$$K_{eq} = \frac{[RH^+][H_2O]}{[R][H_2O.H^+]} \tag{19}$$

In the equations above, T is the absolute temperature, R is the universal gas constant, and the square brackets around the chemical compounds refer to their concentrations in the gas phase.

Tab. 2: Proton affinities of some chosen molecules [68]

Molecule	**Formula**	***PA* (kJ/mol)**	**Molecule**	**Formula**	***PA* (kJ/mol)**
Noble gases	Ar, Ne, He	346, 174, 149	Formaldehyde	CH_2O	713
Oxygen, ozone	O_2, O_3	396, 596	Acetonitrile	CH_3CN	779
Nitrogen	N	465	Acetone	CH_3COCH_3	782
Carbon dioxide	CO_2	516	Carboxylic acids	CH_2O_2 CH_3COOH	784 797
Methane	CH_4	544	Ammonia	NH_3	853
Water	**H_2O**	**660**	Aromatic hydrocarbons	C_6H_6 C_7H_8	750 784

Employing thermodynamics to determine if a reaction is likely to take place is only the first condition. The other important factor is the rate of the reaction and it is possible for a reaction that is thermodynamically allowed to be very slow in practice. A slow reaction will result if there is an excessive energy barrier for the reactants to transform themselves into products [68], [73], [74].

In general, the bimolecular ion-molecules reactions are rapid, a class of reactions involving proton transfer reactions. The reasons are twofold. First, since such reactions usually involve the transfer of a charged particle from one site to another without any rupture of normal chemical bonds. There is only little or even no activation energy. Secondly, the long attractive forces between the ionic and neutral molecules can serve to increase the collision cross-section beyond what would be expected based on the nominal sizes of the individual molecules. In other words, the trajectories of ion and molecule that would otherwise lead to a near leak can be assembled and created to collide with the help of large-range forces as shown in Fig. 15 [68], [70], [74].

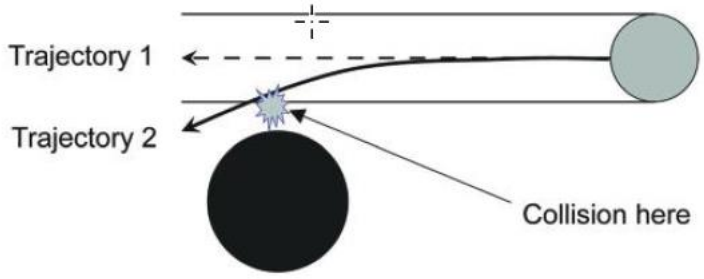

Fig. 15: Trajectories for two hypothetical spherical molecules. Trajectory 1 is the trajectory that would be taken in the absence of any attractive intermolecular forces, which would see the two molecules miss each other. Trajectory 2 (solid line) is modified by long range attractive forces which create an effective collision cross section that is larger than the hard-sphere limit. In this particular case, the modification leads to a successful collision [68].

Long-range Van der Waals forces are also present in neutral–neutral reactions but these are much weaker and therefore less effective in influencing the reaction cross section, whereas in an ion–molecule system there are much stronger electrostatic forces present such as charge–dipole or charge-induced dipole forces [68], [70], [71].

From the kinetic point of view, it is a second order reaction:

$$\frac{d[H_3O^+]}{dt} = k \cdot [H_3O^+] \cdot [R], \tag{20}$$

Since the reaction gas is in large excess [H_3O^+] >> [R], it is true that [H_3O^+] is quasi-constant and thus the reaction is pseudo-first order. Considering that RH^+ is the only product, a simple kinetic equation can be written [68], [72], [75]:

$$\frac{[RH^+]}{[H_3O^+]} = k \cdot [R] \cdot t, \tag{21}$$

where *k* represents the proton transfer rate constant and *t* is the reaction time.
Fast bimolecular ion–molecule reactions typically show rate coefficients $k \geq 10^{-9}$ $cm^3 \cdot s^{-1}$, whereas in neutral–neutral reactions they are at least an order of magnitude smaller [68], [71].

There are some theoretical prescriptions for determining rate coefficients of ion–molecule reactions. One of them originates from concepts developed by Langevin and applies to a reaction between a point ion and a spherical (non-polar) molecule [68], [76]. The dominant long-range attractive force in this case is the ion-induced dipole interaction, which can be written as

$$V(r) = -\frac{1}{4\pi\varepsilon_0}\frac{\alpha q^2}{2r^4}, \tag{22}$$

where q is the charge on the ion, α is the polarizability of the neutral reactant molecule and ε_0 is the permittivity of free space. The above expression gives the potential energy as a function of the ion–molecule separation, r. Incorporation of the attractive potential into a simple collision model allows the prediction of the reaction cross section and the reaction rate coefficient. The Langevin rate coefficient is given by [76], [77].

$$k_L = \sqrt{\frac{\pi\alpha q^2}{\mu\varepsilon_0}}, \tag{23}$$

where μ is the reduced mass of the colliding partners ($\mu = m_1m_2/(m_1 + m_2)$ where m_1 and m_2 are the masses of the ion and the neutral molecule). This kind of rate coefficient expressions presented below are also commonly referred to as capture rate coefficients because the long-range attractive force ‘captures’ the approaching reactants and can bring them into a propitious trajectory for reaction. Equation 23 predicts the collision rate coefficient for many reactions between ions and non-polar molecules quite accurately [68], [75].

A more accurate description (mainly in case of polar molecules where Langevin theory is not sufficient) was provided by Su and Bowers and is known as the average dipole orientation (ADO) theory [68], [76], [77]. The ADO rate coefficient is given by

$$k_{ADO} = \sqrt{\frac{\pi\alpha q^2}{\mu\varepsilon_0}} + \frac{C\mu_D q}{\varepsilon_0}\sqrt{\frac{1}{2\pi\mu kT}}, \tag{24}$$

where *k* is the Boltzmann constant. The ion-permanent dipole interaction is accounted for in the second term. *C* is a dimensionless 'locking' parameter ($0 \leq C \leq 1$) that accounts for the average orientation of the permanent dipole moment of the neutral molecule. When $C = 1$, Equation 24 is equivalent to the locked-dipole theory [68], [76].

The calculated dipole moments and polarizabilities are employed in ADO calculations to obtain thermal rate coefficients. In practice, for most molecules, the predicted proton transfer rate coefficient was within ±25% of the value determined from SIFT (selected-ion flow-tube) measurements [68].

The absence of a mass filter before the drift tube results in less H_3O^+ losses resulting in an extremely low detection rate that reaches up to pptv. At the end of the drift tube, the protonated molecules are separated by a suitable analyzer. Quite a widespread analysis system is still a quadrupole mass filter [70], [72].

The quadrupole was very advantageous at the time of its creation by not requiring a magnetic field. It consists of 4 rods, two of which are conductively connected. The radio frequency voltage is applied on them, which creates an electric field and oscillations. Electrostatic attraction and repulsion begin to affect the ion that flows between the quadrupole rods [72], [74]. With set parameters, only ions with an exact value of *m/z* can reach the stable trajectory and these ions hit the detector. Other ions do not generate the signal. These parameters can be set and therefore is sometimes quadrupole called a tunable filter [71], [73].

The mass spectrometer used in this work is equipped by a time-of-flight analyser (TOF) which in addition to high sensitivity, has a very good resolution. Measurements based on TOF are running in flight tubes of different lengths or diameter. There is mostly no electric or magnetic field in the flow tube. TOF is a pulsing technique because the ions are accelerated by the energy pulse at the inlet to the take-up tube. Ions with different *m/z* gain the same kinetic energy, meaning that the product of mass and velocity square is constant. It follows that heavier ions need longer time to overcome the flight tube than lighter ions [68], [72].

$$E_p = ezU = \frac{1}{2}mv^2 = E_k, \tag{25}$$

where E_p is the potential energy given by the electric field, *e* is the elemental charge, *z* is the number of electric charges, *m* is the mass and *v* is the speed.

$$v = \frac{L}{t}, \tag{26}$$

where *L* is the length of the flight tube [[68][69]].

$$\frac{m}{z} = 2eU\frac{t^2}{L^2}, \tag{27}$$

In the real ion sources for TOF-MS, the initial velocity and direction of ions have a negative effect. Ions with the initial velocity toward the detector arrive earlier than the ions with the opposite direction, which are first slowed and rotated. As a result, the resolution is

reduced. Increasing of the resolution is achieved by reflectron [68]. Reflectron is a set of electrodes with continuosly increasing potential. Higher energy ions penetrate deeper into the electrostatic field, thereby extending their path. This penetration depth does not depend on the *m/z* ratio, but only on kinetic energy.

Reflectrons increase resolution by extending the flight ion path [70], [71].

$$R = \frac{m}{\Delta m} = \frac{t}{2\Delta t}, \tag{28}$$

where *R* is the resolution, *t* is the flight time and *Δt* is the ion detection time interval with the same *m/z*.

PTR-MS is a soft ionization technique with little to no fragmentation which makes its spectra simpler. This is advantageous in on-line monitoring or quantitative analysis, since the signal of the protonated analyte is directly proportional to the concentration of components in the sample. That is, if *k* and *t* are known in equation 21 (p. 22) and the signal is measured, so theoretically there is no problem in determining the absolute concentration of analyte R [68], [74]. However, PTR-MS is not a unique analytical method for determining the identity of substances with the same *m/z* ratio. Limited specificity can be improved by a variety of methods including isotope ratio measurement, reduced field variation, use of alternative ions (NH_4^+, O_2^+, NO^+) or, in particular, PTR-MS coupling with gas chromatography to separate isomers. The last option seems to be necessary to make the spectra readable and for distinguish heavy molecules where a lot of isomers are occurred [75], [76].

3. EXPERIMENTAL PART

3.1. Tasks

- Experimental simulation of the atmosphere processes in Titan.
- Exploring the possibility of synthesizing complex compounds in prebiotic atmospheres due to electrical discharges.
- Deepening of knowledge in diagnostic method PTR-TOF-MS.
- Extended results by the additional analytical techniques as ion mobility spectrometry and FTIR.
- Characterize the effect of changing the composition of the gaseous mixture, temperature, pressure, power and electrode arrangement on synthetized products in a simulated atmosphere.

3.2. Reactor and other instrumentation

To be able to simulate the atmospheres, a special multifunctional stainless-steel reactor was designed, which is also ideal for experiments in an oxygen-free atmosphere, while ensuring a high vacuum. The multifunctional character of the reactor lies in the wide range of possible electrode arrangements, thanks to which it is possible to achieve different types of electric discharges. Among the possible electric discharges in the reactor are also corona discharge, dielectric barrier discharge and gliding arc discharge.

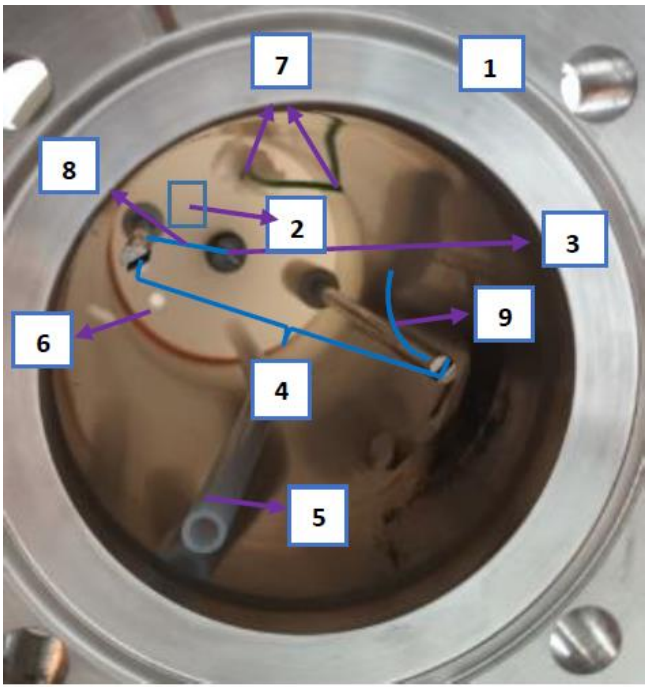

Fig. 16. Scheme of the reactor (view from below): 1 - stainless steel case; 2 - PE (for low temperature) flange on top of the reactor; 3 - HV throughput; 4 - electrode holders; 5 - gas inlet; 6 - gas outlet; 7 - thermocouples (one to measure the temperature in the upper part of the reactor and second for the lower part); 8 - connection between electrode and HV throughput; 9 - flexible wall contact for grounded electrode.

The constructed reactor can be easily connected to the analytical equipment by means of valves. This reactor as well as electrode arrangements for abnormal atmospheric pressure glow discharge (Fig. 17) with pair of stainless-steel electrodes in shape of the raindrop in the distance of 1-2 mm were used in experiments with FTIR, IMS and PTR-ToF-MS at ambient as well as at lower temeperature. Experiments with OES were also done in this reactor as it contains also 50 mm fused silica window.

Fig. 17 Stainless steel high vacuum reactor used in experiments.

During the experiments at the liquid nitrogen temperature a lot of condensates started to form in the reactor and the whole reactor was completely fogged. It is further described at p. 65. This small window was not sufficient to be able to see and describe these conditions at the reactor bottom so the experiments at lower temperature as well as with different applied power and different mixture composition were moved to the pyrex glass reactor (Fig. 18) with electrode arrangement for glow discharge.

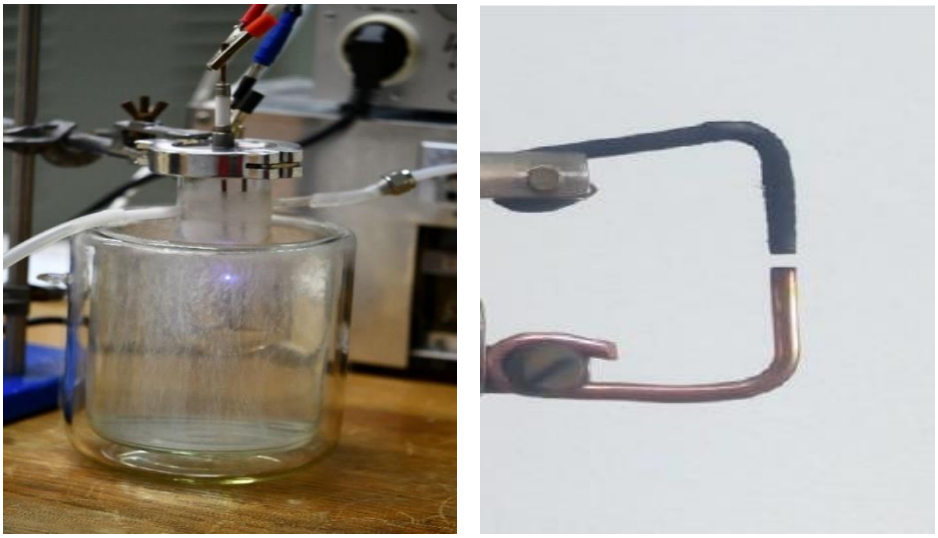

Fig. 18 Pyrex glass reactor and electrode arrangements on the right side.

The experiments themselves were done at two different workplaces, thanks to which it was possible to use a wider range of analytical methods.

The first set of experiments was performed at the home working place of the Faculty of Chemistry of the Brno University of Technology, where optical emission spectrometry (OES) was performed for plasma diagnostics and *in situ* proton ionization mass spectrometry (PTR-ToF-MS) as an analytical method used for identification of the composition of gaseous substances of discharge products.

The second set of experiments took place at the Comenius University in Bratislava at the Faculty of Mathematics, Physics and Informatics, where the analytical techniques ion mobility spectroscopy (IMS) and Fourier transform infrared spectroscopy (FTIR) were used.

Thus, four analytical techniques were used in the experiments to analyze the products of chemical reactions, using two different electrode arrangements in two different reactors.

The general scheme of the instrumentation can be seen at the Fig. 19. At the bottom there can be seen the Tab. 15 with all the devices used in the experiments and their specifications are there mentioned too.

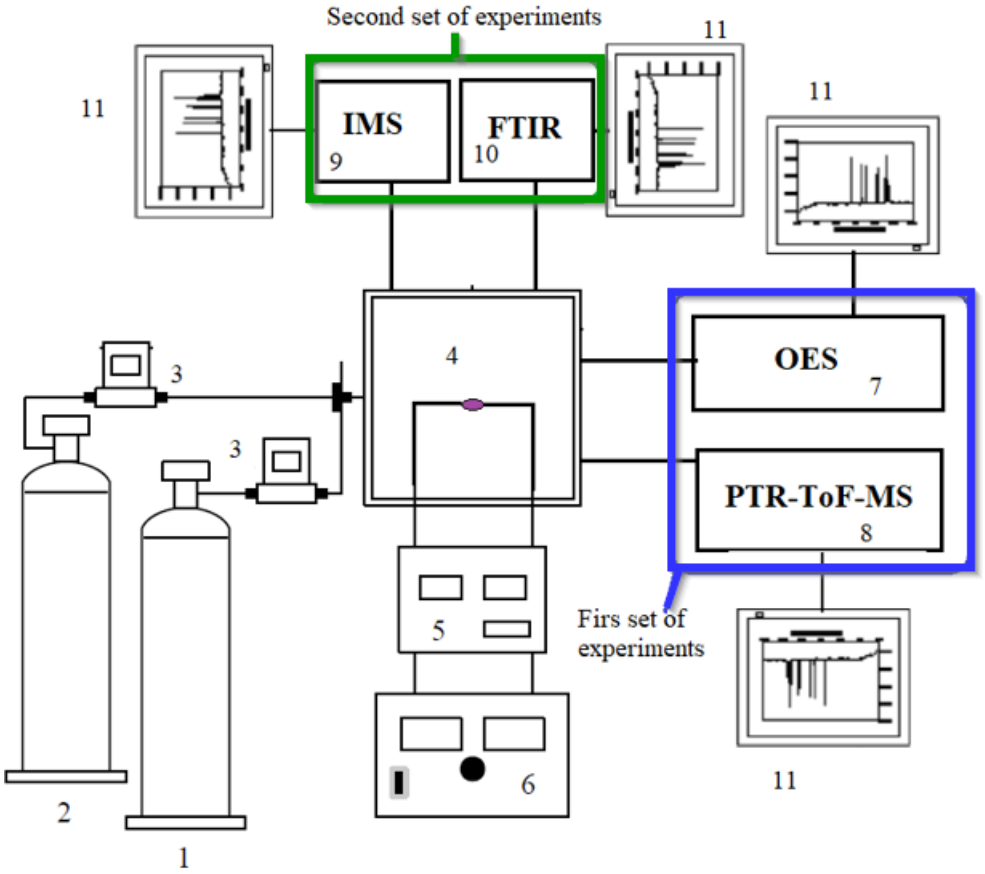

Fig. 19: Experimental set up: 1 – nitrogen bottle; 2 – methane bottle; 3 – mass flow controllers; 4 – reactor with electrode arrangement; 5 – HV DC power supply, 6 – AC autotransformer, 7 – OES, 8 – PTR-TOF-MS, 9 – IMS spectrometer; 10 – FTIR spectrometer; 11 - computers.

Tab. 3: Specification of main devices

Device	Specification
Power supply	FUG HCP 1 400–20 000, DC, high-voltage
Mass flow controller	Bronkhorst, El-Flow mass flow controller, range 20 and 200 sccm, calibrated for N_2
Mass flow controller	Bronkhorst, El-Flow mass flow controller, range 5 sccm, calibrated for CH_4
OES spectrometer	Jobin Yvon TRIAX 550
OES detector	Liquid nitrogen cooled CCD
Rotary oil pump	VR005-20
FTIR spectrometer	Bruker Vector 22
IMS	Masstech IMS instrument
Mass spectrometer	Ionicon, PTR-TOF-MS 1000
Ionizer	Ionicon, proton-transfer-reaction
Analyzer	Time of flight – TOF

3.3. Optical emission spectroscopy

Optical diagnostic methods which often carry the collective name of plasma spectroscopy, can be divided into the two basic groups according to the nature of the radiation used. In the first group, emission spectroscopy methods are based on the analysis of radiation emitted directly by the own plasma. The advantage of these methods is the relative simplicity and, in particular, the non-destructiveness, since the plasma is not influenced itself. In the second group, the methods are then based on radiation absorption. It is also possible to combine both methods [78], [79].

The main methods include optical emission spectroscopy which belongs to the first group and it is based on the analysis of emitted radiation by excited particles in plasma. Optical Emission Spectroscopy (OES) techniques are commonly used besides the qualitative analyzis of plasma radiative species composition for gas temperature determination of plasmas at atmospheric pressure. The rotational temperature derived from them is considered as a good estimation of the kinetic temperature of the plasma heavy particles due to the strong coupling between translational and rotational energy states under these high pressure conditions [78], [80]. Emissions of molecular bands of the diatomic species OH, N_2, N_2^+, CN, NH, NO, CH, C_2 and SiH, among others, have been traditionally employed with this purpose. But, the use of molecular spectroscopy is not always easy for gas temperature determination [78], [81]. In this way, N_2, N_2^+, and CN emission bands are commonly overlapped in plasmas containing nitrogen, what often makes very difficult to get reliable values of the gas

temperature. If these plasmas also contain some OH species, the OH band appears overlapped to N_2 band [81], [82].

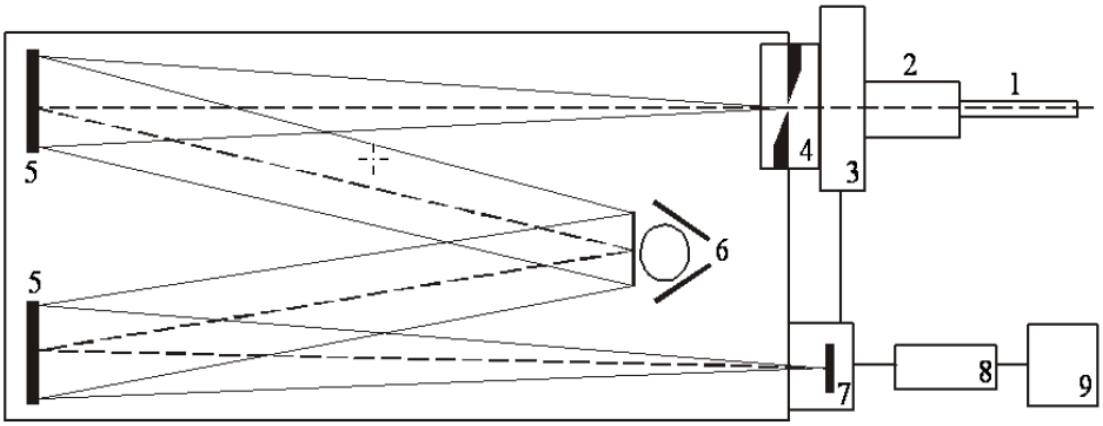

Fig. 20: Optical emission spectrometer in Czerny-Turner configuration: 1 - quartz optical cable, 2 - adapter, 3 - optical filters, 4 - input slit with shutter, 5 - spherical mirrors, 6 - circular holder with rotating exchangable gratings, 7 - CCD detector, 8 - controller, 9 – computer [81].

The light emitted from the reactor is led to the spectrometer using a quartz optical cable which is set directly on the fused silica window of the reactor. This cable brings light to the input slit in front of which is located the adapter using to alignment the beam directly to the entrance slit. There are still some optical filters before the signal enters to the device to filter out a specific range of wavelengths and filter spectra of higher orders. It is possible to adjust the size of opening on the entrance slit using the software and thereby partially control the intensity of the radiation entering the device or its overall resolution. There are three various gratings in the spectrometer to disperse the light which are mounted to the circular holder. The circular holder can be rotated to exchange individual gratings [82], [83].

Hence, OES is mainly used to obtain plasma parameters such as discharge ionization degree, plasma density or temperature (rotational, vibration, electron excitation) which can be determined based on spectral lines or molecular bands intensities. This determination assumes that the distribution of populations at individual energy levels can be described by the Boltzmann distribution. Plasma parameters can be also determined based on the shape and width of the spectral lines. This method works with a natural line profile that differs from the Dirac function δ due to the Heisenberg principle of uncertainty and other nearby broadenings. Characteristic emission lines appear also at certain wavelengths in the optical emission spectrum from which can be gotten the information of the elemental composition of the plasma radiating species [80], [83].

3.3.1. Experimental settings used for OES measurements

Optical emission spectroscopy was used to determine plasma parameters, such as calculating the rotational or vibrational temperature from selected spectral systems and characterizing the dependence of the ionization degree on the dissipated power.

All measurements were done at the atmospheric pressure and ambient temperature. Measurements at lower temperature were not possible due to the presence of dense fog in the

reactor (see Fig. 54). There were series of measurements with different methane concetration (1.0, 1.5, 2.0, 2.5, 3.0, 3.5, 4.0 sccm in 200 sccm of Nitrogen) and different applied current (15, 25, 35, 45 mA)

Tab. 4: Jobin Yvon TRIAX 550 optical emission spectrometer specification.

Aperture	f/6.4
Focal length	55 cm
Difraction grating size	76 mm x 76 mm
Input slit size	0 – 2 mm
Image area	1.2 cm high x 3 cm wide
Possible granting densities	300 grooves/mm; 1200 gr/mm; 3600 gr/mm
Maximum spectral resolution	0.025 nm for 1200 gr/mm at 550 nm
CCD detector temperature	150 – 155 K

Tab. 5: Used experimental settings of the spectrometer in the present work

Grating density	1200 grooves/mm
Integration time	1.0 s
Input slit width	30 μm
Number of acquisition	1
Wavelength range	300 – 700 nm

3.3.2. Calculation of rotational and vibrational temperatures

The rotational temperature characterizes the rotational distribution of molecular states. Since the Boltzmann distribution is rapidly re-established (in the order of ps at atmospheric pressure) when the rotational state is changed, the rotational temperature is often considered to be the temperature of the neutral gas. It is therefore an important characteristic of plasmas. This is especially fulfilled if the plasma consists of only a single gas molecule. If different mixtures are present, the Boltzmann distribution is violated and the different temperatures can be calculated for each molecule [84], [87].

Thus, it assumes that the number of molecules located at different rotational levels of a given vibrational level and in a given electron state can be described by the Boltzmann distribution law

$$\frac{N_J}{N_{J=0}} = \exp\left(\frac{hcBJ(J+1)}{kT}\right), \tag{29}$$

where N_J is the number of molecules in the excited state, $N_{J=0}$ is the number of molecules in the ground state, h represents Planck's constant and k is the Boltzmann's constant, B is the rotational constant of the upper electronic state, J represents the given rotational state. The numerator in this equation (29) is an approximation of the rotational energy E_r that neglects, e.g., centrifugal distortion of molecules, multiplets, etc. Then, based on quantum mechanics, using the measured intensities of the individual rotational lines of a given vibrational band to construct a linear dependence (pyrometric line)

$$\ln\frac{I^{n,v,J}_{n',v',J'}}{S_J} = -\frac{hcB}{kT}J \tag{30}$$

where $I^{n,v,J}_{n',v',J'}$ represents the intensity of the rotational line and S_J is the Hönel-London factor which could be approximated in this case as J+1:

$$\ln\frac{I^{n,v,J}_{n',v',J'}}{J+1} = -\frac{hcB}{kT}J \tag{31}$$

From the pyrometric line slope K in equation (31) it is possible to calculate the rotational temperature [84], [87]

$$T_r = -\frac{hcB}{Kk}. \tag{32}$$

In this work, the rotational temperature was calculated specifically from the nitrogen second positive system $N_2^*(C^3\Pi_u \rightarrow B^3\Pi_g)$, because it was among the dominant bands in the spectrum. The 0-0 transition was used for the calculations because there was no significant overlap with other bands, the commonly used 0-2 band was overlapped with the rotational band of the violet CN spectral system in the current experiments. The resulting rotational temperatures then did not have the expected trend that could be compared with other publications. The value of the rotational constant for the upper state of this transition is 181,491 m^{-1} and the Hönel-London factor for the given spectral lines can be used $J + 1$ [87].

The vibrational or also excitation temperature characterizes the vibrational distribution of the molecular states. Under the thermodynamic equilibrium, it can also characterize the temperature of a neutral gas. In a non-isothermal plasma, it tends to be higher than the rotational and smaller than the electron temperature. As in the previous case, the calculation assumes the Boltzmann distribution of molecules at each vibrational level [84], [89], [90].
The intensity of one vibration band can then be expressed [84],

$$I_{v',v''} = \text{const}\, v^4 A(v'v'') \exp\left(-\frac{E_v}{kT_v}\right), \tag{33}$$

where $I_{v',v''}$represents the intensity of the vibrational band, v is the vibrational band wavenumber (or band edge wavenumber), $A(v'v'')$ is the transition probability (tabulated), and $v'v''$ are the vibrational quantum numbers of the upper and lower quantum levels. To asses whether or not the vibrational distribution is Boltzmann, the dependence of the $\ln \frac{I_{v',v''}}{v^4 A(v'v'')}$ on vibrational energy E_v has to be linear. If the dependence is linear, it is possible to construct the dependence by logarithmizing equation (54) [84]

$$\ln \frac{I_{v',v''}}{v^4 A(v'v'')} = -\frac{1}{kT_v} E_v + const. \tag{34}$$

From the slope *K* in dependence described by equation (33) it is possible to calculate the vibrational temperature [84]

$$T_v = -\frac{1}{Kk}. \tag{35}$$

In addition to the nitrogen second positive system mentioned above $N_2^*(C^3\Pi_u \rightarrow B^3\Pi_g)$, another important system in the spectrum, namely the violet CN radical system CN ($B^2\sum^+ \rightarrow X^2\sum^+$), which is well resolved and does not overlap significantly with other bands, was used to calculate the vibrational temperature. Again, it was very important to select which bands of the nitrogen second positive system to calculate the vibrational temperature from, since bands 0-2 to 4-6 in the 360-380 nm wavelength region were overlapped by the bands of the CN spectral system. This also had an impact on the resulting vibrational temperature values and trends. Therefore, bands 1-0, 2-1 and 3-2 in the 311-316 nm wavelength region, which were sufficiently resolved and separated from the other spectral systems, were selected for the calculation. The last system used to calculate the vibrational temperature was the first negative molecular nitrogen ion system N_2^* ($B^2\sum_u^+ \rightarrow X^2\sum_g^+$), which was not in high intensity as the previous systems but it was sufficiently resolved from the noise. The bands selected for the vibrational temperature calculation are shown in Tab. 6.

Tab. 6: List of spectral bands used to calculate vibrational temperatures

Spectral system	Used transitions
The nitrogen first negative system	0–2; 1–3; 2–4
The nitrogen second positive system	1–0; 2–1; 3–2
CN violet system	0–1; 1–2; 2–3; 3–4; 4–5

3.3.3. Results from OES measurements

As mentioned above all measurements were proceeded at the atmospheric pressure and laboratory temperature. Fig. 21 shows a selected OES spectrum in a gaseous mixture of 2 sccm of methane in 200 sccm of nitrogen at an applied current of 25 mA. The intensity in

the spectrum was calculated as the integral of the intensity of the band head, i.e. the peak maximum minus the mean value of the minimum. The plot shows the dominant spectral systems, which were also further used for the calculation of vibrational and rotational temperatures. In particular, the nitrogen second positive system N_2^* ($C^3\Pi_u \rightarrow B^3\Pi_g$), and the CN violet system CN ($B^2\sum^+ \rightarrow X^2\sum^+$) which are well resolved and do not overlap significantly with other bands. Another spectral system (the first negative system of the molecular nitrogen ion N_2^* ($B^2\sum_u^+ \rightarrow X^2\sum_g^+$)) is the less intense, which is still well resolved from the noise. The Swan system of the C_2 molecule was not sufficiently intense under the given conditions. This result is pretty suprising because the low intensity of the Swan spectral system C_2 indicates a low degree of CH_4 decomposition, which is in contrary to the almost unmeasurable intensity of the bands corresponding to CH_x fragments and their ions. In addition to the molecular bands there were also identified intense atomic lines as hydrogen H_α (656 nm) and H_β (486 nm).

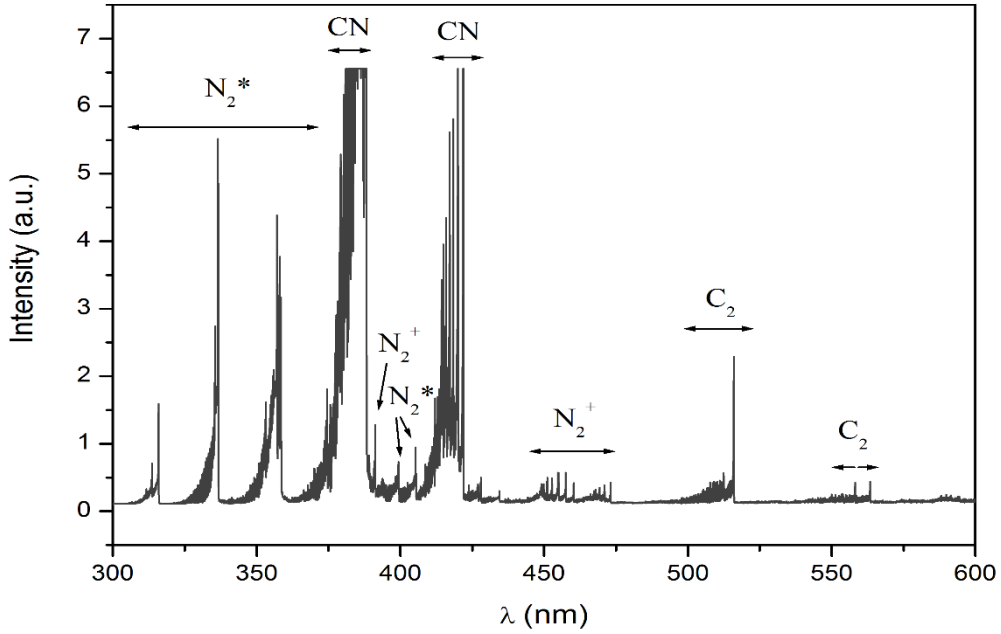

Fig. 21 Emission spectrum of a gas mixture of 2 sccm CH_4 in 200 sccm of N_2 and a current of 25 mA. The vibrational bands of each spectral system are indicated in the spectrum.

The rotational temperature, which is assumed to approximately corresponding to the neutral gas temperature, was calculated from the second positive spectral system of nitrogen, namely the 0-0 transition (Fig. 22).

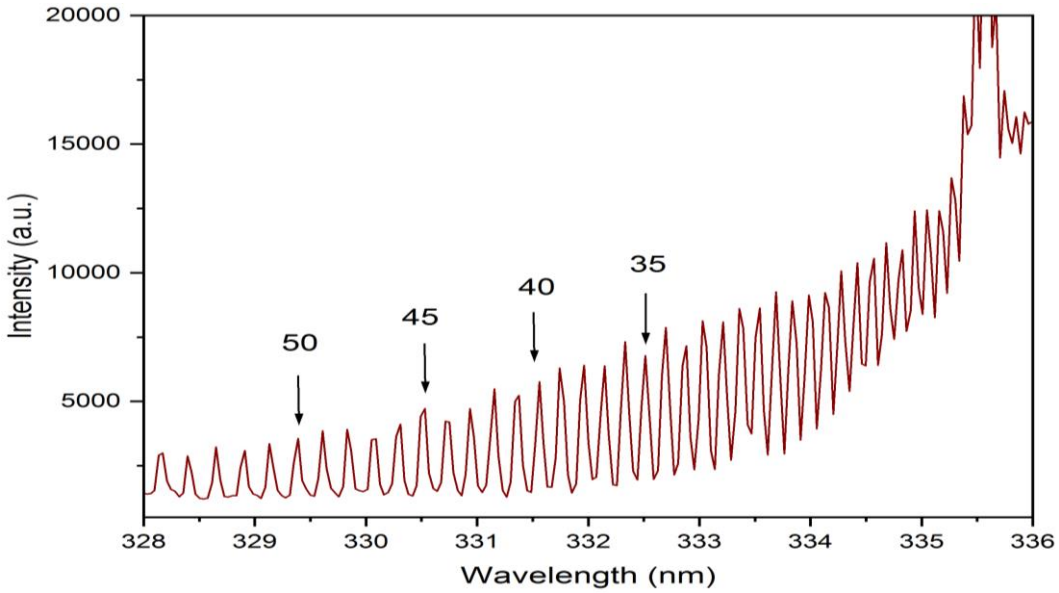

Fig. 22 Example of the emission spectrum of the nitrogen second positive system with marked 0-0 rotational levels. At 2 sccm CH_4 in 200 sccm of N_2 and a current of 25 mA.

Fig. 22 also shows the rotational states of upper electronic state that were used in the calculation of the rotational temperature. Higher rotational states were chosen because they are better distinguished in contrary to the lower rotational states (Fig. 23).

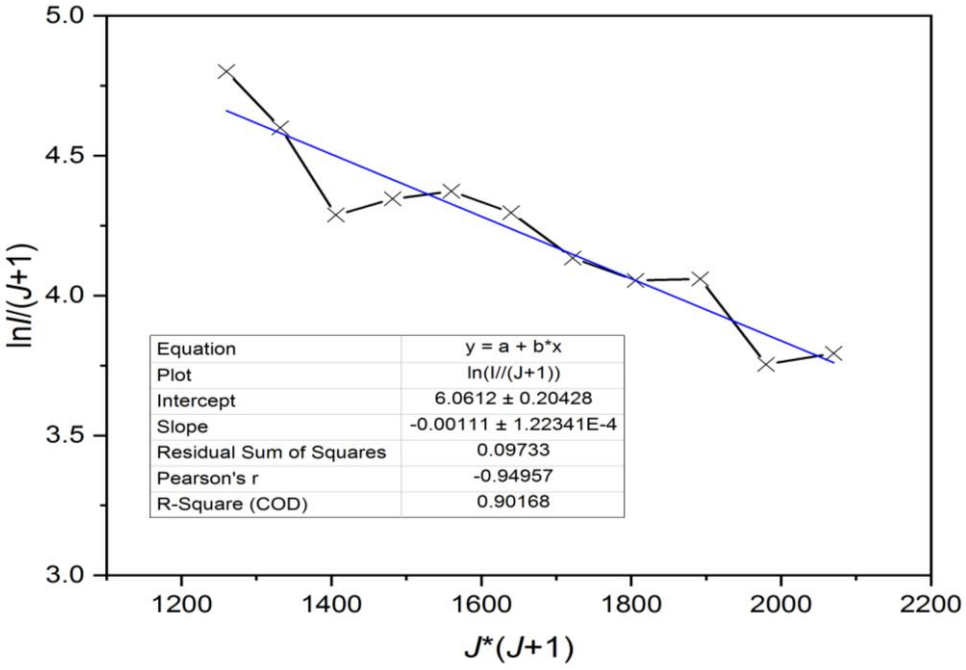

Fig. 23 The Boltzmann plot whose linear approximation is used to calculate the rotational temperature of the second of the positive nitrogen system.

Using the pyrometric line slope obtained by linear regression, the values of the rotational temperature as a function of the gas mixture composition and the power supplied to the reactor were calculated. The resulting average values of the rotational temperatures, which are rounded to the nearest tenth considering the uncertainty, are shown in Tab. 7.

Tab. 7: Rotational temperatures of the nitrogen second positive system at different power and composition of the mixture.

Q (sccm)	1	2	3	4
I (mA)	**Rotational temperature T_r (K)**			
15	2290 ± 40	2230 ± 40	2260 ± 40	2370 ± 40
25	2340 ± 40	2340 ± 40	2310 ± 40	2380 ± 40
35	2360 ± 50	2350 ± 50	2370 ± 50	2340 ± 50
45	2380 ± 50	2370 ± 50	2370 ± 50	2400 ± 50

Graphical representation of Tab. 7 can be seen at the Fig. 24. Each point represents a certain temperature interval because it is an error-bar. In the presence of the error bars, the points would overlap and therefore the standard deviations calculated of the temperatures are not shown in the graph, but they are mentioned in the Tab. 7 above. The uncertainty is approximately 40-50 K.

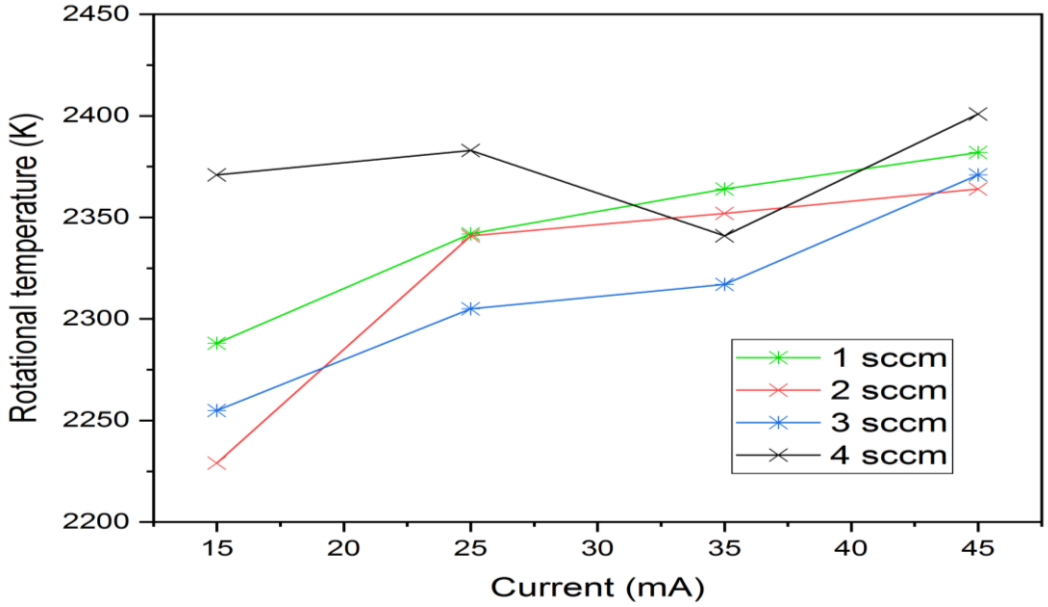

Fig. 24 Dependence of rotational temperatures on the power supplied to the discharge and the methane concentration flow for the nitrogen second positiveband 0-0 system.

From the Fig. 24 it can be seen that the rotational temperature increases with increasing power. As mentioned above, the rotational temperature is also often considered as the neutral gas temperature. Thus, it can be assumed that a higher energy input to the gas mixture will heat that mixture to a higher temperature. It can also be seen from the graph that increasing methane concentration causes the temperature in the simulated atmosphere to increase.

Further characterization of the discharge was carried out using vibrational temperatures. In the optical emission spectrum, the CN and N_2 vibrational bands, which were also well resolved from the other transitions, had sufficient intensity, and for these reasons were chosen for the calculation of the vibrational temperatures. Examples of the spectra are shown in Fig. 26 and Fig. 27 also with the vibrational bands marked. In the case of the nitrogen first

negative system, only bands 0-2, 1-3, 2-4 were used for the vibrational temperature calculation. Band 3-5 was not intense enough in some of the measured spectra (Fig. 25).

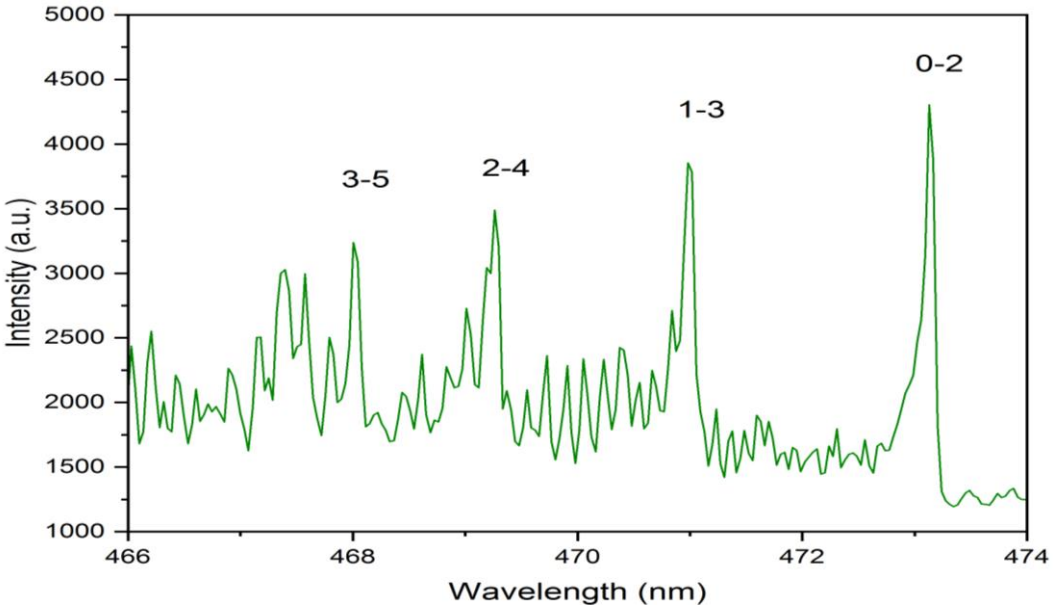

Fig. 25 Example of the 1st negative nitrogen emission spectrum with the vibrational bands identification measured at 2 sccm CH_4 in 200 sccm of N_2 and a current of 25 mA.

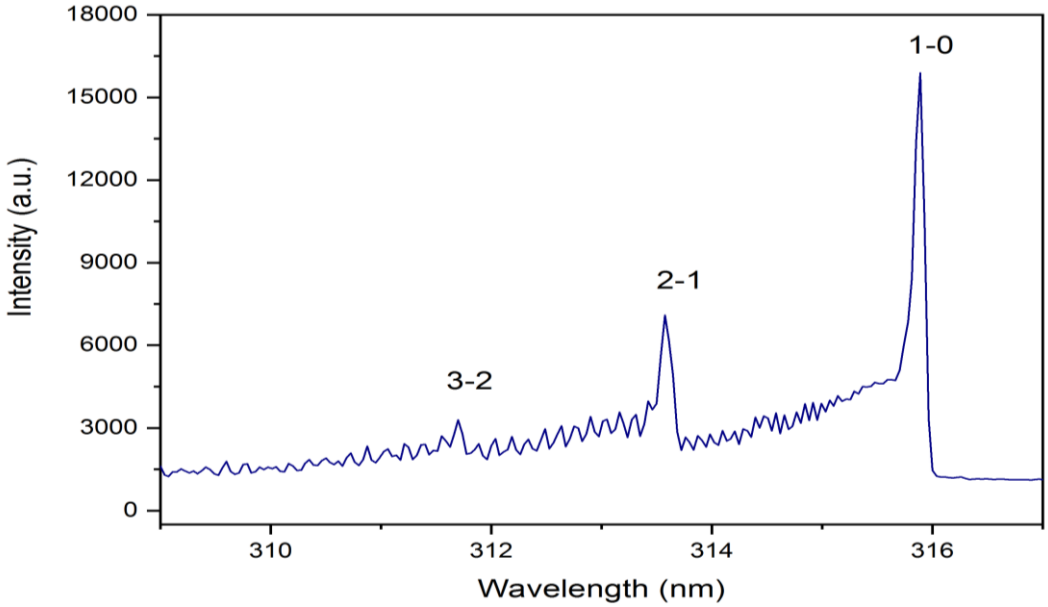

Fig. 26 Example of the 2nd positive nitrogen emission spectrum with the vibrational bands identification measured at 2 sccm CH_4 in 200 sccm of N_2 and a current of 25 mA.

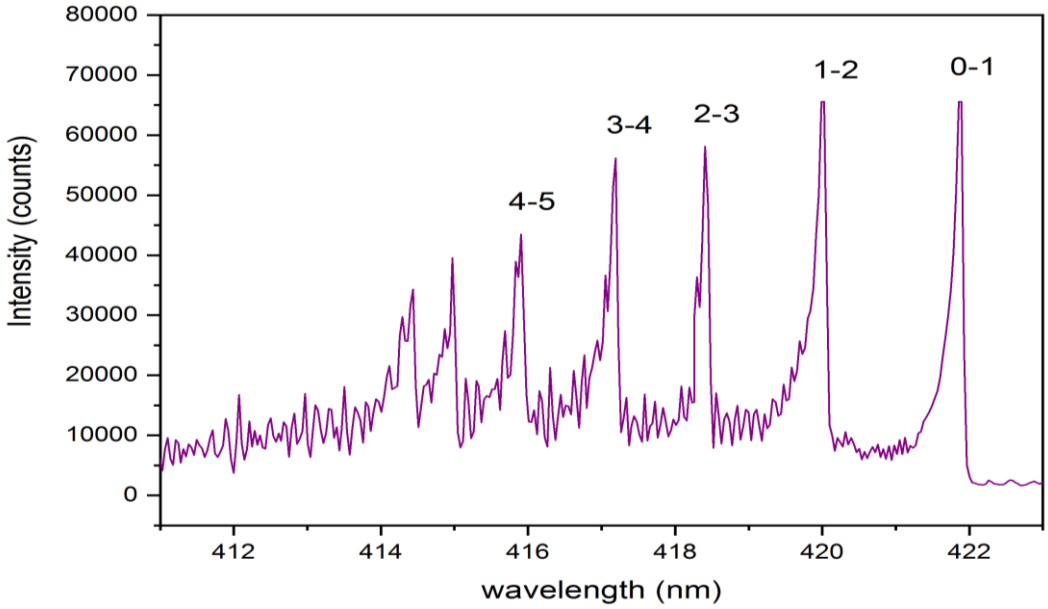

Fig. 27 Example of the CN violet emission spectrum with the vibrational bands identification measured at 2 sccm CH_4 in 200 sccm of N_2 and a current of 25 mA.

Calculating the vibrational temperature only has real meaning if the vibrational distribution is Boltzmann. In this case, to a first approximation, the dependence of the $\ln \frac{I_{v',v''}}{v^4 A(v' v'')}$ on vibrational energy E_v is linear.

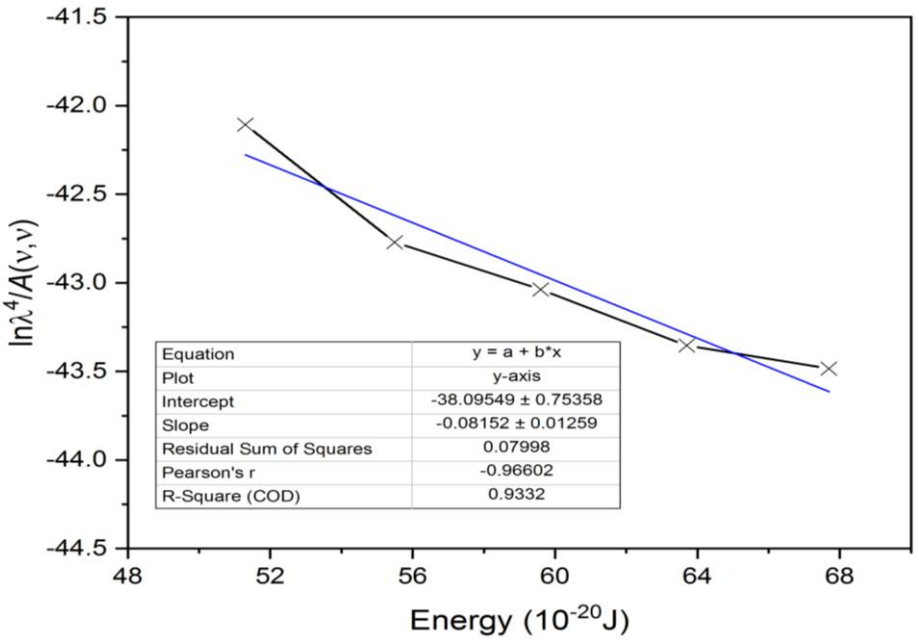

Fig. 28 The Boltzmann plot whose linear approximation is used to calculate the vibrational temperature of the CN violet spectral system

Using the previous pyrometric lines, the vibrational temperatures for each optical emission spectrum were calculated. For each composition of the working gas mixture and different delivered discharge current (15-45 mA), vibrational temperatures were calculated from the six spectra. The average temperature values of each selected spectral system are

shown in Tab. 8 - Tab. 10. The calculated values were then plotted on graphs showing how individual changes in initial concentration or power affect the resulting conditions in the reactor.

Tab. 8: Vibrational temperatures calculated from the nitrogen first negative system at different power and composition of the mixture

Q (sccm)	1	2	3	4
I (mA)	**vibrational temperature T_v N_2^{1-} (K)**			
15	4050 ± 100	3950 ± 100	4000 ± 100	3950 ± 100
25	4150 ± 110	4100 ± 110	4000 ± 110	3900 ± 110
35	4200 ± 130	4050 ± 130	4050 ± 130	4000 ± 130
45	4350 ± 120	4250 ± 120	4100 ± 120	4050 ± 120

Tab. 9: Vibrational temperatures calculated from the nitrogen second positive system at different power and composition of the mixture

Q (sccm)	1	2	3	4
I (mA)	**vibrational temperature T_v N_2^{2+} (K)**			
15	3100 ± 120	3150 ± 120	3300 ± 120	3300 ± 120
25	3100 ± 120	3300 ± 120	3200 ± 120	3300 ± 120
35	3100 ± 130	3200 ± 130	3300 ± 130	3350 ± 130
45	3100 ± 130	3250 ± 130	3300 ± 130	3400 ± 130

Tab. 10: Vibrational temperatures calculated from the violet CN spectral system at different power and composition of the mixture

Q (sccm)	1	2	3	4
I (mA)	**vibrational temperature T_v CN (K)**			
15	6200 ± 230	6100 ± 230	6100 ± 230	5900 ± 230
25	6500 ± 250	6700 ± 250	6200 ± 250	6500 ± 250
35	7400 ± 270	6800 ± 270	6900 ± 270	6500 ± 270
45	7700 ± 250	7800 ± 250	7500 ± 250	7300 ± 250

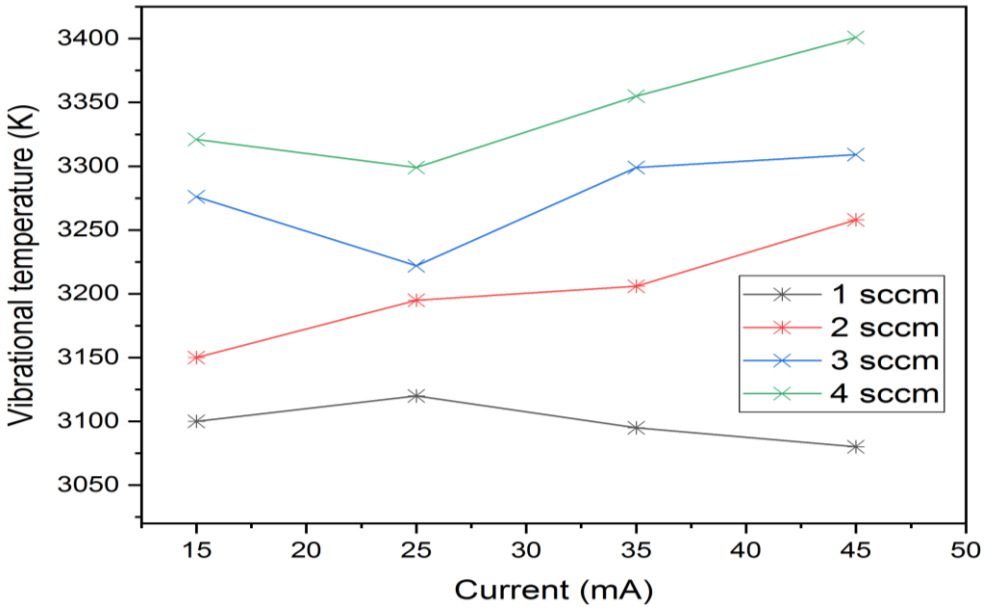

Fig. 29 Dependence of vibrational temperatures on the power supplied to the discharge and the methane concentration for the nitrogen second positive system.

From the dependence in Fig. 29, it can be seen that the vibrational temperature for the nitrogen second positive system does not change with increasing current supplied to the discharge. Similar to the rotational temperature calculated for this system, an increase in vibrational temperature occurs as the methane concentration in the working gas mixture increases.

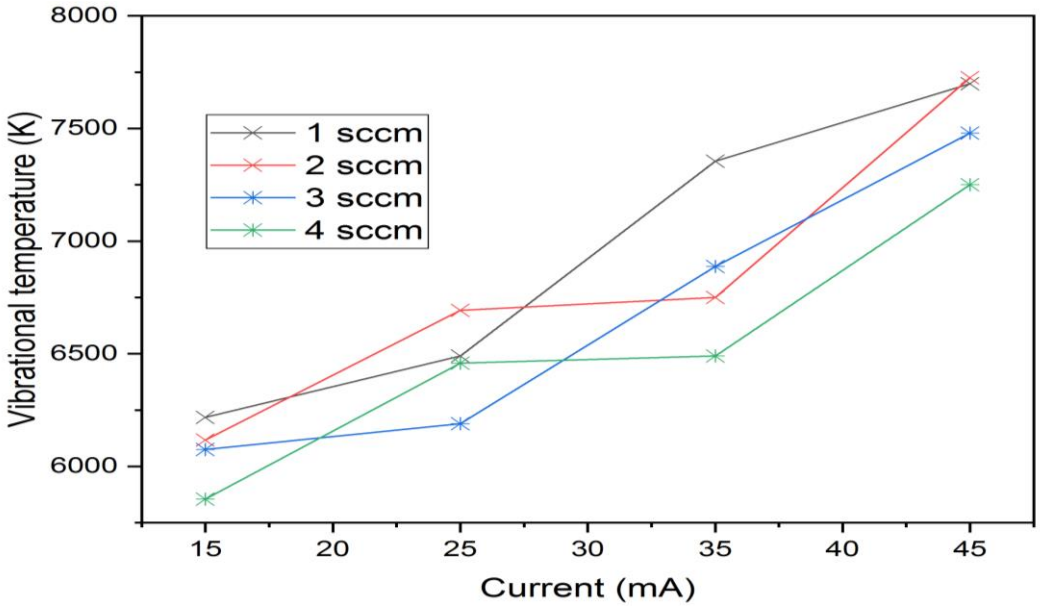

Fig. 30 Dependence of vibrational temperatures on the current supplied to the discharge and the methane concentration for the CN violet system.

The vibrational temperature of the CN violet spectral system seems to bring the most valuable information. This is evident from the fact that this system is dominant in the spectrum, is stable and does not overlap with any other systems. It can be seen from the

dependence in Fig. 30 that the vibrational temperature increases with increasing power and decreases with increasing methane concentration. This decreasing dependence may be due to the fact that the dissociation or excitation energy of CH_4 is less than the energy required to excite nitrogen to higher vibrational levels.

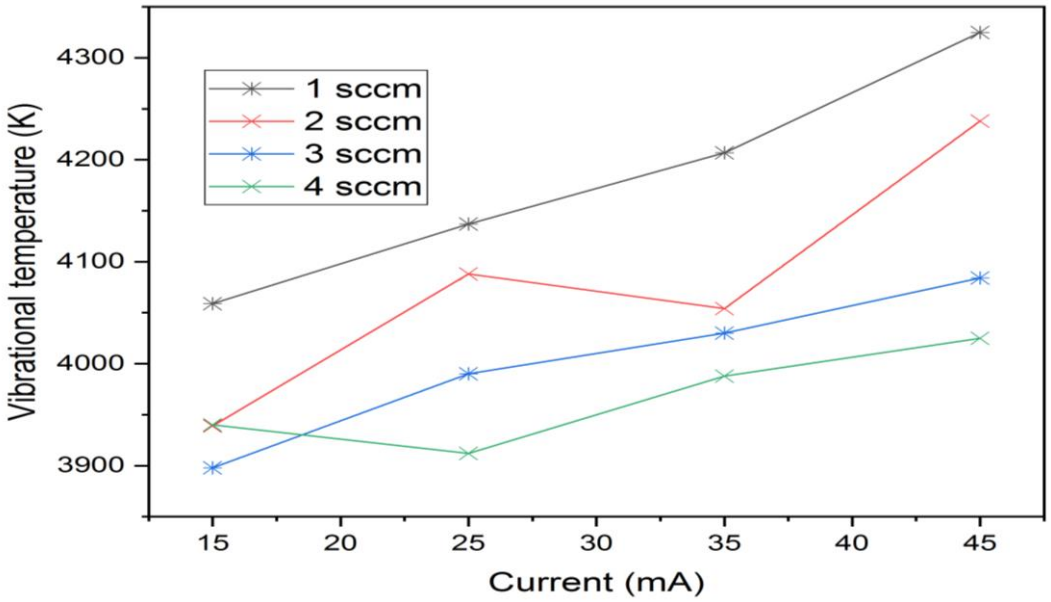

Fig. 31 Dependence of vibrational temperatures on the current supplied to the discharge and the methane concentration for the nitrogen first negative system.

As it can be seen from previous graph Fig. 29 the vibrational temperature dependence of the nitrogen second positive system is different from the vibrational temperatures of the nitrogen molecule ion and the CN radical, which may be related to excitation mechanisms. The nitrogen second positive system is excited primarily by collisions with high-energy electrons, while the other two systems are excited primarily by collisions with metastable ground-state nitrogen molecules with vibrational quantum number $v \geq 12$ [85].

Therefore, energy is preferentially consumed for dissociation and excitation of methane products, which may ultimately result in a lower nitrogen population at higher vibrational levels.

The increasing dependence of vibrational temperature on increasing power can also be seen in Fig. 31 for the molecule ion or the nitrogen first negative system, respectively. In contrast, the vibrational temperature decreases with increasing methane concentration, because without CN the so-called v-v process takes place, when vibrationally excited nitrogen ground state molecules collide (they are metastable because nitrogen is homonuclear molecule) one moves one level up and one level down and the excess energy goes into heat. When there is more CN, this process slows down above level 12, so the higher ones are then occupied less, and therefore the temperature comes out lower at higher concentrations.

Measurements of the optical emission spectra of the atmospheric pressure discharge of a gaseous mixture of N_2 with CH_4, confirmed that N_2 will participate in a numeruos reactions due to its dominance in the gaseous mixture. The dissociation of nitrogen occurs predominantly by electron impact, as indicated in reactions 36 to 42 [86]

$$N_2\left(X^1\sum_g^+\right) + e(11{,}1\ eV) = N_2(C^3\Pi_u^+) + e\ , \quad (36)$$

$$N_2\left(X^1\sum_g^+\right) + e(15{,}63\ eV) = N_2^+\left(X^2\sum_g^+\right) + 2e\ , \quad (37)$$

$$N_2\left(X^1\sum_g^+\right) + e(16{,}84\ eV) = N_2^+(A^2\Pi_u) + 2e\ , \quad (38)$$

$$N_2\left(X^1\sum_g^+\right) + e(18{,}76\ eV) = N_2^+(B^2\sum_u^+) + 2e\ , \quad (39)$$

$$N_2\left(X^1\sum_g^+\right) + e(23{,}53\ eV) = N_2^+\left(C^2\sum_g^+\right) + 2e\ , \quad (40)$$

$$N_2\left(X^1\sum_g^+\right) + e(26{,}66\ eV) = N^+\ (\ ^3P) + N(\ ^2D) + 2e\ , \quad (41)$$

$$N_2\left(A^3\sum_u^+, a^1\Pi_g, a^1\sum_u^-\right) + e = N^+\ (\ ^3P) + N(\ ^2D) + 2e\ , \quad (42)$$

The excited state of N_2 ($C^3\Pi_u^+$) of the second positive system is produced by direct impact of electrons exciting the ground state $X^1\sum_g^+$ [86]. It is the result of collision with electrons according to reaction (35) whose energy is higher than the excited state threshold (11.1 eV). Reaction (38) is responsible for ionization with simultaneous excitation of the N_2 molecule from the ground state to the N_2^+ state ($B^2\sum_u^+$), which is the upper state of the first negative system of the molecular nitrogen ion. The measured spectra also show weak lines of N^+ ions, which can be produced by reaction (40), where the electron energy is higher than 26 eV, or by several different processes via metastable nitrogen products that proceed in multiple steps see e.g. reaction (41) [86], [87].

3.4. Proton transfer mass spectrometry

The study of ongoing chemical processes, analysis of discharge synthetized products and their transformation into more complex substances, was carried out using mass spectrometry with proton ionization in the present work. The PTR-TOF-MS mass spectrometer took *in situ* samples in real time and processed the results with a very fast response time. Due to the high sensitivity of the spectrometer and the fast saturation, the resulting gaseous mixture had to be diluted before entering with an auxiliary stream of nitrogen. The general specification of the device is given in Tab. 11.

Tab. 11: Specification of PTR-ToF-MS 1000

Type of ionisation	H_3O^+ ions
Resolution FWHM	> 1500 m/Δm; at m/z > 60
Sensitivity	> 40 cps/ppbv
Detection limit	< 10 pptv
Linear range	10 pptv – 20 ppmv
Response time	< 100 ms
Current of ion source	5 mA
Range of molecular weight	1 – 520 amu (possible up to 10 000 amu)
Acquisition frequency	58 kHz

The measured spectrum was in the range of molar masses from 10 to 520 $g \cdot mol^{-1}$. Before starting to detect gaseous products from the discharge, it was necessary to perform the calibration of the spectrometer (the whole calibration is described in my master thesis) [88]. Subsequently, it was necessary to determine the stability of the measurement due to the optimal interval of cycles in which the response of the detector is stable. This measurement was performed within 1100 scans, which lasted about 18 minutes. The measurement result for HCN, which was the most abundant gaseous product in the discharge, is shown at the Fig. 32.

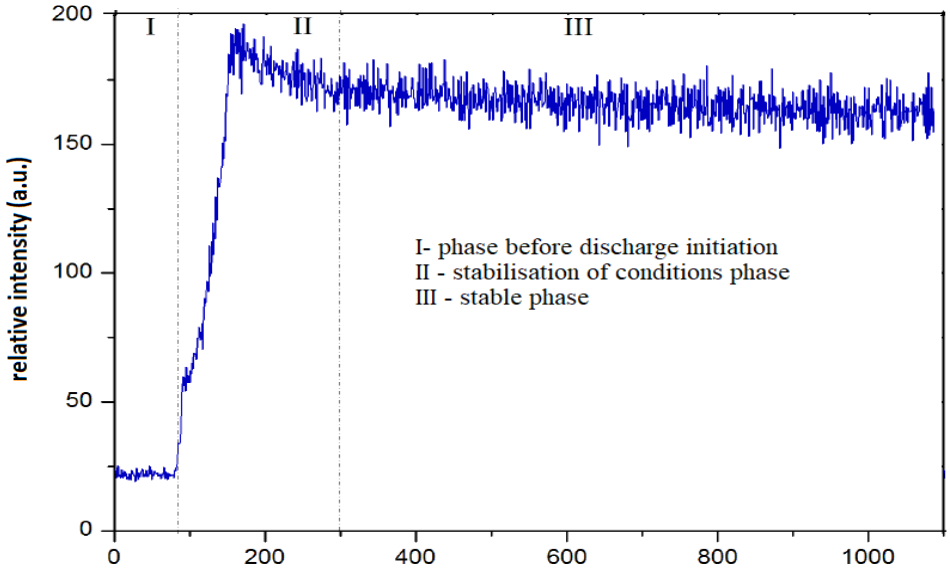

Fig. 32: Stabilization of discharge operation conditions of PTR-TOF-MS detector for HCN.

In the first phase without discharge, when HCN has not yet been formed, the intensity is very low. This phase lasted approximately 85 seconds. In the next phase, the conditions stabilized after the discharge ignition. The duration of this phase was about 225 seconds. Immediately after ignition, HCN began to form and the intensity increased very sharply. Subsequently, it dropped slightly to a value that has already remained relatively stable for approximately 800 scans. In the stable phase, the intensity does not decrease rapidly or increase, it is more or less stable. This trend appears with an increasing number of scans, and this may be due to the increasingly saturated system. Based on Fig. 32, the resulting spectra were taken as an average from range at 300 to 350 seconds, when the response was stable and the system was not yet saturated.

3.4.1. Measurements with PTR-ToF-MS at laboratory temperature

This experiment was also published in Q2 journal ACS Earth and Space Chemistry [89]. The full article is attached at the end of the dissertation.

The experiment was carried out in the flowing regime at laboratory temperature and atmospheric pressure. The discharge was operating at the constant current of I = 25 mA (corresponding power was of 10 W). This power was selected based on the preliminary experiments. It supplied sufficient energy without significant heating of the whole system (reactor wall temperature during the discharge operation was below 40 °C). The gas mixture composition of nitrogen and methane was controlled by the Bronkhorst mass

flow controllers wherein the total gas mixture flow rate into the reactor was 200−204 sccm. The specific composition of the individual gas mixtures used in the experiments is shown in Tab. 12.

Tab. 12: Composition of the individual gas mixtures

Mixture	CH_4 (sccm)	N_2 (sccm)	CH_4 (%)
1	0.2	200	0.1
2	0.5	200	0.3
3	0.8	200	0.4
4	1.0	200	0.5
5	1.3	200	0.7
6	1.6	200	0.8
7	2.0	200	1.0
8	2.5	200	1.3
9	3.0	200	1.5
10	3.5	200	1.8
11	4.0	200	2.0

To minimize presence of other gases in the reactor it was necessary to pre-vacuate the reactor before each experiment by using a rotary oil pump and simultaneously, to control the sealing of the reactor for 60 minutes. Since the gas flow velocity through the inlet/outlet tubes was only 28 $cm \cdot s^{-1}$, the outlet tube was constricted to eliminate a possible back-diffusion of air into the reactor. Once the gas mixture flow has started, the reactor was purged by the working gaseous mixture for 45 minutes to achieve the stable and correct pressure. Just after this time, the discharge was ignited by the increasing voltage. The discharge itself was ignited when the voltage was applied to the electrodes in the range of 5−5.5 kV, and immediately after the discharge ignition, the voltage dropped rapidly to 0.4–0.5 kV.

The experiment was completed following the scheme in Fig. 33.

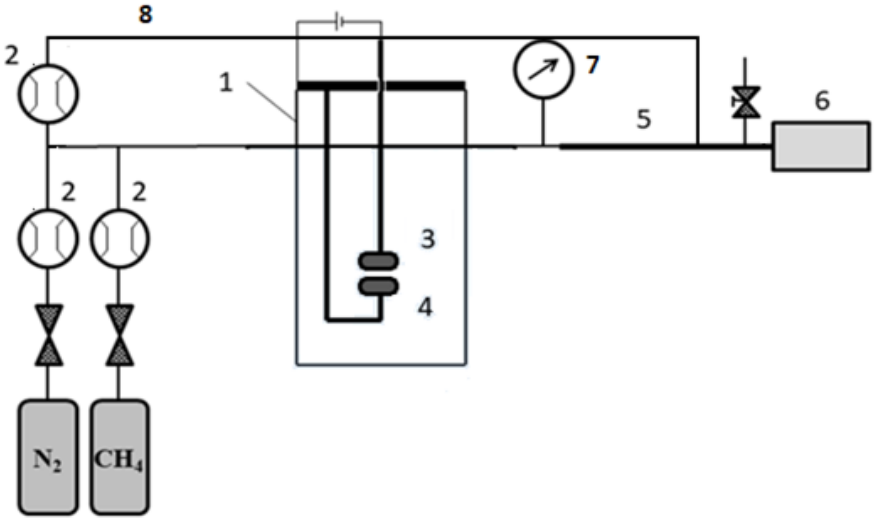

Fig. 33. Scheme of the experimental set up: 1 – stainless steel reactor vessel; 2 – mass flow controller; 3 – cathode; 4 – anode; 5 – heated exhaust gas sampling line; 6 – proton transfer reaction time of flight mass spectrometer; 7 – membrane pressure gauge; 8 – heated diluting inlet

The used gasses were of the following purities: nitrogen 99.999 %, methane 99.95 %. The whole line (made of PTFE, stainless steel and PEEK) to the PTR-TOF mass spectrometer was heated up to 80 °C to avoid discharge products condensation.

Reactor was not opened or cleaned between experiments, so some contamination (mainly by some deposited material on the electrode surfaces) was possible. To eliminate this contamination effect, experiments started in pure nitrogen and methane concentration was increased from experiment to experiment.

A direct connection from the reactor outlet to the PTR-MS was used for the transfer of gaseous products created by chemical reactions initiated by the discharge. Due to the high sensitivity of the equipment, it was necessary to dilute the discharge products gaseous flow by 1000 sccm of nitrogen (purity of 99.999 %) before the PTR-TOF inlet to avoid saturation limit as much as possible and to improve the quality of the analysis itself.

The following figures (Fig. 34, Fig. 35 and Fig. 36) show the spectra at methane concentration of 0.3, 1.0 and 2.0 %. All spectra are subtracted from the background and they are already corrected by -1 to get their real molecular weight (not protonated as measured by the device). The dependence on the methane flow shows how the quantity and ratio of the products is developed and the formation of new higher molecular weight substances is clearly demonstrated. The supplementary material also shows spectra for the other flows of methane that confirm a similar trend.

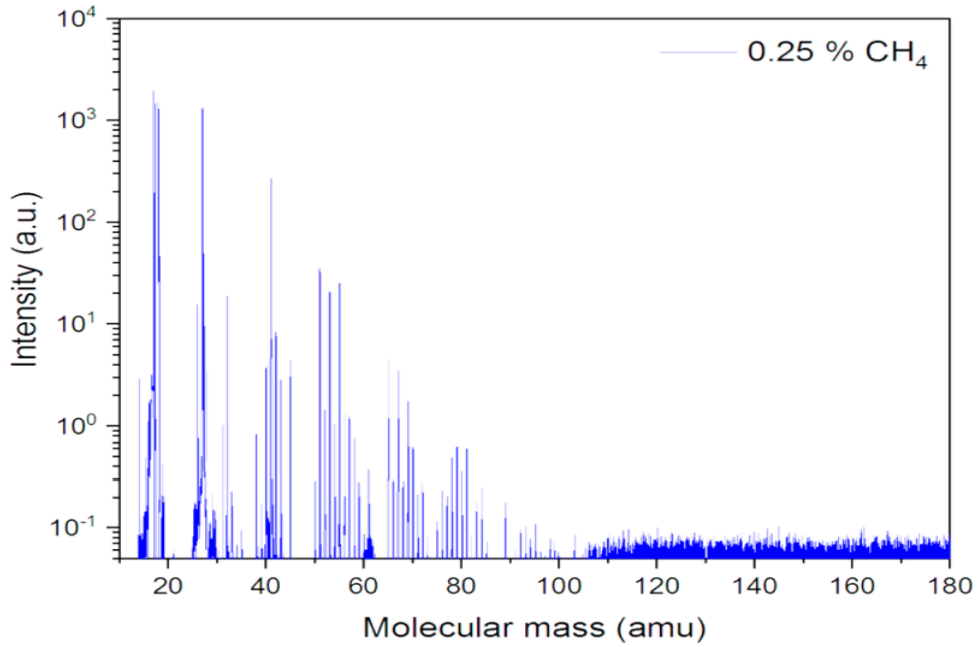

Fig. 34: PTR-TOF mass spectrum of gaseous products produced in the discharge at the methane concentration of 0.25 % in nitrogen.

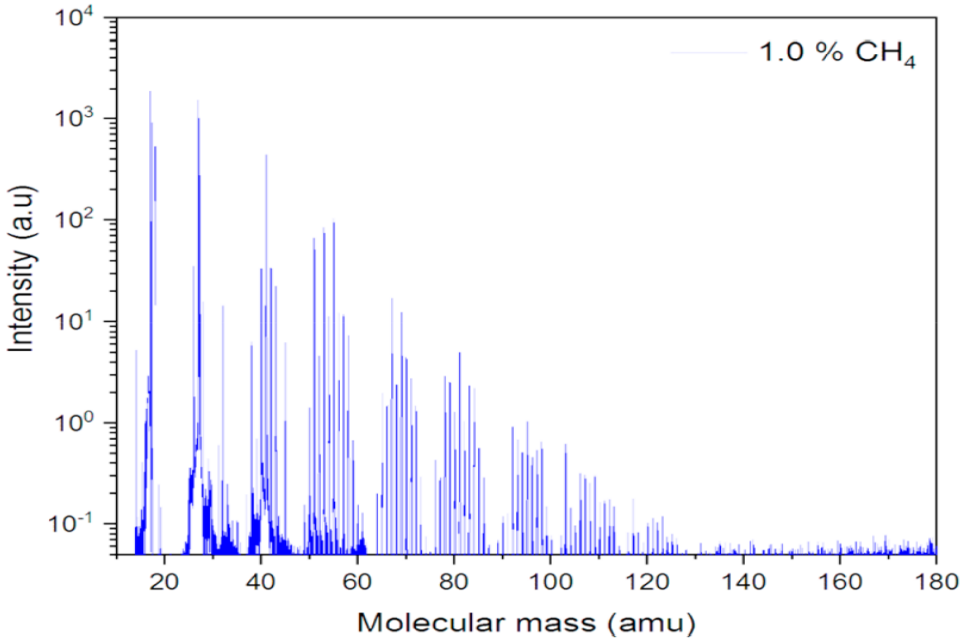

Fig. 35: PTR-TOF mass spectrum of gaseous products produced in the discharge at the methane concentration of 1 % in nitrogen.

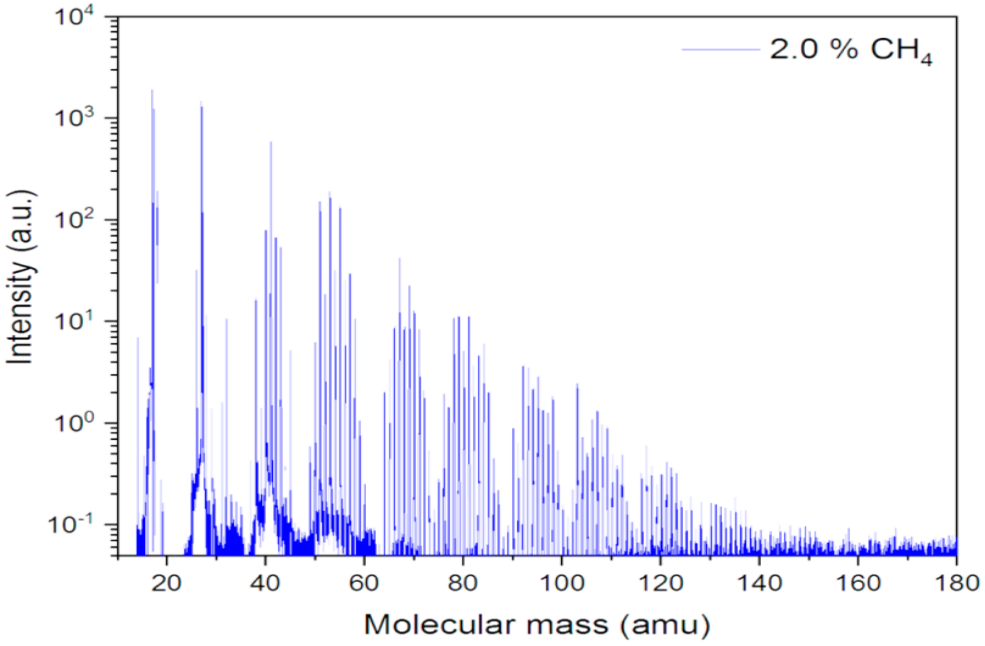

Fig. 36: PTR-TOF mass spectrum of gaseous products produced in the discharge at the methane concentration of 2 % in nitrogen.

The presented spectra demonstrate the expected fact that the total intensity of the detected products increases with the increasing CH_4 flow. This trend is most apparent for substances with the molecular weight higher than 75 amu. Significant differences in the intensity are well visible for example in case of benzene (C_6H_6) having the molecular weight of 78 amu. Substances with the molecular weight over 100 amu have intensities close to the noise level at low flows of methane, and their intensities increase very rapidly (almost exponentially, see later) at the higher methane concentrations from 1.3 to 2 %.

Fig. 37, Fig. 38, Fig. 39 and Fig. 40 show the mass spectrum at the methane concentration of 1.5 %. The spectrum is divided into 4 parts for a better graphical representation of the detected gaseous products in the discharge exhaust gas, in which the individual substances are better distinguished and marked.

The acetylene (H_2C_2; 26 amu), hydrogen cyanide (HCN; 27 amu), acetonitrile (CH_3CN; 41 amu), cyanoacetylene (C_3HN; 51 amu), propane nitrile (C_2H_5CN; 55 amu), (butanenitrile; 69 amu) and (benzene; 78 amu) were the major compounds detected by the PTR-TOF-MS under the presented conditions. Relative intensity ratios indicate that the most abundant products in the discharge were hydrogen cyanide and acetonitrile. All compounds mentioned above were detected or at least expected to be presented on the Titan according to the theoretical models [94], [95]. However, their relative concentrations cannot be correctly compared with the data obtained from the Titan atmosphere because the current experiment was carried out at ambient laboratory temperature and thus bigger molecules like tholins were not synthesized effectively enough. Among more stable molecules, the C_4N_2 molecules were detected in the current experiment thanks to the very low limit of detection of the PTR-ToF-MS. As it was explained in the work of P. Coll et al. [94], C_4N_2 has a very low stability at room temperature, so it is very difficult to analyse this compound at ambient temperature. Results of the presented experiments are also in a very good agreement with other experimental studies.[96], [97], Peng et al. **[**96] used UV-VUV synchrotron radiation. The C_2, C_3, C_4 and most probably also C_5 compounds were detected by IMS; the most abundant compounds were HCN, CH_3CN and C_2N_2. N. Carrasco et al. [97] demonstrated the important role of methane concentration on the production of ammonia and consequent synthesis of heavier molecules [97]. The processes were studied in the PAMPRE plasma reactor via the optical emission spectroscopy [97].

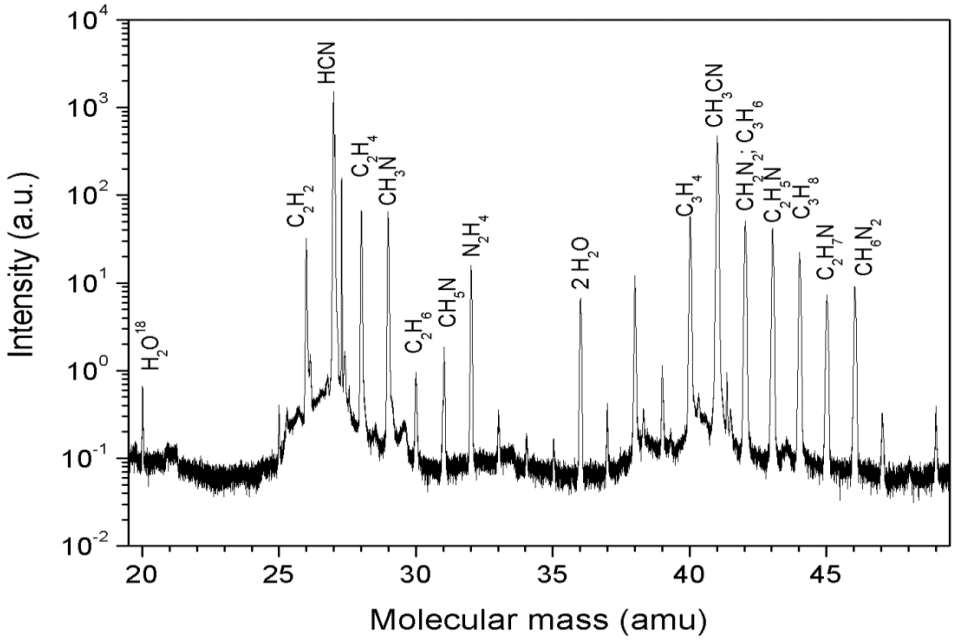

Fig. 37: The identified mass spectrum (range of 20−50 g/mol) measured in the discharge at the methane concentration of 1.5 %.

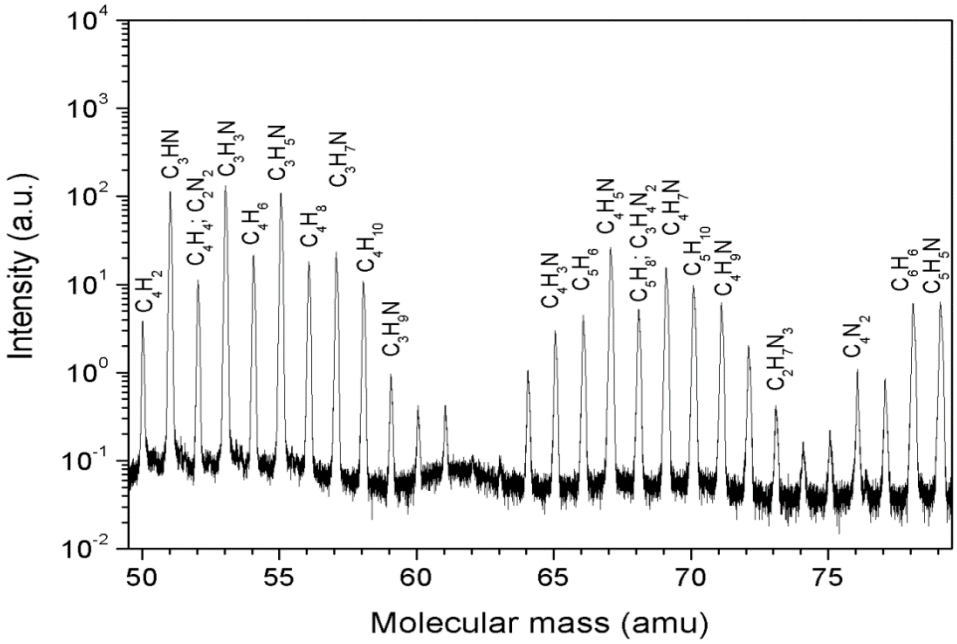

Fig. 38: The identified mass spectrum (range of 50−80 g/mol) measured in the discharge at the methane concentration of 1.5 %.

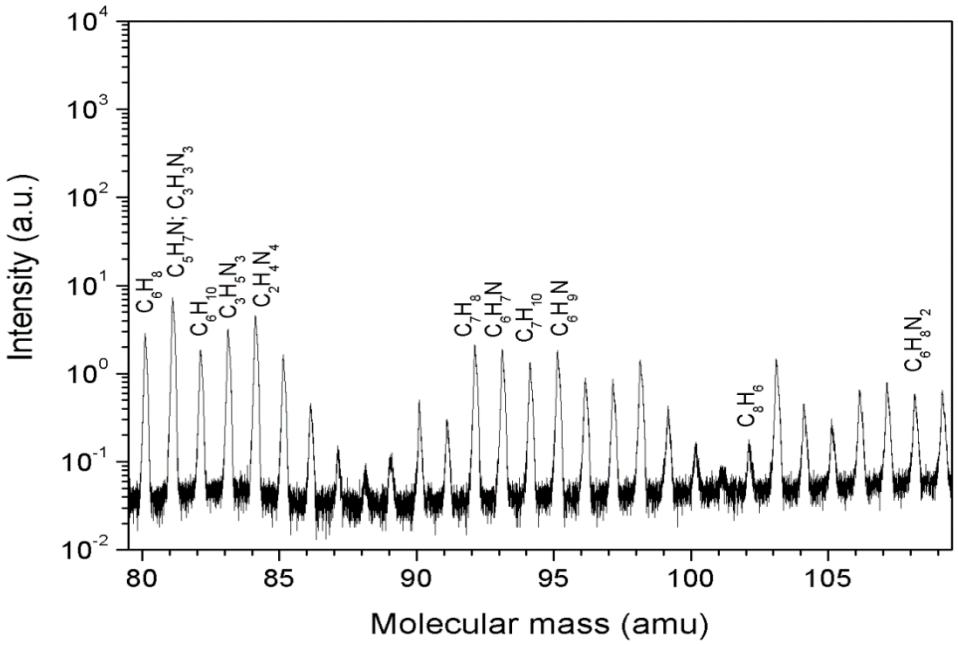

Fig. 39: The identified mass spectrum (range of 80−110 g/mol) measured in the discharge at the methane concentration of 1.5 %.

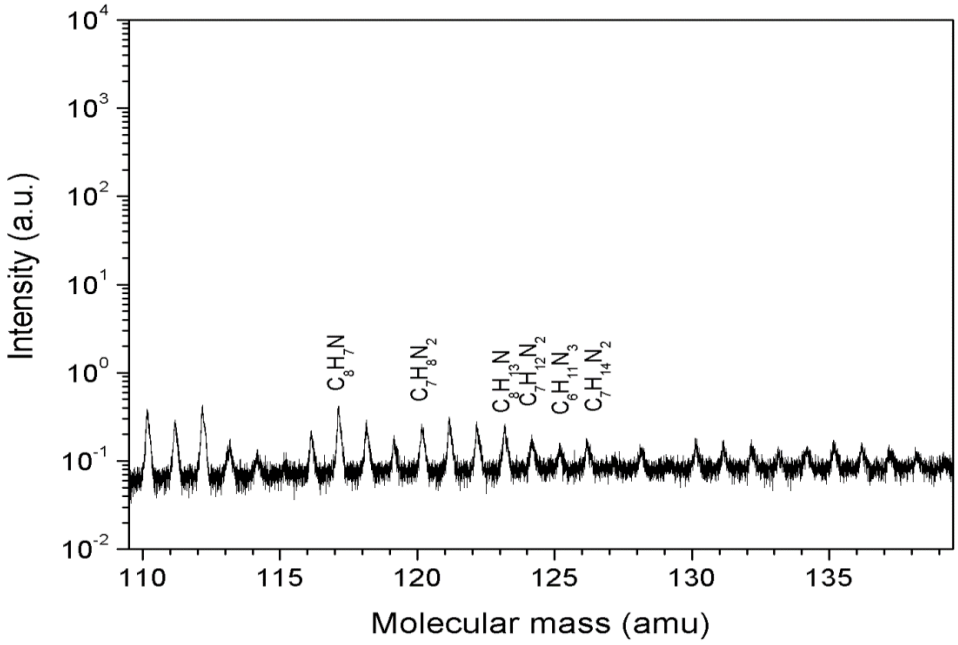

Fig. 40: The identified mass spectrum (range of 110−140 g/mol) measured in the discharge at the methane concentration of 1.5 %.

The full list of all up to now identified hydrocarbons and nitrogen containing compounds is presented in the table below. The relations to the other laboratory data as well as confirmed presence in the Titan atmosphere (marked by * and with a bold reference) are included in the table, too.

Tab. 13: Detected hydrocarbons and nitrogen containing compounds by PTR-TOF-MS.

Molecular weight	Formula	Name
17	NH_3	Ammonia [97]
27	HCN	Hydrogen cyanide*[98][99]
28	C_2H_4	Ethylene*[98][99]
29	CH_3N	Methanimine [100]
30	C_2H_6	Ethane*[98][99]
31	CH_5N	Methanamine [101]
32	N_2H_4	Hydrazine [102]
40	C_3H_4	Propyne*[98][99]
41	C_2H_3N	Acetonitrile*[98][99]
42	H_2CN_2	Cyanamid [102]
42	C_3H_6	Propene [94]
43	C_2H_5N	Aziridine [100]
44	C_3H_8	Propane*[98][99]
45	C_2H_7N	Dimethylamine [103]
46	CH_6N_2	Methanediamine
50	C_4H_2	Diacetylene*[98][99]
51	C_3HN	Cyanoacetylene*[98][99]
52	C_4H_4	Cyclobutadiene [102]
52	C_2N_2	Cynogen [102]
53	C_3H_3N	Acrylonitrile [103]
54	C_4H_6	Butadiene [102]
55	C_3H_5N	Propionitrile [103]
56	C_4H_8	Cyclobutane [102]
57	C_3H_7N	Allylamine [103]
58	C_4H_{10}	Butane [102]
59	C_3H_9N	(2-Hexyne) [105]
65	C_4H_3N	Cyanopropyne*[104]
66	C_5H_6	Cyclopentadiene [105]
67	C_4H_5N	Pyrrole [107]
68	$C_3H_4N_2$	Imidazole [106]
68	C_5H_8	1-Pentyne [105]
69	C_4H_7N	Butyronitrile [107]
70	C_5H_{10}	1-Pentene [105]
71	C_4H_9N	(m,p,Xylene) [105]
73	$C_2H_7N_3$	(o-Xylene) [105]
76	C_4N_2	Dicyanoacetylene*[98][99]

Molecular weight	Formula	Name
78	C_6H_6	Benzene*[98][99]
79	C_5H_5N	Pyridine [108]
80	C_6H_8	Cyclohexadiene [105]
81	$C_3H_3N_3$	1,3,5-triazine [107]
81	C_5H_7N	Cyclopropylacetonitrile [107]
82	C_6H_{10}	Hexyne [105]
83	$C_3H_5N_3$	Pentanenitrile [107]
84	$C_2H_4N_4$	Cyanoguanidine [107]
92	C_7H_8	Toluene [105]
93	C_6H_7N	Aniline [108]
94	C_7H_{10}	1-Hepten-6-yne [105]
95	C_6H_9N	Cyclopentanecarbonitrile
102	C_8H_6	Phenylacetylene [105]
108	$C_6H_8N_2$	Hexane dinitrile
117	C_8H_7N	benzyl cyanide [109]
120	$C_7H_8N_2$	9H-Purine
123	$C_8H_{13}N$	Cycloheptanecarbonitrile
124	$C_7H_{12}N_2$	Butylimidazole
125	$C_6H_{11}N_3$	Octanenitrile
126	$C_7H_{14}N_2$	Diisopropylcyanamide

Fig. 41 and Fig. 42 show relative intensities of selected species in the dependence on the methane concentration. Representative substances from different groups (aliphatic hydrocarbons, cyano and aromatic compounds) were chosen to demonstrate how they arise or are not influenced by the methane concentration. The highest intensity increase is observed for the higher molecular weight substances such as benzene or toluene, especially at methane concentrations of 1−1.5 %. The intensities of lower molecular weight molecules like hydrogen cyanide, acetylene or acetonitrile, are nearly independent on methane concentration in the range of 1−2 % (2−4 sccm). This well reflects that lower molecular weight substances could be predominantly consumed for creation of higher molecular weight products at higher methane concentrations. HCN concentration reached the saturation limit of the current device during the discharge operation and thus, dependence of its intensity does not reflect the running processes properly.

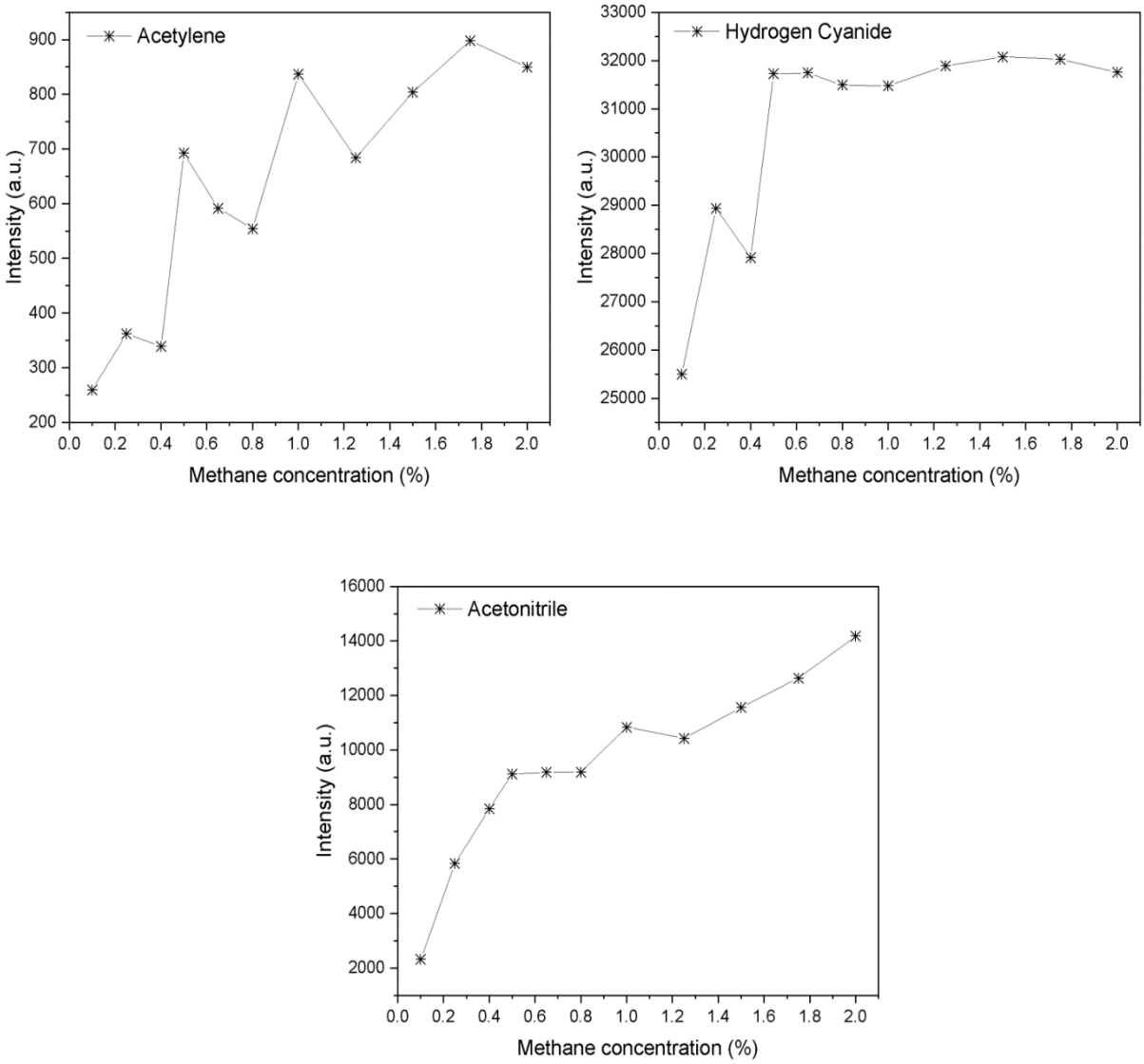

Fig. 41: Dependence of the relative intensity of acetylene, hydrogen cyanide and acetonitrile on the methane concentration in nitrogen.

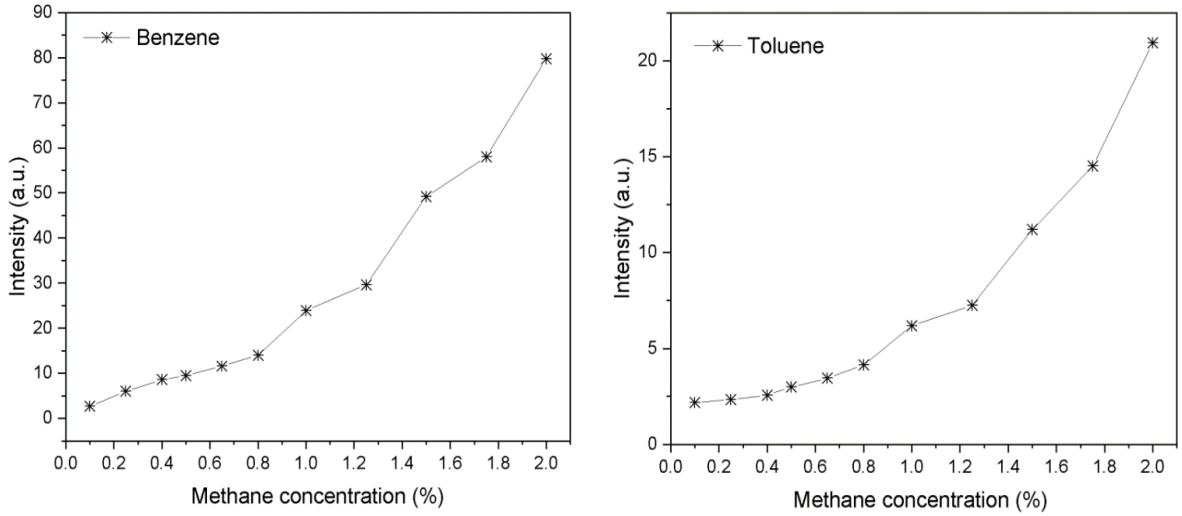

Fig. 42: Dependence of the relative intensity of benzene and toluene on the methane concentration in nitrogen.

The presented intensity dependencies reveal that the formation of hydrogen cyanide also increases with the increasing methane concentration. This is also consistent with the comparison of the results from the optical emission spectroscopy [110] which shows an increase of the CN radicals concentration at lower methane concentrations, only [111], [112]. The PTR-TOF technique has a disadvantage that its resolution is limited and thus, some compounds could not been distinguished. This is, unfortunately, also the case of HCN. The exact molecular weight of HCN M = 27.0253 g·mol^{-1} is very similar to the molecular weight of the C_2H_3 vinyl radical M = 27.0446 g·mol^{-1}. Since the mass resolving power for m/z < 60 is FWHM > 1000 $m/\Delta m$ so this particular difference Δm = 0.0193 at m/z = 28 is smaller than the instrument is able to distinguish and therefore, both peaks are merged in one. At lower concentrations of methane, a large amount of CN radical is produced, causing a high HCN peak. As the concentration of methane increases, substances with higher molecular weights are produced, and thus CN radicals are consumed and their concentration is decreasing. This causes a decrease in the intensity of the vinyl radical. However, the total hydrogen cyanide concentration is increasing. The peak deconvolution was applied to distinguish HCN and vinyl, and thus the relative intensity was calculated separately for HCN.

3.4.2. Measurements with PTR-ToF-MS at lower temperature

The experiment was carried out in the simple glass reactor (see Fig. 43) equipped by a pair of tungsten rod electrodes (diameter of 1 mm) in a distance of 0.7 mm as well as stainless steel high vacuum reactor with electrode arrangements for abnormal atmospheric pressure glow discharge (Fig. 17) with pair of stainless steel electrodes in shape of the raindrop in the distance of 1-2 mm. The glow discharge was operating at the current of 25 mA (corresponding powers of 10 W). Reactor was immersed into the liquid nitrogen up to above the electrode system, so the reactor wall temperature was fixed at 77 K. The gas temperature inside the reactor was at -160 °C 2 cm above the reactor bottom and -30 °C 2 cm from the

reactor top. The gas mixture composition was controlled by Bronkhorst MCFs. Used gasses were nitrogen, methane, oxygen and CO_2. Four mixtures were used for the current experiments: pure nitrogen with flow of 200 sccm, nitrogen with addition of 5 sccm of methane and the same mixture enriched by oxygen or CO_2 with flows only up to 1 sccm. Pressure in the reactor during the experiment was kept at 1.5 atmosphere and was measured by digital manometer (Fig. 43 and part 8). Preliminary results showed significant decrease of water ion concentration after analyte injection (mainly at higher methane concentrations) and thus analyte dilution was applied.

Whole line (made of PTFE and stainless steel) to PTR-TOF mass spectrometer was heated up to 80 °C to avoid discharge products condensation. Reactor was not opened or cleaned between experiments, so some contamination (mainly by some deposited material on electrode surfaces) was possible.

Experiment was completed following the scheme:

1) -300 s start of reaction mixture flow
2) 0 s start of measurement
3) 60 s discharge turn on
4) 600 s starting reaction vessel cooling
5) 1800 s discharge off
6) 2400 s end of vessel cooling
7) 3000 s start of reactor heating by hair drier
8) 3300 s end of reactor heating by hair drier; nitrogen (99.999%) high flow of 5 Slm purge flow on, opening of exhaust gas valve at the PTR-TOF input
9) 4200 s, nitrogen purge flow off; end of experiment

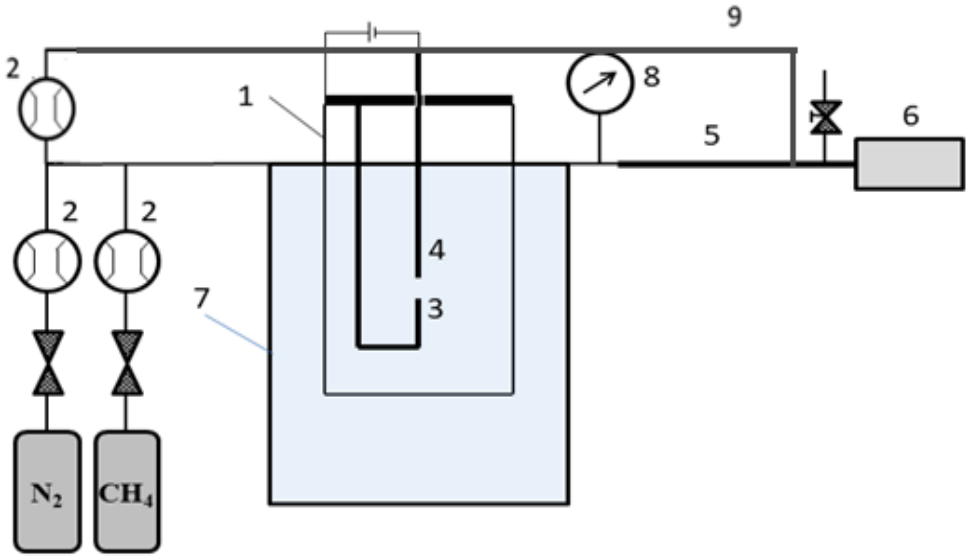

Fig. 43: Scheme of the first experimental set up: 1 – Pyrex glass reactor vessel; 2 – mass flow controller; 3 – cathode; 4 – anode (in stainless steel reactor, the electrodes were in horizontal position); 5 – heated exhaust gas sampling line; 6 – proton transfer reaction time of flight mass spectrometer; 7 - liquid nitrogen vessel; 8 – membrane manometer; 9 – heated diluting inlet.

3.4.2.1. Results in gas mixture N_2 + CH_4

The figures (Fig. 44 and Fig. 45) show the mass spectra at laboratory temperature compared to the spectrum obtained at the temperature of liquid nitrogen. From these spectra there can be seen very strong dependence on temperature, how the quantity and ratio of the products are developed and the formation of new substances at the higher molecular weight respectively.

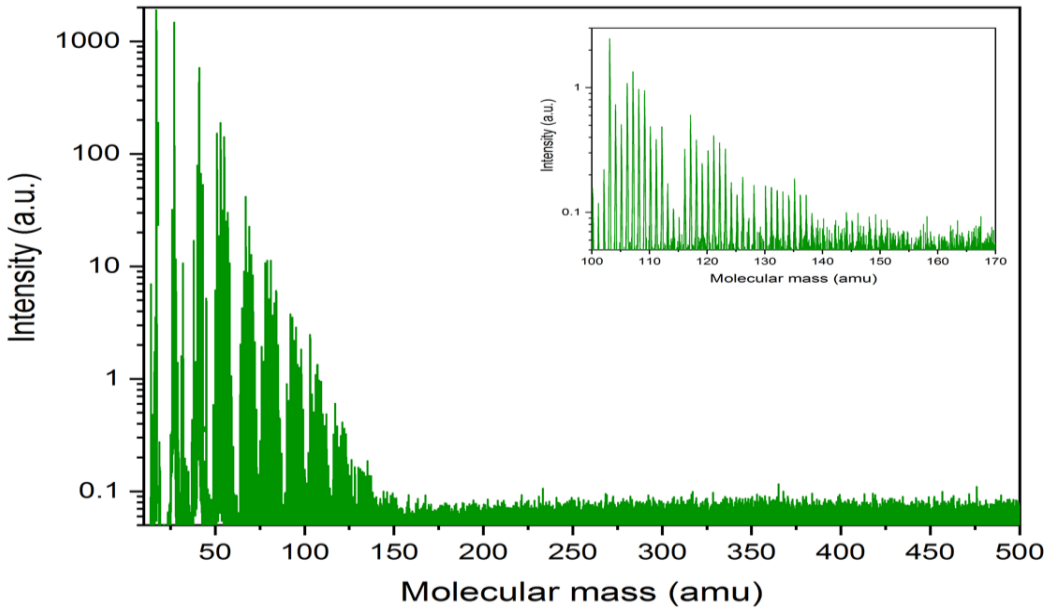

Fig. 44: Mass spectrum of gaseous products produced in a discharge at a concentration of 4 sccm of methane in 200 sccm of nitrogen at a power of 10 W at ambient wall temperature.

Fig. 45 shows an example of TOF mass spectrum resulting at temperature closer to Titan's surface temperature.

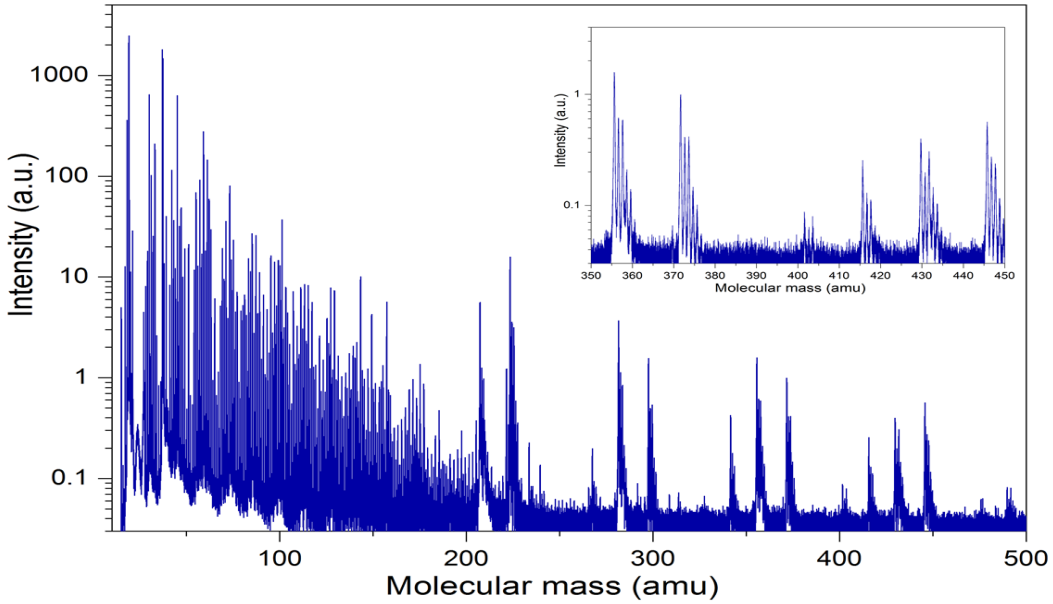

Fig. 45: Mass spectrum of gaseous products produced in a discharge at a concentration of 3 sccm of methane and 1 sccm of oxygen in 200 sccm of nitrogen at a power of 10 W at 77 K wall temperature.

It can be clearly seen that the discharge gaseous products are detected up too much higher molecular masses than at the ambient temperature. There are high intensities even over the 350 $g \cdot mol^{-1}$. At the Fig. 46 the predicted formation of heavier and heavier molecules in the discharge by adding the functional groups $-CH_2$ and $-NH_2$, respectively, is shown.

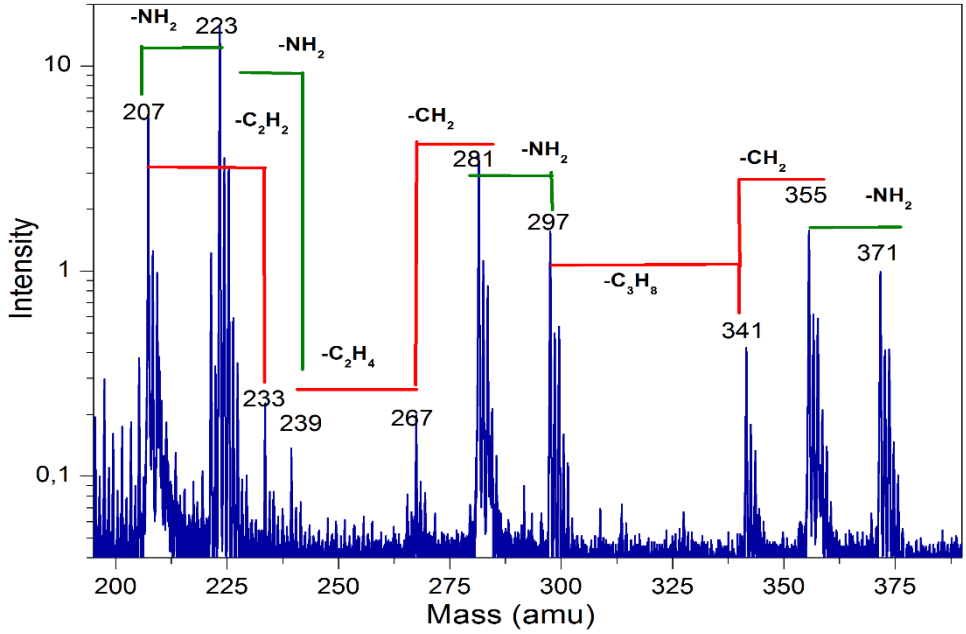

Fig. 46: Formation of heavier molecules in the discharge by adding the functional groups $-CH_2$ (red line) and $-NH_2$ (green line).

Fig. 47 and Fig. 48 show relative intensities of selected compounds in the dependence on the methane concentration. The dependence is very similar as at the ambient temperature which means they increase with increasing methane concentration. But HCN was not the most abundant compound as at the ambient temperature probably because at a low temperature it remained in the reactor in the liquid phase and even in the form of crystals. The highest intensity increase is again observed for the higher molecular weight substances but at the low temperature there are even higher molecules than benzene or toluene such as Nornicotine $C_9H_{12}N_2$ (148 amu) or decyl-pyrolle $C_{14}H_{25}N$ (207 amu). The assumption that lower molecular weight substances could be predominantly consumed for creation of higher molecular weight products at higher methane concentrations is also confirmed at lower temperature. Based on Fig. 32, the resulting spectra were taken as an average from range at 300 to 350 seconds, when the response was stable, and the system was not yet saturated.

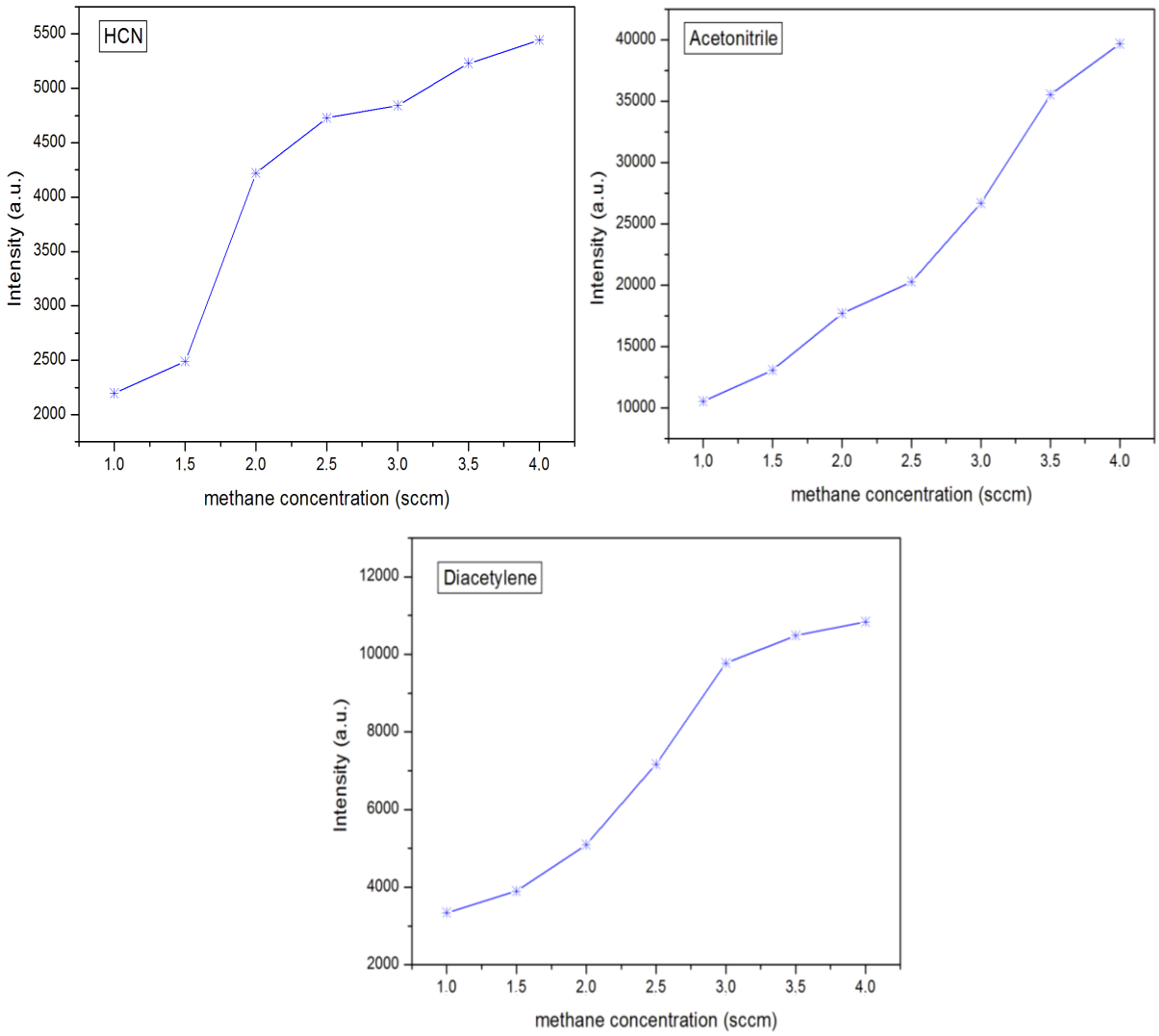

Fig. 47: Dependence of the relative intensity of HCN, acetonitrile and diacetylene on the methane concentration in 200 sccm of nitrogen.

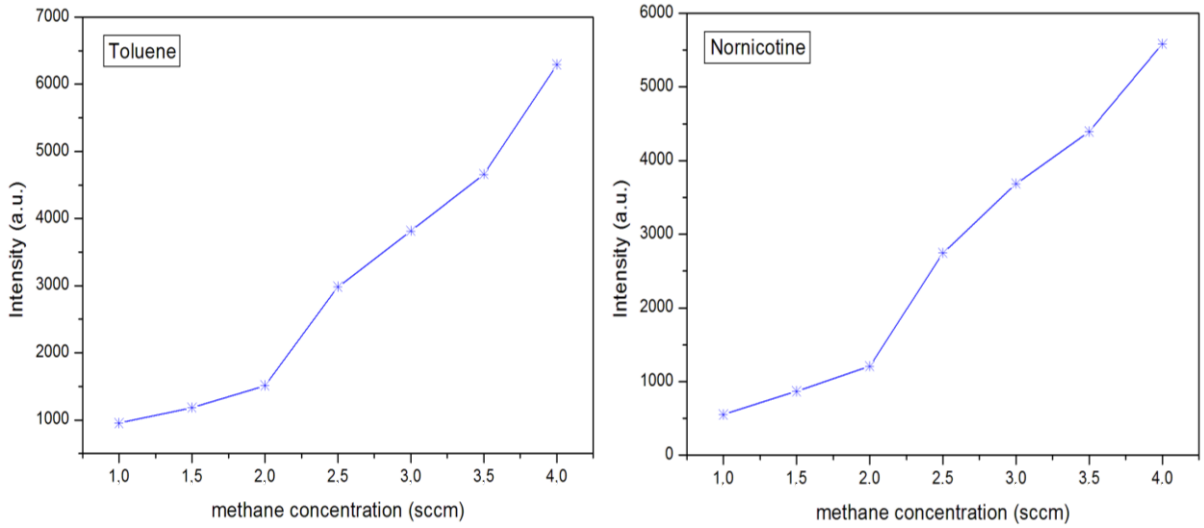

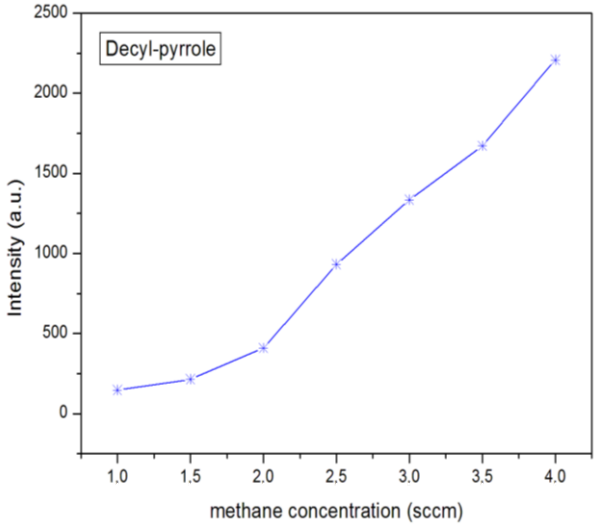

Fig. 48: Dependence of the relative intensity of toluene, nornicotine and decyl-pyrrole on the methane concentration in 200 sccm of nitrogen.

3.4.2.2. Results in composition $N_2 + CH_4 + O_2$ at the nitrogen liquid temperature

Fig. 49, Fig. 50 and Fig. 51 below show the spectrum at a flow 3 sccm of methane, 1 sccm of oxygen in 200 sccm of nitrogen divided into 3 parts for a better graphical representation of detected gaseous products in the discharge, in which the individual substances are better distinguished and marked.

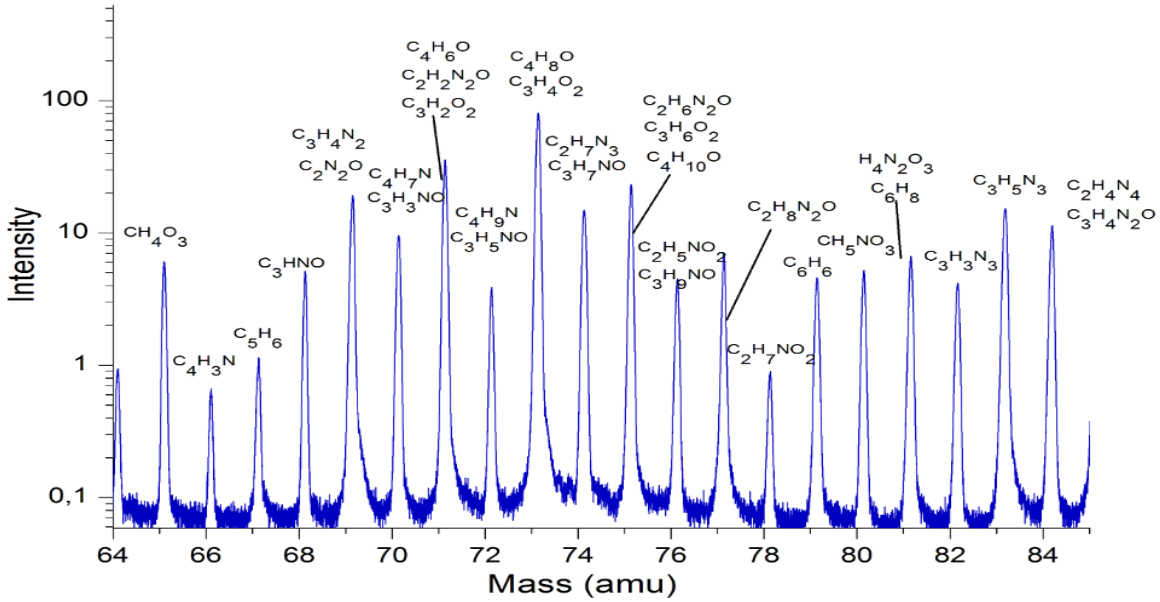

Fig. 49: Example of identified mass spectrum with molecular weight between 65-85 g/mol detected in the discharge at a concentration of 3 sccm of methane and 1 sccm of oxygen in 200 sccm of nitrogen and a current of 25 mA.

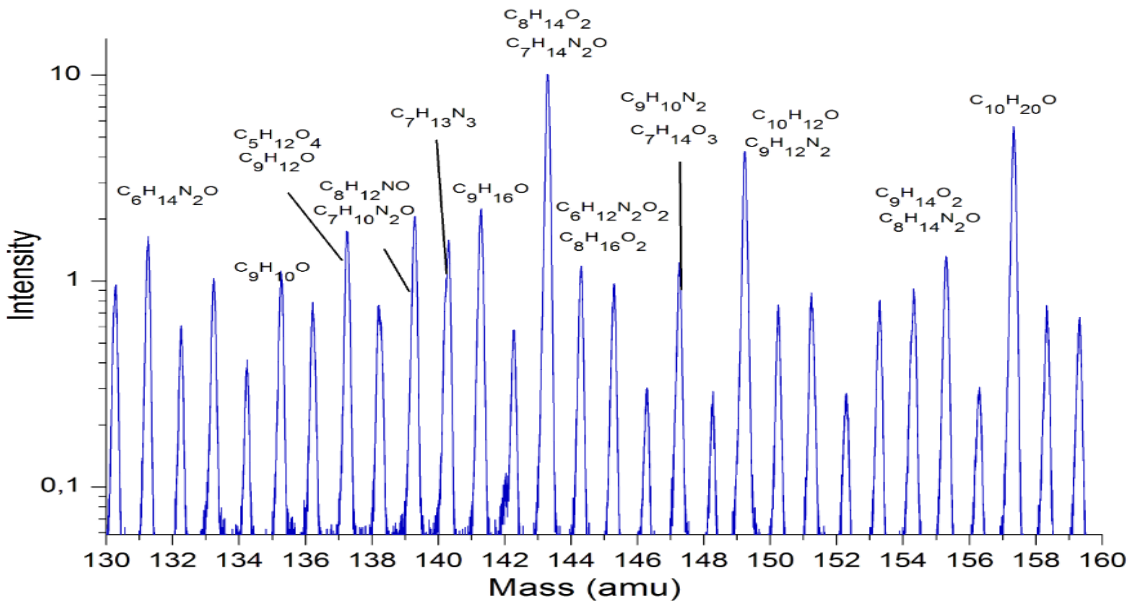

Fig. 50: Example of identified mass spectrum with molecular weight between 130-160 g/mol detected in the discharge at a concentration of 3 sccm of methane and 1 sccm of oxygen in 200 sccm of nitrogen and a current of 25 mA.

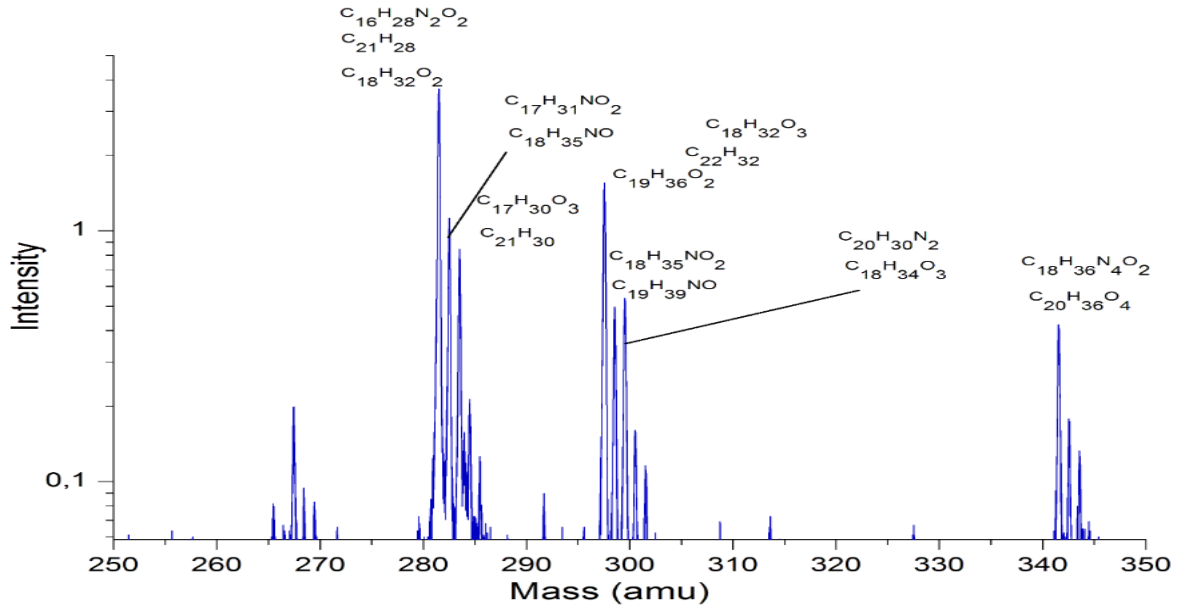

Fig. 51: Example of identified mass spectrum with molecular weight between 250-350 g/mol detected in the discharge at a concentration of 3 sccm of methane and 1 sccm of oxygen in 200 sccm of nitrogen and a current of 25 mA.

Fig. 47 and Fig. 48 show relative intensities of selected oxygen compounds in the dependence on the methane concentration in nitrogen with traces of oxygen. Intensity of all compounds are increasing with increasing methane concentration, so it means that dependence is basically very similar as for the non-oxygen compounds.

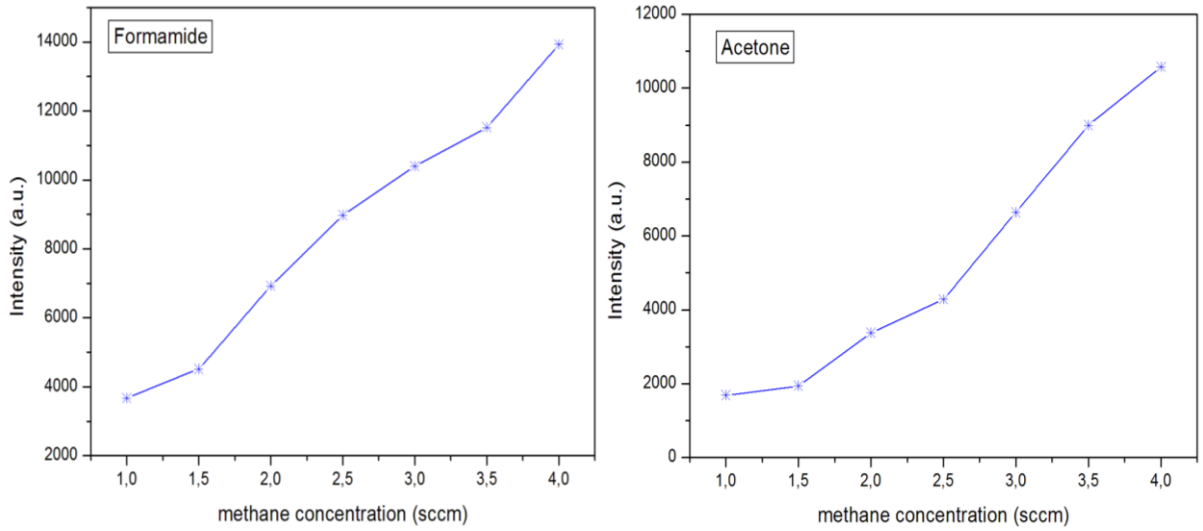

Fig. 52: Dependence of the relative intensity of formamide and acetone on the methane concentration with 1 sccm of oxygen in 200 sccm of nitrogen.

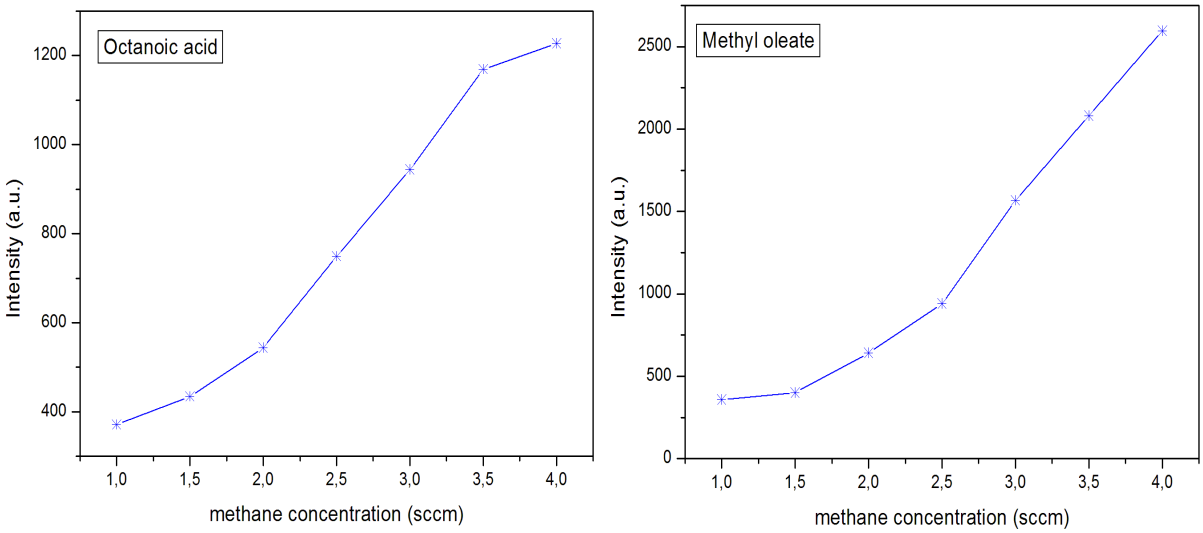

Fig. 53: Dependence of the relative intensity of octanoic acid and methyl oleate on the methane concentration with 1 sccm of oxygen in 200 sccm of nitrogen.

Under the conditions of this experiment, about the 200 possible compounds have been detected by PTR-TOF-MS in the spectrum. These compounds are listed in the Tab. 14. The major oxygen non-containing compounds were more or less similar as at the ambient temperature, so it means acetylene H_2C_2 (26 amu), N_2H_4 hydrazine (32 amu), acetonitrile CH_3CN (41 amu), formamide CH_3NO (45 amu), diacetylene C_4H_2 (51 amu), acetone C_3H_6O (58 amu), butanenitrile (69 amu), or benzene (78 amu) and of course hydrogen cyanide HCN (27 amu) but as mentioned below it is not the most abundant at low temperature. Only presence of oxygen had no significant impact on spectra at ambient temperature as it was measured during the diploma thesis [88]. It has to be also said that the spectrum at low temperature was very similar in presence of oxygen as well as without oxygen. There was only difference in intensities of compounds containing oxygen (this is also well demonstrated in chapter 3.4.3.1). The formation of oxygen compounds even in the N_2 + CH_4 mixture can be

explained most probably by the fact that there is a lot of absorbed oxygen on the walls of the silicon tubes that lead to and from the reactor. The instrument is sensitive in the orders of ppb and so it is extremely difficult to fully remove of the oxygen completely. But it is definitely an interesting task for further experiments.

Tab. 14: Detected hydrocarbons, nitrogen and oxygen compounds by PTR-TOF-MS.

Protonated mass	**Formula**	**Name of the compound**
18	NH_3	Ammonia
28	HCN	Hydrogen cyanide
29	C_2H_4	Ethylene
30	CH_3N	Methanimine
31	H_2CO	Formaldehyde
31	N_2H_2	Diazene
32	CH_5N	Methanamine
33	N_2H_4	Hydrazine
41	C_3H_4	Propyne
42	C_2H_3N	Acetonitrile
43	H_2C_2O	Ethenone
43	H_2CN_2	Cyanamid
43	C_3H_6	Propene
44	HNCO	Isocyanic acid
44	C_2H_5N	Aziridine
45	C_3H_8	Propane
45	C_2H_4O	Acetaldehyde
46	CH_3NO	Formamide
46	C_2H_7N	Dimethylamine
47	C_2H_6O	Ethanol
48	HNO_2	Nitrous acid
49	CH_4O_2	Methanediol
51	C_4H_2	Diacetylene
52	C_3HN	Cyanoacetylene
53	C_4H_4	Cyclobutadiene
54	C_3H_3N	Acrylonitrile
55	C_4H_6	Butadiene
55	C_3H_2O	Propynal
56	C_3H_5N	Propionitrile
57	C_4H_8	Cyclobutane
57	C_3H_4O	Cyclopropanone
58	C_3H_7N	Allylamine
59	C_3H_6O	Acetone

Protonated mass	Formula	Name of the compound
60	C_3H_9N	Propylamine
60	C_2H_5NO	Acetamide
61	$C_2H_4O_2$	Acetic acid
61	CH_4N_2O	Urea
62	CH_3NO_2	Nitromethane
62	C_2H_7NO	Ethanolamine
63	H_2CO_3	Carbonic acid
64	CH_5NO_2	Ammonium formate
65	CH_4O_3	Orthoformic acid
66	C_4H_3N	Cyanopropyne
67	C_5H_6	Cyclopentadiene
68	C_3HNO	Cyanoketene
69	C_2N_2O	Cyano cyanate
69	$C_3H_4N_2$	Imidazole
70	C_3H_3NO	Oxazole
70	C_4H_7N	Butyronitrile
71	$C_3H_2O_2$	Propiolic acid
71	$C_2H_2N_2O$	Furazan
71	C_4H_6O	Crotonaldehyde
72	C_3H_5NO	Acrylamide
72	C_4H_9N	Pyrrolidine
73	C_4H_8O	Butyraldehyde
73	$C_3H_4O_2$	Acrylic acid
74	$C_2H_7N_3$	Methylguanidine
74	C_3H_7NO	Dimethylformamide
75	$C_4H_{10}O$	Diethyl ether
75	$C_3H_6O_2$	Methyl acetate
75	$C_2H_6N_2O$	Glycinamide
76	C_3H_9NO	1-Amino-2-propanol
76	$C_2H_5NO_2$	Glycine
77	$C_2H_8N_2O$	Diaminoethanole
78	$C_2H_7NO_2$	Ammonium acetate
79	C_6H_6	Benzene
80	CH_5NO_3	Ammonium bicarbonate
81	C_6H_8	Cyclohexadiene
81	$H_4N_2O_3$	Ammonium nitrate
82	$C_3H_3N_3$	1,3,5-triazine
84	$C_3H_5N_3$	Methyltriazole

Protonated mass	Formula	Name of the compound
85	$C_2H_4N_4$	Cyanoguanidine
85	$C_3H_4N_2O$	Cyanoacetamide
86	C_4H_7NO	Methacrylamide
87	$C_3H_6N_2O$	Imidazolidinone
87	$C_5H_{10}O$	Pentanone
88	C_4H_9NO	Butyramide
89	$C_3H_8N_2O$	Dimethylurea
89	$C_2H_4N_2O_2$	Oxamide
90	$C_2H_7N_3O$	Methylaminourea
91	$C_3H_6O_3$	Glyceraldehyde
91	$C_2H_6N_2O_2$	Dimethylnitramine
91	$C_4H_{10}O_2$	Butanediol
93	$C_3H_8O_3$	Glycerin
93	C_7H_8	Toluene
94	C_6H_7N	Aniline
94	C_5H_3NO	Furonitrile
95	C_6H_6O	Phenol
96	C_5H_5NO	Pyridone
97	$C_4H_4N_2O$	Pyrimidinol
97	$CH_8N_2O_3$	Ammonium carbonate
98	$C_3H_3N_3O$	4-nitro-Pyrazole
98	C_5H_7NO	Furfurylamine
99	$C_5H_6O_2$	Furanmethanol
99	$C_4H_6N_2O$	Dimethyl furazan
100	$C_4H_5NO_2$	Succinimide
100	$C_3H_5N_3O$	Cyacetacide
101	$C_3H_4N_2O_2$	Hydantoin
101	$C_5H_8O_2$	Ethyl acrylate
102	$C_4H_7NO_2$	Diacetamide
103	C_8H_6	Phenylacetylene
103	$C_3H_6N_2O_2$	Malonamide
104	$C_2H_5N_3O_2$	Biuret
104	$C_4H_9NO_2$	Nitrobuthane (alpha-Aminobutyric acid)
105	$C_3H_8N_2O_2$	Hydroxyethyl-urea
105	$CH_4N_4O_2$	Nitroguanidine
107	$C_4H_{10}O_3$	Diethylene glycol
107	C_7H_6O	Benzaldehyde
108	C_6H_5NO	Nitrosobenzene

Protonated mass	Formula	Name of the compound
109	C_7H_8O	Anisole
110	C_6H_7NO	4-aminophenol
111	$C_7H_{10}O$	Methylcyclohexenone
112	C_6H_9NO	Vinylpyrrolidone
113	$C_7H_{12}O$	Cycloheptanone
113	$C_5H_8N_2O$	5-Amino-3,4-dimethyl-isoxazole
114	$C_6H_{11}NO$	Caprolactam
115	$C_5H_{10}N_2O$	Prolinamide
116	$C_5H_9NO_2$	Proline
117	$C_5H_{12}N_2O$	Tetramethylurea
117	$C_6H_{12}O_2$	Ethyl butyrate
118	$C_5H_{11}NO_2$	Valine
118	C_8H_7N	Indole
119	$C_4H_{10}N_2O_2$	2,4-Diaminobutanoic acid
121	$C_5H_{12}O_3$	Trimethylolethane
121	$C_7H_8N_2$	Benzamidine
123	$C_8H_{10}O$	2-phenylethanol
125	$C_7H_{12}N_2$	Butylimidazole
125	$C_8H_{12}O$	4-acetylcyclohexene
126	$C_6H_{11}N_3$	1-methylhistamine
127	$C_7H_{14}N_2$	Diisopropylcyanamide
127	$C_6H_{10}N_2O$	4-morpholineacetonitrile
128	$C_5H_9N_3O$	1-Azido-3-methylbutan-2-one
129	$C_6H_{12}N_2O$	L-Lysine, hydrate (1:1)
131	$C_6H_{14}N_2O$	Leucinamide
135	$C_9H_{10}O$	Propiophenone
137	$C_9H_{12}O$	Phenylpropanol
137	$C_5H_{12}O_4$	Pentaerythritol
139	$C_8H_{12}NO$	1-(2-Methoxyethyl)pyridinium
139	$C_7H_{10}N_2O$	3,4-diaminoanisole
140	$C_7H_{13}N_3$	Triazabicyclodecene
141	$C_9H_{16}O$	Cyclohexylacetone
143	$C_7H_{14}N_2O$	Cyclohexylurea
143	$C_8H_{14}O_2$	Cyclohexyl acetate
145	$C_8H_{16}O_2$	Octanoic acid
145	$C_6H_{12}N_2O_2$	Adipamide
147	$C_7H_{14}O_3$	2-Hydroxyheptanoic acid
147	$C_9H_{10}N_2$	Myosmine

Protonated mass	Formula	Name of the compound
149	$C_9H_{12}N_2$	Nornicotine
155	$C_8H_{14}N_2O$	Loline
155	$C_9H_{14}O_2$	Cyclohexyl acrylate
157	$C_{10}H_{20}O$	Menthol
169	$C_{10}H_{20}N_2$	Cyclohexylpiperazine
169	$C_{11}H_{20}O$	10-undecenal
171	$C_{11}H_{22}O$	Undecanone
171	$C_9H_{18}N_2O$	4-morpholinopiperidine
175	$C_9H_{18}O_3$	Carbonic acid, dibutyl ester
175	$C_{11}H_{14}N_2$	Indopan
177	$C_9H_{20}O_3$	Ethyl orthopropionate
177	$C_{11}H_{16}N_2$	Benzylpiperazine
185	$C_{10}H_{20}N_2O$	Cyclopentylvalinamide
207	$C_{13}H_{22}N_2$	Dicyclohexylcarbodiimide
207	$C_{14}H_{22}O$	Octylphenol
207	$C_{12}H_{18}N_2O$	Isoproturon
208	$C_{14}H_{25}N$	Decyl-pyrrole
221	$C_{12}H_{20}N_4$	2,5-Dimethyl-1,4-dipropionitrile piperazine
221	$C_{11}H_{24}O_4$	Propane, 1,1,3,3-tetraethoxy
223	$C_{13}H_{22}N_2O$	N-methylammodendrine
223	$C_{14}H_{22}O_2$	1,2-Benzenediol, 3,5-bis(1,1-dimethylethyl)-
223	$C_{10}H_{22}O_5$	Tetraglyme
224	$C_{13}H_{21}NO_2$	Tropigline
224	$C_{10}H_{17}N_5O$	Prometon
225	$C_{13}H_{20}O_3$	Vomifoliol
225	$C_{15}H_{16}N_2$	N,N'-Di-p-tolyl-formamideine
281	$C_{18}H_{32}O_2$	Geranyl caprylate
281	$C_{21}H_{28}$	1,1'-Biphenyl, 3,4',5-triisopropyl
281	$C_{16}H_{28}N_2O_2$	Phygrine
282	$C_{18}H_{35}NO$	Oleamide
282	$C_{17}H_{31}NO_2$	Tetradecyl ester cyanoacetic acid
283	$C_{21}H_{30}$	Undecylnaphthalene
283	$C_{17}H_{30}O_3$	12-Hydroxy-heptadec-16-ynoic acid
297	$C_{19}H_{36}O_2$	Methyl oleate
297	$C_{22}H_{32}$	Dodecylnaphthalene
297	$C_{18}H_{32}O_3$	Dimorphecolic acid
298	$C_{19}H_{39}NO$	Nonadecanamide
298	$C_{18}H_{35}NO_2$	Spiroxamine

Protonated mass	Formula	Name of the compound
299	$C_{18}H_{34}O_3$	Ricinoleic acid
299	$C_{20}H_{30}N_2$	E-Diazene, bis(1-adamantyl)-
341	$C_{20}H_{36}O_4$	Di(2-ethylhexyl) fumarate
355	$C_{21}H_{42}N_2O_2$	Diamide, N,N'-di(2-octyl)- Glutaric acid
355	$C_{22}H_{42}O_3$	10-Oxo-docosanoic acid
355	$C_{21}H_{38}O_4$	Glyceryl linoleate
371	$C_{22}H_{42}O_4$	Diisooctyl adipate
415	$C_{24}H_{38}N_4O_2$	2,2',6,6'-(Dimethylaminomethyl)-4,4'-diphenol
429	$C_{31}H_{56}$	13-phenyl-Pentacosane
429	$C_{30}H_{52}O$	Lanostan-3-one
446	$C_{23}H_{15}N_3O_7$	Benzfluorene picric acid
446	$C_{29}H_{48}O_3$	Cholesteryl methyl carbonate

Analysis of the system by optical emission spectroscopy was basically not possible because of fog creation inside of reactor (Fig. 54). This didn´t happen before at laboratory temperature. This is one of the reasons why the experiment was moved into the "glass reactor" to find the root cause. There can be seen flashes that changed the colour of the discharge occurred during the experiment. The flash occurs by something dripping down into a liquid methane at reactor bottom. Because droplet is warmer, the methane evaporates, so the pressure increases, but mainly methane is in the gas phase and therefore the color of the discharge is changing. But just for a while before he condenses again. So, it turns out to be a flash, but the discharge is still only between the electrodes. It is probably that there at a low temperature condenses something else that previously was not presented.

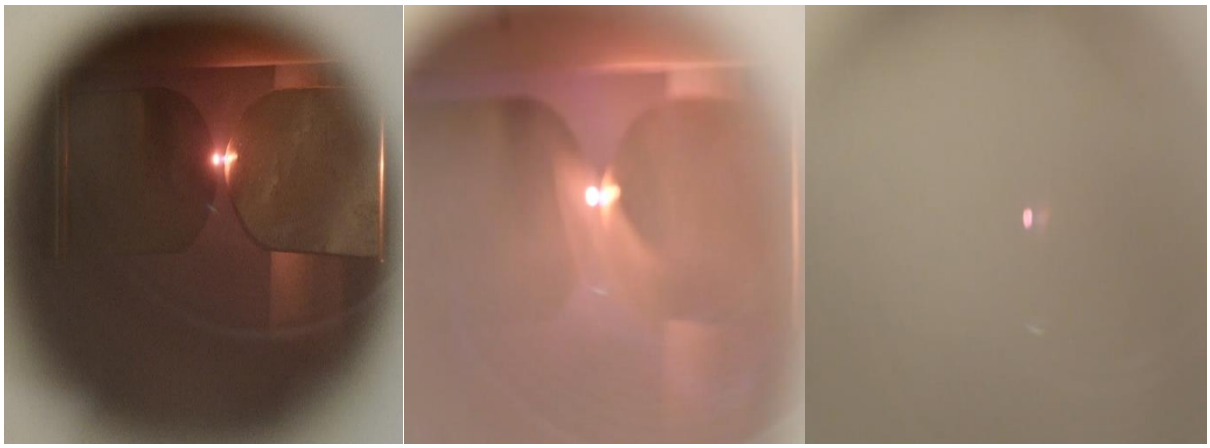

Fig. 54: Fog development during the experiment at the liquid nitrogen temperature

First ideas were about formamide which was detected also by PTR-TOF- MS (Fig. 55). It was then confirmed also by FTIR (Fig. 78 and Fig. 79).

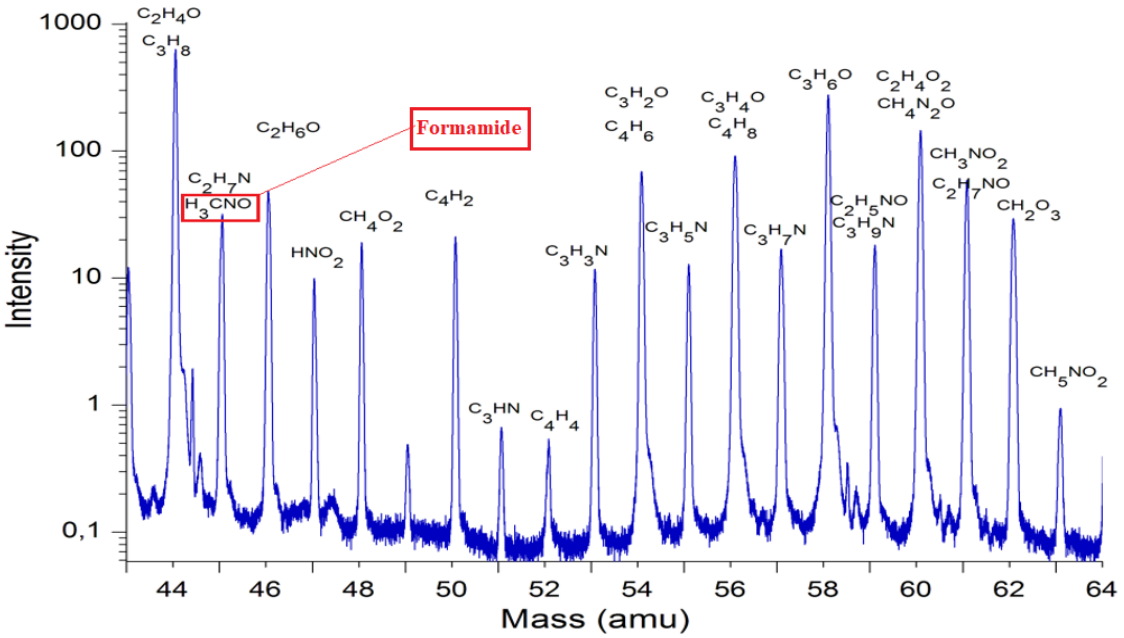

Fig. 55: Mass spectrum analysis of gaseous products resulting from the discharge at a flow of 3 sccm of methane and 1 sccm of CO_2 in 200 sccm of nitrogen at 30 mA at temperature of liquid nitrogen.

Its formation is very well supported by oxygen presence because this molecule contains oxygen in its structure. In the next chapter, 3.4.3.1 (p. 68) there will be found very important note that formamide is formed by discharge also in the case when no additional oxygen is added into the reaction mixture, so even small traces from nitrogen and methane pressure cylinder together with some oxygen adsorbed on wall are sufficient for its remarkable production. This is very important, as formamide is known as a nuclear acids bases compounds precursor. Miller´s chemistry of early Earths assumes formamide and its chemical connection with HCN and ammonium formate ($NH_4^+HCOO^-$) where formamide could accumulate in sufficiently high amounts to serve as the building block and reaction medium for the synthesis of the first biogenic molecules [44].

At the Fig. 55 there can be seen that the peak of formamide is shared also with Ethylamine or N,N-dimethylamine respectively.

Below at Fig. 56 there is a peak which is supposed to belong to formamide closely analysed in time. It can be seen that compound with protonated molecular weight 46 is stable produced during the whole experiment in every cycle.

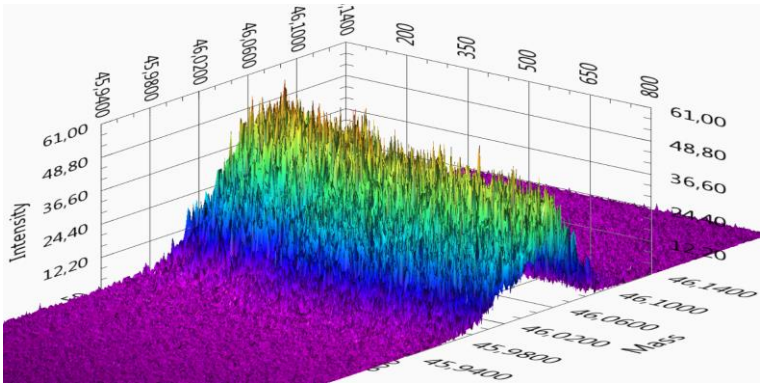

Fig. 56: formamide in 3D graph to see the peak development in time. Picture was generated by the PTR-MS softwer of Ionicon.

3.4.3. Measurements with PTR-ToF-MS at different applied power and different mixture composition at liquid nitrogen temperature

This experiment was also carried out in the simple glass reactor (see Fig. 57) equipped by a pair of tungsten rod electrodes (diameter of 1 mm) in distance of 0.7 mm. The glow discharge was operating at the currents of 10, 20, and 30 mA (corresponding powers of 4.0, 8.0, and 12 W). Reactor was placed into a Dewar vessel fill able by liquid nitrogen above the electrode system. Four mixtures are used for the current experiments: pure nitrogen with flow of 200 sccm, nitrogen with addition of 5 sccm of methane and the same mixture enriched by oxygen or CO_2 with flows of 1 sccm. Pressure in the reactor during the experiment was kept at 1.5 atmosphere and it was measured on-line.

Experiment is completed following the scheme:

1. -300 s start of reaction mixture flow
2. 0 s start of measurement
3. 60 s discharge turn on
4. 300 s starting reaction vessel cooling
5. 1200 s discharge off
6. 1500 s end of vessel cooling
7. 2100 s start of reactor heating by hair drier
8. 2400 s end of reactor heating by hair drier
9. 2700 s nitrogen (99.999%) high flow of 5 slm purge flow on
10. 3000 s end of experiment

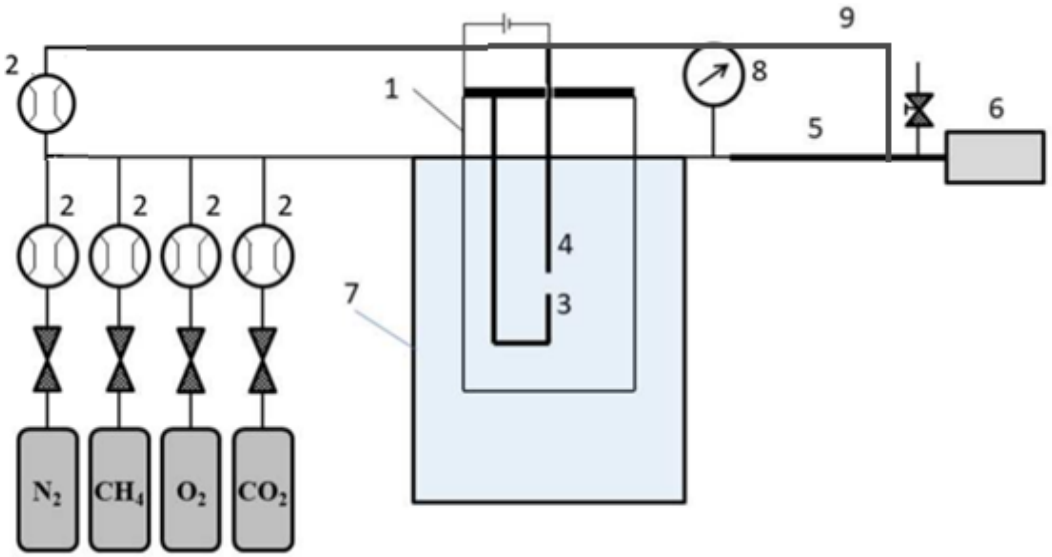

Fig. 57: Scheme of the first experimental set up: 1 – Pyrex glass reactor vessel; 2 – mass flow controller; 3 – cathode; 4 – anode; 5 – heated exhaust gas sampling line; 6 – proton transfer reaction time of flight mass spectrometer; 7 – liquid nitrogen vessel; 8 – membrane manometer; 9 – nitrogen diluting inlet.

3.4.3.1. Results from measurements at different mixture

The time profiles of concentrations for the selected compounds are given in Fig. 58 - Fig. 61. The hydrogen cyanide HCN (Fig. 58) and acetonitrile C_2H_3N (Fig. 59) are the main compounds formed by the discharge in nitrogen-methane mixtures. Both these compounds reached during the discharge operation and later evaporation of condensed discharge products the saturation limit of the device and thus there are rather complicated to relate them to appropriate kinetic processes. The ammoniac (NH_4^+) was difficult to detect because its mass is nearly the same as of H_2O^+ (formed in PTR-TOF ionization discharge source) and the device resolution is about 1000, only. Their concentration time dependence clearly follows the experimental scheme. The initial increases of their concentrations after the discharge turn on in generally independent on the reaction gas mixture. In couple of ten seconds after starting the reactor vessel cooling, the concentrations drop down due to compounds trapping on the frozen reactor wall and only a small part of formed species can continue to the PTR-TOF. When discharge is stopped, concentrations rapidly decrease. This decrease is the same in case of hydrogen cyanide at all conditions but differs in case of acetonitrile. This can be explained that this specie is further oxidized when oxygen containing gas is presented in the reaction mixture.

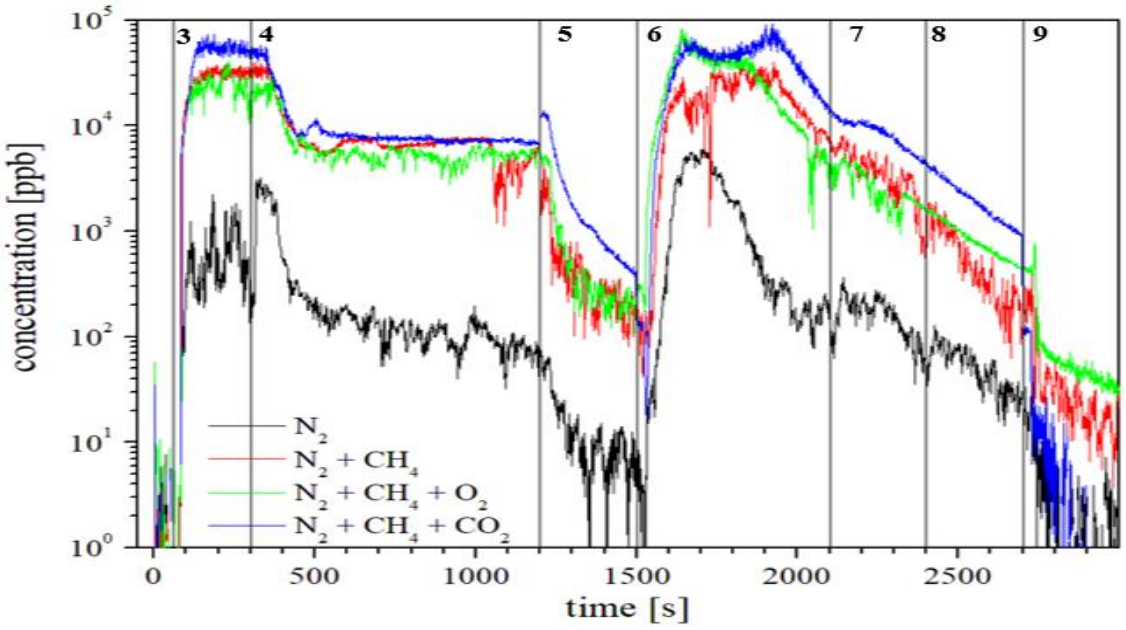

Fig. 58: Concentration of hydrogen cyanide during the experiment at 8.0 W. The vertical lines indicate experimental setting points given in experiment description above. Note that saturation limit for the used detection technique is about 60 000 ppb for this compound.

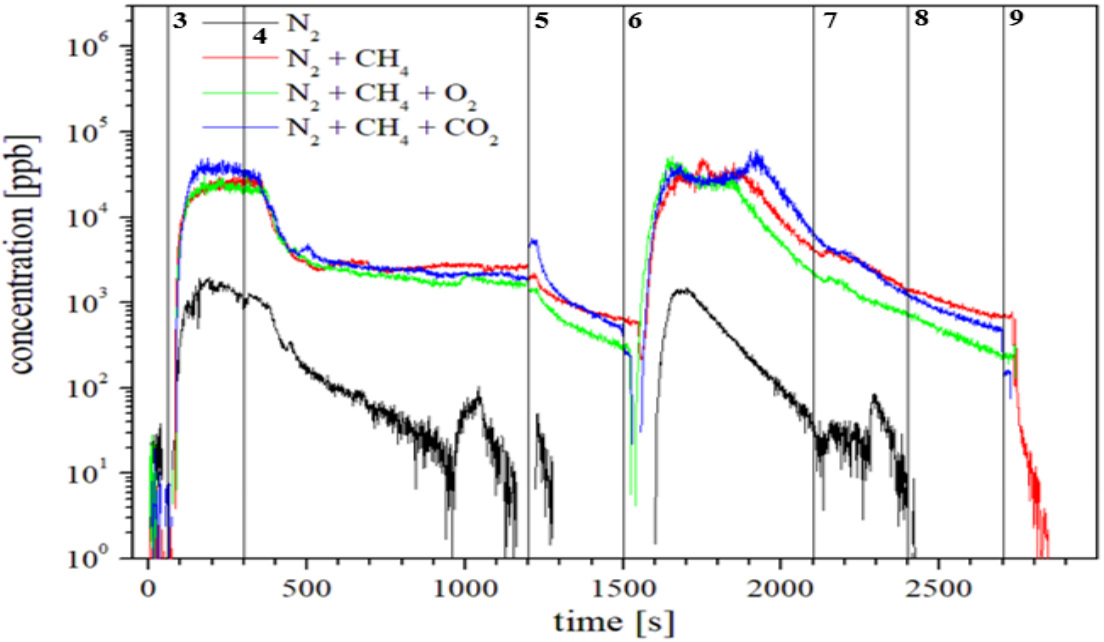

Fig. 59: Concentration of acetonitrile during the experiment 8.0 W. The vertical lines indicate experimental setting points given in experiment description above. Note that saturation limit for the used detection technique is about 60 000 ppb for this compound.

The increase of all concentrations in the case of oxygen containing mixture could not reflect discharge/cooling effect because it is observed just at the moment of discharge turn off and there is no delay necessary for the species transfer from reactor to PTR-TOF (it is about 12 s at these experimental conditions). The later concentrations increase (after 1500 s) reflects

reactor vessel spontaneous heating followed by the evaporation of condensed species. Also, at this experimental period the further oxidation of acetonitrile is possible.

Besides the main formed compounds many tens of other species were identified as mentioned above. The benzene C_6H_6 and formamide CH_3NO were selected to present here, only. The first one represents the cyclic hydrocarbons that are important for the synthesis of more complicated organic compounds; formamide is known as the precursor of nuclear acids basis components that can be formed thermally.

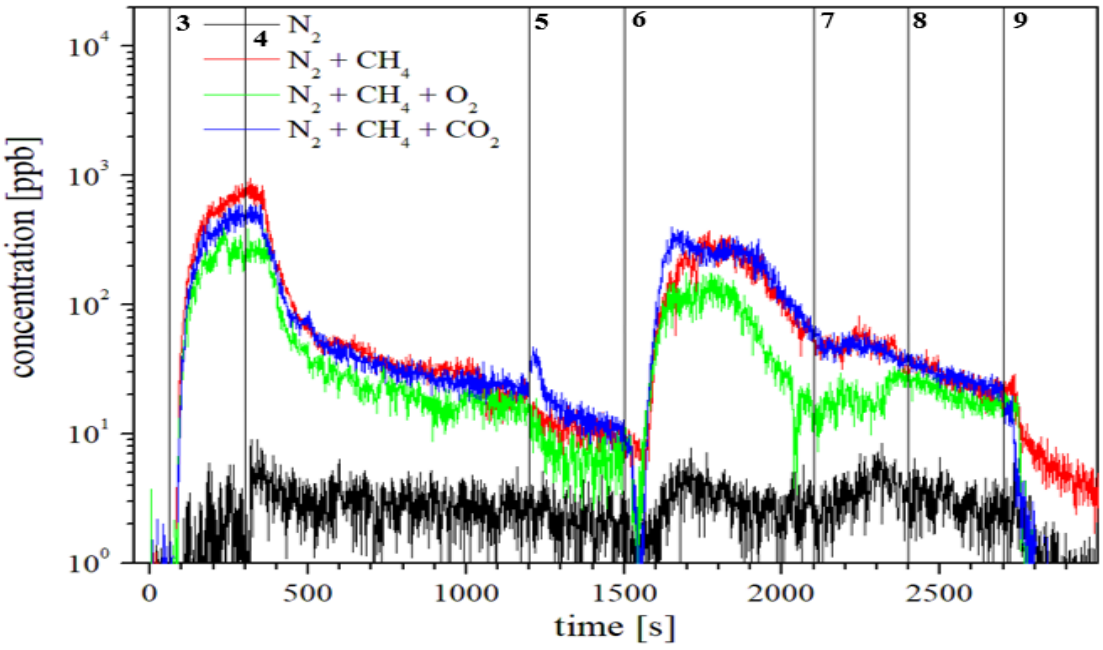

Fig. 60: Concentration of benzene during the experiment 8.0 W. The vertical lines indicate experimental setting points given in experiment description above.

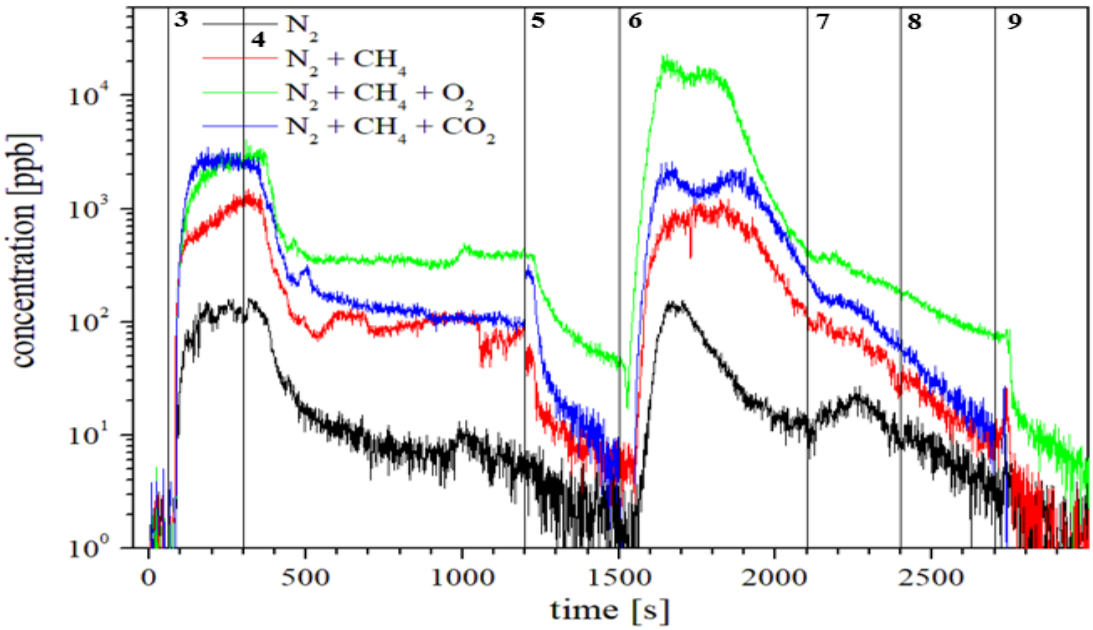

Fig. 61: Concentration of formamide during the experiment 8.0 W. The vertical lines indicate experimental setting points given in experiment description above.

The benzene formation is significantly quenched by the presence of oxygen atoms in the reaction mixture. On the other hand, formamide formation is supported by oxygen presence because this molecule contains oxygen in its structure. It is important to note that formamide is formed by discharge also in the case when no additional oxygen is added into the reaction mixture, so even small traces from nitrogen and methane pressure cylinder together with some oxygen adsorbed on wall are sufficient for its remarkable production.

3.4.3.2. Results from measurements at different applied power

Dependencies on applied power for the selected compounds are given in Fig. **62** - Fig. **65**. The time profile of the HCN (Fig. 62) shows a strong dependence on the applied power. At the lowest one, the simple production in the discharge is visible followed by concentration decrease during the cooling (due to trapping on the cold reactor walls) followed by the strong concentration increase during the reactor heating. The profile obtained at the medium power of 8 W shows more complicated behaviour. The significant concentration decrease is observed during the discharge operation at the ambient temperature. The additional concentration drop is visible just at the beginning of the discharge cooling and later the concentration reaches nearly the same value as at the lowest power up to the discharge off. The concentration profile after the reactor heating is nearly the same as at the lowest applied power. The most complicated curve was obtained at the highest power. The behaviour up to end of cooling is similar as at the medium power but the first concentration drop starts sooner and it is deeper when before. Also, the concentration during the cooling period is about 30% lower than at the medium power. The dependence after the start of reactor self-heating shows three huge peaks of the HCN concentration (2500, 2700 and 2950 s). There is no reason for this besides the secondary formation of HCN molecules from some bigger clusters deposited (trapped) on the reactor walls.

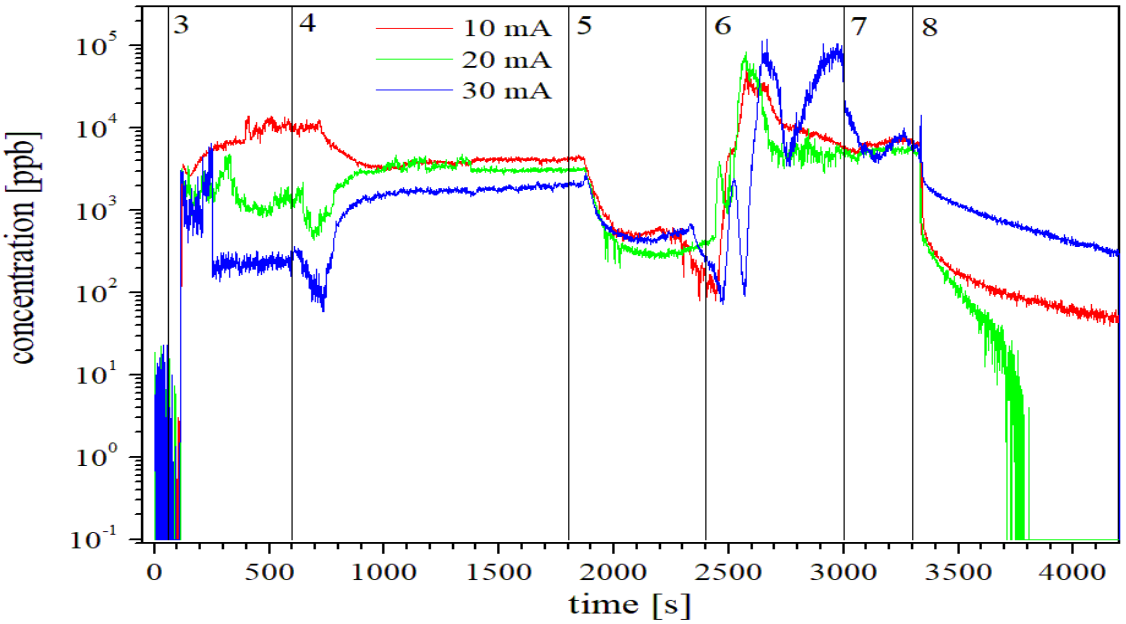

Fig. 62: Concentration of hydrogen cyanide during the experiment. The vertical lines indicate experimental setting points given in experiment description above. Note that saturation limit for the used detection technique is about 60 000 ppb for this compound.

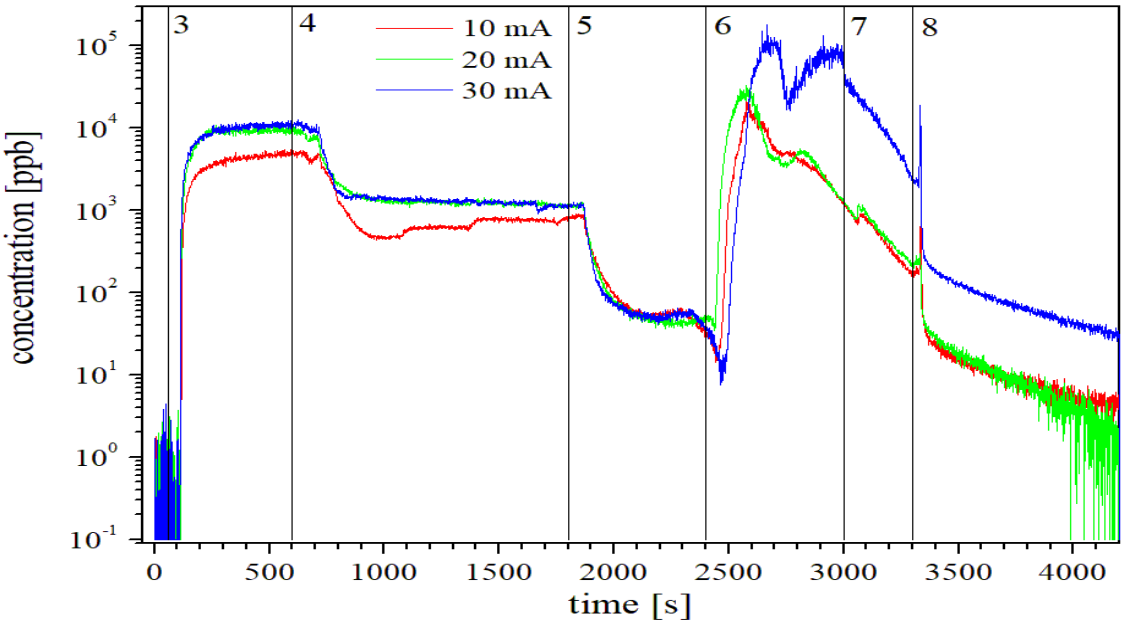

Fig. 63: Concentration of acetonitrile during the experiment. The vertical lines indicate experimental setting points given in experiment description above. Note that saturation limit for the used detection technique is about 60 000 ppb for this compound.

The production of acetonitrile (Fig. 63) in the discharge is increasing with the applied power but it has probably some saturation limit. No unexpected points like in case of HCN were recorded. The concentration time profile during the heating part of experiment shows nearly the same dependences for both the applied powers with faster concentration increase in case of the medium power. The two concentration peaks are visible for the highest applied power, similar like in the case of HCN (the concentration drop is at the same time for the both compounds).

Besides the main formed compounds many tens of other species were successfully identified (as it is shown in the Tab. 14). The benzene and formamide were selected to present here, only. The first one represents the cyclic hydrocarbons that are important for the synthesis of more complicated organic compounds; formamide is known as the precursor's of nuclear acids basis components that can be formed thermally.

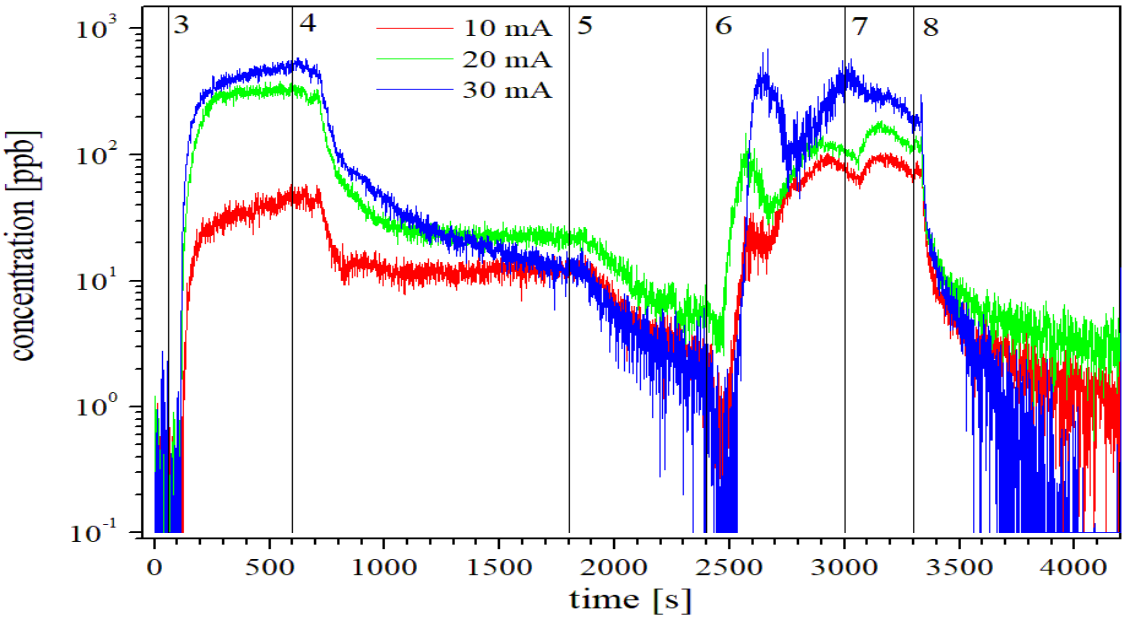

Fig. 64: Concentration of benzene during the experiment. The vertical lines indicate experimental setting points given in experiment description above.

Formation of benzene (Fig. 64) in the discharge at ambient temperature shows strong power dependence. The significant decrease of benzene concentration is visible at the highest applied power during the discharge operating at the liquid nitrogen temperature. We can suppose two effects. The first one is better benzene trapping due to the presence of some other molecules trapped on the glass reactor wall (i.e. surface conditions changes). The second one is formation of some other (probably bigger molecules) at these conditions. This second possibility is more probable because the concentration time dependence during the reactor heating is different from other in the case of highest applied power. The secondary reactions as described in case of HCN are also probable in case of benzene (see curve between point 6 and 7). The final enhancement of benzene concentration after the heating switch on is due to its evaporation from walls.

Concentration time profiles for formamide are shown in Fig. 65. The curves up to the cooling down are similar for all applied powers. Concentrations during the cooled period are similar besides the lowest applied power. The high formamide concentrations are detected during the heating period at the highest applied power. This behaviour is very similar as in the case of acetonitrile (Fig. 63) but without formation of two concentration peaks. This means that reactions of their formation must be different.

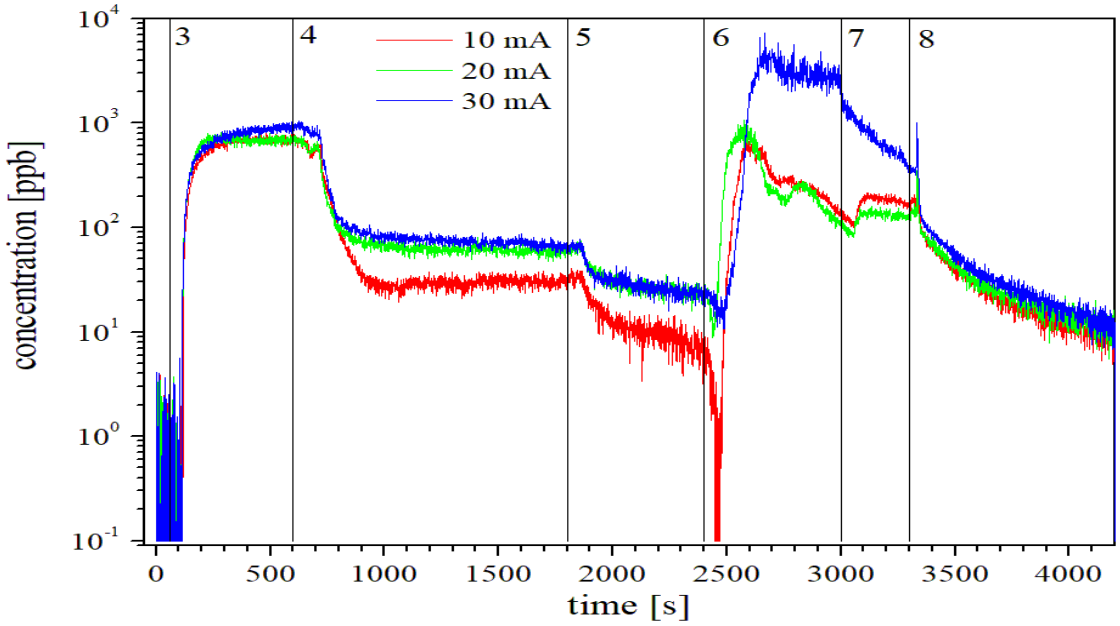

Fig. 65: Concentration of formamide during the experiment. The vertical lines indicate experimental setting points given in experiment description above.

The further experiments including analysis of all peaks (even not identified, yet) in the PTR-TOF spectra will be necessary to carry out to be able to understand whole very complex kinetics. Based on the obtained experimental data also the complex kinetic model will be needed to detailed understanding of the possible life precursor's synthesis in the Titan atmosphere.

3.5. Ion mobility spectrometry

3.5.1 Principles of ion mobility spectrometry

Ion mobility spectrometry (IMS) belongs to the category of the separation methods. The ions are separated on the basis of their movement in the gas phase in the drift gas in the mobility cell to which the electric field is applied. The speed of movement depends on the charge, the weight and the particle cross-section represented by ion mobility in given buffer gas [117]. This means that the larger the cross-sectional area of the ion, the greater the number of collisions with the drift gas, the greater the time it takes for the ion to travel the distance to the detector. Thus, ions with a larger cross-section arrive at the detector later than those with a smaller cross-sectional area. Differences in ion mobility are the crucial condition for their separation. Ions of the same mass but with different molecular shapes can also be separated by IMS. Thanks to this fact, IMS can also be used for isomer separations, which cannot be achieved with some other separation techniques [118], [119].

The sample enters the chamber where it is exposed to ionizing radiation and the individual molecules are transformed into ions. ^{63}Ni, which produces β particles, is commonly used as an ionization source. Latest designs sometimes use ^{241}Am, which produces α particles and γ radiation. The ions are accelerated by an electric field and enter the flight tube. The

flight time up to the impact on the detector is specific for individual molecules. The quantitative indicator is then the signal intensity of the detector [118], [120].

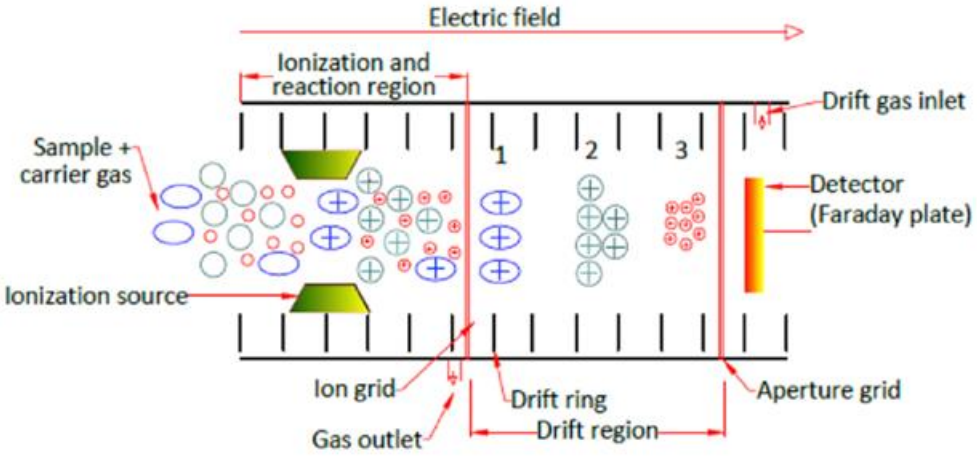

Fig. 66: Scheme of Drift-Tube Ion Mobility Spectrometry. Drift tube IMS uses a long, gas-filled tube with a constant (and relatively low) electric field. Ions are injected at one end, and the time taken to travel the length of the tube is recorded. From this, the velocity of travel can be directly calculated, and if the field strength is known, the ions' mobilities can also be determined. If the travel time is known, ions must be injected into the system in short pulses, and then all the ions must be allowed to travel through the detector before another pulse is injected [121].

In contrast with conventional ToF analyzers, which work in a vacuum, IMS works at atmospheric pressure, which is a great advantage over MS because the demands on the size and price of the device are reduced. An important element is the countercurrent flow of air which resists the movement of ions and reduces their speed. Another function is the removal of non-ionized molecules and ions of opposite polarity. Ions with the same charge are accelerated in the electric field by the same force. The differences in ToF are due to the differently large forces acting against the movement of ions [118], [122]. Thus, the ions are separated on the basis of different viscous forces acting in countercurrent gas and not on the basis of molecular weight as it is in MS. The analyte molecules are usually not ionized directly by electrons from the ionization source but the so-called soft ionization technique or chemical ionization is used [118], [124].

The core of modern IMS equipment is a cylindrical tube approximately 6 cm long with a diameter of 1 cm. The electric shutter divides the tube into two parts: First one is a shorter reaction zone containing an ionization source and second one is a longer flight zone at the end of which the detector is connected via an amplifier to a suitable output [120], [125]. Samples in the form of solution or gas can be analyzed, and dry pieces of clothing are often used. Shortly after the sample is applied, the electrical gate is opened and the ions are accelerated through the flight tube. The time of flight of the individual components is in the range of milliseconds [118].

In general, the IMS method is used in security screening (detection of explosives and drugs) and environmental monitoring [126].

3.5.2. Experimental setup in measurements with ion mobility spectrometry

The IMS instrument used in this work is a Masstech IMS instrument produced at the Comenius University of the Faculty of Informatics, Mathematics and Physics with Atmospheric-pressure chemical ionization (APCI) source based on corona discharge [127]. The IMS was operated in positive polarity (it is possible to measure also on negative polarity but it was not used under the current study) and at atmospheric pressure. Sampling line was connected directly from reactor by the capillary inlet. All operating parameters are summarized in Tab. 15. The ion mobility scale was calibrated using 2,6-di-tert-butylpyridine (Sigma-Aldrich) as a standard compound with the well-known reduced mobility of 1.42 $cm^2 \cdot V^{-1} \cdot s^{-1}$ [127],[128]. Pure nitrogen passed through the additional moisture trap (in this experiment was Agilent) which was used as a drift gas in IMS [127],[128].

In the experiment, there were used 2 gases nitrogen and methane while nitrogen was with constant flow 200 sccm and methane in the range from 0.5 to 4.0 sccm of CH_4 and the power was also constant during all experiments at level of 10 W. All mesaurements within this range were done at laboratory temperatrue and pressure in stainless steel high vacuum reactor (Fig. 16). There was also one measurement done at nitrogen liquid temperature with flow of methane 0.5 sccm.

Tab. 15: Parameters of IMS used in the experiment

IMS drift tube length	11.87 cm
Drift field intensity	674 $V \cdot cm^{-1}$
IMS operating temperatures	376 K
Drift gas flow rate	800 $mL \cdot min^{-1}$
Sample gas flow rate	20 $mL \cdot min^{-1}$
CD current	10 µA
Shutter grid pulse width	80 µs
Range	0.8 – 4.0 $cm^2 \cdot V^{-1} \cdot s^{-1}$

3.5.3. Results from IMS measurements

The setting for positive polarity was used in all these measurements. There are generally two main reactive ions H_3O^+ with the highest intensity as it can be seen at Fig. 67 and $NO^+(H_2O)_n$. Sometimes there is also a low signal of reactive ion NH_4^+ which can occur e.g. from the sweat of the hands. Index „*n*“ could reach values 3 or 4 which could be calculated from the mass spectrum (it would be peak eaither 55 or 73).

The development of the spectra through the increasing concentration of methane can be seen at the Fig. 67. Before this spectrum was obtained it was necessary to re-calculate the value to have peaks at the same ion mobility values. These shifts are caused due to the fluctuations of conditions during the measurements. Eventhough there was set up still the same temperature 376 K the moisture could be changed which would also lead to the little changes of temperature.

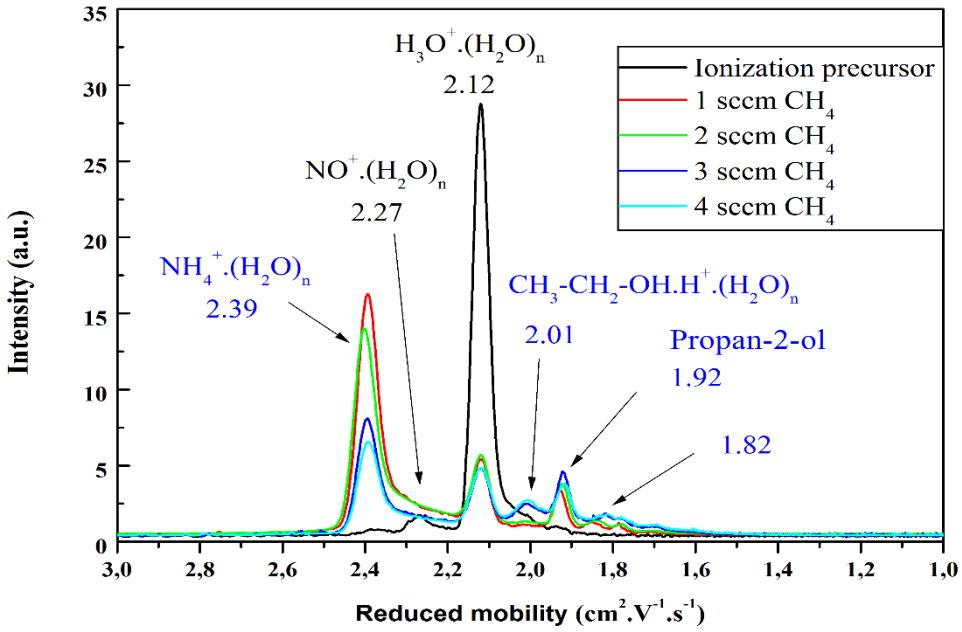

Fig. 67: Ion mobility spectra with increasing methan concetration from 1 to 4 sccm in nitrogen (200 sccm).

Higher temperature would cause creation of little clusters which means lower molecular weights. Lower molecules are of course faster and so they have higher ion mobility values → the whole spectrum is shifted to the left. At the Fig. 68 there it can be seen the original spectra before correction.

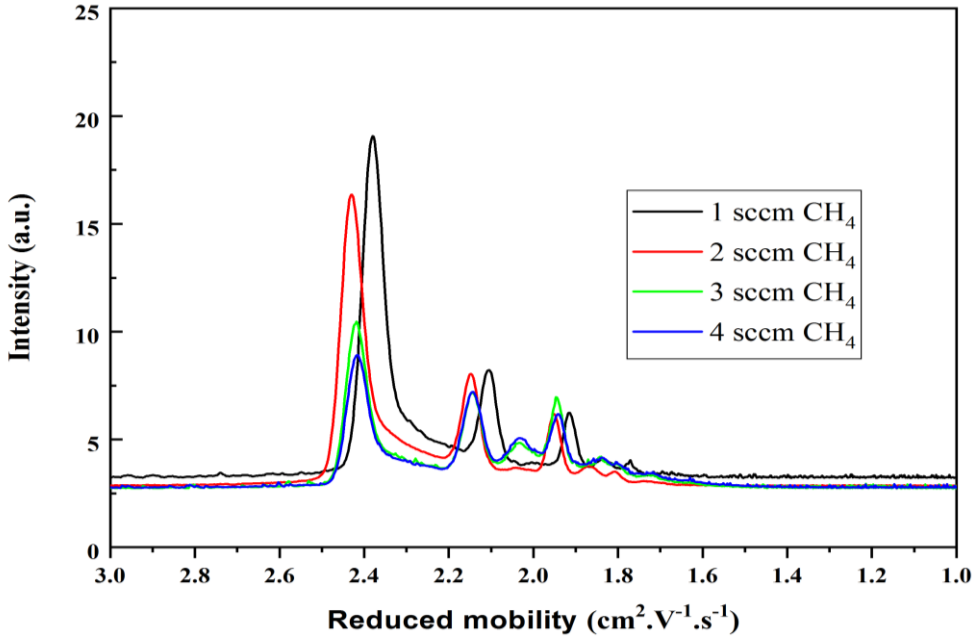

Fig. 68: Ion mobility spectra with increasing methan concetration from 1 to 4 sccm in nitrogen (200 sccm) before correction.

It is known from previous experiments (see the chapter measurements with PTR-TOF-MS) that under the given conditions in reaction mixture of nitrogen with methane the most

abundant products are acetonitrile, ammonia and hydrogen cyanide. High intensity of ammonia is shown also in this spectrum but there cannot be seen HCN because hydrogen cyanide forms negative ions, only, and thus this can not be detected in IMS positive ions settings [129].

At the spectrum Fig. 67 there can be also seen that the concentration of ammonia is decreasing with methane concentration increasing. This is most probably caused by the consumption of ammonia in reactions forming heavier molecules.

The second highest peak in the spectrum is at ion mobility 1.92 $cm^2 \cdot V^{-1} \cdot s^{-1}$ and it belongs probably to the propan-2-ol. It is only an estimation based on the available data from literature [129]. It is necessay to use combination of IMS with e.g. MS technique to be able to link the peak with compounds more precisely.

The other detected peak is at 2.02 $cm^2 \cdot V^{-1} \cdot s^{-1}$ which is most probably ethanol. The reaction behined could be following:

$$CH_2{=}CH_2 + H_2O \rightarrow C_2H_5OH \qquad (80)$$

The last detected peak is at ion mobility 1.82 $cm^2 \cdot V^{-1} \cdot s^{-1}$ and this could belong either to the higher alcohol or also to diethylamine [129].

At the Fig. 69 there can be seen the dependencies of all 3 detected peaks on the methane flow. It is obvious that the peak at 1.92 $cm^2 \cdot V^{-1} \cdot s^{-1}$ is with the highest intensity and its maximum is reached at the methane concentrationof 3 sccm which is actually not the highest concentration of methane. The strongest dependency on methane concentration shows the peak at 2.02 $cm^2 \cdot V^{-1} \cdot s^{-1}$ which is most probably the ethanol and the breakdown happened at the methane contrentration of 2.5 sccm.

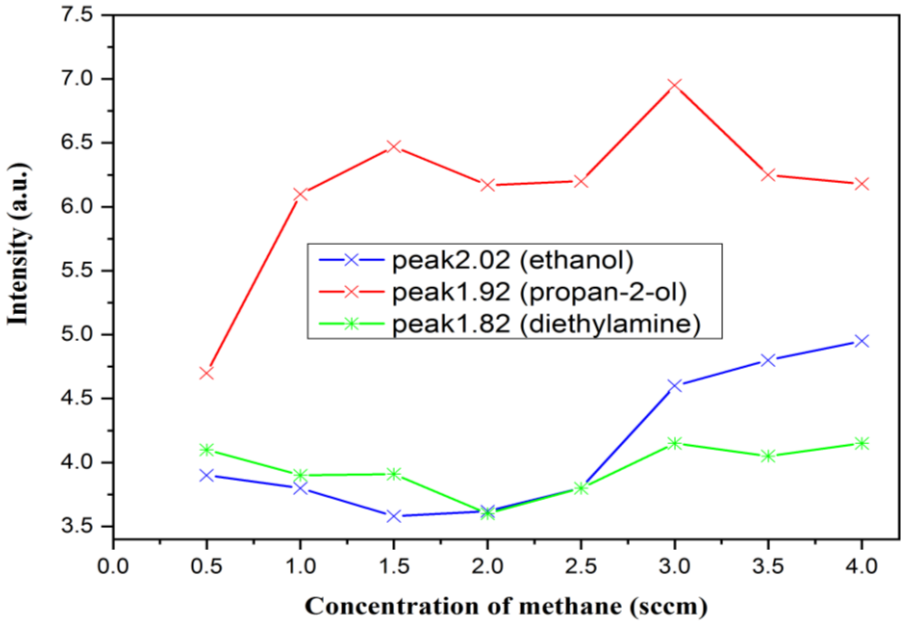

Fig. 69: Dependencies of the detected compounds on methane flow in 200 sccm of nitrogen

Fig. 70 shows the comparison of spectra between measurements at laboratory temperature vs measurements at liquid nitrogen temperature. It is obvious that the compounds

couldn’t condensate in reactor at the low temperature and so they did not reach out of the reactor to the detector. Unfortunately, when the reactor was heated up to get the compounds out of the reactor, the device became totally saturated and the measurement was not feasible.

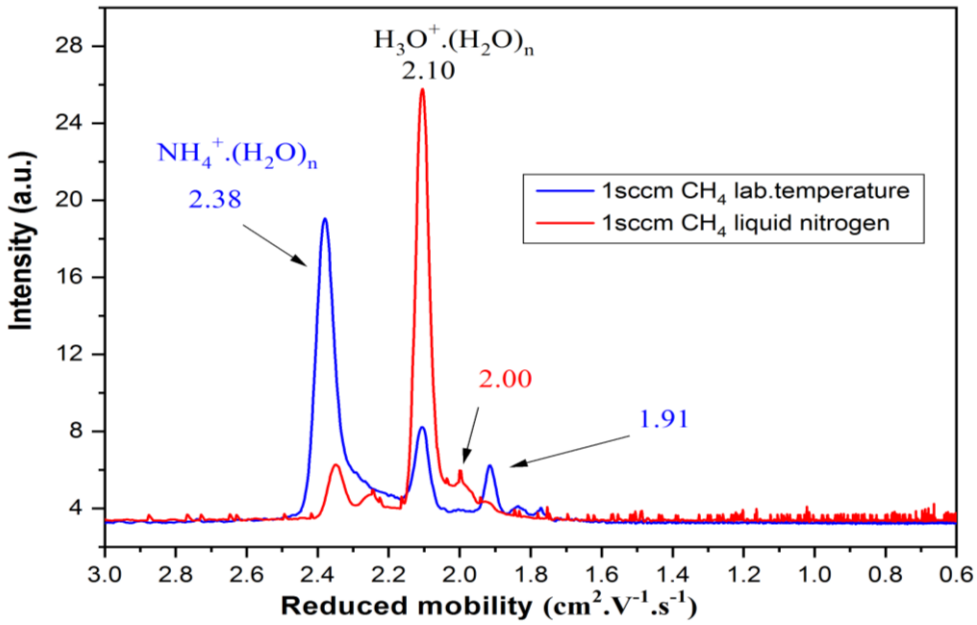

Fig. 70: Comparison of IMS spectra at ambient temperature vs temperature at liquid nitrogen

Majority of the coumpounds which were detected by PTR-ToF-MS measurements do not have known mobilities in database up to now. It means that they cannot be correctly measured and evaluated by IMS technique. So IMS measurement of chosen compounds which are considered as products at given conditions will be a task for further investigation.

3.6. Fourier-transform infrared spectroscopy (FTIR)

3.6.1. Principles of FTIR

Infrared spectroscopy (IR) is based on the interaction of molecules with electromagnetic energy in the infrared spectral region, which is in the wavelength range 0.8 to 1000 μm [130], [131]. This infrared range is usually divided into four areas called as near, middle, thermal, and far infrared. The peculiarity of the mid-infrared range (4000 to 400 cm^{-1}) is that it includes the so-called fundamental vibrations of molecules. When a molecule absorbs infrared radiation at frequencies corresponding to its own molecular vibrations, it results in an increase in the amplitude of the vibrations at these frequencies [130], [132]. Because each frequency corresponds to a given amount of energy and specific molecular motion (eg, stretching, bending, or shrinking chemical bonds), the mid-infrared spectrum can reveal the type of molecular motions and bonds (functional groups) that are present in the molecule and therefore serve as a unique fingerprint of a specific compound. In addition, most functional groups have characteristic absorption bands that do not change much as they transition from one compound to another [131], [133].

Nowadays, Fourier Transform Infrared Spectrometry (FTIR) is the preferred method for the mid-infrared region because it provides quantitative information in a fast and accurate manner. Unlike disperse spectrometers, the FTIR spectrometer measures all wavelengths at once [133], [134]. The basic principle of this method is the recording of the signal from the sample by an interferometer in the form of an interferogram and the subsequent application of the Fourier transform based on which the IR spectrum of the sample is obtained. The main part of the FTIR spectrometer is a Michelson interferometer, which consists of a beam splitter and two mirrors, one fixed and the other movable (see the Fig. 71) [134].

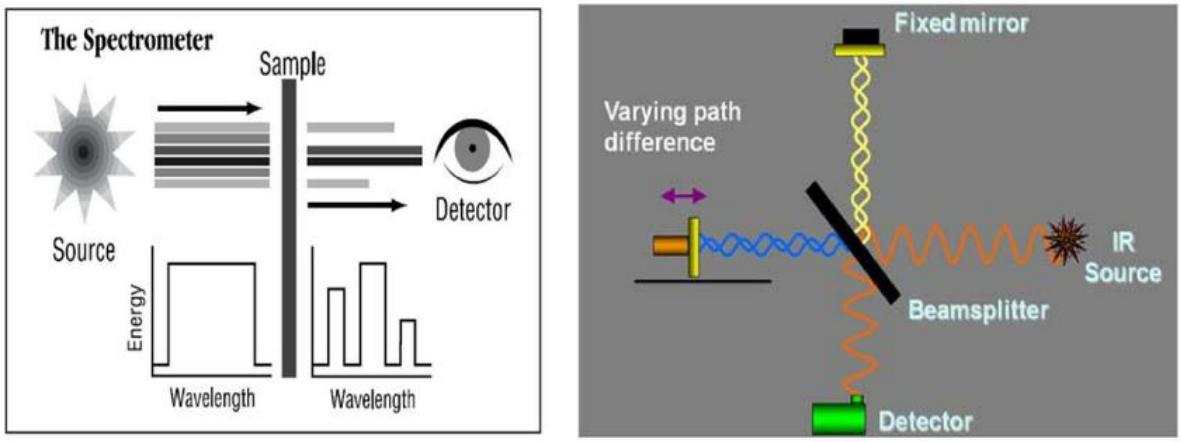

Fig. 71 Principle of operation of the Infrared Spectrometer; a) Basic illustration of the Transmission mode b) FTIR spectroscopy [134].

The light from the source falls on the beam splitter, which divides the beam into two halves. One beam impinges on the stationary mirror, reflects and returns back on the beam splitter, passing path $2L$. A similar process takes place for the second part of the split beam, the position of the second mirror is not stable, but can vary very precisely in the range x. The path taken by the second beam is then 2 $(L + x)$. Both beams interact with each other on the beam splitter, showing a difference in optical paths given by $2x$, which means that the individual beams are spatially coherent and they interfere. The beam, which emerges from the Michelson interferometer, passes further through the part in which the sample is located and is then focused on the detector [130], [131], [135].

The record that is obtained with an FTIR spectrometer is called an interferogram. The recorded interferogram must then be converted to the spectrum of the measured signal (transmittance, reflection, absorption, etc.) and this process is done using the mathematical method of Fourier transform (FT). The basis of the recording is the difference in optical path (OPD - Optical Path Difference). OPD is the difference between the light beams that travel in the two parts of the interferometer (the moving and the fixed part). The reference point for FTIR is the state when both the stable and the moving mirror are at the same distance from the beam splitter, this situation is referred to as the zero difference in optical distance (ZPD-Zero Path Difference) and from this point the change in the position of the moving mirrors is measured [131], [136].

Tab. 16: Specification of FTIR instrument for in-situ analysis of gaseous products

Spectrometer	Bruker Vector 22
Number of scans	5
Resolution	2 cm^{-1}
Measurement of quantities	Absorbance
Detector	DTGS KBr
IC radiation source	EverGlo
The length of the absorption path	320 cm (external multipass cuvette)
Measuring range	4000 - 400 cm^{-1}

As in the first set of experiments, pure nitrogen (purity 99.999%) flowed through the first branch, methane (purity 99.995%) through the second branch.

There were 3 kinds of mesaruments done by FTIR.

1. 0.5-4.0 sccm of CH_4 in 200 sccm of N_2 at power 2 W.
2. 0.5-4.0 sccm of CH_4 in 200 sccm of N_2 at power 4 W.
3. 0.5-4.0 sccm of CH_4 in 200 sccm of N_2 at power 6 W.

In all 3 experiments there were 9 measurements including the background. Between every mesaurement there was 30 minutes for reaching the stable conditions in the reactor and then the spectrum was taken. From the spectra were identified tens of compounds which will be described in next chapter 3.6.2.

From the measured absorbances of selected compounds, concentrations were calculated according to Lambert-Beer's law:

$$A = n.l.\sigma\ , \tag{81}$$

where A is the measured experimental absorbance, n (cm^{-3}) is the concentration of the detected compound, l (cm) is the length of the absorption path in the IR cuvette and σ (cm^2) is the effective absorption cross section. The absorption cross-sections can be also written in cm^2/mole through multiplying by the Avogadro's number: $6.022 \cdot 10^{23}$ molecule/mole. The effective cross-sections of the individual substances were calculated using the values given in the previously mentioned databases [138], [139] according to the formula:

$$\sigma = \frac{n.l}{A} \tag{82}$$

The selected wavelength value, to which the absorbance value used in the calculation of the effective cross section belongs, was further used to calculate the individual concentrations of the other substances. Two compounds were selected for quantitative analysis, namely hydrogen cyanide (713 cm^{-1}) and acetylene (730 cm^{-1})[140].

The NIST (National Institute of Standards) database was used for qualitative and partly also for quantitative analysis and Technology) [141]. It is suitable for both individual determination compounds as well as their stretching and bending bands.

3.6.2. Results obtained by FTIR

A typical infrared spectrum from an in-situ FTIR analysis obtained using a multipass external cuvette at ambient temperature can be seen in Fig. 72. The spectrum was measured under experimental conditions of a gas mixture composition of 2 sccm CH_4 and 200 sccm N_2 at a power delivered to the discharge of 4 W. On this spectrum there can be seen the methane structure. The vibrational bands at wavenbumers 1300 and 3000 belongs to the methane as it can be seen at Fig. 73.

The spectral bands in wavelenght range 2800–3000 cm^{-1} belong to the group of substances with –CH bonds. The absorption peaks between 3200 and 3400 cm^{-1} belong to the group of compounds with NH substituents. There could be typicall seen sharp peaks. Other weaker peaks of aromatic hydrocarbons are seen between 3000 and 3200 cm^{-1}. In the range of the absorption bands around 2800 to 3100 cm^{-1} there can be included compounds with bound $–CH_2$ and $–CH_3$ groups. Secondary and tertiary amines attached to CH_2 or CH_3 methyl groups may also be assumed due to the presence of absorption bands in the region between 2820-2750 cm^{-1}. Absorption bands around 3050-3100 cm^{-1} are attributed to aromatic compounds, but their abundance is very small due to the lack or very small amount of C-H bonded aromatic compounds.

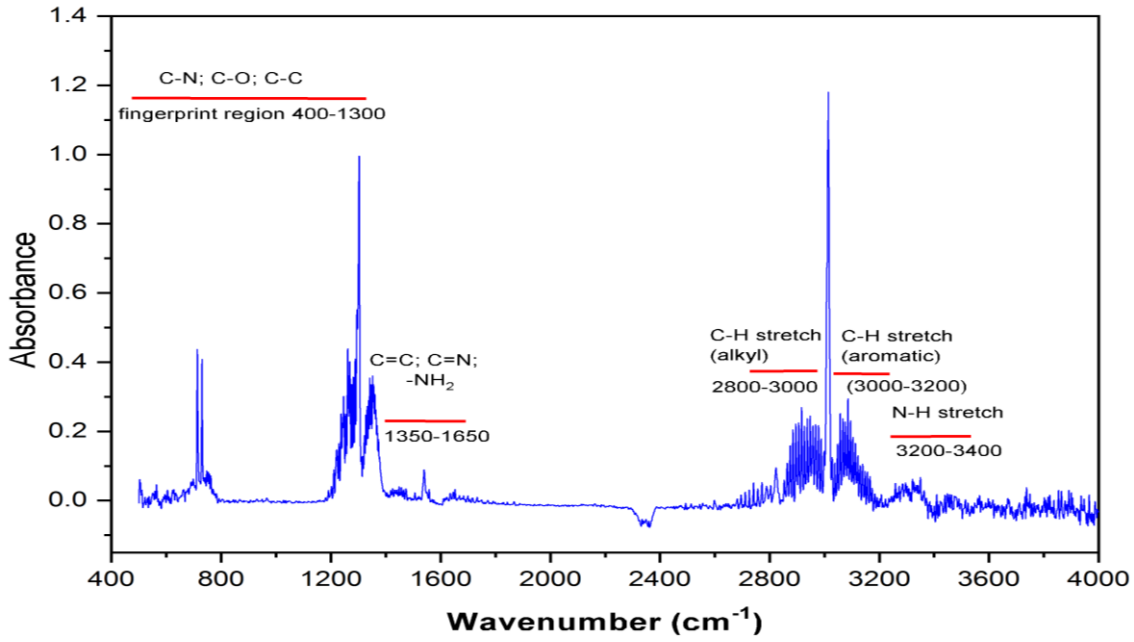

Fig. 72: Identification of a typical FTIR spectrum and organic products of an atmospheric discharge, divided into five main parts according to wavenumber.

The absorption peaks between absorption bands around 1350-1650 cm^{-1} belong to compounds with chemical bonds typical of the -CN, C=C and $–NH_2$ groups in the range. In addition, there are compounds with methyl radicals $=CH_2$ and $-CH_3$ in the range 1400-1470 cm^{-1}. The peak at 1600 cm^{-1} is classified as an aromatic compound.

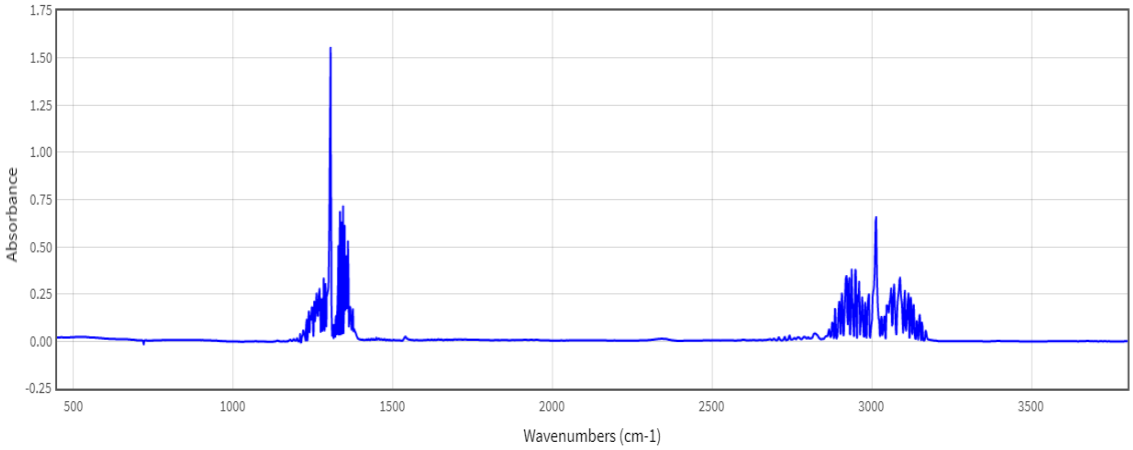

Fig. 73: FTIR spectra of methane (NIST) [142].

Aliphatic hydrocarbons

In the region of 3050-2800 cm^{-1} there is a specific absorption of aliphatic hydrocarbons methane, acetylene, etc., these are asymmetric and symmetric valence vibrations of C-H bonds. Obviously, variously substituted aliphatic compounds fall into this region.

The asymmetric C-H bond vibration of methane occurs exactly at 3013 cm^{-1}. Other typical absorption bands can be seen at ~1330 cm^{-1} and ~1310 cm^{-1}; they are corresponding to the deformation asymmetric and symmetric vibrations.

The doublet of absorption bands at ~ 757 cm^{-1} and ~ 752 cm^{-1} can be attributed to the asymmetric vibration of the C-H bonds in acetylene. Furthermore, an absorption band, typical of the C-H bond deformation vibration in acetylene, can be observed in the spectra at 1352 cm^{-1}. Due to the presence of absorption bands in the region of 1550-1400 cm^{-1} and 2780-2760 cm^{-1}, the presence of ethane, among others, can be considered.

Aromatic compounds:

At a wavenumber 1506 cm^{-1} the valence vibration of C=C bonds in aromatics (benzene and toluene) occurs. In the case of toluene, a pair of absorption bands can also be observed at 730 cm^{-1} and 700 cm^{-1}, corresponding to the out-of-plane strain vibration of mono-substituted aromatics, as it is toluene. There could be also expected an absorption band at 1600 cm^{-1}, but it appears that minority moisture (water) absorption rather occurs in this region with a maximum at 1650 cm^{-1}.

Nitrogen-substituted aliphatic hydrocarbons

According to FTIR analysis, the hypothesis of the presence of ammonia, whose most significant isolated absorption bands are found in the region 970-930 cm^{-1} cannot be supported. These peaks are generally very high.

A typical absorption band of hydrogen cyanide occurs at 712 cm^{-1}. At higher wavenumbers, describing the relevant absorption bands would be rather problematic and confusing.

The presence of acetonitrile was confirmed by absorption bands at 2598 cm^{-1} and ~1425 cm^{-1}, corresponding to the valence vibrations of the CN bonds. Since acetonitrile is measured in the gaseous state, the typical absorption bands at 2400-2200 cm^{-1} usually appear very faint in the spectra. An absorption band at 700 cm^{-1} can also be found, but it is in the region of specific absorption of other components in the discharge.

The presence of multiple carbon nitriles can be inferred from the less intense signals at 1465 cm^{-1} and 1220 cm^{-1}, the former associated with the deformation vibration of the C-H bond and the latter of the CN bonds, but it is not possible to distinguish between C_3 and C_4 nitriles.

On the basis of the measured spectra, the absorption bands characteristic of cyanoacetylene cannot be discerned, since these absorption signals are located in the regions of the populations of molecules already mentioned.

From the spectra at Fig. 74 and Fig. 75 there can be seen that creation of more compounds is supported very significantly with increasing of methane concentration in the gaseous mixture. From the spectra, there is also visible that a lot of methane is not converted while with increasing methane concentration also significantly increases the intensity of pure methane. On the other hand, increasing of power delivered to the discharge causes decreasing of methane concentration so more methane is converted into the heavier molecules. This is in perfect alignment with results obtained from PTR-MS measurements.

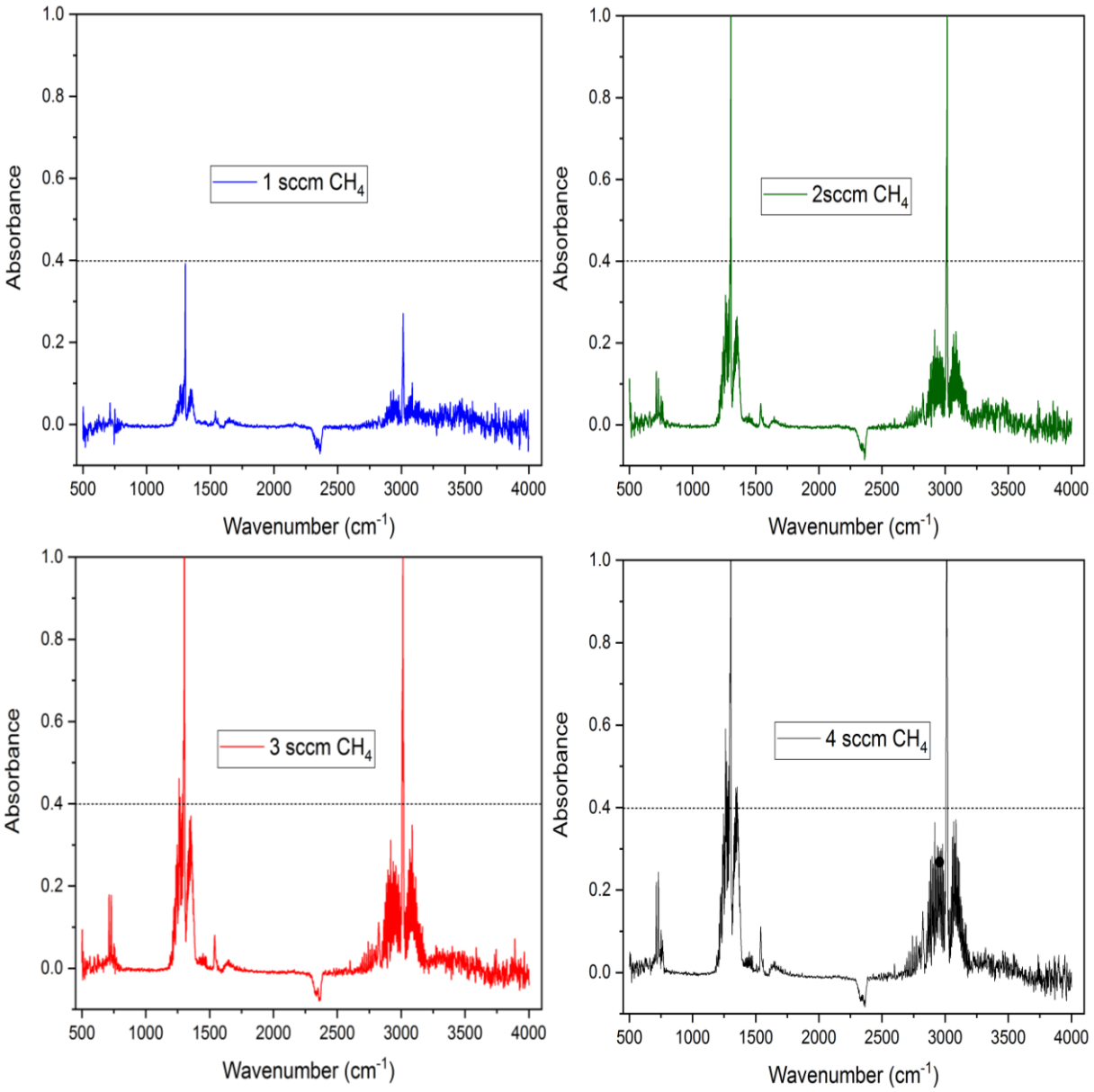

Fig. 74 FTIR spectra with increasing methan concentration from 1 to 4 sccm in nitrogen (200 sccm). The dotted line crosses the value 0.4 for better clarity in the comparison of spectra.

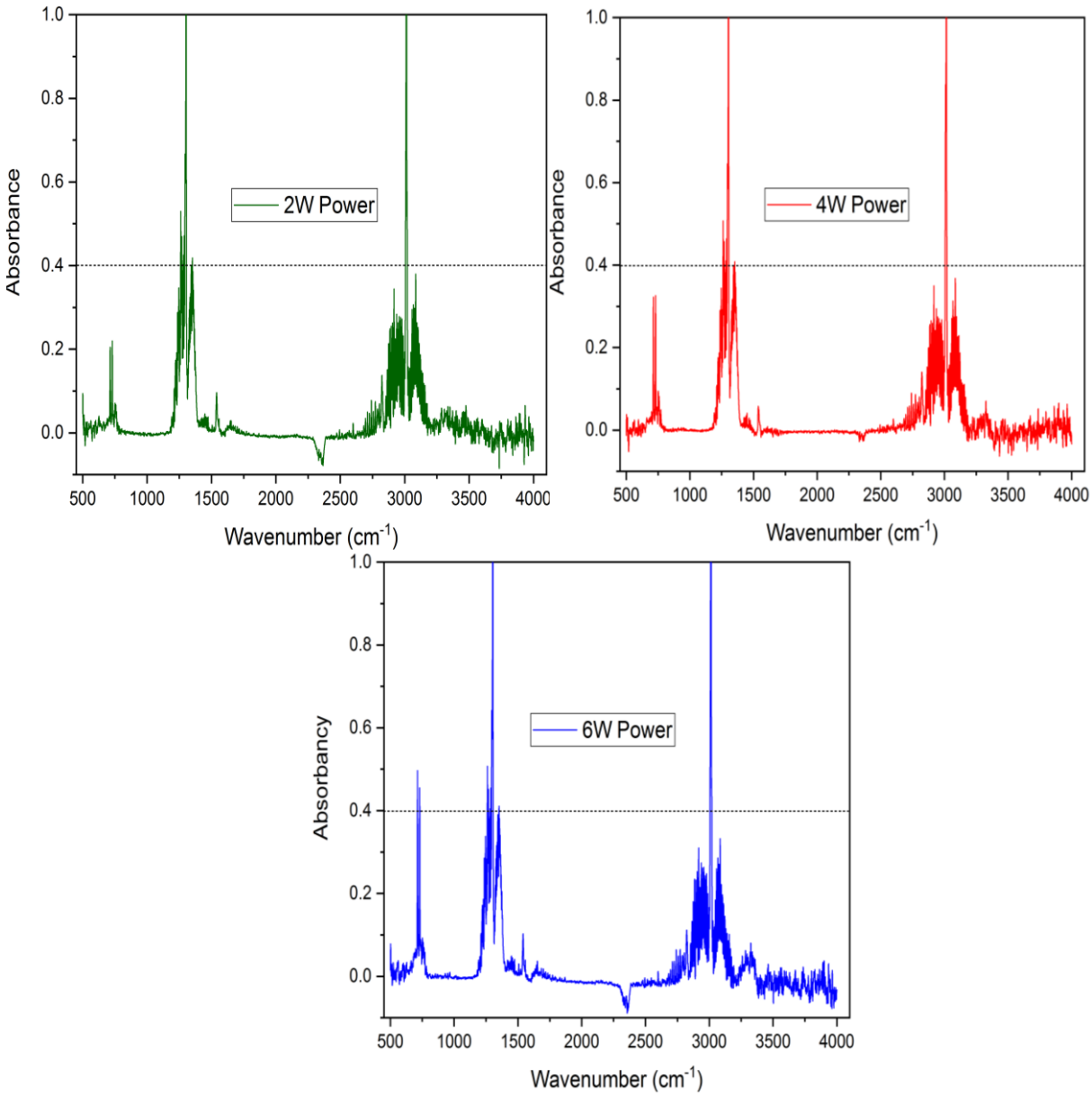

Fig. 75 FTIR spectra with increasing power from 2 through 4 up to 6 W in nitrogen (200 sccm) and 3.5 sccm of CH_4. The dotted line crosses the value 0.4 for better clarity in the comparison of spectra.

Considering the number of absorption peaks identical for most compounds, only two compounds could be selected for quantitative analysis, namely hydrogen cyanide HCN (713 cm^{-1}) and acetylene C_2H_2 (729 cm^{-1}). The dependence of the concentration of HCN and C_2H_2 on the composition of the gas mixture entering the discharge is shown at Fig. 76 and Fig. 77. Increasing the concentration of CH_4 from 1.0 sccm to 4.0 sccm in the mixture with nitrogen leads not only to an increase in the concentration of hydrogen cyanide and acetylene, but also to an increase in the production of more complex species (Fig. 74). As shown in the figures, the concentration of the discharge products is also affected by the value of the current supplied to the discharge. The larger the value of the current from 2-6 W, the more HCN and C_2H_2 were produced in the discharge. This dependence is more typical for smaller molecules as for instance HCN or C_2H_2. The increase in both absorbances has almost the same trend.

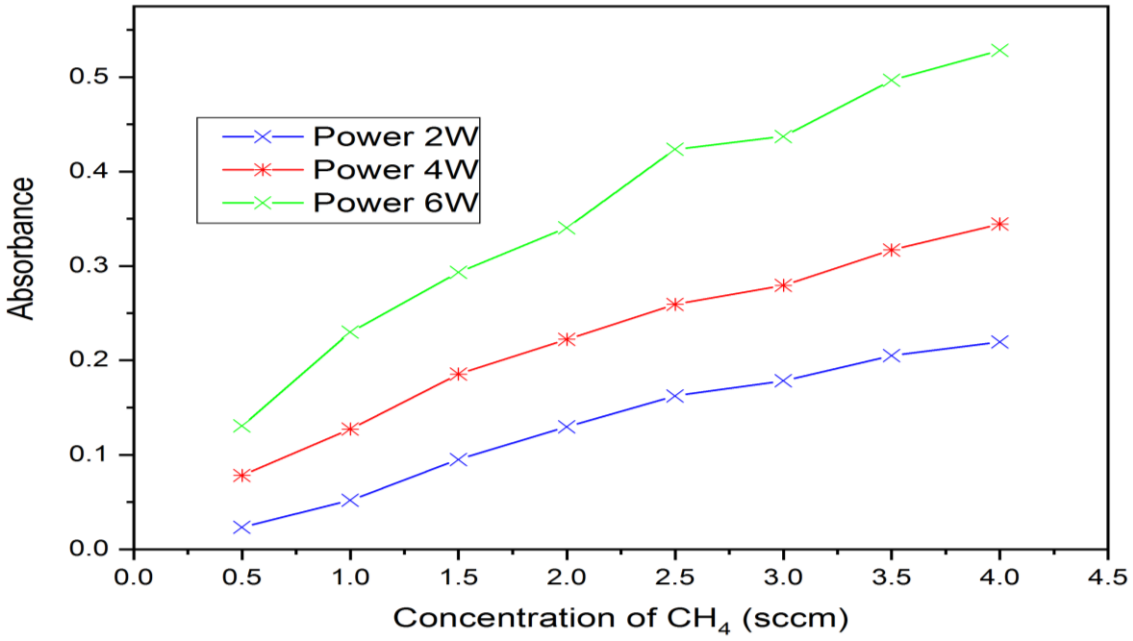

Fig. 76 Dependence of hydrogen cyanide concentration on discharge current and composition of the methane-nitrogen gas mixture.

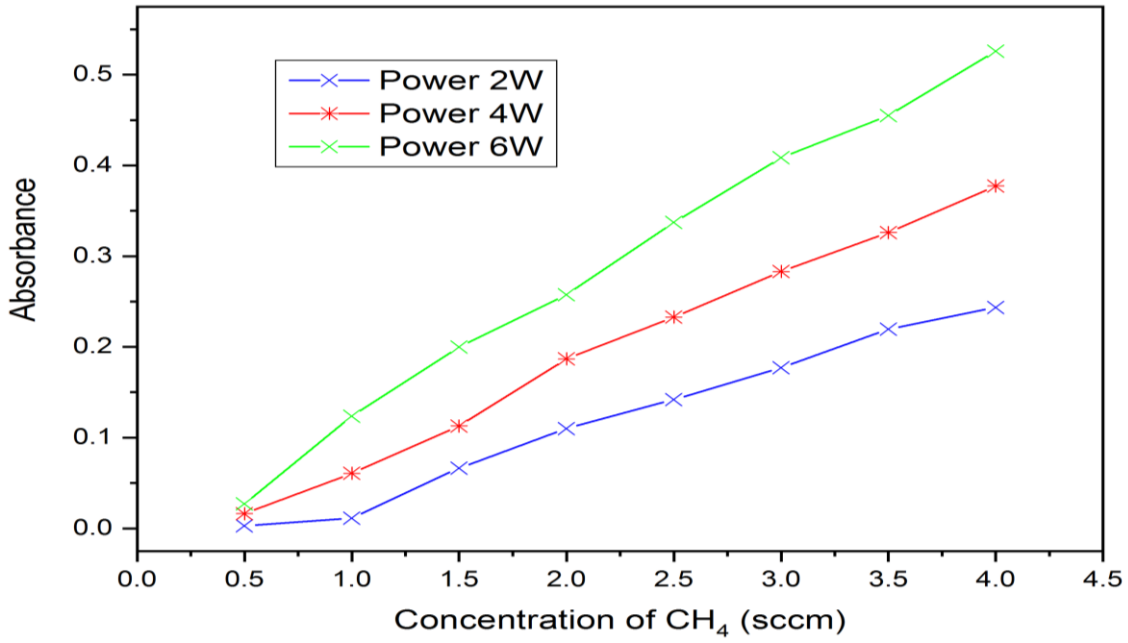

Fig. 77 Dependence of acetylene concentration on discharge current and composition of the methane-nitrogen gas mixture.

3.6.3. Results from FTIR measurements of the liquid product produced in reactor at low temperature

As it is mentioned above in chapter 3.4.2 there were flashes in the reactor occurred during the experiment. The flash occurs by something dripping down into a liquid methane. The first guesses were that this condensate is formamide which was detected also by PTR-ToF-MS. So the reactor was opened after the experiment and the drop from the bottom and crystals from the reactor wall were taken to the FTIR equipment to confirm this hypothesis.

Below at the pictures there can be seen spectra of both the droplet and the crystal, which was all over the reactor wall, and a spectrum of pure formamide for comparison.

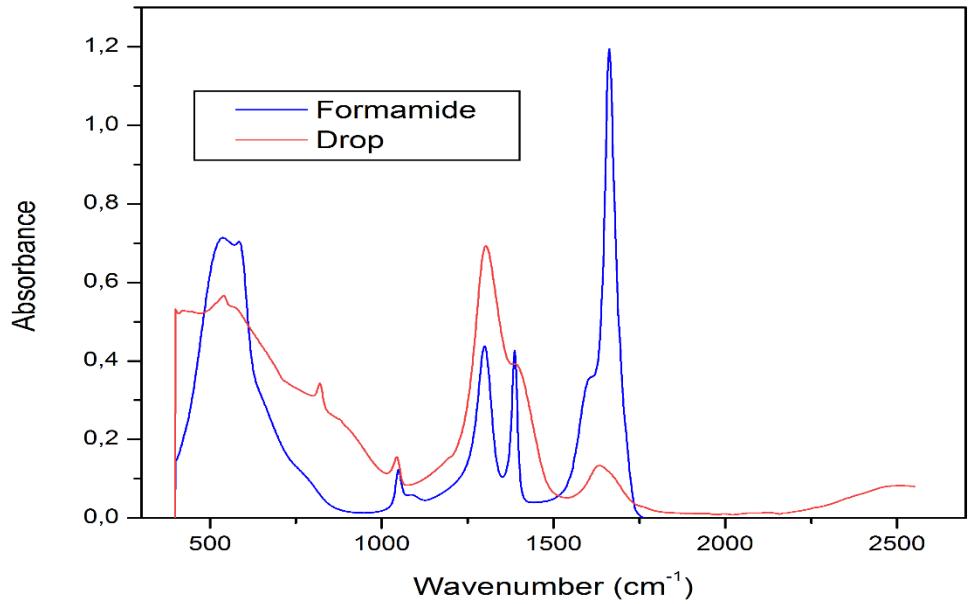

Fig. 78 FTIR comparison spectra of formamide with drop created in a reactor during the experiments at low temperature.

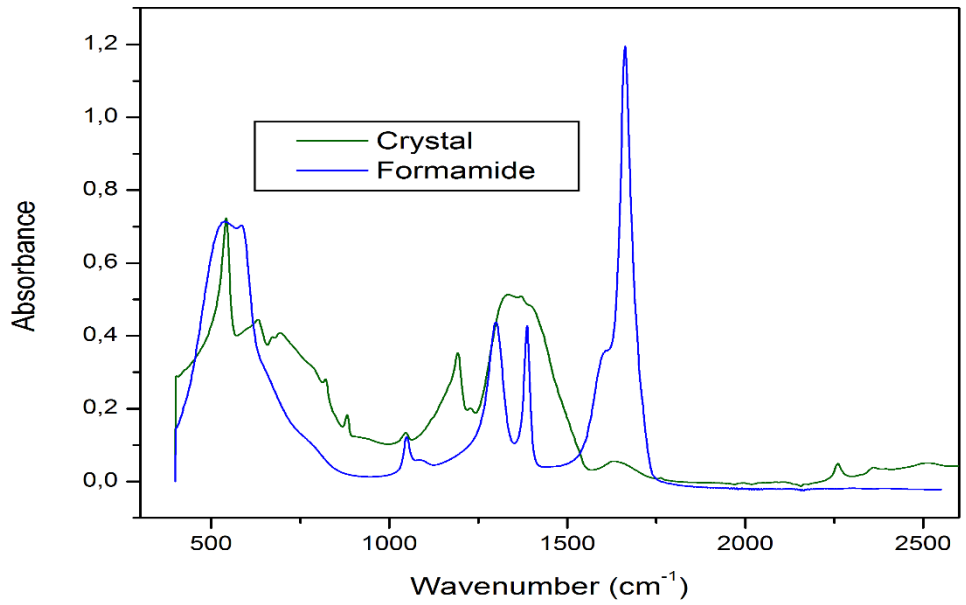

Fig. 79 FTIR comparison spectra of formamide with crystal created in a reactor during the experiments at low temperature.

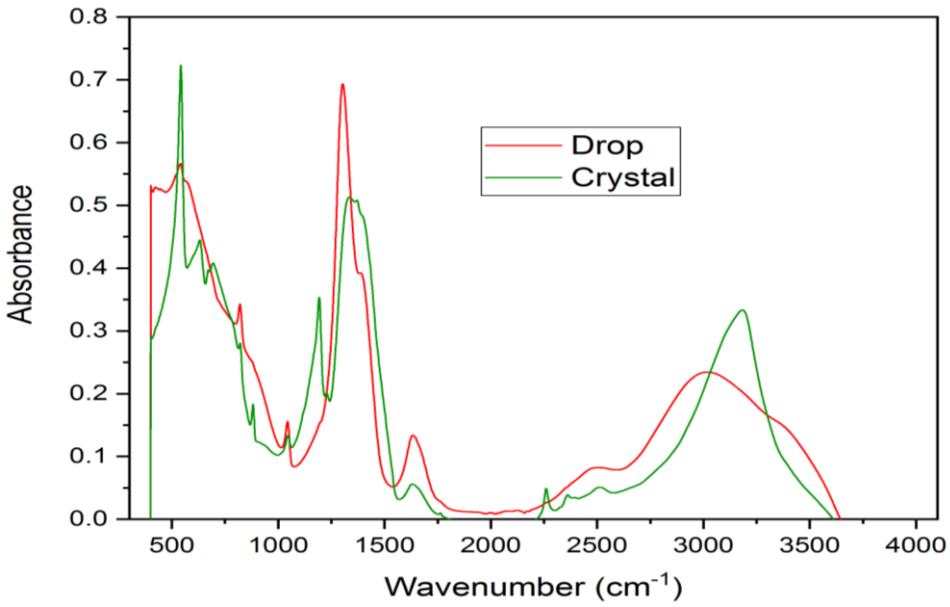

Fig. 80 FTIR comparison spectra of drop from the bottom of the reactor and crystal from the wall created in a reactor during the experiments at low temperature.

Based on these spectra results, it is not possible to evaluate this material for 100% but most likely there is a formamide and something extra in the drop. Maybe water from air humidity and some other impurity as well. The sample was not volatile and it was colorless which means it could not be any –CN compound. Crystal seems to be in a higher match with formamide and with less impurities. This is very promising results which needs to be further investigated.

3.7. Some possible reactions in electrical discharges based on methane

Methane is quite abundant in space and also in our Solar system (such as Titan's atmosphere). On Earth, closer to Sun than Titan, CH_4 was photochemically removed from the early atmosphere [48], [60]. The later CH_4 cycle, either from an extraterrestrial source or from volcanic activity, was responsible for maintaining a certain concentration of methane in the atmosphere. Even the small presence of CH_4 could significantly enrich the range of organic compounds that can be synthesized in the "neutral" prebiotic atmosphere of Earth [62], [114].

In thermal plasmas, CH_4 is good converted into acetylene C_2H_2 and as a next step with additional energy can be C_2H_2 transformed into black carbon and H_2 [48],

$$2CH_4 \rightarrow C_2H_6(+H_2) \rightarrow C_2H_4(+H_2) \rightarrow C_2H_2(+H_2) \rightarrow 2C(+H_2) \quad (43)$$

In nonthermal plasmas, there occur direct electron impact processes forming all possible CH_x radicals, including atomic carbon [48], [62],

$$CH_4 + e^- \rightarrow \cdot CH_3 + \cdot H + e^- \quad (44)$$

$$CH_4 + e^- \rightarrow :CH_2 + 2\cdot H + e^- \quad (45)$$

$$CH_4 + e^- \rightarrow \cdot CH + 3\cdot H + e^- \quad (46)$$

$$CH_4 + e^- \rightarrow C + 4\cdot H + e^- \quad (47)$$

Created radicals can then initiate a lot of subsequent reactions and thus lead to the formation of many products. The major products are hydrocarbons (such as C_2H_6, C_3H_8 etc). But it is needed to keep in mind that the selectivity for the conversion of methane to various hydrocarbons decreases with increasing of number carbon atoms. The presence of some different compounds as CO_2 or N_2 can significantly complicate the pure methane plasma chemistry. For example, the excited nitrogen can lead the dissociation of CH_4 [48], [114],

$$CH_4 + N_2^* \rightarrow {\cdot}CH_3 + N_2 + {\cdot}H \quad (48)$$

But from the chemical evolution of life point of view, the ability of CH_x radicals to produce ·CN and HCN is more important. Below are shown some possible reactions ways [48], [114]:

$${\cdot}CH_3 + N \rightarrow HCN + H_2 \quad (49)$$

$${\cdot}CH_3 + N \rightarrow H_2CN + {\cdot}H \quad (50)$$

$$:CH_2 + N \rightarrow HCN + {\cdot}H \quad (51)$$

$$:CH_2 + N \rightarrow {\cdot}CN + H_2 \quad (52)$$

$$CH + N \rightarrow {\cdot}CN + {\cdot}H \quad (53)$$

$$H_2CN + N \rightarrow HCN + :NH \quad (54)$$

$$CH_4 + CN \rightarrow {\cdot}CH_3 + HCN \quad (55)$$

The formation and reactions of CN and HCN have also been found in experiments simulating chemical processes in the atmosphere of Titan (among others also in my diploma thesis [88]). From chemical development point of view, the most valuable reaction in CH_4-CO_2 mixtures is the production of oxygenates (partially oxidized hydrocarbons). The concentrations of oxygen atoms and OH radicals that can cause partial or total oxidation of CH_4 to oxygen compounds are taken into account [48], [61].

Many organic substances were formed from CO_2 or steam reforming of CH_4 in various types of plasma, as for example formaldehyde, methanol, formic acid, acetaldehyde or acetic acid. The following chemical reactions show the formation of formaldehyde (H_2CO), which is very presumably an important compound in the chemical life development [48]. It was also detected in significant amount in current experiments.

$$CH_4 + O \rightarrow {\cdot}CH_3 + {\cdot}OH \quad (56)$$

$$CH_4 + {\cdot}OH \rightarrow {\cdot}CH_3 + H_2O \quad (57)$$

$${\cdot}CH_3 + O \rightarrow H_2CO + {\cdot}H \quad (58)$$

Hydrogen cyanide formation can occur with varying probabilities in a single step as outlined in the following reactions: [111], [112]

$$CH + N_2 = HCN + N;\ \Delta H_r^\circ{}_{298K} = 11{,}89\ \text{kJ/mol}, \quad (58)$$

$$CH_2 + N_2 = HCN + NH;\ \Delta H_r^\circ{}_{298K} = 103{,}48\ \text{kJ/mol}, \quad (59)$$

$$C_2H + N_2 = HCN + CN;\ \Delta H_r^\circ{}_{298K} = 9{,}83\ \text{kJ/mol}, \quad (60)$$

where $\Delta H_r^\circ{}_{298K}$ is standard enthalpy of reaction.

Another possibility is the formation of hydrogen cyanide in two steps through the highly unstable intermediate H_2CN: [111], [112]

$$N + CH_3 = H_2CN + H \quad (61)$$

$$H_2CN + N = HCN + NH, \quad (62)$$

or through the radical $CN^{\cdot}$:

$$N + CH_2 = CN + H_2 \quad (63)$$

$$CN + CH_4 = HCN + CH_3 \quad (64)$$

Reactions 63 and 64 seem to be the most likely in this case, due to the high CN concentration in the discharge, which was also confirmed by the OES results [110].

During the electric discharge taking place in the mixture of N_2-CH_4, the molecules dissociate with the formation of methane radicals (CH_3, CH_2, CH), and C, H, N atoms. These substances are then precursors for the formation of other substances in the chain of chemical reactions [113], [115]. Possible reactions in a mixture of N_2-CH_4 are reported in the work of Legrand et al [113]. They paid particular attention to the degree of methane decomposition and the formation of stable products, along with many important reactions in the formation of other individual compounds.

Second order reactions for hydrocarbons and radicals [113], [115], [116]

$CH_4 + CH_3 \rightarrow C_2H_5 + H_2$	$1.7\times10^{-11}\times\exp(-11.500/T_g)$ $cm^3\cdot s^{-1}$	(67)
$CH_4 + CH_2 \rightarrow CH_3+CH_3$	$7.1\times10^{-12}\times\exp(-5020/T_g)$ $cm^3\cdot s^{-1}$	(68)
$CH_4 + CH \rightarrow C_2H_4 + H$	$5.0\times10^{-11}\times\exp(200/T_g)$ $cm^3\cdot s^{-1}$	(69)
$CH_4 + C_2H \rightarrow C_2H_2 + CH_3$	$3.0\times10^{-12}\times\exp(-250/T_g)$ $cm^3\cdot s^{-1}$	(70)
$CH_3 + C_2H_5 \rightarrow C_3H_8$	4.7×10^{-11} $cm^3\cdot s^{-1}$	(71)
$C_2H_5 + H \rightarrow C_2H_6$	6.0×10^{-11} $cm^3\cdot s^{-1}$	(72)
$C_2H_6 + CH_3 \rightarrow C_2H_5 + CH_4$	$2.5\times10^{-31}\times T_g^{-6.0}\times\exp(-3043/T_g)$ $cm^3\cdot s^{-1}$	(73)
$C_2H_6 + C_2H \rightarrow C_2H_2 + C_2H_5$	6.0×10^{-12} $cm^3\cdot s^{-1}$	(74)

T_g is gas temperature.

Reactions between hydrocarbons and nitrogen [113], [115], [116]

$CH_3 + N \rightarrow HCN + H_2$	1.4×10^{-11} $cm^3\cdot s^{-1}$	(75)
$CH_3 + N \rightarrow H_2CN + H$	1.3×10^{-10} $cm^3\cdot s^{-1}$	(76)
$CH_3 + H + N_2 \rightarrow CH_4 + N_2$	$6.0\times10^{-29}\times(T_g/300)^{-1.8}$ $cm^6\cdot s^{-1}$	(77)
$C_2H_2 + H + N_2 \rightarrow C_2H_3 + N_2$	$1.05\times10^{-7}\times T_g^{-7.27}\times\exp(-3632/T_g)$ $cm^6\cdot s^{-1}$	(78)
$H + H + N_2 \rightarrow H_2 + N_2$	$1.5\times10^{-29}\times T_g^{-1.3}$ $cm^6\cdot s^{-1}$	(79)

The above reactions are only a small indication of the processes that can take place in a given system. It is a highly complex process involving a number of parameters such as mixture composition, pressure, temperature, power, etc. Thus, a full understanding of what is happening is not possible without detailed numerical models, which are beyond the scope of this work, and are only realistically possible in a large international collaboration.

4. CONCLUSIONS

The thesis was focused on the simulation and study of chemical processes in the atmosphere of Titan, a moon of Saturn, the second largest moon in the solar system. There were done also a lot of experiments with Mars atmosphere, but these results were presented in another diploma thesis [143]. Measurements were carried out at an atmospheric pressure of 10^5 Pa and at a pressure of 1.5 atm, both at laboratory temperature as well as at the low temperature of liquid nitrogen. A stainless-steel high-vacuum reactor was constructed for the experiments, which allowed operation in an oxygen-free atmosphere. It was constructed in such a way that the electrode system could be changed. In this work, the discharge was initiated by a DC electric discharge in a Gild-Arc electrode configuration. Experiments were also carried out in a smaller glass reactor during low temperature measurements.

Gaseous mixtures of nitrogen N_2 and methane CH_4 was used in the experiments at various ratios from 0.2 sccm to 4 sccm in 200 sccm of nitrogen (0.1 - 2%). Some of the experiments were also conducted with oxygen and carbon dioxide admixtures.

The main objective was the identification of the stable products formed in the reactor, which was carried out mostly by *in situ* mass spectrometry with proton ionization, then by *in situ* Fourier transform infrared spectrometry and last by *in situ* ion mobility spectrometry. Optical emission spectroscopy was used to characterize the electrical discharge itself.

Optical emission spectra were measured in the range 300-600 nm for different experimental conditions. The measurements were carried out at a flow rate of 200 sccm nitrogen with methane from 1 sccm to 4 sccm and varying current from 15-45 mA (6-18 W). Based on the measurement results, the violet system of radical CN ($B^2\sum^+ \rightarrow X^2\sum^+$), the nitrogen second positive system N_2^* ($C^3\Pi_u \rightarrow B^3\Pi_g$), were further used for the vibrational temperature calculations. From nitrogen second positive system the rotational temperature was also determined. The first negative molecular nitrogen ion system N_2^+ ($B^2\sum_u^+ \rightarrow X^2\sum_g^+$), was also used to calculate the vibrational temperature. The Swan system of the C_2 molecule was no longer sufficiently intense under the given conditions. In addition to the molecular spectral systems, the atomic hydrogen Balmer series lines H_α (656 nm) and H_β (486 nm) were also identified.

The rotational temperature was determined from the nitrogen second positive system to be approximately 2300 - 2400 K with uncertainty of about 40 – 50 K. This temperature shows minimal dependence on the methane concentration and increases only very slowly with increasing power. The vibrational temperature for the nitrogen second positive system was calculated at 3100 - 3400 K with a uncertainty of 120 - 130 K. For the nitrogen first negative system, the vibrational temperature was set to an approximate value of 3950 – 4350 K with uncertainty of 100 - 130 K, and for the violet spectral CN radical system, the vibrational temperature was set to 5900 - 7700 K with uncertainty of 230 – 270 K. In the case of the nitrogen second positive system, the vibrational temperature increases with methane concentration and, conversely, decreases for the nitrogen first negative system and the violet system of CN radical. This general difference could be explained by the different excitation mechanism of the above spectral systems. While in the first case (nitrogen second positive

system) the excitation is mainly initiated by electron collisions, the collisional energy transfer from the metastable levels of the ground state nitrogen molecule participates significantly in the excitation in the second case. This process probably plays a role outside the active part of the discharge and is virtually impossible to separate.

The main compounds detected by in situ proton ionization mass spectrometry at laboratory temperature were mainly nitriles with bound functional groups, mainly cyano (-CN), amino (-NH2, -NH) and also imino groups (-C=N-). The most detected compounds were acetylene (H_2C_2; 26 amu), hydrogen cyanide (HCN; 27 amu), acetonitrile (CH_3CN; 41 amu), cyanoacetylene (C_3HN; 51 amu), propane nitrile (C_2H_5CN; 55 amu), (butanenitrile; 69 amu) and (benzene; 78 amu). All of the above compounds have either been detected or are at least expected to be present in Titan's atmosphere. Substances with molecular weights above 130 amu at laboratory temperature have intensities close to noise.

The results of the measurements under near realistic conditions and thus under low temperature liquid nitrogen yielded the detection of up to about 200 compounds in the molecular weight range up to 450 amu. The major compounds were more or less similar as at the ambient temperature so it means acetylene H_2C_2 (26 amu), N_2H_4 hydrazine (32 amu), acetonitrile CH_3CN (41 amu), formamide CH_3NO (45 amu), diacetylene C_4H_2 (51 amu), acetone C_3H_6O (58 amu) , butanenitrile (69 amu), or benzene (78 amu) and of course hydrogen cyanide HCN (27 amu) but HCN was not the most abundant compound as at the ambient temperature probably because at such a low temperature it remained in the reactor in the liquid phase and even in the form of crystals. Measurements at low temperature were carried out in the same mixture as in the laboratory, i.e. CH_4 in N_2 and in the next series also with a small admixture of oxygen and carbon dioxide. It has to be said that the spectrum at low temperature was very similar in presence of oxygen as well as without oxygen. There was only a difference in intensities of compounds containing oxygen. The formation of oxygen compounds in the mixture of N_2 + CH_4 without oxygen can be explained most probably by the fact that there is a lot of absorbed oxygen on the walls of the silicon tubes that lead to and from the reactor. The instrument is sensitive in the orders of ppb and so it is extremely difficult to get rid of the oxygen completely. But it is definitely a task for further experiments.

In both sets of experiments at laboratory and low temperature, the spectra show a high dependence of the products formed on increasing methane concentration. This trend is significantly more visible for molecules with mass above 75 amu. For molecules above 100 amu the dependence is almost exponential. This can probably be explained by the fact that at higher methane concentrations smaller molecules are consumed to form heavier molecules.

The thesis also includes measurements by the ion mobility spectrometry. The most important gas detected was ammonia, followed by propane-2-ol, ethanol and most likely diethylamine. Most of the compounds that were detected in the work using PTR-ToF-MS have no known mobilities in the database. This means that they cannot be properly measured and evaluated by the IMS technique. So, IMS measurement of selected compounds that are considered to be products of the given conditions will be a great task for further research.

The last set of measurements was *in situ* FTIR measurements, which showed that a large number of different products are generated, which are very difficult to analyse and separate from each other. The main products detected by FTIR are HCN (713 cm^{-1}) and C_2H_2 (729 cm^{-1}), from which concentration dependence plots for methane were obtained. The significant abundance of these compounds and the increasing dependence on methane concentration is in agreement with the results from PTR-TOF-MS. The basic discharge spectrum is the methane structure and the spectrum shows intense bands belonging to both aliphatic hydrocarbons (3050-2800 cm^{-1}) and aromatic compounds (benzene at 1506 cm^{-1}), and there are also bands belonging to nitrogen-substituted hydrocarbons (1350-1600 cm^{-1} and 3200-3400 cm^{-1}, respectively) in the spectrum. Comparing the overall spectra at different methane concentrations, it can be seen that a large fraction of the methane passes through the reactor into the detector unreacted. However, this proportion of unreacted methane decreases significantly with increasing power supplied to the system.

In experiments at low temperature, a thick haze was formed in the reactor, which condensed to crystallize in the reactor. Thus OES measurements were impossible to complete at low temperature experiemnts. These droplets and also the crystals were also identified by FTIR, which confirmed that they were probably formamide containing certain impurities. This is a significant finding as formamide is considered an ideal precursor for prebiotic synthesis.

The lower molecular weight compounds detected in this work are in a good agreement with the available literature and also with species detected in Titan's atmosphere by the Cassini Space mission with the Huygens module. The heavier molecules detected in the work, such as bezenene or toluene, have not been detected on Titan so far but their presence is expected based on model simulations. In particular, experiments under low temperature liquid nitrogen have yielded interesting results that will need to be extended by many further studies. Coupling with model-based computational software such as Monte Carlo simulations and detailed temperature dependent kinetic models will be necessary to understand the complex thermodynamic and kinetic processes occurring in the system. In the experiments it will be important to ensure a more perfect dilution of the gas mixture with nitrogen and especially to ensure an oxygen-free atmosphere. For the next experiments there is a plan to use different kind of discharges in the current reactor as well as it will be very interesting to do the measurements in the stationary regime, where higher methane conversion and the formation of more complex molecules can be expected, especially at lower temperatures.

5. REFERENCES

[1] BRENNAN, P. PlanetQuest. NASA*: The search for life*. [online]. **2019**. [cit. 2019-08-04]. Dostupné z: http://planetquest.jpl.nasa.gov/.

[2] KAMMER, J.A., D.E. SHEMANSKY, X. ZHANG a Y.L. YUNG. Composition of Titan's upper atmosphere from Cassini UVIS EUV stellar occultations. *Planetary and Space Science*. **2013**, 88, 86-92. DOI: 10.1016/j.pss.2013.08.003. ISSN 00320633.

[3] MCFADDEN, L.A.A., WEISSMAN, P.R., JOHNSON, T. V. Encyclopedia of the solar system. 2nd ed. Amsterdam: Academic Press, **2007**. ISBN 978-0-12-088589-3.

[4] THAXTON, Ch. B., BRADLEY, W.L., OLSEN, R.L. The Mystery of Life's Origin: Reassessing Current Theories. Philosophical Library, **1984**. ISBN-13: 978-0802224477.

[5] SIDNEY W. F., DOSE, K. Sidney W. Fox, Klaus Dose a WITH A FOREWORD BY A. OPARIN. Molecular evolution and the origin of life. San Francisco: W.H. Freeman, **1972**. ISBN 978-071-6701-637.

[6] BERNARD, J., QUIRICO, E., BRISSAUD, O.et al. Reflectance spectra and chemical structure of Titan's tholins: Application to the analysis of Cassini–Huygens observations. *Icarus*. **2006**, 185(1), 301-ISSN 00191035.

[7] IMANAKA, H., KHARE, B.N., ELSILA, J.E. et al. Laboratory experiments of Titan tholin formed in cold plasma at various pressures: implications for nitrogen-containing polycyclic aromatic compounds in Titan haze. *Icarus*. **2004**, 168(2), 344-366. DOI: 10.1016/j.icarus.2003.12.014. ISSN 00191035.

[8] JOHNSON, R.E., TUCKER, O.J., VOLKOV, A.N. Evolution of an early Titan atmosphere. *Icarus*. **2016**, 271, 202-206. DOI: 10.1016/j.icarus.2016.01.014. ISSN 00191035.

[9] KAMMER, J.A., SHEMANSKY, D.E., ZHANG, X. et al. Composition of Titan's upper atmosphere from Cassini UVIS EUV stellar occultations. *Planetary and Space Science*. **2013**, 88, 86-92. DOI: 10.1016/j.pss.2013.08.003. ISSN 00320633.

[10] HÖRST, S. M. Titan's atmosphere and climate. Journal of Geophysical Research: Planets. **2017**, 122(3), 432-482. DOI:10.1002/2016JE005240. ISSN 21699097.

[11] HENDRIX, A.R, YUNG, Y.L. Energy Options for Future Humans on Titan. *Journal of Astrobiology & Outreach*. **2017**, 05(02). DOI: 10.4172/2332-2519.1000157. ISSN 23322519.

[12] GILLIAM, A.E., LERMAN, A. Titan’s missing ethane: From the atmosphere to the subsurface. *Icarus*. **2016**, 275, 252-258. DOI: 10.1016/j.icarus.2016.04.025. ISSN 00191035.

[13] MOINELO, C., ABILDGAARD, A., S., MUÑOZ, A. G., et al. No statistical evidence of lightning in Venus night-side atmosphere from VIRTIS-Venus Express Visible observations. *Icarus*. **2016**, 277, 395-400. ISSN 00191035. doi:10.1016/j.icarus.2016.05.027

[14] ZARKA, P., FARRELL, W.M., KAISER, M.L., et al. Study of solar system planetary lightning with LOFAR. *Planetary and Space Science*. **2004**, 52(15), 1435-1447. ISSN 00320633. doi:10.1016/j.pss.2004.09.011

[15] DYUDINA, U., DELGENIO, A., INGERSOLL A. et al. Lightning on Jupiter observed in the line by the Cassini imaging science subsystem. *Icarus*. **2004**, 172(1), 24-36. ISSN 00191035. doi:10.1016/j.icarus.2004.07.014

[16] KONOVALENKO, A.A., KALINICHENKO, N.N., RUCKER, H.O. et al. Earliest recorded ground-based decameter wavelength observations of Saturn's lightning during the giant E-storm detected by Cassini spacecraft in early 2006. *Icarus*. **2013**, 224(1), 14-23. ISSN 00191035. doi:10.1016/j.icarus.2012.07.024
[17] GIBBARD, S.G., LEVY, E.H., LUNINE, J.I., et al. Lightning on Neptune. *Icarus*. **1999**, 139(2), 227-234. ISSN 00191035. Dostupné z: doi:10.1006/icar.1999.6101
[18] APLIN, K.L., FISCHER, G. Lightning detection in planetary atmospheres. *Weather*. **2017**, **72**(2), 46-50. DOI: 10.1002/wea.2817. ISSN 00431656.
[19] GILES, R.S., GREATHOUSE, T.K., BONFOND, B., et al. Possible Transient Luminous Events Observed in Jupiter's Upper Atmosphere. *Journal of Geophysical Research: Planets*. **2020**, 125 (11). ISSN 2169-9097. DOI: 10.1029/2020JE006659.
[20] SOSNIN, E.A., BABAEVA, N.Y., KOZHEVNIKOV, V.Y., et al. Modeling of transient luminous events in Earth's middle atmosphere with apokamp discharge. *Physics-Uspekhi*. **2021**, 64(2), 191-210. ISSN 1063-7869. DOI:10.3367/UFNe.2020.03.038735
[21] LORENZ, R.D., CRISP, D., HUBER, L. Venus atmospheric structure and dynamics from the VEGA lander and balloons: New results and PDS archive. *Icarus*. **2018**, 305, 277-283. DOI: 10.1016/j.icarus.2017.12.044. ISSN 00191035.
[22] PATON, M.D., S.F. GREEN, A.J. BALL, J.C. ZARNECKI a A. HAGERMANN. Detection of structure in asteroid analogue materials and Titan's regolith by a landing spacecraft. *Advances in Space Research*. **2016**, 58(3), 415-437. DOI: 10.1016/j.asr.2016.04.026. ISSN 02731177.
[23] LAVVAS, P., R.V. YELLE, A.N. HEAYS, L. CAMPBELL, M.J. BRUNGER, M. GALAND a V. VUITTON. N2 state population in Titan's atmosphere. *Icarus*. **2015**, 260, 29-59. DOI: 10.1016/j.icarus.2015.06.033. ISSN 00191035.
[24] TOKANO, Tetsuya. Nitrogen condensation in Titan's atmosphere under contemporary atmospheric composition. *Icarus*. **2017**, 289, 120-133. DOI: 10.1016/j.icarus.2017.02.005. ISSN 00191035.
[25] BROSSIER, J.F., RODRIGUEZ, S., CORNET, T., et al. Geological Evolution of Titan's Equatorial Regions: Possible Nature and Origin of the Dune Material. *Journal of Geophysical Research: Planets*. **2018**, 123(5), 1089-1112 DOI: 10.1029/2017JE005399. ISSN 21699097.
[26] DOBRIJEVIC, M. DUTOUR, I. The distribution of hydrocarbons in Titan's atmosphere: An evolutionary algorithm-based model. *Planetary and Space Science*. **2007**, 55(14), 2128-2136. DOI: 10.1016/j.pss.2007.06.003. ISSN 00320633.
[27] ZEBKER, A.H., STILES, B., HENSLEY, S. et al. Size and Shape of Saturn's Moon Titan. *Science*. **2009**, vol. 324, n. 5929, p. 921-923. ISSN 0036-8075
[28] FISCHER, G., TOKANO, T. MACHER, W., et al. Energy dissipation of possible Titan lightning strokes. *Planetary and Space Science*. **2004**, 52(5-6), 447-458. ISSN 00320633. doi:10.1016/j.pss.2003.05.011
[29] FANTINO, E., M. GRASSI, P. PASOLINI, et al. The Small Mars System. *Acta Astronautica*. **2017**, 137, 168-181. DOI: 10.1016/j.actaastro.2017.04.024. ISSN 00945765.

[30] SHOLES, S., Megan, F., SMITH, L., et al. Anoxic atmospheres on Mars driven by volcanism: Implications for past environments and life. *Icarus*. **2017**, 290, 46-62. DOI: 10.1016/j.icarus.2017.02.022. ISSN 00191035.
[31] JAKOSKY, B.M., BRAIN, D. CHAFFIN, M., et al. Loss of the Martian atmosphere to space: Present-day loss rates determined from MAVEN observations and integrated loss through time. *Icarus*. **2018**, 315, 146-15. DOI: 10.1016/j.icarus.2018.05.030. ISSN 00191035.
[32] BELL, J., WOLFF, M. NASA: Hubble Takes Mars Portrait Near Close Approach. [online]. 12.5.2016 [cit. 2016-10-10]. Dostupné z :http://mars.nasa.gov/multimedia/images/?ImageID=7834
[33] RULL, F.M., VENERANDA, J.A., MANRIQUE-MARTINEZ, et al. Spectroscopic study of terrestrial analogues to support rover missions to Mars – A Raman-centred review. *Analytica Chimica Acta*. **2021**. ISSN 00032670. DOI:10.1016/j.aca.2021.339003
[34] MCFADDEN, L.A.A., WEISSMAN, P.R., JOHNSON, T. V. Encyclopedia of the solar system. 2nd ed. Amsterdam: Academic Press, **2007**. ISBN 978-0-12-088589-3.
[35] READ, W., Leslie, G., TAMPPARI, K. et al., Retrieval of wind, temperature, water vapor and other trace constituents in the Martian Atmosphere. Planetary and Space Science. **2018**, 161, 26-40. DOI: 10.1016/j.pss.2018.05.004. ISSN 00320633.
[36] GRANT, J., Matthew, A., GOLOMBEK, P., et al. The science process for selecting the landing site for the 2020 Mars rover. *Planetary and Space Science*. **2018**. DOI: 10.1016/j.pss.2018.07.001. ISSN 00320633.
[37] STEELE, L., Matthew, J., BALME, R., et al. The water cycle and regolith–atmosphere interaction at Gale crater, Mars. *Icarus*. **2017**, 289, 56-79. DOI: 10.1016/j.icarus.2017.02.010. ISSN 00191035
[38] HIGGS, P.G. Origin of Life, RNA World and. *Encyclopedia of Evolutionary Biology*. Elsevier, **2016**, s. 175-180. DOI: 10.1016/B978-0-12-800049-6.00164-5. ISBN 9780128004265.
[39] WAYNE, R. The Origin of Life. *Plant Cell Biology*. Elsevier, **2010**, 2010, s. 299-318. DOI: 10.1016/B978-0-12-374233-9.00018-0. ISBN 9780123742339.
[40] DI GIULIO, M. Biological evidence against the panspermia theory. *Journal of Theoretical Biology*. **2010**, 266(4), 569-572. DOI: 10.1016/j.jtbi.2010.07.017. ISSN 00225193.
[41] TEPFER, D. The origin of life, panspermia and a proposal to seed the Universe. *Plant Science*. **2008**, 175(6), 756-760. DOI: 10.1016/j.plantsci.2008.08.007. ISSN 01689452.
[42] PÉREZ-VILLA, A., PIETRUCCI, F., Marco SAITTA, A. Prebiotic chemistry and origins of life research with atomistic computer simulations. *Physics of Life Reviews*. **2018**. DOI: 10.1016/j.plrev.2018.09.004. ISSN 15710645.
[43] PERETÓ, J. Origin of Life, Theories of ☆. *Reference Module in Life Sciences*. Elsevier, **2017**. DOI: 10.1016/B978-0-12-809633-8.06845-X. ISBN 9780128096338.
[44] PARKER, E.T., CLEAVES J.H., BURTON A.S., et al. Conducting Miller-Urey Experiments. *Journal of Visualized Experiments*. **2014**, 83. DOI: 10.3791/51039. ISSN 1940-087X.

[45] MCCOLLOM, T.M. Miller-Urey and Beyond: What Have We Learned About Prebiotic Organic Synthesis Reactions in the Past 60 Years? *Annual Review of Earth and Planetary Sciences*. **2013**, 41(1), 207-229. DOI: 10.1146/annurev-earth-040610-133457. ISSN 0084-6597.
[46] CLEAVES, H. NEISH, J. C., CALLAHAN, M.P., et al. Amino acids generated from hydrated Titan tholins: Comparison with Miller–Urey electric discharge products. *Icarus*. **2014**, 237, 182-189. DOI: 10.1016/j.icarus.2014.04.042. ISSN 00191035.
[47] SANKARAN, N. How the discovery of ribozymes cast RNA in the roles of both chicken and egg in origin-of-life theories. *Studies in History and Philosophy of Science Part C: Studies in History and Philosophy of Biological and Biomedical Sciences*. **2012**, 43(4), 741-750. DOI: 10.1016/j.shpsc.2012.06.002. ISSN 13698486.
[48] JANDA, M., MACHALA, Z., Electrical discharges. *Encyclopedia of Physical Organic Chemistry.* First edition. **2017**. ISBN 978-1-118-46858-6.
[49] FDEZ-ARROYABE, P., KOURTIDIS, K., HALDOUPIS, Ch., et al. Glossary on atmospheric electricity and its effects on biology. *International Journal of Biometeorology*. **2021**, 65(1), 5-29. ISSN 0020-7128. DOI:10.1007/s00484-020-02013-9
[50] LAWRENCE, M.G., CHAMEIDES, W.L., KASIBHATLA, P.S., et al. *Handbook of Atmospheric Electrodynamics.* CRC Press, 1st edition, **1995**. eISBN 9780203719503
[51] GEORGIOU, A. Electrical Activity Inside Humans and Other Animals Is Eerily Similar to Electrical Fields in the Atmosphere. *Tech & Science.* **2020**. [online]. [cit. 28.11.2021]. Available at: https://www.newsweek.com/electrical-activity-inside-humans-other-animals-eerily-similar-electrical-fields-atmosphere-1502228
[52] HANEY, M.M., VAN EATON, A.R., LYONS, J.J., et al. Characteristics of thunder and electromagnetic pulses from volcanic lightning at Bogoslof volcano, Alaska. *Bulletin of Volcanology*. **2020**, 82(2). ISSN 0258-8900. DOI:10.1007/s00445-019-1349-y
[53] SMITH, C.M., GAUDIN, D., VAN EATON, A.R., et al. Impulsive Volcanic Plumes Generate Volcanic Lightning and Vent Discharges: A Statistical Analysis of Sakurajima Volcano in 2015. *Geophysical Research Letters*. **2021**, 48(11). ISSN 0094-8276. DOI:10.1029/2020GL092323
[54] BERMAN-VAPORIS, I., TREAT, J., VAN EATON, A. Volcanic Voltage. *National Geographic – Decoder.* [online]. **2021**. [cit. 2021-12-12]. Available in https://www.nationalgeographic.com/magazine/graphics/see-how-volcanoes-spark-lightning-storms
[55] CASTRO, J.M., KELLER, F., FEISEL, Y., et al. Lightning-induced weathering of Cascadian volcanic peaks. *Earth and Planetary Science Letters*. **2020**, 552. ISSN 0012821X. DOI:10.1016/j.epsl.2020.116595
[56] VAN EATON, A.R., AMIGO, Á., BERTIN, D., et al. Volcanic lightning and plume behavior reveal evolving hazards during the April 2015 eruption of Calbuco volcano, Chile. *Geophysical Research Letters*. **2016**, 43(7), 3563-3571. ISSN 0094-8276. DOI:10.1002/2016GL068076.

[57] SURKOV, V.V. and HAYAKAWA, M. Progress in the Study of Transient Luminous and Atmospheric Events: A Review. *Surveys in Geophysics*. **2020**, 41(5), 1101-1142. ISSN 0169-3298.DOI:10.1007/s10712-020-09597-2.
[58] BLANC, E. Space observations of Transient Luminous Events and associated emissions in the upper atmosphere above thunderstorm areas. *Comptes Rendus Geoscience*. **2010**, 342(4-5), 312-322. ISSN 16310713. DOI:10.1016/j.crte.2010.01.010
[59] DI MARTINO, M. and CARBOGNANI, A. *Observation of luminous transient phenomena on planetary bodies*. **2006**, s. 255-270. DOI:10.1142/9789812707192_0024.
[60] PLANKENSTEINER, K., REINER, H., SCHRANZ, B. Prebiotic Formation of Amino Acids in a Neutral Atmosphere by Electric Discharge. *Angewandte Chemie International Edition*. **2004**, 43(14), 1886-1888. DOI: 10.1002/anie.200353135. ISSN 1433-7851
[61] CLEAVES, H. J., CHALMERS, J. H., LAZCANO, A., et al. A Reassessment of Prebiotic Organic Synthesis in Neutral Planetary Atmospheres. *Origins of Life and Evolution of Biospheres*. **2008**, 38(2), 105-115. DOI: 10.1007/s11084-007-9120-3. ISSN 0169-6149.
[62] WANG, Z., ed. *Encyclopedia of Physical Organic Chemistry, 5 Volume Set*. Hoboken, NJ, USA: John Wiley & Sons, **2016**. DOI: 10.1002/9781118468586. ISBN 9781118470459.
[63] WATKINS, M. 404 - StoryLine. *Login to StoryLine* [online]. [cit. 25.04.2019]. Available at: https://upnorthlive.com/news/local/next-two-nights-provide-chance-to-catch-northern-lights
[64] LEE, H., SEKIGUCHI, H. Plasma–catalytic hybrid system using spouted bed with a gliding arc discharge: CH_4 reforming as a model reaction. *Journal of Physics D: Applied Physics*. **2011**, 44(27). DOI: 10.1088/0022-3727/44/27/274008. ISSN 0022-3727.
[65] EL-ARAGI, G.M. Gliding Arc Discharge (GAD) Experiment. IEEE Transactions on Plasma Science. **2016**, vol. 44, n. 7, p. 1155-1159. ISSN 1939-9375.
[66] TÖRÖKOVÁ, L. Studium chemických procesů v atmosféře Titanu iniciovaných výbojem v elektrodové konfiguraci klouzavého obloukového výboje. Brno: Vysoké učení technické v Brně, Fakulta chemická, **2015**. Vedoucí disertační práce doc. RNDr. František Krčma, Ph.D.
[67] PASLOW, S. The Eerie Saint Elmo's Fire – Mystic Sciences. *Mystic Sciences – Paranormal activity, ghosts and the supernatural* [online]. Copyright © **2019**. All Rights Reserved. [cit. 07.04.2019]. Available at: https://mysticsciences.com/2016/11/17/the-eerie-saint-elmos-fire/.
[68] ELLIS, A.M., MAYHEW, C. *Proton transfer reaction mass spectrometry: principles and applications*. Chichester, West Sussex: John Wiley & Sons, **2014**. ISBN 978-1-4051-7668-2.
[69] SEKIMOTO, K., LI, S.M., YUAN, B.U., KOSS, A. et al. Calculation of the sensitivity of proton-transfer-reaction mass spectrometry (PTR-MS) for organic trace gases using molecular properties. *International Journal of Mass Spectrometry*. **2017**, 421, 71-94. DOI: 10.1016/j.ijms.2017.04.006. ISSN 13873806.
[70] DUNNE, E., GALBALLY, I.E., LAWSON, S., et al. Interference in the PTR-MS measurement of acetonitrile at m/z 42 in polluted urban air—A study using switchable

reagent ion PTR-MS. *International Journal of Mass Spectrometry*. **2012**, 319-320, 40-47. DOI: 10.1016/j.ijms.2012.05.004. ISSN 13873806.
[71] MAJCHRZAK, T., WOJNOWSKI, W., LUBINSKA-SZCZYGEŁ, M., et al. PTR-MS and GC-MS as complementary techniques for analysis of volatiles: A tutorial review. *Analytica Chimica Acta*. **2018**, 1035, 1-13. DOI: 10.1016/j.aca.2018.06.056. ISSN 00032670.
[72] PAPURELLO, D., BOSCHETTI, A., SILVESTRI, S., et. Al. Real-time monitoring of removal of trace compounds with PTR-MS: Biochar experimental investigation. *Renewable Energy*. **2018**, 125, 344-355. DOI: 10.1016/j.renene.2018.02.122. ISSN 09601481.
[73] MANCUSO, S., TAITI, C., BAZIHIZINA, N., et al. Soil volatile analysis by proton transfer reaction-time of flight mass spectrometry (PTR-TOF-MS). *Applied Soil Ecology*. **2015**, 86, 182-191. DOI: 10.1016/j.apsoil.2014.10.018. ISSN 09291393.
[74] PANG, X. Biogenic volatile organic compound analyses by PTR-TOF-MS: Calibration, humidity effect and reduced electric field dependency. Journal of Environmental *Sciences*. **2015**, vol. 32, p. 196–206. ISSN 1001-0742.
[75] YOUSFI, M., N., MERBAHI, J. P., EICHWALD, O., et al. Non Thermal Plasma Sources of Production of Active Species for Biomedical Uses: Analyses, Optimization and Prospect. FAZEL, Reza, ed. *Biomedical Engineering - Frontiers and Challenges*. InTech, **2011**, 2011-08-01. DOI: 10.5772/19129. ISBN 978-953-307-309-5.
[76] SU, T. Theory of ion-polar molecule collisions. Comparison with experimental charge transfer reactions of rare gas ions to geometric isomers of difluorobenzene and dichloroethylene. *The Journal of Chemical Physics*. **1973**, 58(7). DOI: 10.1063/1.1679615. ISSN 00219606
[77] GOEBBERT, D.J., WENTHOLD, P.J. Water Dimer Proton Affinity from the Kinetic Method: Dissociation Energy of the Water Dimer. *European Journal of Mass Spectrometry*. **2017**, 10(6), 837-845. DOI: 10.1255/ejms.684. ISSN 1469-0667.
[78] UJIYAMA-NOVAK, J.H., GADDAM, C.K., DAS, D. et al. Detection of explosives by plasma optical emission spectroscopy. *Sensors and Actuators B: Chemical*. **2013**, 176, 985-993. DOI: 10.1016/j.snb.2012.08.063. ISSN 09254005.
[79] RAHMAN, M. M., BALKI, O., ELSAYED-ALI, H. Diagnostics of a spark-discharge coupled to laser aluminum plasma by optical emission spectroscopy and ion time-of-flight. *Optics & Laser Technology*. **2018**. DOI: 10.1016/j.optlastec.2018.09.013. ISSN 00303992.
[80] YUBERO, C., GARCÍA, M.C., VARO, M., et al. Gas temperature determination in microwave discharges at atmospheric pressure by using different Optical Emission Spectroscopy techniques. Spectrochimica Acta Part B: *Atomic Spectroscopy*. **2013**, 90, 61 - 67. DOI: 10.1016/j.sab.2013.10.004. ISSN 05848547.
[81] MAZÁNKOVÁ V. Spektroskopické studium dohasínajících výbojů v dusíku a jeho směsích. Brno: Vysoké učení technické, Fakulta chemická; **2009**.
[82] ZHANG, J.L., LIU, T.A., DENG, X. Rotational temperature of nitrogen glow discharge obtained by optical emission spectroscopy. *Spectrochimica Acta Part A: Molecular and Biomolecular Spectroscopy*. **2002**, 58(9), 1915-1922. DOI: 10.1016/S1386-1425(01)00658-8. ISSN 13861425.

[83] GRIEM, H.R. Principles of Plasma Spectroscopy Cambridge: Cambridge University Press, **1997**. ISBN 9780511524578.
[84] KRČMA F., SLAVÍČEK P.: *Optické metody diagnostiky plazmatu pro depozice tenkých vrstev za nízkého tlaku*. Zpravodaj České Vakuové Společnosti – Sborník Letní školy vakuové techniky, **2005**, roč. 13., č. 2, Malá Morávka 2005.
[85] GUERRA, V., P. A. SÁ a J. LOUREIRO. Kinetic modeling of low-pressure nitrogen discharges and post-discharges. *The European Physical Journal Applied Physics*. **2004**, 28(2), 125-152. ISSN 1286-0042. DOI: 10.1051/epjap:2004188.
[86] MD, B.; ZHANG, Z.T; BAI, X.Y; GAO H.H. Synthesis of ammonia using CH_4/N_2 plasmas based on micro-gap discharge under environmentally friendly condition. *Plasma Chemistry and Plasma Processing*. **2008** Aug;28(4):405-14.
[87] ZHAO, T.L., XU, Y., SONG, Y.H. et al. Determination of vibrational and rotational temperatures in a gliding arc discharge by using overlapped molecular emission spectra. *Journal of Physics D: Applied Physics*. **2013**, vol. 46, n. 34, 12 p. ISSN: 1361-6463.
[88] CHUDJÁK, S. Štúdium chemických procesov v atmosférach exoplanét. Brno: Vysoké učení technické v Brne, Fakulta chemická, **2017**. 68 s. Vedúci diplomovej práce doc. RNDr. František Krčma, Ph.D.
[89] CHUDJÁK, S., KOZÁKOVÁ, Z. and KRČMA, F. Study of Chemical Processes Initiated by Electrical Discharge in Titan-Related Atmosphere at Laboratory Temperature and Pressure. *ACS Earth and Space Chemistry*. **202**1. 5(3), 535-543. ISSN 2472-3452. Doi:10.1021/acsearthspacechem.0c00308
[90] HORVÁTH, G.; KRČMA, F.; POLÁCHOVÁ, L.; et al. Organic chemistry of NH_3 and HCN induced by an atmospheric abnormal glow discharge in N 2 -CH 4 mixtures. *The European Physical Journal Applied Physics*. **2011**, 53(1). ISSN 1286-0042. DOI:10.1051/epjap/2010100191
[91] RICARD, A.; ČERNOGORA, G.; FITAIRE, M.; et al. Measurements in N_2-CH_4(C_2H_2) discharges of reaction rates and thermochemical constants for Titan atmosphere study. *Planetary and Space Science*. **1995**, 43(1-2), 41-46. ISSN 00320633. DOI:10.1016/0032-0633(94)00162-K
[92] DAGAUT, P.; GLARBORG, P.; ALZUETA, M.U. The oxidation of hydrogen cyanide and related chemistry. *Progress in Energy and Combustion Science.* **2008**, vol. 34, p. 1–46. ISSN 0360-1285
[93] PINTASSILGO, C.D.; LOUREIRO, J.; ČERNOGORA, G.; TOUZEAU, M. Methane decomposition and active nitrogen in a N_2-CH_4 glow discharge at low pressures. *Plasma Sources Science and Technology*. **1999**, 8(3), 463-478. ISSN 0963-0252. DOI:10.1088/0963-0252/8/3/317
[94] COLL, P.; COSCIA, D.; GAZEAU, M.C.; et al. Organic chemistry in Titan's Atmosphere: new data from laboratory simulations at low temperature. *Advances in Space Research.* **1995.** vol. 16 (2), p. 93-103. ISSN 0273-1177. DOI:10.1016/0273-1177(95)00197-M

[95] BERNARD, J.-M., P. COLL, A. COUSTENIS A F. RAULIN. Experimental simulation of Titan's atmosphere: Detection of ammonia and ethylene oxide. *Planetary and Space Science*. **2003**, 51(14-15), 1003-1011. ISSN 00320633. DOI:10.1016/j.pss.2003.05.009
[96] PENG, Z.; GAUTIER, T.; CARRASCO, N.; et al. Titan's atmosphere simulation experiment using continuum UV-VUV synchrotron radiation. *Journal of Geophysical Research*: Planets. **2013**, 118(4), 778-788. ISSN 21699097. DOI:10.1002/jgre.20064
[97] CARRASCO, N.; GAUTIER, T.; ES-SEBBAR, E.T.; et al. Volatile products controlling Titan's tholins production. Icarus. **2012**, 219(1), 230-240. ISSN 00191035. DOI:10.1016/j.icarus.2012.02.034
[98] SAGAN, C.; THOMPSON, W.R. Production and condensation of organic gases in the atmosphere of Titan. *Icarus*. **1984**, 59(2), 133-161. ISSN 00191035. DOI:10.1016/0019-1035(84)90018-6
[99] COUSTENIS, A.; JENNINGS, D.E.; NIXON, C.A.; et al. Titan trace gaseous composition from CIRS at the end of the Cassini–Huygens prime mission. *Icarus*. **2010**, 207(1), 461-476. ISSN 00191035. DOI:10.1016/j.icarus.**2009**.11.027.
[100] TRIGO-RODRIGUEZ, J.M.; RAULIN, F.; MULLER, CH.; et al. *The Early Evolution of the Atmospheres of Terrestrial Planets*. New York, NY: Springer New York, **2013**. Astrophysics and Space Science Proceedings. ISBN 978-1-4614-5190-7. DOI:10.1007/978-1-4614-5191-4.
[101] CABLE, M.L.; HÖRST, S.M.; STOCKTON, A.M.; et al. Identification of primary amines in Titan tholins using microchip nonaqueous capillary electrophoresis. *Earth and Planetary Science Letters*. **2014**, 403, 99-107. ISSN 0012821X. DOI:10.1016/j.epsl.2014.06.028.
[102] WILLACY, K.; ALLEN, M.; YUNG, A.Y. A New Astrobiological Model Of The Atmosphere Of Titan. *The Astrophysical Journal*. **2016**, 829(2). ISSN 1538-4357. DOI:10.3847/0004-637X/829/2/79.
[103] DEMARAIS, N.; ZHIBO YANG, J,Z.; SNOW, T.P.; BIERBAUM, V.M. Chemistry of $HCNH^+$: mechanisms, structures, and relevance to Titan's atmosphere. *Structural Chemistry*. **2013**, 24(6), 1957-1963. ISSN 1040-0400. DOI:10.1007/s11224-013-0275-4.
[104] THELEN, A.E.; CORDINER, M.A.; NIXON, C.A.; et al. Detection of CH_3C_3N in Titan's Atmosphere. *The Astrophysical Journal*. **2020**, 903(1). ISSN 2041-8213. DOI:10.3847/2041-8213/abc1e1.
[105] TRAN, B.N.; JOSEPH, J.C.; FORCE, M.; et a. Photochemical processes on Titan: Irradiation of mixtures of gases that simulate Titan's atmosphere. *Icarus*. **2005**, 177(1), 106-115. ISSN 00191035. DOI:10.1016/j.icarus.2005.03.015.
[106] POCH, O.; COLL, P.; BUCH, A.; et al. Production yields of organics of astrobiological interest from H_2O–NH_3 hydrolysis of Titan's tholins. *Planetary and Space Science*. **2012**, 61(1), 114-123. ISSN 00320633. DOI:10.1016/j.pss.2011.04.009.
[107] GAUTIER, T.; CARRASCO, N.; BUCH, A.; et al. Nitrile gas chemistry in Titan's atmosphere. *Icarus*. **2011**, 213(2), 625-635. ISSN 00191035. DOI:10.1016/j.icarus.2011.04.005

[108] BERRY, J.L.; UGELOW, M.S.; TOLBERT, M.A.; BROWNE, E.C. Chemical Composition of Gas-Phase Positive Ions during Laboratory Simulations of Titan's Haze Formation. *ACS Earth and Space Chemistry*. **2019**, 3(2), 202-211. ISSN 2472-3452. DOI:10.1021/acsearthspacechem.8b00139.
[109] HE, CH.; SMITH, M.A. Identification of nitrogenous organic species in Titan aerosols analogs: Nitrogen fixation routes in early atmospheres. *Icarus*. **2013**, 226(1), 33-40. ISSN 00191035. DOI:10.1016/j.icarus.2013.05.013.
[110] TOROKOVÁ, L.; WATSON, J.; KRČMA, F.; et al. Gas Chromatography Analysis of Discharge Products in N 2 -CH 4 Gas Mixture at Atmospheric Pressure: Study of Mimic Titan's Atmosphere. *Contributions to Plasma Physics*. **2015**, 55(6), 470-480. ISSN 08631042. DOI:10.1002/ctpp.201400052
[111] HENDRIX, A.R, YUNG, Y.L. Energy Options for Future Humans on Titan. *Journal of Astrobiology & Outreach*. **2017**, 05(02). DOI: 10.4172/2332-2519.1000157. ISSN 23322519.
[112] WAITE, H. The process of tholin formation in Titan's upper atmosphere. *Science*. **2007**, vol. 316, n. 5826, p. 870-875. ISSN 1095-9203.
[113] LEGRAND, J-C.; DIAMY, A.M.;HRACH, R.;HRACHOVÁ, V. Kinetics of reactions in CH_4-N_2 afterglow plasma: a simplified model. *Vacuum*. **1998**, 50(3-4), 491-495. ISSN 0042207X. DOI:10.1016/S0042-207X(98)00085-2
[114] MARTIN F., KUBELÍK P., KNÍŽEK, A., et al. High Energy Radical Chemistry Formation of HCN-rich Atmospheres on early Earth. *Scientific Reports.* **2017**. **7**(6275), 1-9. DOI:10.1038/s41598-017-06489-1. ISSN 2045-2322.
[115] LOISON, J.C.; HÉBRARD, E.; DOBRIJEVIC, M.; et al. The neutral photochemistry of nitriles, amines and imines in the atmosphere of Titan. *Icarus*. **2015**, 247, 218-247. ISSN 00191035. DOI:10.1016/j.icarus.2014.09.039
[116] LEGRAND, J.C; DIAMY, A.M.; HRACH, R.; HRACHOVÁ, V. Methane Conversion in the Flowing Afterglow of a Dinitrogen Microwave Plasma: Initiation of the Reaction. *Contributions to Plasma Physics*. **1997**, 37(6), 521-537. ISSN 08631042. DOI:10.1002/ctpp.2150370606
[117] LAPTHORN C., PULLEN F., CHOWDHRY B. Z.: Ion mobility spectrometry-mass spectrometry (IMS-MS) of small molecules: Separating and assigning structures to ions. *Journal of Mass Spectrometry*. **2013**. Rev. 1, 43-71. ISSN: 1096-9888.
[118] EICEMAN G., KARPAS Z.: *Ion Mobility Spectrometry*. 2nd Edn., CRC, Boca Raton **2005**, pp. 3-7. ISBN 0-8493-2247-2.
[119] KANU, A. B., DWIVEDI, P., TAM, M. et al. Ion mobility-mass spectrometry. *Journal of Mass Spectrometry*. **2008**, 43(1), 1-22. ISSN 10765174. doi:10.1002/jms.1383
[120] BORSDORF, H. and EICEMAN, G.A. Ion Mobility Spectrometry: Principles and Applications. *Applied Spectroscopy Reviews*. **2006**, 41(4), 323-375. ISSN 0570-4928. doi:10.1080/05704920600663469.
[121] KAFLE, G.K., KHOT, L.R., SANKARAN, S. et al. State of ion mobility spectrometry and applications in agriculture: A review. *Engineering in Agriculture, Environment and Food*. **2016**, 9(4), 346-357. ISSN 18818366. DOI:10.1016/j.eaef.2016.05.004.

[122] KAFLE, G.K., KHOT, L.R., SANKARAN, S., et al. State of ion mobility spectrometry and applications in agriculture: A review. *Engineering in Agriculture, Environment and Food*. **2016**, **9**(4), 346-357. ISSN 18818366. DOI:10.1016/j.eaef.2016.05.004
[123] GABELICA, V. and MARKLUND, E. Fundamentals of ion mobility spectrometry. *Current Opinion in Chemical Biology*. **2018**, 42, 51-59. ISSN 13675931. doi:10.1016/j.cbpa.2017.10.022
[124] D'ATRI, V., CAUSON, T., HERNANDEZ-ALBA, O., et al. Adding a new separation dimension to MS and LC-MS: What is the utility of ion mobility spectrometry? *Journal of Separation Science*. **2018**, 41(1), 20-67. ISSN 16159306. doi:10.1002/jssc.201700919
[125] BOWMAN, A.P., ABZALIMOV, R.R., SHVARTSBURG, A.A. Broad Separation of Isomeric Lipids by High-Resolution Differential Ion Mobility Spectrometry with Tandem Mass Spectrometry. *Journal of the American Society for Mass Spectrometry*. **2017**, *28* (8), 1552-1561. DOI: 10.1021/jasms.8b05620
[126] WOODFIN R. L.: Ion Mobility Spectrometry. In Trace Chemical Sensing of Explosive, Ed. Woodfin R. L., Wiley, Hoboken **2007**, pp. 211-218.
[127] MICHALCZUK, B., MORAVSKÝ, L., PAPP, P. et al. Isomer and conformer selective atmospheric pressure chemical ionisation of dimethyl phthalate. *Physical Chemistry Chemical Physics*. **2019**, 21(25), 13679-13685. ISSN 1463-9076. doi:10.1039/C9CP02069A
[128] MICHALCZUK, B., SABO, M., JATZOVÁ, K., et al. Fast quantification of whisky lactone in oak wood by ion mobility spectrometer. *Talanta*. **2020**, 209. ISSN 00399140. doi:10.1016/j.talanta.2019.120567
[129] MICHALCZUK, B.; MORAVSKÝ, L.; HRDÁ, J.; MATEJČÍK, Š. Atmospheric Pressure Chemical Ionisation study of selected Volatile Organic Compounds (VOCs) by Ion Mobility Spectrometry coupled with orthogonal acceleration Time Of Flight Mass Spectrometry. *International Journal of Mass Spectrometry*. **2020**, 449. ISSN 13873806. DOI:10.1016/j.ijms.2019.116275
[130] BACSIK, Z., MINK, J., KERESZTURY, G. FTIR Spectroscopy of the Atmosphere. I. Principles and Methods. *Applied Spectroscopy Reviews*. **2004**, 39(3), 295-363. ISSN 0570-4928. doi:10.1081/ASR-200030192
[131] SAWANT, S.V. FT-IR spectroscopy: principle, technique and mathematics. *Pharmaceutical analysis* **2011**, **2** (1), 513-519. ISSN 0975-6299.
[132] Doyle, W.. "Principles and Applications of Fourier Transform Infra-red (FTIR) Process Analysis." (**2017**).
[133] THEULÉ, P., ENDRES, C., HERMANNS, M. et al. High-Resolution Gas Phase Spectroscopy of Molecules Desorbed from an Ice Surface: A Proof-of-Principle Study. *ACS Earth and Space Chemistry*. **2020**, 4(1), 86-91. ISSN 2472-3452. doi:10.1021/acsearthspacechem.9b00246
[134] OLAWUMi, T. Ultra-low k dielectrics and plasma damage control for advanced technology nodes (10nm and below). **2015**. doi:10.13140/RG.2.1.1815.1849.
[135] LEE, B. J., LEE, J. I. A study on the determination method of Global Warming Potential (GWP) by measuring the experiment-based infrared absorption spectra and the

reactivity of the hydroxyl radical. 22nd EGU General Assembly, held online 4-8 May, **2020**, id.2310. DOI: 10.5194/egusphere-egu2020-2310
[136] MAILLARD, J., HUPIN, S., CARRASCO, N. et al. Structural elucidation of soluble organic matter: Application to Titan's haze. *Icarus*. **2020**, 340. ISSN 00191035. doi:10.1016/j.icarus.2020.113627
[137] WHITE, R. Chromatography/Fourier Transform Infrared Spectroscopy and its applications. CRC Press Taylor and Francis, **1990**. ISBN 13:978-0-8247-8191-0.
[138] FEI, P., LIAO, L., CHENG, B., SONG, J. Quantitative analysis of cellulose acetate with a high degree of substitution by FTIR and its application. *Analytical Methods.* **2017**, 9(43), 6194-6201. ISSN 1759-9660. doi:10.1039/C7AY02165H
[139] LOPES, C.A., LIMIRIO, P.H.J.O., NOVAIS, V.R., DECHICHI, P. Fourier transform infrared spectroscopy (FTIR) application chemical characterization of enamel, dentin and bone. *Applied Spectroscopy Reviews*. **2018**, 53(9), 747-769. ISSN 0570-4928. doi:10.1080/05704928.2018.1431923
[140] BELÉN, M., CARRASCO-HERRERA, R., TIMÓN, V., et al. 2-aminooxazole in astrophysical environments: IR spectra and destruction cross sections for energetic processing. *Chemical Physics* [online]. **2021.** [cit. 2021-02-27]. Available in https://arxiv.org/abs/2101.06164v1.
[141] NIST. [online]. [cit. 2021-10-02-12]. Available in https://webbook.nist.gov/chemistry/.
[142] NIST. [online]. [cit. 2022-03-06]. Available in https://webbook.nist.gov/cgi/cbook.cgi?ID=C74828&Type=IR-SPEC&Index=1.
[143] FOJTÍKOVÁ, N. Diagnostika plazmatu generovaného v atmosféře simulující podmínky na Marsu [online]. Brno, **2021**. Dostupné z: https://www.vutbr.cz/studenti/zav-prace/detail/131265. Diplomová práce. Vysoké učení technické v Brně, Fakulta chemická, Ústav fyzikální a spotřební chemie. Vedoucí práce doc. Ing. Zdenka Kozáková, Ph.D.

6. PUBLICATIONS

Papers in journals

TOMAN, J.; JAŠEK, O.; SNIRER, M.; PAVLIŇÁK, D.; NAVRÁTIL, Z.; JURMANOVÁ, J.; CHUDJÁK, S.; KRČMA, F.; KUDRLE, V. ; MICHALIČKA, J. On the Transition of Reaction Pathway during Microwave Plasma Gas-Phase Synthesis of Graphene Nanosheets: From Amorphous to Highly Crystalline Structure. *Plasma Processes and Polymers,* 2021, vol. 18, no. 8, p. 202100008-202100008. ISSN: 1612-8850., citted 4x.

ADÁMKOVÁ, B.; KRČMA, F.; CHUDJÁK, S.; KOZÁKOVÁ, Z. Pinhole Discharge Decomposition of Ethanol. *Journal of Applied Physics,* 2021, vol. 129, no. 14, p. 143304-1 (143304-8 p.) ISSN: 0021-8979.

CHUDJÁK, S.; KOZÁKOVÁ, Z.; KRČMA, F. Study of Chemical Processes Initiated by Electrical Discharge in Titan-Related Atmosphere at Laboratory Temperature and Pressure. *ACS EARTH AND SPACE CHEMISTRY,* 2021, vol. 5, no. 3, p. 535-543. ISSN: 2472-3452.

Full text conference contributions

KRČMA, F.; CHUDJÁK, S. ČERVENKA, A. *Synthesis of chemical compounds in the gaseous mixture related to Titan atmosphere by glow discharge at the relevant temperature and pressure.* Bologna: 2019. p. P1-46-1 (P1-46-4 p.)

KRČMA, F.; CHUDJÁK, S. The Role of Oxygen and Carbon dioxide on Discharge Initiated Chemistry in Titan Related Atmosphere at Relevant Temperatures. In *22nd Symposium on Application of Plasma Processes and 11th EU-Japan Joint Symposium on Plasma Processing, Book of Contributed Papers.* Bratislava: 2019. p. 338-342. ISBN: 978-80-8147-089-9.

CHUDJÁK, S.; KRČMA, F. Formation of Life Precursor Molecules in Titatn Related Atmosphere at Relevant Temperature and Pressure. In *22nd Symposium on Application of Plasma Processes and 11th EU-Japan Joint Symposium on Plasma Processing, Book of Contributed Papers.* Bratislava: 2019. p. 126-130. ISBN: 978-80-8147-089-9.

Conference abstracts

KRČMA, F.; CHUDJÁK, S. *Glow discharge formation of high molecular products in prebiotic atmospheres: PTR-TOF analyzis.* 13th Frontiers in Low Temperature Plasma Diagnostics and 1st Frontiers in Low Temperature Plasma Simulations, Book of Abstracts. Bochum: 2019. p. 18-18.

KRČMA, F.; CHUDJÁK, S. *Formation of high molecular weight products by glow discharge in Titan like gaseous mixture at cryogenic temperatures.* Proceedings of ESCAMPIG XXIV. Glasgow: Glasgow University, 2018. p. 351-352.

KRČMA, F.; CHUDJÁK, S.; MAZÁNKOVÁ, V.; TÖRÖKOVÁ, L.; TRUNEC, D.; MATEJČÍK, Š; MASON, N. *Chemical processes initiated by electrical discharges as laboratory mimics on non-terrestrial atmospheric processes.* IWSSPP 2018 - Book of Abstracts. Sofia: Sofia University, 2018. p. 11-11.

KRČMA, F.; CHUDJÁK, S. *Laboratory mimics of discharge initiated processes in Titan and Mars atmospheres.* Life on Earth and beyond: Emergence, survavibility, and impact on the environment - Book of abstracts. Bertinoro: Bologna University, 2018. p. 1 (1 s.).

KRČMA, F.; CHUDJÁK, S.; MAZÁNKOVÁ, V.; TÖRÖKOVÁ, L.; BLAHOVÁ, L. *PTR-TOF analyzes of stable gaseous discharge products in nitrogen-methane mixtures.* XXII FSO - Book of Abstracts. Brno: 2017.

CHUDJÁK, S.; KRČMA, F.; MAZÁNKOVÁ, V. *PTR-TOF analyzis of glow discharge products in Titan related atmosphere.* ICPIG XXXIII - Book of Abstracts. Lisbon: Univeristy of Lisbon, 2017. p. 362-362.

KRČMA, F.; TÖRÖKOVÁ, L.; MAZÁNKOVÁ, V.; CHUDJÁK, S. *Application of PTR-MS for determination of compounds formed in Titan like gaseous mixtures by electrical discharges.* Early Earth and ExoEarths: origin and evolution of life - Book of Abstracts. Warszawa: 2017. p. 49-49.

7. SUPPLEMENTARY MATERIAL

CHUDJÁK, S.; KOZÁKOVÁ, Z.; KRČMA, F. Study of Chemical Processes Initiated by Electrical Discharge in Titan-Related Atmosphere at Laboratory Temperature and Pressure. *ACS EARTH AND SPACE CHEMISTRY,* 2021, vol. 5, no. 3, p. 535-543. ISSN: 2472-3452.

ACS EARTH AND SPACE CHEMISTRY

http://pubs.acs.org/journal/aesccq

Article

Study of Chemical Processes Initiated by Electrical Discharge in Titan-Related Atmosphere at Laboratory Temperature and Pressure

Stanislav Chudják,* Zdenka Kozáková, and František Krčma*

Cite This: *ACS Earth Space Chem.* 2021, 5, 535−543

Read Online

ACCESS | Metrics & More | Article Recommendations | Supporting Information

ABSTRACT: The chemical processes initiated by electrical discharges in prebiotic atmospheres became a hot topic during the past decade due to the recent extensive discovery of exoplanets. The biggest atmospheric data collection is currently available about the atmosphere of the Saturn's moon Titan that is composed mainly of nitrogen and methane at low surface temperature of about 95 K and pressure of about 1.5 atm. The present work deals with the laboratory simulation of the chemical processes initiated by the electrical discharge in the gaseous mixture related to the Titan atmosphere under laboratory conditions. The ongoing chemical processes, the resulting stable products, and their transformation into more complex substances were studied by the in situ mass spectrometry with proton ionization (PTR-MS) of the exhausting gas. The presence of many aliphatic and some aromatic hydrocarbons was confirmed as well as many amino and cyano compounds. The increasing concentration of methane has produced more substances with higher molecular weight and less simple substances that were consumed in the formation of more complex substances.

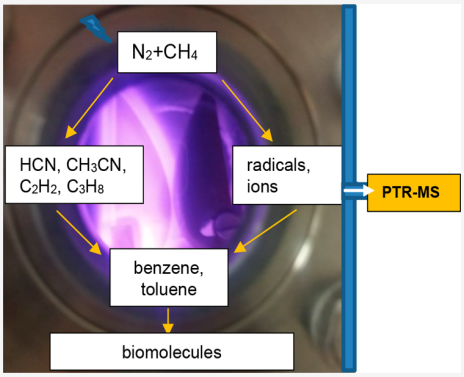

KEYWORDS: *Titan moon, life precursors, proton transfer reaction time-of-flight mass spectrometry, exoplanetary atmospheres, electrical discharge*

1. INTRODUCTION

The research of life origins may be as long as the human civilization. In general, the first step in the life creation is the formation of complex organic molecules from inorganic mixtures. These mixtures are known as prebiotic atmospheres in the gaseous phase.[1] The exact compositions of such atmospheres are still under broad discussion.[1−4] The chemical synthetic processes can be initiated by various agents like cosmic radiation,[5,6] volcanism,[7] or atmospheric electric phenomena (St. Elmo's fire, lightning, etc.).[8−10]

Besides numerous studies of the life formation on the early Earth,[11−14] a couple of investigations showed the presence of the prebiotic atmosphere at other bodies in the Solar system.[15−18] During the past decade, the main attention was attracted to Saturn's moon Titan. Interesting results of the long-term investigations from the Earth led to the development of a successful interplanetary space mission at the beginning of this millennium.[19,20]

The Cassini-Huygens space mission brought a huge number of data from the in situ detailed observations that greatly extended data obtained by the Earth techniques.[21,22] The main contemporary interest is focused on the search of life traces or life molecular precursors and consequently discovering the possible pathways leading to the life origin's formation. Titan's atmosphere is so interesting because it seems to be, by some studies, very similar to Earth's before the origin of life[23,24] and there are a lot of in situ available data, too. The atmosphere of Saturn's moon Titan contains two main components: molecular nitrogen and methane. Nitrogen forms up to about 95% of the atmosphere and the amount of methane increases with the decreasing distance from the troposphere toward Titan's surface. Even though the methane content is low, it is enough to keep nitrogen in the gaseous phase so that nitrogen does not condense in the stratosphere and troposphere.[24,25] Besides nitrogen and methane, Titan's lower atmosphere contains a huge number of other hydrocarbons (such as ethane, etc.) and various simple cyano molecules (like hydrogen cyanide, acetonitrile, etc). Moreover, traces of the simplest space molecules such as carbon monoxide and hydrogen were confirmed.[23,24] Titan's atmosphere is also highly abundant in hydrogen.[25] More complex hydrocarbons arise from the small molecules in the upper atmosphere and then descend into the lower layers where methane condenses. Here, they can become part of the haze and coagulate further down forming the rainfall composed of hydrocarbons. It is assumed that this rain, which is

Received: November 10, 2020
Revised: February 3, 2021
Accepted: February 3, 2021
Published: February 15, 2021

predominantly methane and possibly ethane, creates lakes on Titan. Thus, the methane cycle on Titan is similar to the cycle of water on Earth.[25−27] However, due to Titan's low temperature (about 95 K at the surface), most of its water is presented as ice in the crust and mantle, acting similarly to the bedrock on Earth. Titan's atmosphere is of particular interest because of a small planetary mass with a surface pressure 1.5 times higher than on Earth but with an inferred loss rate due to its lower gravity.[28−30]

Observations of the Cassini mission demonstrated the dominance of the solar energy input in the dayglow measurements but also revealed emissions from Titan's night side for the first-time that are driven by energetic particles originating from Saturn's magnetosphere.[22,23,31,32] The emission spectrum of excited nitrogen demonstrates multiple bands originating at many excited electronic states available and covers a large part of the electromagnetic spectrum. The collisional de-excitation of the N_2 states also contributes to the atmospheric local heating.[23,33,34]

The atmospheric processes initiated by UV and VUV radiation and particles fluxes coming from the space are dominant in the upper atmosphere only because of the dense haze presence.[22] It is assumed that the electrical discharge phenomena can play an important role in the atmospheric chemistry at lower altitudes.[26] Lightning, whcih is well-known in Earth's atmosphere, was confirmed in more planetary atmospheres.[21,27,28,35] While the occurrence of lightning on Venus is still a controversial question,[36,37] there is clear evidence of lightning in the atmospheres of the gas giants like Jupiter, Saturn,[38] and Uranus.[39−41] Lightning is also believed to take place at Neptune.[39,42] Moreover, it was pointed out very recently that the lightning activity in Jupiter's[38] atmosphere is significantly higher than was expected, and thus the same situation can be also assumed in other atmospheres.[43] Besides the classical lightning phenomena, transient lightning events like sprites, jets, and elves were recently also confirmed in the atmospheres of Venus, Mars,[44] and Jupiter.[45]

Although lightning was not observed by cameras or by radio instruments during Cassini's observations or during the descent of the Huygens probe, the atmospheric chemistry suggests the presence of electrical discharges in the atmosphere of Titan.[22,46,47] A problem is that currently it is possible to detect only the strong lightning as it is known from the Earth (by electromagnetic impulses) and weaker discharges with lower energies (like the St. Elmo's fire) are under detection limits. Inception of streamers in Titan's atmosphere strongly depends on the ambient electric field which is still uncertain since it is only provided by models, but not by the direct measurements. In general, the important role of ionic chemistry is known and broadly studied.[48,49] In addition to the ions generated by the discharge,[50] of course, the ions formed by the radiation[51] from the Universe, mainly at the upper atmosphere, are important or even dominant. This means that even if no discharge is presented as it is known, the ions would be existing anyway.[29,33,35]

The planetary scale chemical processes initiated by electrical discharge can be simulated by laboratory experiments using various discharges: corona and DBD conditions are similar to the St. Elmo's fire, spark and arc discharges are related to the lightning, and corona and glow discharge conditions are similar to the conditions in the aurora borealis.[28,34] Up to now, nearly all laboratory studies of Titan's atmosphere and the discharge initiated processes have been carried out at ambient temperature and pressure that were not fully reflecting Titan's real surface conditions.[27,50] The optical emission spectroscopy was broadly used for the determination of atomic and diatomic radiating species[51−53] to obtain the insight into molecular dissociation and formation of the simplest molecules like the CN radical.[54,55] A couple of laboratory studies were devoted to optical emission spectroscopic measurements of DC flowing plasmas in Pyrex/Quartz tubes or stainless steel reactors[56] at pressures of about 1 kPa. The detailed numeric models describing formation of simple species like CN were designed and compared with the experimental data.[57] Unfortunately, the validity of these models for atmospheric pressure has not been completed yet.

The analyses of the discharge exhaust gas were carried out by FTIR and by GC-MS.[58−60] The in situ mass spectroscopy was applied to determine various species at the low pressure RF discharge conditions.[61] But all of these techniques have some limits, mainly their fast detection capability of a broad spectrum of discharge products.

The general aim of the presented study is to demonstrate the applicability of a new complex in situ analytical diagnostic technique, proton transfer reaction time-of-flight mass spectrometry (PTR-TOF MS). To be able to compare results with other laboratory studies, the determination of stable products of the glow discharge generated in Titan-like atmosphere (nitrogen−methane mixtures with selected traces) at the laboratory temperature and atmospheric pressure was carried out. However, the whole system also allows the use of different discharge configurations as well as operation at various pressures and temperatures.

The PTR-MS is commonly applied for the real-time, online measurements of atmospheric VOCs[62−64] or breath analysis in medicine[62,65,66] with a high sensitivity and fast time response and has overcome some of the disadvantages of traditional methodologies with low time resolution. Furthermore, recently available PTR-MS instruments that use time-of-flight (TOF) mass analysers with high mass resolution facilitate the separation of nominally isobaric species which increases the number of measurable atmospheric VOCs (>100 species) and reduces possible chemical interferences.[62,67,68]

In principle, PTR-MS allows the simultaneous detection of all compounds with proton affinity higher than proton affinity of water molecules.[62] Thus, it is not sensitive to any of the reaction mixture gases used in the present study (N_2, CH_4, CO_2, NO, H_2), because their proton affinity is smaller than the proton affinity of water. Unfortunately, it is impossible to distinguish isomers.[69−71] Thus, PTR-MS seems to be a good tool for the in situ determination of stable discharge products.

2. EXPERIMENTAL SETUP

A special stainless steel vacuum reactor with an inner diameter of 50 mm was designed for the experimental simulation of Titan's atmosphere. Although the reactor was designed to be used for several types of electric discharges, an electrode arrangement for the abnormal atmospheric pressure glow discharge[72] with a pair of stainless steel electrodes in the shape of a raindrop with the distance of 1−2 mm was used in all experiments. The discharge was located directly between the electrodes and its volume was of about 1 mm^3. The electrode area directly affected by the discharge channel was about 1 mm^2. The distance of the discharge from the reactor walls was about 25 mm, so the surface processes play a role at small electrode spots, only. This is contrary to some other experiments[57,73,74] where plasma was in direct contact with surfaces and thus heterogeneous processes were more important. The plasma in our reactor was weakly

https://dx.doi.org/10.1021/acsearthspacechem.0c00308
ACS Earth Space Chem. 2021, 5, 535−543

ionized, and it was characterized by a lack of local thermodynamic equilibrium because the mean electron energy of about 11 600 K was significantly higher than the temperature of neutral gas (characterized by the rotational temperature of 2100 K).[72]

The experiment was carried out in the flowing regime at laboratory temperature and atmospheric pressure. The discharge was operating at the constant current of I = 25 mA (corresponding power was 10 W). This power was selected based on the preliminary experiments. It supplied sufficient energy without significant heating of the whole system (reactor wall temperature during the discharge operation was below 40 °C). The gas mixture composition of nitrogen and methane was controlled by the Bronkhorst mass flow controllers wherein the total gas mixture flow rate into the reactor was 200−204 sccm. The specific composition of the individual gas mixtures used in the experiments is shown in Table 1.

Table 1. Composition of the Individual Gas Mixtures

mixture	CH_4 (sccm)	N_2 (sccm)	CH_4 (%)
1	0.2	200	0.1
2	0.5	200	0.3
3	0.8	200	0.4
4	1.0	200	0.5
5	1.3	200	0.7
6	1.6	200	0.8
7	2.0	200	1.0
8	2.5	200	1.3
9	3.0	200	1.5
10	3.5	200	1.8
11	4.0	200	2.0

To minimize the presence of other gases in the reactor it was necessary to prevacuate the reactor before each experiment by using a rotary oil pump and simultaneously control the sealing of the reactor for 60 min. Since the gas flow velocity through the inlet/outlet tubes was only 28 cm·s^{-1}, the outlet tube was constructed to eliminate a possible back-diffusion of air into the reactor. Once the gas mixture flow has started, the reactor was purged by the working gaseous mixture for 45 min to achieve the stable and correct pressure. Just after this time, the discharge was ignited by the increasing voltage. The discharge itself was ignited when the voltage was applied to the electrodes in the range of 5−5.5 kV, and immediately after the discharge ignition the voltage dropped rapidly to 0.4−0.5 kV. The experiment was completed following the scheme in Figure 1.

The used gases were of the following purities: nitrogen, 99.999%, and methane, 99.95%. The whole line (made of PTFE, stainless steel and PEEK) to the PTR-TOF mass spectrometer was heated up to 80 °C to avoid discharge product condensation.

The reactor was not opened or cleaned between experiments, so some contamination (mainly by some deposited material on the electrode surfaces) was possible. To eliminate this contamination effect, experiments started in pure nitrogen, and methane concentration was increased from experiment to experiment.

A direct connection from the reactor outlet to the PTR-MS was used for the transfer of gaseous products created by chemical reactions initiated by the discharge. Because of the high sensitivity of the equipment, it was necessary to dilute the flow of the discharge gaseous products by 1000 sccm of nitrogen (purity

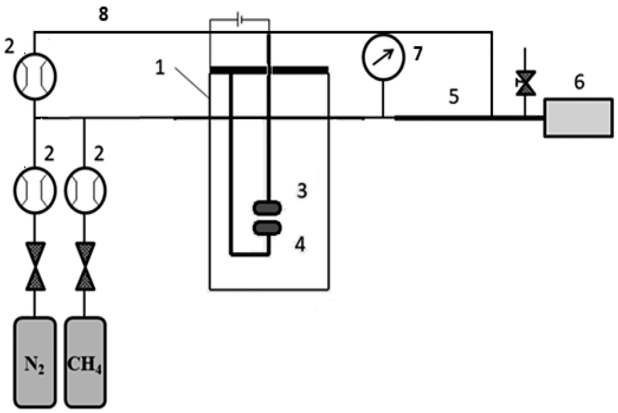

Figure 1. Scheme of the experimental set up: 1, stainless steel reactor vessel; 2, mass flow controller; 3, cathode; 4, anode; 5, heated exhaust gas sampling line; 6, proton transfer reaction time-of-flight mass spectrometer; 7, membrane pressure gauge; 8, heated diluting inlet

of 99.999%) before the PTR-TOF inlet to avoid the saturation limit as much as possible and to improve the quality of the analysis itself.

Ongoing chemical processes, emerging products and their transformation into more complex substances were studied by the in situ proton-transfer-reaction time-of-flight mass spectrometry (PTR-TOF-MS).[62] The scheme of the device is shown in Figure 2.

3. RESULTS

All measurements were carried out at atmospheric pressure and at laboratory temperature. The discharge current was kept at 25 mA during all measurements. Thus, the conditions of the individual measurements differed only in the composition of the gaseous mixture entering the reactor from 0.1 to 2.0% of methane in nitrogen at the total mixture flow of 200 sccm. Figures 3, 4, and 5 show the spectra at a methane concentration of 0.3, 1.0, and 2.0%. All spectra are subtracted from the background and they are already corrected by −1 to get their real molecular weight (not protonated as measured by the device). The dependence on the methane flow shows how the quantity and the ratio of the products are developed, and the formation of new higher molecular weight substances is clearly demonstrated. The Supporting Information also shows spectra for the other flows of methane that confirm a similar trend.

The presented spectra demonstrate the expected fact that the total intensity of the detected products increases with the increasing CH_4 flow. This trend is most apparent for substances with the molecular weight higher than 75 amu. Significant differences in the intensity are very visible, for example, in the case of benzene (C_6H_6) having the molecular weight of 78 amu. Substances with the molecular weight over 100 amu have intensities close to the noise level at low flows of methane, and their intensities increase very rapidly (almost exponentially, see later) at the higher methane concentrations from 1.3 to 2%.

Figures 6, 7, 8, and 9 show the mass spectrum at the methane concentration of 1.5%. The spectrum is divided into four parts for a better graphical representation of the detected gaseous products in the discharge exhaust gas in which the individual substances are better distinguished and marked.

Acetylene (H_2C_2; 26 amu), hydrogen cyanide (HCN; 27 amu), acetonitrile (CH_3CN; 41 amu), cyanoacetylene (C_3HN; 51 amu), propane nitrile (C_2H_5CN; 55 amu), (butanenitrile; 69 amu), and (benzene; 78 amu) were the major compounds

https://dx.doi.org/10.1021/acsearthspacechem.0c00308
ACS Earth Space Chem. 2021, 5, 535−543

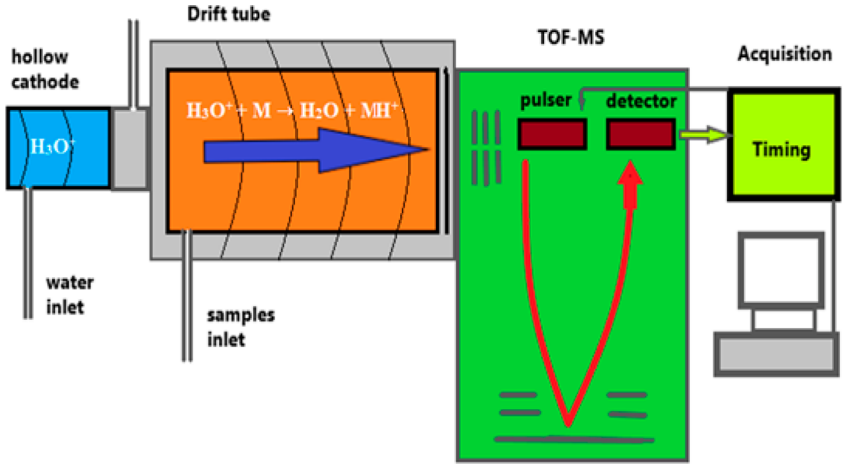

Figure 2. General scheme of the PTR-ToF-MS instrument.

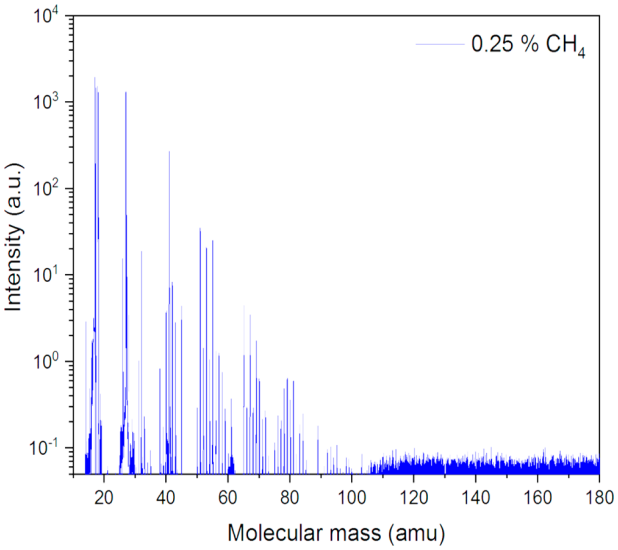

Figure 3. PTR-TOF mass spectrum of gaseous products produced in the discharge at the methane concentration of 0.25% in nitrogen.

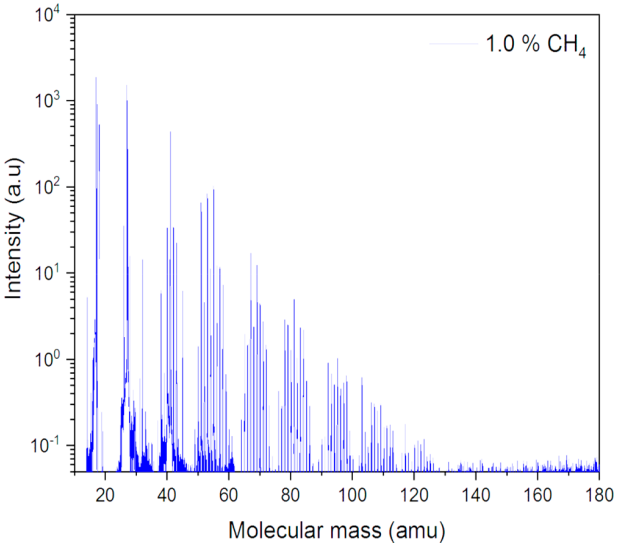

Figure 4. Mass spectrum of gaseous products produced in the discharge at themethane concentration of 1% in nitrogen.

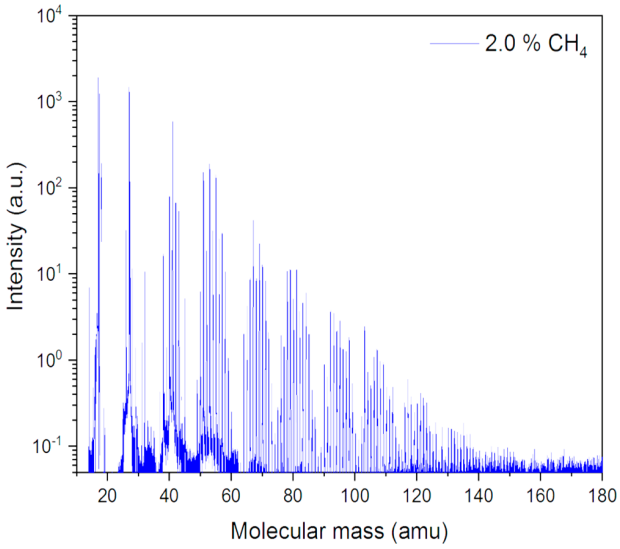

Figure 5. Mass spectrum of gaseous products produced in the discharge at themethane concentration of 2% in nitrogen.

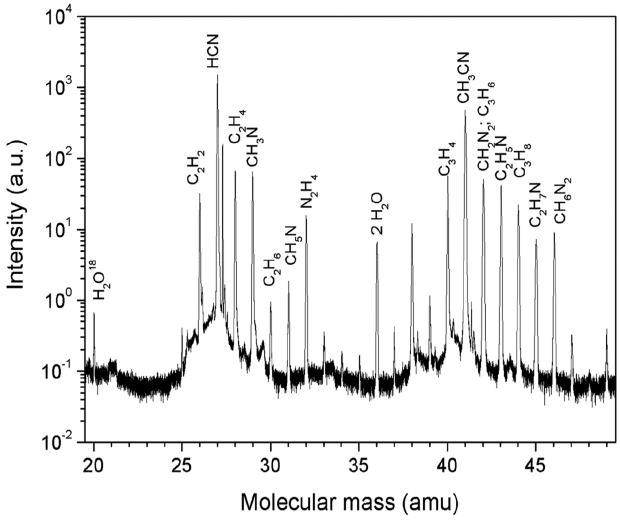

Figure 6. Identified mass spectrum (range of 20−50 g·mol^{-1}) measured in the discharge at the methane concentration of 1.5%.

detected by the PTR-TOF-MS under the presented conditions. Relative intensity ratios indicate that the most abundant products in the discharge were hydrogen cyanide and acetonitrile. All compounds mentioned above were detected

https://dx.doi.org/10.1021/acsearthspacechem.0c00308
ACS Earth Space Chem. 2021, 5, 535−543

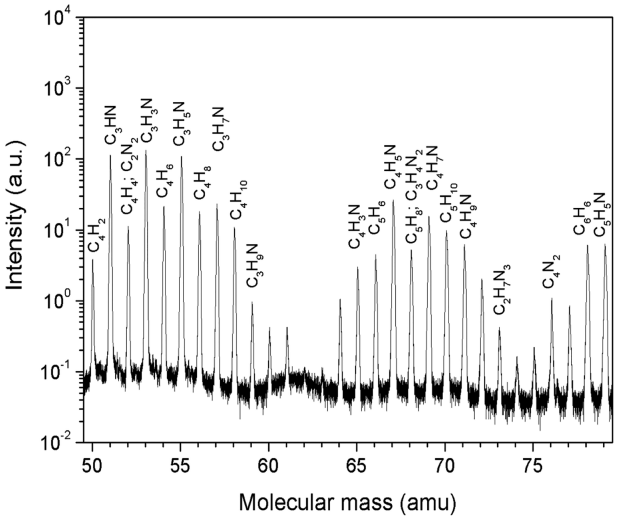

Figure 7. Identified mass spectrum (range of 50−80 g·mol^{-1}) measured in the discharge at the methane concentration of 1.5%.

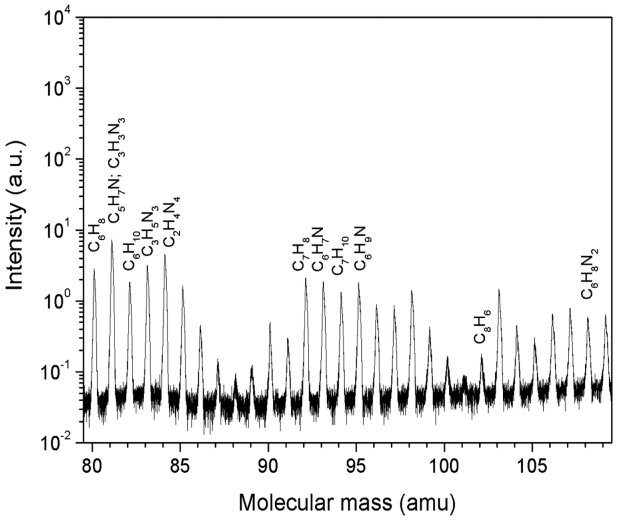

Figure 8. Identified mass spectrum (range of 80−110 g·mol^{-1}) measured in the discharge at the methane concentration of 1.5%.

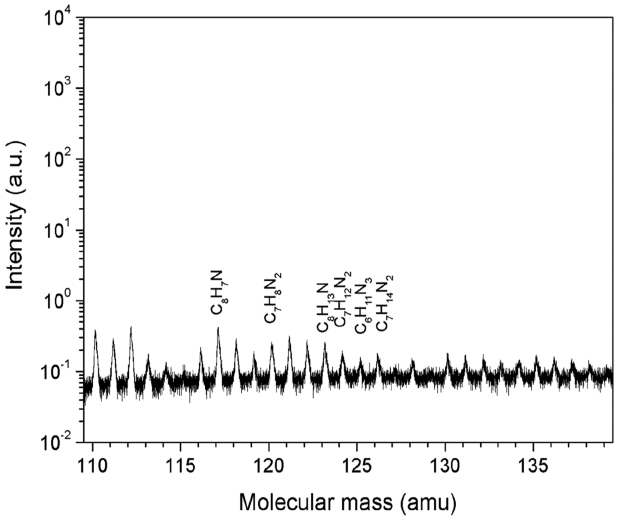

Figure 9. Identified mass spectrum (range of 110−140 g·mol^{-1}) measured in the discharge at the methane concentration of 1.5%.

or at least expected to be present on Titan according to the theoretical models[75,76] but their relative concentrations cannot be correctly compared with the data obtained from Titan's atmosphere because the current experiment was carried out at ambient laboratory temperature and thus bigger molecules like tholins were not synthesized effectively enough. Among more stable molecules, the C_4N_2 molecules were detected in the current experiment thanks to the very low limit of detection of the PTR-ToF-MS. As it was explained in the work of Coll et al.,[75] C_4N_2 has a very low stability at room temperature, so it is very difficult to analyze this compound at ambient temperature. Results of the presented experiments are also in very good agreement with other experimental studies.[77−79] Peng et al.[77] used UV-VUV synchrotron radiation. The C2, C3, C4, and most probably also C5 compounds were detected by INMS; the most abundant compounds were HCN, CH_3CN, and C_2N_2. Carrasco et al.[78] demonstrated the important role of methane concentration on the production of ammonia and consequent synthesis of heavier molecules.[78] The processes were studied in the PAMPRE plasma reactor via the optical emission spectroscopy.[78]

The full list of all up to now identified hydrocarbons and nitrogen-containing compounds is presented in Supporting Information. The relations to the other laboratory data as well as confirmed presence in Titan's atmosphere are also included there.

Figures 10 and 11 show relative intensities of selected species in the dependence on the methane concentration. Representative substances from different groups (aliphatic hydrocarbons, cyano, and aromatic compounds) were chosen to demonstrate how they arise or are not influenced by the methane concentration. The highest intensity increase is observed for the higher molecular weight substances such as benzene or toluene, especially at methane concentrations of 1−1.5%. The intensities of lower molecular weight molecules like hydrogen cyanide, acetylene, or acetonitrile are nearly independent of methane concentration in the range of 1−2% (2−4 sccm). This well reflects that lower molecular weight substances could be predominantly consumed for creation of higher molecular weight products at higher methane concentrations. HCN concentration reached the saturation limit of the current device during the discharge operation and thus, dependence of its intensity does not reflect the running processes properly.

The presented intensity dependencies reveal that the formation of hydrogen cyanide also increases with the increasing methane concentration. This is also consistent with the comparison of the results from the optical emission spectroscopy,[78] which shows an increase of the CN radicals' concentration at lower methane concentrations only.[25,30] The PTR-TOF technique has a disadvantage in its resolution limit and thus some compounds could not be distinguished. This is, unfortunately, also the case of HCN. The exact molecular weight of HCN M = 27.0253 g·mol^{-1} is very similar to the molecular weight of the C_2H_3 vinyl radical M = 27.0446 g·mol^{-1}. Because the mass resolving power for m/z < 60 is fwhm >1000 $m/\Delta m$, this particular difference Δm = 0.0193 at m/z = 28 is smaller than the instrument is able to distinguish and therefore both peaks are merged in one. At lower concentrations of methane, a large amount of CN radical is produced, causing a high HCN peak. As the concentration of methane increases, substances with higher molecular weights are produced and thus CN radicals are consumed and their concentration decreases. This causes a decrease in the intensity of the vinyl radical. However,

https://dx.doi.org/10.1021/acsearthspacechem.0c00308
ACS Earth Space Chem. 2021, 5, 535−543

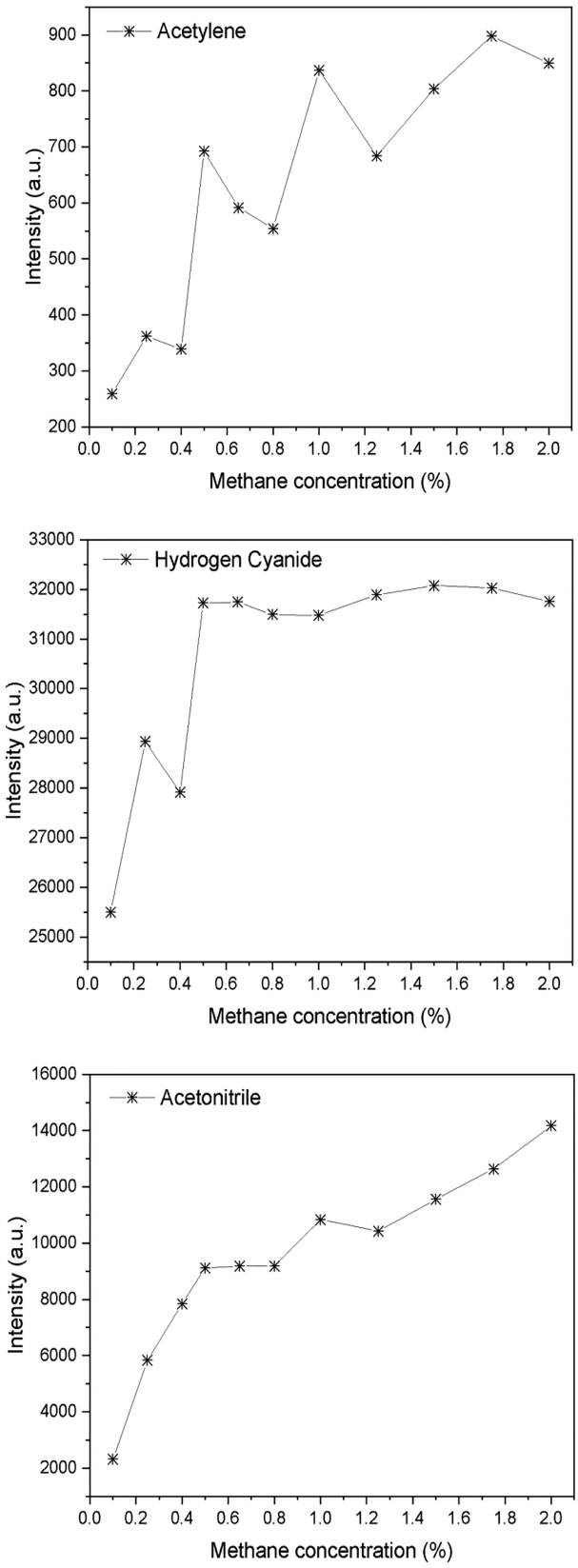

Figure 10. Dependence of the relative intensity of acetylene, hydrogen cyanide, and acetonitrile on the methane concentration in nitrogen.

the total hydrogen cyanide concentration is increasing. The peak deconvolution was applied to distinguish HCN and vinyl, and thus the relative intensity was calculated separately for HCN.

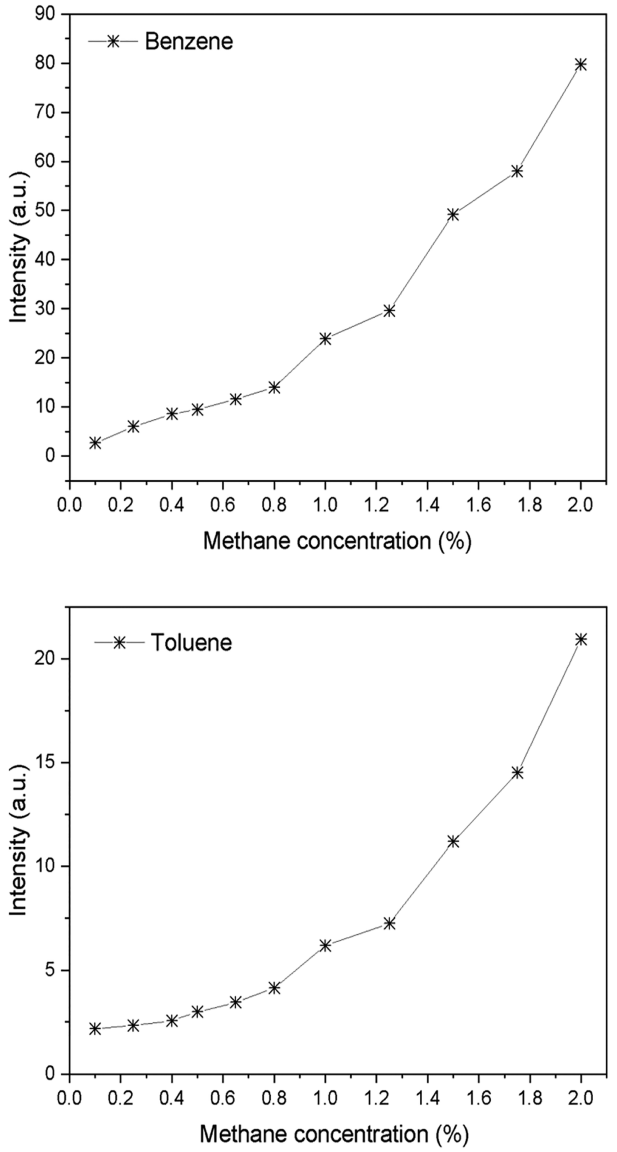

Figure 11. Dependence of the relative intensity of benzene and toluene on the methane concentration in nitrogen.

Reactions in the N_2–CH_4 Mixture. Hydrogen cyanide formation can occur with varying probabilities in a single step as outlined in the following reactions[25,26]

$$CH + N_2 \rightarrow HCN + N; \quad \Delta H_r^{\circ}{}_{298K} = 11.89\ kJ\cdot mol^{-1} \tag{1}$$

$$CH_2 + N_2 \rightarrow HCN + NH; \quad \Delta H_r^{\circ}{}_{298K} = 103.48\ kJ\cdot mol^{-1} \tag{2}$$

$$C_2H + N_2 \rightarrow HCN + CN; \quad \Delta H_r^{\circ}{}_{298K} = 9.83\ kJ\cdot mol^{-1} \tag{3}$$

where $\Delta H_r^{\circ}{}_{298K}$ is the standard enthalpy of the reaction.

Another possibility is the formation of hydrogen cyanide in two steps through the highly unstable intermediate H_2CN[25,26]

$$N + CH_3 \rightarrow H_2CN + H \tag{4}$$

$$H_2CN + N \rightarrow HCN + NH \tag{5}$$

or through the radical CN·:

$$N + CH_2 \rightarrow CN + H_2 \tag{6}$$

https://dx.doi.org/10.1021/acsearthspacechem.0c00308
ACS Earth Space Chem. 2021, 5, 535−543

$$CN + CH_4 \rightarrow HCN + CH_3 \quad (7)$$

Reactions 6 and 7 seem to be the most probable in this case due to the high CN concentration in the discharge, which was also confirmed by the OES results.[42]

During the electric discharge taking place in the mixture of N_2-CH_4, the molecules dissociate to form methane radicals (CH_3, CH_2, and CH), and C, H, and N atoms. Subsequently, these substances are precursors for the formation of other substances in the chain of chemical reactions.[80,81] Possible reactions in the mixture of N_2-CH_4 are reported in the work of Legrand et al.[80] They paid particular attention to the degree of methane decomposition and the formation of stable products along with many important reactions in the formation of other individual compounds.

Second order reactions for hydrocarbons and radicals can proceed as follows[80−82]

$$CH_4 + CH_3 \rightarrow C_2H_5 + H_2 \quad 1.7 \times 10^{-11} \times \exp(-11.500/T_g)\ cm^3 \cdot s^{-1} \quad (8)$$

$$CH_4 + CH_2 \rightarrow CH_3 + CH_3 \quad 7.1 \times 10^{-12} \times \exp(-5020/T_g)\ cm^3 \cdot s^{-1} \quad (9)$$

$$CH_4 + CH \rightarrow C_2H_4 + H_3 \quad 5.0 \times 10^{-11} \times \exp(-200/T_g)\ cm^3 \cdot s^{-1} \quad (10)$$

$$CH_4 + C_2H \rightarrow C_2H_2 + CH_3 \quad 3.0 \times 10^{-12} \times \exp(-250/T_g)\ cm^3 \cdot s^{-1} \quad (11)$$

$$CH_3 + C_2H_5 \rightarrow C_3H_8 \quad 4.7 \times 10^{-11}\ cm^3 \cdot s^{-1} \quad (12)$$

$$C_2H_5 + H \rightarrow C_2H_6 \quad 6.0 \times 10^{-11}\ cm^3 \cdot s^{-1} \quad (13)$$

$$C_2H_6 + CH_3 \rightarrow C_2H_5 + CH_4 \quad 2.5 \times 10^{-31} \times T_g^{-6.0} \times \exp(-3043/T_g)\ cm^3 \cdot s^{-1} \quad (14)$$

$$C_2H_6 + C_2H \rightarrow C_2H_2 + C_2H_5 \quad 6.0 \times 10^{-12}\ cm^3 \cdot s^{-1} \quad (15)$$

where T_g is the gas temperature.

Reactions between hydrocarbons and nitrogen can be the following[80−82]

$$CH_3 + N \rightarrow HCN + H_2 \quad 1.4 \times 10^{-11}\ cm^3 \cdot s^{-1} \quad (16)$$

$$CH_3 + N \rightarrow H_2CN + H \quad 1.3 \times 10^{-10}\ cm^3 \cdot s^{-1} \quad (17)$$

$$CH_3 + H + N_2 \rightarrow CH_4 + N_2 \quad 6.0 \times 10^{-29} \times (T_g/300)^{-1.8}\ cm^6 \cdot s^{-1} \quad (18)$$

$$C_2H_2 + H + N_2 \rightarrow C_2H_3 + N_2 \quad 1.05 \times 10^{-7} \times T_g^{-7.27} \times \exp(-3632/T_g)\ cm^6 \cdot s^{-1} \quad (19)$$

$$H + H + N_2 \rightarrow H_2 + N_2 \quad 1.5 \times 10^{-29} \times T_g^{-1.3}\ cm^6 \cdot s^{-1} \quad (20)$$

4. CONCLUSION

The presented paper was focused on the simulation of chemical processes in the gaseous mixture-like atmosphere of the moon Titan initiated by the abnormal glow discharge at atmospheric pressure and laboratory temperature. The stable discharge products were determined by the in situ PTR-TOF-MS, which was used for such experiments for the first time. A total number of about 40 aliphatic hydrocarbons, cyano, and amino compounds have been successfully identified and some aromatic compounds at higher methane concentrations were synthesized, too. The measured intensities show that a higher amount of higher molecular weight substances are produced with increasing concentration of methane.

Most of molecules created by the discharge were observed also in other laboratory experiments and they were also found in the atmosphere of Titan. Some peaks in the PTR-TOF-MS spectra have not been fully identified yet and therefore offer the possibility for further investigation. The use of the in situ PTR-TOF-MS was confirmed as a powerful tool for the fast determination of the stable discharge products. Moreover, the experiment design allows operation at low wall temperature, and thus conditions closer to Titan's surface can be established. The next paper will present the first results obtained at such conditions.

■ ASSOCIATED CONTENT

Supporting Information

The Supporting Information is available free of charge at https://pubs.acs.org/doi/10.1021/acsearthspacechem.0c00308.

Table S1, detected hydrocarbons and nitrogen compounds by PTR-TOF-MS; Figure S1, mass spectrum of products at a methane concentration of 0.1%; Figure S2, mass spectrum of products at a methane concentration of 0.4%; Figure S3, mass spectrum of products at a methane concentration of 0.5%; Figure S4, mass spectrum of products at a methane concentration of 0.65%; Figure S5, mass spectrum of products at a methane concentration of 0.8%; Figure S6, mass spectrum of products at a methane concentration of 1.25%; Figure S7, mass spectrum of products at a methane concentration of 1.5%; Figure S8, mass spectrum of products at a methane concentration of 1.75% (PDF)

■ AUTHOR INFORMATION

Corresponding Authors

Stanislav Chudják − *Faculty of Chemistry, Brno University of Technology, 612 00 Brno, Czech Republic*; orcid.org/0000-0001-5730-1961; Email: xcchudjak@fch.vut.cz

František Krčma − *Faculty of Chemistry, Brno University of Technology, 612 00 Brno, Czech Republic*; Email: krcma@fch.vut.cz

Author

Zdenka Kozáková − *Faculty of Chemistry, Brno University of Technology, 612 00 Brno, Czech Republic*

Complete contact information is available at: https://pubs.acs.org/10.1021/acsearthspacechem.0c00308

Notes

The authors declare no competing financial interest.

■ ACKNOWLEDGMENTS

This work was carried out within the frame of COST Action TD1308 and was partially supported by the Czech Ministry of Education, Youth, and Sports, Project No. LD15011.

■ REFERENCES

(1) Thaxton, Ch. B.; Bradley, W. L.; Olsen, R. L. *The Mystery of Life's Origin: Reassessing Current Theories*; Philosophical Library, 1984.

(2) Trainer, M. G. Atmospheric Prebiotic Chemistry and Organic Hazes. *Curr. Org. Chem.* **2013**, *17*, 1710−1723.
(3) Rimmer, P. B.; Rugheimer, S. Hydrogen cyanide in nitrogen-rich atmospheres of rocky exoplanets. *Icarus* **2019**, *329*, 124−131.
(4) Ranjan, S.; Sasselov, D. D. Influence of the UV Environment on the Synthesis of Prebiotic Molecules. *Astrobiology* **2016**, *16* (1), 68−88.
(5) Argento, D. C.; Reedy, R. C.; Stone, J. O. Modeling the earth's cosmic radiation. *Nucl. Instrum. Methods Phys. Res., Sect. B* **2013**, *294*, 464−469.
(6) He, Ch; Hörst, S. M.; Lewis, N. K.; et al. Gas Phase Chemistry of Cool Exoplanet Atmospheres: Insight from Laboratory Simulations. *ACS Earth and Space Chemistry.* **2019**, *3* (1), 39−50.
(7) Wogan, N.; Krissansen-Totton, J.; Catling, D. C. Abundant Atmospheric Methane from Volcanism on Terrestrial Planets Is Unlikely and Strengthens the Case for Methane as a Biosignature. *The Planetary Science Journal* **2020**, *1* (3), 58.
(8) Aplin, K. L. *Electrifying Atmospheres: Charging, Ionisation and Lightning in the Solar System and Beyond*; Springer Briefs in Astronomy; Springer Netherlands: Dordrecht, 2013.
(9) Ardaseva, A.; Rimmer, P. B.; Waldmann, I.; et al. Lightning chemistry on Earth-like exoplanets. *Mon. Not. R. Astron. Soc.* **2017**, *470* (1), 187−196.
(10) Riousset, J. A.; Nag, A.; Palotai, C. Scaling of conventional breakdown threshold: Impact for predictions of lightning and TLEs on Earth, Venus, and Mars. *Icarus* **2020**, *338*, 113506.
(11) Shaw, G. H. Earth's atmosphere - Hadean to early Proterozoic. *Chem. Erde* **2008**, *68* (3), 235−264.
(12) Catling, D. C.; Claire, M. W. How Earth's atmosphere evolved to an oxic state: A status report. *Earth Planet. Sci. Lett.* **2005**, *237* (1−2), 1−20.
(13) Wen, J. S.; Pinto, J.-P.; Yung, Y. L. Photochemistry of CO and H 2 O: Analysis of laboratory experiments and applications to the prebiotic Earth's atmosphere. *Journal of Geophysical Research: Atmospheres.* **1989**, *94* (D12), 14957−14970.
(14) Dewitt, H. L.; Trainer, M. T.; Pavlov, A. A.; et al. Reduction in Haze Formation Rate on Prebiotic Earth in the Presence of Hydrogen. *Astrobiology* **2009**, *9* (5), 447−453.
(15) Vasconcelos, F.A.; Pilling, S.; Agnihotri, A.; Rothard, H.; Boduch, P.; et al. Methylenimine and cyanomethanimine synthesis from ion irradiation of N_2-CH_4 ice: Implication on the formation of prebiotic molecules in outer solar system bodies. *Icarus* **2020**, *351*, 113944.
(16) Kaye, J. A.; Strobel, D. F. HCN formation on Jupiter: The coupled photochemistry of ammonia and acetylene. *Icarus* **1983**, *54* (3), 417−433.
(17) Wordsworth, R. D. Atmospheric nitrogen evolution on Earth and Venus. *Earth Planet. Sci. Lett.* **2016**, *447*, 103−111.
(18) Sholes, S. F.; Smith, M. L.; Claire, M. V.; et al. Anoxic atmospheres on Mars driven by volcanism: Implications for past environments and life. *Icarus* **2017**, *290*, 46−62.
(19) Daerden, F.; Neary, L.; Viscardy, S.; Garcia Munoz, A.; Clancy, R.T.; Smith, M.D.; Encrenaz, T.; Fedorova, A.; et al. Mars atmospheric chemistry simulations with the GEM-Mars general circulation model. *Icarus* **2019**, *326*, 197−224.
(20) Thøgersen, J.; Bak, E. N.; Finster, K.; et al. Light on windy nights on Mars: A study of saltation-mediated ionization of argon in a Mars-like atmosphere. *Icarus* **2019**, *332*, 14−18.
(21) Johnson, R. E.; Tucker, O. J.; Volkov, A A.N. Evolution of an early Titan atmosphere. *Icarus* **2016**, *271*, 202−206.
(22) Kammer, J.A.; Shemansky, D.E.; Zhang, X.; Yung, Y.L. Composition of Titan's upper atmosphere from Cassini UVIS EUV stellar occultations. *Planet. Space Sci.* **2013**, *88*, 86−92.
(23) Tokano, T. Nitrogen condensation in Titan's atmosphere under contemporary atmospheric composition. *Icarus* **2017**, *289*, 120−133.
(24) Hörst, S. M. Titan's atmosphere and climate. *Journal of Geophysical Research:Planets.* **2017**, *122* (3), 432−482.
(25) Hendrix, A. R.; Yung, Y. L. Energy Options for Future Humans on Titan. *Journal of Astrobiology & Outreach* **2017**, *05* (02), No. 1000157.
(26) Waite, J. H.; Young, D. T.; Cravens, T. E.; Coates, A. J.; Crary, F. J.; Magee, B.; Westlake, J. The process of tholin formation in Titan's upper atmosphere. *Science* **2007**, *316* (5826), 870−875.
(27) Paton, M. D.; Green, S. F.; Ball, A. J.; Zarnecki, J. C.; Hagermann, A. A. Detection of structure in asteroid analogue materials and Titan's regolith by a landing spacecraft. *Adv. Space Res.* **2016**, *58* (3), 415−437.
(28) Ferus, M.; Kubelik, P.; Knizek, A.; Pastorek, A.; Sutherland, J.; Civis, S.; et al. High Energy Radical Chemistry Formation of HCN-rich Atmospheres on early Earth. *Sci. Rep.* **2017**, *7* (6275), 1−9.
(29) Cleaves, H. J.; Chalmers, J. H.; Lazcano, A. L.; et al. A Reassessment of Prebiotic Organic Synthesis in Neutral Planetary Atmospheres. *Origins Life Evol. Biospheres* **2008**, *38* (2), 105−115.
(30) Lavvas, P.; Yelle, R. V.; Heays, A. N.; et al. N2 state population in Titan's atmosphere. *Icarus* **2015**, *260*, 29−59.
(31) Mcfadden, L. A. A.; Weissman, R. P.; Johnson, T. V. *Encyclopedia of the solar system*, 2nd ed.; Academic Press: Boston, 2007.
(32) Janda, M.; Machala, Z.; Electrical discharges. *Encyclopedia of Physical Organic Chemistry*; first ed.; 2017.
(33) *Encyclopedia of Physical Organic Chemistry*; Wang, Z.; Ed.; John Wiley & Sons, Hoboken, NJ, 2016.
(34) Zebker, A. H.; Stiles, B.; Hensley, S.; et al. Size and Shape of Saturn's Moon Titan. *Science* **2009**, *324* (5929), 921−923.
(35) Gilliam, A. E.; Lerman, A. Titan's missing ethane: From the atmosphere to the subsurface. *Icarus* **2016**, *275*, 252−258.
(36) Cardesin Moinelo, A.; Abildgaard, S.; Garcia Munoz, A.; Piccioni, G.; Grassi, D.; et al. No statistical evidence of lightning in Venus night-side atmosphere from VIRTIS-Venus Express Visible observations. *Icarus* **2016**, *277*, 395−400.
(37) Delitsky, M. L.; Baines, K. H. Storms on Venus: Lightning-induced chemistry and predicted products. *Planet. Space Sci.* **2015**, *113−114*, 184−192.
(38) Ingersoll, A. P. Cassini Exploration of the Planet Saturn: A Comprehensive Review. *Space Sci. Rev.* **2020**, *216* (8), No. 122.
(39) Zarka, P.; Farrell, W. M.; Kaiser, M. L.; et al. Study of solar system planetary lightning with LOFAR. *Planet. Space Sci.* **2004**, *52* (15), 1435−1447.
(40) Dyudina, U.; Delgenio, A.; Ingersoll, A.; et al. Lightning on Jupiter observed in the line by the Cassini imaging science subsystem. *Icarus* **2004**, *172* (1), 24−36.
(41) Konovalenko, A. A.; Kalinichenko, N. N.; Rucker, H. O.; et al. Earliest recorded ground-based decameter wavelength observations of Saturn's lightning during the giant E-storm detected by Cassini spacecraft in early 2006. *Icarus* **2013**, *224* (1), 14−23.
(42) Gibbard, S. G.; Levy, E. H.; Lunine, J. I.; et al. Lightning on Neptune. *Icarus* **1999**, *139* (2), 227−234.
(43) Becker, H. N.; Alexander, J. W.; Atreya, S. K.; et al. Small lightning flashes from shallow electrical storms on Jupiter. *Nature* **2020**, *584* (7819), 55−58.
(44) Riousset, J. A.; Nag, A.; Palotai, C. Scaling of conventional breakdown threshold: Impact for predictions of lightning and TLEs on Earth, Venus, and Mars. *Icarus* **2020**, *338*, 113506.
(45) Giles, R. S.; Greathouse, T. K.; Bonfond, B.; et al. Possible Transient Luminous Events Observed in Jupiter's Upper Atmosphere. *J. Geophys. Res.: Planets* **2020**, *125* (11), No. e2020JE006659.
(46) Fischer, G.; Tokano, T.; Macher, W.; et al. Energy dissipation of possible Titan lightning strokes. *Planet. Space Sci.* **2004**, *52* (5−6), 447−458.
(47) Ali, A.; Sittler, E. C.; Chornay, D.; et al. Organic chemistry in Titan's upper atmosphere and its astrobiological consequences: I. Views towards Cassini plasma spectrometer (CAPS) and ion neutral mass spectrometer (INMS) experiments in space. *Planet. Space Sci.* **2015**, *109−110*, 46−63.
(48) Ferus, M.; Kubelík, P.; Knížek, A. High Energy Radical Chemistry Formation of HCN-rich Atmospheres on early Earth. *Scientific Reports.* **2017**, *7* (1), 6275 DOI: 10.1038/s41598-017-06489-1.
(49) Bourgalais, J.; Carrasco, N.; Changeat, Q.; et al. Ions in the Thermosphere of Exoplanets: Observable Constraints Revealed by

Innovative Laboratory Experiments. *The Astrophysical Journal* **2020**, *895* (2), No. 77.
(50) Plankensteiner, K.; Reiner, H.; Schranz, B.; Rode, B. M. Prebiotic Formation of Amino Acids in a Neutral Atmosphere by Electric Discharge. *Angew. Chem., Int. Ed.* **2004**, *43* (14), 1886−1888.
(51) Bourgalais, J.; Carrasco, N.; Vettier, L.; Pernot, P. Low-Pressure EUV Photochemical Experiments: Insight on the Ion Chemistry Occurring in Titan's Atmosphere. *J. Geophys. Res.: Space Phys.* **2019**, *124* (11), 9214−9228.
(52) Cooke, I. R.; Sims, I. R. Experimental Studies of Gas-Phase Reactivity in Relation to Complex Organic Molecules in Star-Forming Regions. *ACS Earth and Space Chemistry.* **2019**, *3* (7), 1109−1134.
(53) da Silva, R. S.; Ventura, L. R.; Fellows, C. E.; Ballester, M. Y.; et al. A novel investigation of the N_2 (C3 Π u - B3 Π g) and N_2 (C″ 5 Π u - A ′; 5 Σ g +) band systems using accurate functional forms. *J. Quant. Spectrosc. Radiat. Transfer* **2020**, *253*, 107130.
(54) He, Ch; Hörst, S. M.; Lewis, N. K.; et al. Sulfur-driven haze formation in warm CO2-rich exoplanet atmospheres. *Nature Astronomy.* **2020**, *4* (10), 986−993.
(55) Mcguire, B. A.; Asvany, O.; Brünken, S.; Schlemmer, S. Laboratory spectroscopy techniques to enable observations of interstellar ion chemistry. *Nature Reviews Physics.* **2020**, *2* (8), 402−410.
(56) Alcouffe, G.; Cavarroc, M.; Cernogora, G.; et al. Capacitively coupled plasma used to simulate Titan's atmospheric chemistry. *Plasma Sources Sci. Technol.* **2010**, *19* (1), No. 015008.
(57) Pintassilgo, C. D.; Loureiro, J.; Cernogora, G.; Touzeau, M. Methane decomposition and active nitrogen in a N_2-CH_4 glow discharge at low pressures. *Plasma Sources Sci. Technol.* **1999**, *8* (3), 463−478.
(58) Mazankova, V.; Torokova, L.; Krcma, F.; et al. The Influence of CO_2 Admixtures on the Product Composition in a Nitrogen-Methane Atmospheric Glow Discharge Used as a Prebiotic Atmosphere Mimic. *Origins Life Evol. Biospheres* **2016**, *46* (4), 499−506.
(59) Esposito, A.; Lappa, M.; Zuppardi, G.; et al. On the Formation and Accumulation of Solid Carbon Particles in High-Enthalpy Flows Mimicking Re-Entry in the Titan Atmosphere. *Fluids* **2020**, *5* (2), 93.
(60) Dubois, D.; Carrasco, N.; Petrucciani, M.; et al. In situ investigation of neutrals involved in the formation of Titan tholins. *Icarus* **2019**, *317*, 182−196.
(61) Fleury, B.; Carrasco, N.; Gautier, T.; et al. Influence of CO on Titan atmospheric reactivity. *Icarus* **2014**, *238*, 221−229.
(62) Ellis, A. M.; Mayhew, C. *Proton transfer reaction mass spectrometry: principles and applications*; John Wiley & Sons: Chichester, West Sussex, 2014.
(63) Majchrzak, T.; Wojnowski, W.; Lubinska-Szczygeł, M.; Rozanska, A.; Namiesnik, J.; Dymerski, T.; et al. PTR-MS and GC-MS as complementary techniques for analysis of volatiles: A tutorial review. *Anal. Chim. Acta* **2018**, *1035*, 1−13.
(64) Pang, X. Biogenic volatile organic compound analyses by PTR-TOF-MS: Calibration, humidity effect and reduced electric field dependency. *J. Environ. Sci.* **2015**, *32*, 196−206.
(65) Pleil, J. D.; Hansel, A.; Beauchamp, J. Advances in proton transfer reaction mass spectrometry (PTR-MS): applications in exhaled breath analysis, food science, and atmospheric chemistry. *Journal of Breath Research* **2019**, *13* (3), No. 039002.
(66) Malásková, M.; Olivenza-León, D.; Piel, F.; et al. Compendium of the Reactions of H_3O^+ With Selected Ketones of Relevance to Breath Analysis Using Proton Transfer Reaction Mass Spectrometry. *Front. Chem.* **2019**, *7*, 7.
(67) Sekimoto, K.; Li, S. M.; Yuan, B.; et al. Calculation of the sensitivity of proton-transfer-reaction mass spectrometry (PTR-MS) for organic trace gases using molecular properties. *Int. J. Mass Spectrom.* **2017**, *421*, 71−94.
(68) Dunne, E.; Galbally, I. E.; Lawson, S.; et al. Interference in the PTR-MS measurement of acetonitrile at m/z 42 in polluted urban air—A study using switchable reagent ion PTR-MS. *Int. J. Mass Spectrom.* **2012**, *319*−*320*, 40−47.
(69) Papurello, D.; Boschetti, A.; Silvestri, S.; et al. Real-time monitoring of removal of trace compounds with PTR-MS: Biochar experimental investigation. *Renewable Energy* **2018**, *125*, 344−355.
(70) Mancuso, S.; Taiti, C.; Bazihizina, N.; et al. Soil volatile analysis by proton transfer reaction-time of flight mass spectrometry (PTR-TOF-MS). *Applied Soil Ecology.* **2015**, *86*, 182−191.
(71) Brilli, F.; Gioli, B.; Ciccioli, B.; et al. Proton Transfer Reaction Time-of-Flight Mass Spectrometric (PTR-TOF-MS) determination of volatile organic compounds (VOCs) emitted from a biomass fire developed under stable nocturnal conditions. *Atmos. Environ.* **2014**, *97*, 54−67.
(72) Horvath, G.; Krcma, F.; Polachova, L.; et al. Organic chemistry of NH_3 and HCN induced by an atmospheric abnormal glow discharge in N_2-CH_4 mixtures. *Eur. Phys. J.: Appl. Phys.* **2011**, *53* (1), No. 11001.
(73) Ricard, A.; Cernogora, G.; Fitaire, M.; et al. Measurements in N_2-CH_4(C_2H_2) discharges of reaction rates and thermochemical constants for Titan atmosphere study. *Planet. Space Sci.* **1995**, *43* (1−2), 41−46.
(74) Dagaut, P.; Glarborg, P.; Alzueta, M. U. The oxidation of hydrogen cyanide and related chemistry. *Prog. Energy Combust. Sci.* **2008**, *34*, 1−46.
(75) Coll, P.; Coscia, D.; Gazeau, M. C.; et al. Organic chemistry in Titan's Atmosphere: new data from laboratory simulations at low temperature. *Adv. Space Res.* **1995**, *16* (2), 93−103.
(76) Bernard, J.-M.; Coll, P.; Coustenis, A.; Raulin, A. F. Experimental simulation of Titan's atmosphere: Detection of ammonia and ethylene oxide. *Planet. Space Sci.* **2003**, *51* (14−15), 1003−1011.
(77) Peng, Z.; Gautier, T.; Carrasco, N.; et al. Titan's atmosphere simulation experiment using continuum UV-VUV synchrotron radiation. *Journal of Geophysical Research: Planets.* **2013**, *118* (4), 778−788.
(78) Carrasco, N.; Gautier, T.; Es-Sebbar, E. T.; et al. Volatile products controlling Titan's tholins production. *Icarus* **2012**, *219* (1), 230−240.
(79) Torokova, L.; Watson, J.; Krcma, F.; et al. Gas Chromatography Analysis of Discharge Products in N 2 -CH 4 Gas Mixture at Atmospheric Pressure: Study of Mimic Titan's Atmosphere. *Contrib. Plasma Phys.* **2015**, *55* (6), 470−480.
(80) Legrand, J.-C.; Diamy, A. M.; Hrach, R.; Hrachová, V. Kinetics of reactions in CH_4-N_2 afterglow plasma: a simplified model. *Vacuum* **1998**, *50* (3−4), 491−495.
(81) Loison, J. C.; Hébrard, E.; Dobrijevic, M.; et al. The neutral photochemistry of nitriles, amines and imines in the atmosphere of Titan. *Icarus* **2015**, *247*, 218−247.
(82) Legrand, J. C.; Diamy, A. M.; Hrach, R.; Hrachova, V. Methane Conversion in the Flowing Afterglow of a Dinitrogen Microwave Plasma: Initiation of the Reaction. *Contrib. Plasma Phys.* **1997**, *37* (6), 521−537.

https://dx.doi.org/10.1021/acsearthspacechem.0c00308
ACS Earth Space Chem. 2021, 5, 535−543